

Hydrologic connectivity In the McMurdo Dry Valleys, Antarctica: Water-mediated mass and energy fluxes in streams and soils

By

Adam N. Wlostowski

B.S., The Pennsylvania State University, 2010

M.S., The Pennsylvania State University, 2012

A dissertation submitted to the
Faculty of the Graduate School of the
University of Colorado in partial fulfillment
of the requirement for the degree of
Doctor of Philosophy
Department of Civil, Environmental, and Architectural Engineering
2017

This dissertation entitled:

Hydrologic connectivity In the McMurdo Dry Valleys, Antarctica: Water-mediated mass and energy fluxes in streams and soils

written by Adam N. Wlostowski

has been approved for the Department of Civil, Environmental, and Architectural Engineering

Dr. Michael N. Gooseff

Dr. Diane McKnight

Dr. Roseanna Neupauer

Dr. Ben Livneh

Dr. Robert S. Anderson

Date _____

The final copy of this thesis has been examined by the signatories, and we find that both the content and the form meet acceptable presentation standards of scholarly work in the above mentioned discipline.

Wlostowski, Adam Nicholas (Ph.D., Civil, Environmental and Architectural Engineering)

Hydrologic connectivity In the McMurdo Dry Valleys, Antarctica: Water-mediated mass and energy fluxes in streams and soils

Thesis directed by Associate Professor Michael N. Gooseff

The McMurdo Dry Valleys (MDV) of Antarctica is an ideal landscape for studying the relationship between hydrologic connectivity and ecosystems. In the MDVs, aquatic and terrestrial ecosystems are controlled by patterns of hydrologic connectivity. It is hypothesized that climate warming in the MDV ecosystem will amplify hydrologic connectivity among landscape units (glaciers, streams, soils, and lakes), causing changes in the structure and function of the MDV ecosystem. This dissertation is devoted to understanding the current and future state of water-mediated mass and energy fluxes in MDV streams and soils.

Chapter 1 synthesizes 20 years of stream gauge observations (discharge, water temperature, and specific conductance) to assess patterns of hydrologic connectivity between glaciers, streams and lakes. Results reveal hydrologic patterns across daily, annual and inter-annual timescales, which together characterize the hydrologic regime of MDV streams. Also, stream gauge data display a relationship between stream length and hydrologic regime. Longer streams are more intermittent, warmer, and saltier than shorter streams. This work provides physical context for understanding biological differences among MDV streams, while providing a methodological template for quantifying hydrologic connectivity.

Chapter 2 investigates the nature of concentration-discharge relationships for weathering-derived solutes in MDV streams. The relative simplicity of MDV “watersheds” permits the use of concentration-discharge relationships to infer hydrologic and chemical mixing dynamics occurring along the river corridor. Long-term stream geochemical data show that weathering derived solutes exhibit chemostatic C-Q relationships. Chemostasis implies that rates of solute production and/or mobilization scale proportionately with stream discharge. A numerical weathering and solute transport model suggests that chemostasis is maintained by a positive relationship between weathering rate and discharge along the stream corridor.

Finally, Chapters 3 and 4 investigate water-mediated energy fluxes within the soil habitat. Nematode communities in MDV are highly sensitive to the thermodynamic regime of active layer soils. Soil moisture and air temperature data were collected across natural wetness gradients adjacent to fluvial features to assess the control of soil moisture on the soil thermal regime. Observations show that wetter soils freeze less frequently and more gradually than drier soils. Also, a numerical soil heat transfer model suggests that increases in soil moisture and air temperature result in warmer average habitat temperature, an extension of the duration of time the soil habitat spends above freezing, and a reduction in the rate and frequency of freezing. The results of this chapter provide a physical context for understanding current and future patterns of ecosystem structure and function in MDV soils.

This is for:

Judy and Paul Wlostowski

Matt, Colleen, Samuel and Oliver Wlostowski

Mary Jane and Raymond Blatner

Anita and Stanley Wlostowski

and

Erika May Smull

Without your love and support, this document wouldn't exist.

ACKNOWLEDGEMENTS

I would like to thank my advisor, Dr. Michael N. Gooseff, for his enduring support and encouragement. Dr. Gooseff is an exemplary role model as a person and a scientist. There is no better motivation for excellence than his never-ending enthusiasm for science.

I must also thank my committee members for taking time to read and comment on this work. Their comments and suggestions have enhanced the quality of this science. Technical advice from Dr. Adam S. Ward over the last 5 years have helped to define the direction and scope of this work, specifically Chapter 2. My peers at the University of Colorado Department of Civil Engineering, Institute of Arctic and Alpine Research, and the Gooseff Lab group have provided ongoing constructive criticisms that have and continue to improve this work.

This research was funded by the National Science Foundation in support of the McMurdo Long-Term Ecological Research program (grants 9614938, 9810219, 0423595, 0096250, 0832755, 1041742, and 1115245). Any opinions, findings, conclusions, or recommendations expressed in this dissertation are those of the authors and do not necessarily reflect the views of the National Science Foundation.

CONTENTS

CHAPTER 1: Patterns of hydrologic connectivity in the McMurdo Dry Valleys, Antarctica: a synthesis of 20 years of hydrologic data.....	1
1.1 INTRODUCTION	1
1.2 STUDY SITE.....	4
1.2.1 Lake Fryxell Basin and New Harbor	6
1.2.2 Lake Hoare Basin.....	7
1.2.3 Lake Bonney Basin	8
1.2.4 Lake Vanda Basin	9
1.3 METHODS	10
1.3.1 Measurement methods	10
1.3.2 Available Data	11
1.3.3 Characterizing Connectivity on Annual Timescales.....	11
1.3.4 Characterizing Connectivity on Daily Timescales	12
1.3.5 Characterizing Connectivity on Inter-annual Timescales.....	14
1.4 RESULTS	16
1.4.1 Inter-annual Connectivity Dynamics	16
1.4.2 Annual Connectivity Dynamics.....	27
1.4.3 Daily Connectivity Dynamics.....	30
1.5 DISCUSSION.....	33
1.5.1 Annual electrical conductivity patterns infer differences in the connectivity of hyporheic zones	33
1.5.2 Biological implications of variability in annual flow connectivity	36
1.5.3 The control of stream length and valley position on stream temperature dynamics ...	38
1.5.4 Electrical Conductivity – discharge relationships.....	40
1.5.5 Climatic control on inter-annual flow variability	42
1.6 CONCLUSIONS.....	43
1.7 APPENDIX.....	45

CHAPTER 2: Concentration–discharge relationships of weathering-derived solutes in streams of the McMurdo Dry Valleys, Antarctica	50
2.1 INTRODUCTION	50
2.1.1 Concentration discharge relationships and catchment function.....	50
2.1.2 Silicon cycle in Antarctic streams.....	52
2.1.3 Chapter goals and hypotheses	55
2.2 STUDY SITE.....	56
2.3 METHODS	60
2.3.1 Long-term stream geochemical sampling and analysis	60
2.3.2 Numerical weathering and transport model.....	62
2.3.3 Model parameterization	66
2.3.4 Model simulations.....	71
2.4 RESULTS	73
2.4.1 Long-term geochemical observations.....	73
2.4.2 Short-term Stream Channel and Hyporheic Si and $\delta^{18}\text{O}$ Observations	79
2.4.3 Numerical Model Simulations of Si weathering and transport in Von Guerard Stream	81
2.5 DISCUSSION.....	92
2.5.1 Chemical weathering in Antarctic streams and hyporheic zones	92
2.5.2 Dynamic hydrologic controls on C-Q relationships	94
2.5.3 Dynamic Geochemical Controls on C-Q relationships.....	98
2.6 CONCLUSION.....	100
2.7 APPENDIX.....	102
CHAPTER 3: The control of soil moisture on the frequency and rate of freezing events in shallow active layer soils in the McMurdo Dry Valleys, Antarctica	109
3.1 INTRODUCTION	109
3.2 STUDY SITE.....	112
3.3 METHODS	121
3.4 RESULTS	127
3.5 DISCUSSION	134

3.6 CONCLUSION.....	139
3.7 APPENDIX.....	141
CHAPTER 4: The thermodynamic regime of Antarctic soils under a warmer and wetter future	
.....	145
4.1 INTRODUCTION	145
4.2 METHODS & STUDY SITE	146
4.2.1 Surface energy budget and subsurface thermal models.....	146
4.2.2 Meteorological Forcing Data	149
4.2.3 Study Site.....	150
4.3 RESULTS	150
4.3.1 Meteorological Data.....	150
4.3.2 Ground temperature modeling results.....	154
4.3.3 Scenario analysis.....	166
4.4 DISCUSSION.....	171
4.5 CONCLUSION.....	178
4.6 APPENDIX.....	179
CHAPTER 5: Conclusions	197
BIBLIOGRAPHY.....	204

FIGURES

Figure 1.1: Select photos of glacial meltwater streams in the McMurdo Dry Valleys. (Top Left) Adams Stream flowing from Adams Glacier. (Top right) Eastward looking aerial view of the Onyx River flowing through Wright Valley. (Bottom left) Meltwater from the Sues Glacier flows through House Stream and into western Lake Hoare (a.k.a Lake Chad). (Bottom right) A Parshall flume at the gauge on Andersen Creek measures discharge entering the eastern end of Lake Hoare..... 2

Figure 1.2: Site map showing gauged streams in the Taylor and Wright Valleys. The Onyx River flows through the Wright Valley from Lake Brownworth to Lake Vanda. The Taylor Valley has three primary lake drainages, which are shown in greater detail in Figures 1.3, 1.4, and 1.5..... 6

Figure 1.3: Gauged streams within the Fryxell and New Harbor basins. Gauge locations are shown as black squares along the blue stream path..... 7

Figure 1.4: Gauged streams within the greater Lake Hoare basin..... 8

Figure 1.5: Gauged streams within the Lake Bonney Basin..... 9

Figure 1. 6: Q (blue), EC (black) and T (red) data from a 7-day period on Canada Stream during January 1997. All variables exhibit diurnal variations. Similar diurnal variations are observed at all other gauge locations. 13

Figure 1.7: Flow duration curves for gauged streams draining into Lake Fryxell and the Ross Sea (A, B), Lake Hoare (C), Lake Bonney (D), and Lake Vanda in the Wright Valley (E). Note the larger y-axis range for duration curves for streams in the Wright Valley (E). 17

Figure 1. 8: Flow duration curve slopes for all gauged streams. Red bars show streams draining into Lake Fryxell, the green bar shows Commonwealth stream draining into the Ross Sea, blue bars show streams draining into Lake Hoare, black bars show streams draining into Lake Bonney, and orange bars show the Onyx at Vanda and LWRT. 19

Figure 1.9: Specific conductance duration curves for EC-monitored streams draining into Lake Fryxell and the Ross Sea (A, B), Lake Hoare (C), and Lake Bonney (D)..... 20

Figure 1.10: Conductivity duration curve slopes for streams in the Taylor Valley. Red bars show streams draining into Lake Fryxell, the green bar show Commonwealth Stream draining into the Ross Sea, blue bars show streams draining into Lake Hoare, and black bars show streams draining into Lake Bonney..... 21

Figure 1.11: Water temperature duration curves for temperature monitored streams draining into Lake Fryxell and the Ross Sea (A, B), Lake Hoare (C), and Lake Bonney. 23

Figure 1.12: Temperature duration curve slopes for streams in the Taylor Valley. Red bars show streams draining into Lake Fryxell, the green bar shows Commonwealth Stream draining into the Ross Sea, blue bars show streams draining into Lake Hoare, and black bars show streams draining into Lake Bonney..... 23

Figure 1.13: Historical runoff volumes for the Onyx River at the Vanda gauge (black) and Canada Stream at the Canada gauge (red).	25
Figure 1.14: (A) Annual observed runoff entering Lake Fryxell and (B) stream-specific proportional contributions to annual observed runoff into Lake Fryxell. These data represent only the observed runoff measured at gauge locations. For each year, streams with missing records are indicated with symbols, see key at bottom of plot.	26
Figure 1.15: The mean t_5 (blue dots) and t_{95} (red dots) of annual streamflow for all gauged streams. Black error bars show +/- one standard deviation for start and end times. No error bars are shown for Bohner Stream because only a single year of record is currently available. Average flow season duration is listed for each stream.	28
Figure 1.16: log-log slopes (b parameter) for EC-Q relationships. Red error bars show the 95% confidence interval of the best fitting b parameter.	29
Figure 1.17: Average 24-hour Q, T, and EC patterns for streams within the Taylor Valley. Blue markers show hourly average discharge, red markers show hourly average water temperature, and green markers show hourly average specific conductance. The y-axis has been normalized over the observed range for each variable, such that daily maxima equal unity and daily minima equal zero.	31
Figure 1.18: Variation coefficients of average 24-hour EC (green) and Q (blue) data. The daily average variation in EC is far less than the daily average variation in Q	32
Figure 1.19: Median EC as a function of stream length, from glacier to gauge.	34
Figure 1.20: Median T as a function of stream length from glacier to gauge.	39
Figure 1.A1: log-log plots of EC-Q relationships for 14 streams within the Taylor Valley. Daily average values of Q and EC were used for this analysis. The blue line shows the best-fit slope of the relationship, and the black dashed lines shows a slope of -1, which indicates a pure dilution signal.	48
Figure 1.A2: Daily average T plotted as a function of daily average Q for Canada (blue open circles) and Santa Fe streams (closed red circles).	49
Figure 2.1: (a) An aerial image of a glacier-stream-lake hydrologic system.	52
Figure 2.2: Location map of the McMurdo Dry Valleys. The Taylor Valley, the research hub of the McMurdo Dry Valleys LTER, is indicated. Cartographic credit: Brad Herried, Polar Geospatial Center, University of Minnesota.	57

Figure 2.3: (a) Streamflow record at Canada Stream during the 2009/10 austral summer, and (b) the long-term record of total annual streamflow volumes from all gauged streams in the Lake Fryxell Basin (b). 58

Figure 2.4: Eight streams in eastern Taylor Valley considered in this study. WorldView3 Imagery courtesy of Polar Geospatial Center, University of Minnesota. 59

Figure 2.5: Optimal weathering rate constant values, λ , from *Gooseff et al.* (2002) plotted as a function of Discharge. A vague positive correlation is evident and the range of discharge values considered in this study is all < 14 L/sec. The linear relationship is insignificant at the 5% level. 68

Figure 2.6: Upper boundary forcing data used to drive the GIPL heat transfer model, which is used to approximate thaw depth beneath the streambed of Von Guerard Stream. 69

Figure 2.7: Soil water phase composition curve from 15cm depth in the hyporheic zone of Von Guerard Stream. The abrupt drop in soil moisture content at below freezing temperatures shows that the hyporheic zone freezes rapidly. The freezing characteristic curve is fit with the power law model of Equation 2.8. 71

Figure 2.8: The distribution of dissolved silicon in water samples from eight streams in the Fryxell Basin. Boxplots are arranged from left to right in order of decreasing stream length. 74

Figure 2.9: Stream water Na:Ca and Na:K ratios for eight streams in the Fryxell Basin are shown as box plots. Black asterisk symbols indicate the Na:Ca and Na:K ratios of glacier ice in the ablation zone of source glaciers for each stream (data from Lyons et al., 2003). 75

Figure 2.10: Concentration-discharge relationships of weathering derived solutes (Si, Ca⁺, K⁺, and HCO₃⁻) for eight streams in eastern Taylor Valley. Concentration magnitudes of some solutes are scaled to optimize presentation in log-log space. Scaling y-axis magnitudes does not affect the apparent log-log slope in these plots. 76

Figure 2.11: Optimal *b* parameter values and 95% confidence intervals from power law regression of concentration-discharge relationships. A *b* parameter value equal to 0 indicates a purely chemostatic regime, whereas a *b* parameter value of -1 indicates a dilution dominated regime. All streams exhibit near-chemostatic behavior. 77

Figure 2.12: Silica denudation rates plotted as a function of annual specific discharge for streams in the eastern Taylor Valley. Si denudation rates for other glacier-covered catchments across the world are also shown (data from Anderson et al. [1997a]). 78

Figure 2.13: Daily Si samples on Von Guerard stream during January 2016. The top panel shows discharge and electrical conductivity (EC) observed during this period, and the bottom panel shows Si concentrations observed in the stream channel (blue dots) and hyporheic zone (red dots). 80

Figure 2.14: High-resolution $\delta^{18}\text{O}$ samples from Von Guerard Stream during January 2016. The top panel shows discharge and EC observed during this period, and the bottom panel shows $\delta^{18}\text{O}$ observed in the stream channel (blue dots) and hyporheic zone (red dots). 81

Figure 2.15: Simulated and observed annual cumulative discharge for all flow seasons between 2004/05 and 2012/13..... 82

Figure 2.16: Simulated and observed hydrographs for a low flow year (2005/06) and a high flow year (2008/09). Generally, the flood routing model was better able to simulate low-flow years than high flow years. This discrepancy is attributed to the inability of the simple flood routing scheme to simulate baseflow dynamics. 83

Figure 2.17: Thaw depth simulated by GIPL between July 2004 and July 2006. 84

Figure 2.18: Model 2 Monte-Carlo simulation results for α and λ . Red markers indicate the best performing parameter set. Simulations resulting in Mean Absolute Error (MAE) values above 2 mg/L are not shown. 85

Figure 2. 19: Simulated Si concentrations plotted against observed Si concentrations for each of the three models. 86

Figure 2. 20: Mean absolute error (MAE) of each of the three models. The best performing model is OTIS-mdv with λ as a function of Q..... 87

Figure 2.21: Observed and simulated Si distributions. Simulated Si distributions include only simulated Si concentrations at times when observations were made. 88

Figure 2.22: Observed and simulated Si-Q relationships. All models over predict Si concentrations at low flows and under predict Si concentrations at high flows. However, the best performing model is the OTIS-mdv with λ as a function of Q. 89

Figure 2.23: Simulation results from the 2010/11 season, a high flow year. The top panel shows simulated discharge, main channel concentration, storage zone concentration, and observations. Resultant concentration time series from all three models are shown with different colors. The bottom panel shows storage zone area for model 1 (red) and models 2 and 3 (black line). 90

Figure 2.24: Simulation results from the 2011/12 season, a low flow year. The top panel shows simulated discharge, main channel concentration (C), hyporheic zone concentration (C_{HZ}), and observations. Resultant concentration time series from all three models are shown with different colors. The bottom panel shows storage zone area for model 1 (red) and models 2 and 3 (black line). 91

Figure 2.25: Model 2 results for the 2009/10 flow season under two different exchange rate scenarios. Red lines show model results for the optimal α value (7.9×10^{-5} 1/sec), whereas the black lines show model results for an unrealistically low α value (7.9×10^{-7} 1/sec). 95

Figure 2. 26: Progressive hydrologic turnover of the hyporheic zone for nine flow seasons on Von Guerard Stream. Complete hydrologic turnover is defined here as the time for required for hyporheic zone concentrations to achieve a 90% reduction from an initial concentration. 97

Figure 2.27: Hydrologic turnover time plotted as a function of annual flow for seasons when complete hydrologic turnover was achieved..... 98

Figure 2.A1: Simulation results from the 2004/05 season. The top panel shows simulated discharge, main channel concentration (C), hyporheic zone concentration (C_{HZ}), and observations. Resultant concentration time series from all three models are shown with different colors. The bottom panel shows storage zone area for model 1 (red) and models 2 and 3 (black line). 102

Figure 2.A2: Simulation results from the 2005/06 season. The top panel shows simulated discharge, main channel concentration (C), hyporheic zone concentration (C_{HZ}), and observations. Resultant concentration time series from all three models are shown with different colors. The bottom panel shows storage zone area for model 1 (red) and models 2 and 3 (black line). 103

Figure 2.A3: Simulation results from the 2006/07 season. The top panel shows simulated discharge, main channel concentration (C), hyporheic zone concentration (C_{HZ}), and observations. Resultant concentration time series from all three models are shown with different colors. The bottom panel shows storage zone area for model 1 (red) and models 2 and 3 (black line). 104

Figure 2.A4: A1: Simulation results from the 2007/08 season. The top panel shows simulated discharge, main channel concentration (C), hyporheic zone concentration (C_{HZ}), and observations. Resultant concentration time series from all three models are shown with different colors. The bottom panel shows storage zone area for model 1 (red) and models 2 and 3 (black line). 105

Figure 2.A5: Simulation results from the 2008/09 season. The top panel shows simulated discharge, main channel concentration (C), hyporheic zone concentration (C_{HZ}), and observations. Resultant concentration time series from all three models are shown with different colors. The bottom panel shows storage zone area for model 1 (red) and models 2 and 3 (black line). 106

Figure 2.A6: Simulation results from the 2009/10 season. The top panel shows simulated discharge, main channel concentration (C), hyporheic zone concentration (C_{HZ}), and observations. Resultant concentration time series from all three models are shown with different colors. The bottom panel shows storage zone area for model 1 (red) and models 2 and 3 (black line). 107

Figure 2.A7: Simulation results from the 2012/13 season. The top panel shows simulated discharge, main channel concentration (C), hyporheic zone concentration (C_{HZ}), and observations. Resultant concentration time series from all three models are shown with different

colors. The bottom panel shows storage zone area for model 1 (red) and models 2 and 3 (black line). 108

Figure 3.1: Location map of the Taylor Valley. Met stations and Active Layer Monitoring Sites (ALMS) within the valley are shown..... 115

Figure 3.2: Aerial image of Von Guerard ALMS. Yellow markers show the position of vertical sensor arrays in the channel thalweg, wetter margin, and dry distal soils. Stream flow is oriented from the bottom of the image towards the top of the image. WorldView3 imagery provided by the University of Minnesota Polar Geospatial Center. 118

Figure 3.3: Aerial image of Green Creek ALMS. Yellow markers show the position of vertical sensor arrays in the channel thalweg, wetter margin, and dry distal soils. Stream flow is oriented from left to right in the image. WorldView3 imagery provided by the University of Minnesota Polar Geospatial Center. 119

Figure 3.4: Aerial image of Watertrack B ALMS. Yellow markers show the position of vertical sensor arrays in the channel thalweg, wetter margin, and dry distal soils. Flow is oriented from the bottom to top of the image. WorldView3 imagery provided by the University of Minnesota Polar Geospatial Center. 120

Figure 3.5: Aerial image of Wormherder Creek ALMS. Yellow markers show the position of vertical sensor arrays in the channel thalweg, wetter margin, and dry distal soils. Flow is oriented from right to left in the image. WorldView3 imagery provided by the University of Minnesota Polar Geospatial Center. 121

Figure 3.6: Coincidentally observe temperature and volumetric soil moisture content (θ) at 15 cm depth between February 1, 2015 and March 15, 2015 (top panel) are used to create soil moisture phase composition curves (bottom panel). The freezing window is illustrated on the soil moisture phase composition curve (bottom panel) by two vertical red lines. 126

Figure 3.7: The number of days above freezing (A) and the percentage of observed time above freezing (B) at 10cm depth at each active layer monitoring site. The percentage of time above freezing is the percent of total observation time that ground temperature at 10 cm was above freezing. 128

Figure 3.8: Summer (December - February) mean 10 cm temperature (A), 15 cm volumetric water content (B), and 15 cm specific conductance (C) at active layer monitoring sites. 129

Figure 3.9: Freezing windows at all ALMS locations calculated by moisture phase composition curve thresholds. Red lines show the width of the thermal window at specific ALMS sites, whereas black dashed lines show the average width of the freezing window among all sites. The freezing window was not calculated at several distal sites because soil moisture was too low to generate soil moisture phase composition curves. 130

Figure 3.10: Number of freeze events recorded between January 2014 and February 2016 at active layer monitoring sites.	131
Figure 3.11: Number of freeze-events at 10cm as a function of mean austral summer (December – February) volumetric water content at 15 cm.	132
Figure 3.12: 10 cm Freezing rate plotted as a function of 15 cm antecedent soil moisture	133
Figure 3.13: A pronounced “zero-curtain”, where ground temperature remains nearly constant at 0 C for an extended duration of time, is apparent at VG margin but not detected at VG distal. Zero-curtains are caused by the release of latent heat. Dry soils lack sufficient moisture to exhibit a zero-curtain dynamic, and therefore freeze more frequently and more rapidly than wet soils.	136
Figure 3.A1: 10cm temperature, and 15 cm specific conductance and volumetric water content data at Von Guerard Stream between January 12, 2014 and February 4, 2016 (753 days).....	141
Figure 3.A2: 10cm temperature, and 15 cm specific conductance and volumetric water content data at Green Creek between January 16, 2014 and February 4, 2016 (748 days).....	142
Figure 3.A3: 10cm temperature, and 15 cm specific conductance and volumetric water content data at Watertrack B between January 14, 2014 and February 4, 2016 (751 days).....	143
Figure 3.A4: 10cm temperature, and 15 cm specific conductance and volumetric water content data at Wormherder Creek between January 23, 2014 and February 4, 2016 (741 days).	144
Figure 4.1: MicroMet simulated air temperature (A), SW and LW incident radiation (B), and wind speed (C) at Von Guerard ALMS. These data are needed to inform the surface energy budget model.....	151
Figure 4.2: Air temperature degree-days above freezing (DDAF) at ALMSs. Continuous air temperature data was estimated at ALMSs with MicroMet.	152
Figure 4.3: Cumulative annual solar radiation at ALMSs, as computed from MicroMet estimates.	153
Figure 4.4: Estimated PDF of wind speed at ALMSs. “Estimated”, indicates that PDFs were generated with a kernel smoothing function applied to all available wind speed data between July 1, 2009 and July 1, 2015. Wind speed was approximated at each station using MicroMet.	154
Figure 4.5: Simulated and observed ground temperature at VG ALMS margin site between November 2014 and March 2015. No observations are available between December and mid January due to a sensor malfunction.	157

Figure 4.6: Simulated and observed 10cm ground temperature at VonGuerard margin site. All available ground temperature observations are used and the 1:1 line is shown in red. Simulations over predict observed temperatures between -20 and 0 °C. This over prediction corresponds to spring and early austral summer months (October, November, early December), when snow cover likely insulates shallow ground temperatures. 158

Figure 4.7: Simulated and observed ground temperature at Von Guerard ALMS distal site between November 2014 and March 2015. No observations are available between December and mid January due to a sensor malfunction. Best fitting soil moisture at this site was 0.01 m³/m³, which was less than the maximum observed 15 cm soil moisture at this site. 159

Figure 4.8: Simulated and observed 10cm ground temperature at VonGuerard distal site. All available ground temperature observations are used and the 1:1 line is shown in red. 160

Figure 4.9: Surface energy fluxes at VG ALMS margin location between July 2014 and July 2015. Positive values indicate energy transfer into the ground surface from the atmosphere, and negative values indicate energy transfer from the ground surface to the atmosphere. 161

Figure 4.10: Surface energy fluxes at VG ALMS distal location between July 2014 and July 2015. Positive values indicate energy transfer into the ground surface from the atmosphere, and negative values indicate energy transfer from the ground surface to the atmosphere. 162

Figure 4.11: Daily average conductive flux and 10-day moving average of daily conductive flux at the VG margin site between August 2014 and July 2015. The conductive flux at the soil surface rapidly decreases between December and March. During February and March, the conductive flux is consistently negative which rapidly cools the active layer. 163

Figure 4.12: Cumulative summer (Nov, Dec, Jan, and Feb) surface energy fluxes during the 2014/2015 season at each ALMS. 164

Figure 4.13: Simulated thaw depth at VG ALMS between July 2009 and July 2015. 165

Figure 4. 14: Simulated thaw depth at Von Guerard ALMS between November 2014 and April 2015. The progression of active layer thaw depth shows a similar seasonal trend to other seasons, where soils thaw gradually and freeze rapidly. 166

Figure 4.15: Thermodynamic metrics from control (C) and scenario (S1 – S5) simulations at VG distal location. S1 is +2°C change in air temperature and no change in soil moisture, S2 is +0.1 m³/m³ change in soil moisture and no change in air temperature, S3 is an increase in soil moisture to saturation and no change in air temperature, S4 is a +0.1 m³/m³ change in soil moisture and a +2°C change in air temperature, and S5 is an increase in soil moisture to saturation and a +2°C change in air temperature. 170

Figure 4.16: The percentage of observed time that soils at 10 cm spend above freezing, plotted as a function of mean austral summer (Dec, Jan, Feb) soil moisture at 15 cm depth. A generally negative trend is observed, where wetter soils spend less time above freezing than drier soils. 174

Figure 4.17: Thermal conductivity, volumetric heat capacity, and thermal diffusivity as a function of volumetric water content for thawed and frozen soils. Soil porosity is assumed to be 0.35..... 177

Figure 4.A1: MicroMet simulated meteorological data at Green Creek ALMS. (Top panel) Air temperature (T_{air}), (middle panel) SW and LW radiation (Rad), and (bottom panel) wind speed (wspd) are shown..... 179

Figure 4.A2: MicroMet simulated meteorological data at Watertrack B ALMS. (Top panel) Air temperature (T_{air}), (middle panel) SW and LW radiation (Rad), and (bottom panel) wind speed (wspd) are shown..... 180

Figure 4.A3: MicroMet simulated meteorological data at Green Creek ALMS. (Top panel) Air temperature (T_{air}), (middle panel) SW and LW radiation (Rad), and (bottom panel) wind speed (wspd) are shown..... 181

Figure 4.A4: Simulated and observed 10cm ground temperature at Green Creek margin site. All available ground temperature observations are used and the 1:1 line is shown in red. 182

Figure 4.A5: Simulated and observed 10cm ground temperature at Green Creek distal site. All available ground temperature observations are used and the 1:1 line is shown in red. 183

Figure 4.A6: Simulated and observed 10cm ground temperature at Watertrack B margin site. All available ground temperature observations are used and the 1:1 line is shown in red. 184

Figure 4.A7: Simulated and observed 10cm ground temperature at Watertrack B distal site. All available ground temperature observations are used and the 1:1 line is shown in red. 185

Figure 4.A8: Simulated and observed 10cm ground temperature at Wormherder Creek margin site. All available ground temperature observations are used and the 1:1 line is shown in red. 186

Figure 4.A9: Simulated and observed 10cm ground temperature at Wormherder Creek distal site. All available ground temperature observations are used and the 1:1 line is shown in red. 187

Figure 4.A10: Surface energy fluxes at GC ALMS margin location between July 2014 and July 2015. Positive values indicate energy transfer into the ground surface from the atmosphere, and negative values indicate energy transfer from the ground surface to the atmosphere. The largest positive flux is net SW radiation, which ranges from 0 – 650 W/m². Sensible heat flux is positive in the winter and negative in the summer, ranging from -507 – 252 W/m². Net LW radiation is predominantly negative during, but exhibits a range of -250 – 13 W/m². Conduction oscillates between positive and negative on a diel basis and has a range of -190 – 295 W/m²..... 188

Figure 4.A11: Surface energy fluxes at GC ALMS distal location between July 2014 and July 2015. Positive values indicate energy transfer into the ground surface from the atmosphere, and negative values indicate energy transfer from the ground surface to the atmosphere. The largest positive flux is net SW radiation, which ranges from 0 – 650 W/m². Sensible heat flux is positive

in the winter and negative in the summer, ranging from -510 – 203 W/m². Net LW radiation is predominantly negative during, but exhibits a range of -281 – 10 W/m². Conduction oscillates between positive and negative on a diel basis and has a range of -130 – 245 W/m²..... 189

Figure 4.A12: Surface energy fluxes at WTB ALMS margin location between July 2014 and July 2015. Positive values indicate energy transfer into the ground surface from the atmosphere, and negative values indicate energy transfer from the ground surface to the atmosphere. The largest positive flux is net SW radiation, which ranges from 0 – 697 W/m². Sensible heat flux is positive in the winter and negative in the summer, ranging from -450 – 221 W/m². Net LW radiation is predominantly negative during, but exhibits a range of -252 – 12 W/m². Conduction oscillates between positive and negative on a diel basis and has a range of -162 – 285 W/m²..... 190

Figure 4.A13: Surface energy fluxes at WTB ALMS distal location between July 2014 and July 2015. Positive values indicate energy transfer into the ground surface from the atmosphere, and negative values indicate energy transfer from the ground surface to the atmosphere. The largest positive flux is net SW radiation, which ranges from 0 – 697 W/m². Sensible heat flux is positive in the winter and negative in the summer, ranging from -487– 194 W/m². Net LW radiation is predominantly negative during, but exhibits a range of -268 – 10 W/m². Conduction oscillates between positive and negative on a diel basis and has a range of -192 – 245 W/m²..... 191

Figure 4.A14: Surface energy fluxes at WHC ALMS margin location between July 2014 and July 2015. Positive values indicate energy transfer into the ground surface from the atmosphere, and negative values indicate energy transfer from the ground surface to the atmosphere. The largest positive flux is net SW radiation, which ranges from 0 – 800 W/m². Sensible heat flux is positive in the winter and negative in the summer, ranging from -690– 231 W/m². Net LW radiation is predominantly negative during, but exhibits a range of -205 – 33 W/m². Conduction oscillates between positive and negative on a diel basis and has a range of -260 – 245 W/m².. 192

Figure 4.A15: Surface energy fluxes at WHC ALMS distal location between July 2014 and July 2015. Positive values indicate energy transfer into the ground surface from the atmosphere, and negative values indicate energy transfer from the ground surface to the atmosphere. The largest positive flux is net SW radiation, which ranges from 0 – 800 W/m². Sensible heat flux is positive in the winter and negative in the summer, ranging from -687 – 195 W/m². Net LW radiation is predominantly negative during, but exhibits a range of -245 – 37 W/m². Conduction oscillates between positive and negative on a diel basis and has a range of -200 – 212 W/m²..... 193

Figure 4.A16: Active layer depth at Green Creek distal ($\theta = 0.12$) and margin ($\theta = 0.25$) locations between July 2009 and July 2015. Maximum active layer depth occurred in 2010 at both distal (-0.4 m) and margin (-0.5 m) locations. The shallowest active layer thaw depth occurs in 2015 at both distal (-0.27) and margin (-0.27) locations. At Green Creek, the wetter margin location thaws deeper than or equal to the thaw depth at the distal location. . On a sub-seasonal basis, the wetter margin site begins thawing and refreezes later than the drier distal site. Also, the drier distal site exhibits more sub-seasonal variability in thaw depth than the wetter margin site. 194

Figure 4.A17: Active layer depth at Watertrack B distal ($\theta = 0.10$) and margin ($\theta = 0.18$) locations between July 2009 and July 2015. Maximum active layer depth occurred in 2010 at

both distal (-0.5 m) and margin (-0.5 m) locations. The shallowest active layer thaw depth occurs in 2015 at both distal (-0.33) and margin (-0.27) locations. At Watertrack B, the drier distal location thaws deeper than or equal to the thaw depth at the wetter margin location. On a sub-seasonal basis, the wetter margin site begins thawing and refreezes later than the drier distal site. Also, the drier distal site exhibits more sub-seasonal variability in thaw depth than the wetter margin site..... 195

Figure 4.A18: Active layer depth at Wormherder Creek distal ($\theta = 0.16$) and margin ($\theta = 0.25$) locations between July 2009 and July 2015. Maximum active layer depth occurred in 2014 at both distal (-0.27 m) and margin (-0.33 m) locations. The shallowest active layer thaw depth occurs in 2015 at both distal (-0.18) and margin (-0.18) locations. Wormherder Creek shows the shallowest thaw depths among all other ALMS sites for all years of record considered here. Also, at Wormherder Creek the wetter margin location thaws deeper than or equal to the thaw depth at the drier distal location. On a sub-seasonal basis, the wetter margin site begins thawing and refreezes later than the drier distal site. Sub-seasonal variability between distal and margin sites is similar..... 196

TABLES

Table 1.1: Stream length, gradient, and source glacier for all streams considered in this synthesis.	5
Table 1.A1: Data availability for gauged streams in the Taylor and Wright Valleys between 1993 and 2013. The Onyx River at Vanda and Lower Wright has discharge data available from before 1993, which were used in this study, but not shown in the figure above.	45
Table 2.1: Length and gradient of the eight streams in eastern Taylor Valley. The number of LTER water samples collected on each stream between 1990 and 2015 is also listed (data available from the McMurdo LTER online database, http://www.mcmlter.org).	59
Table 2.2: Parameterization of weathering and transport models 1, 2 and 3	72
Table 3.1: Summary of long-term meteorological observations (1994-2014) from eight sites in the Taylor Valley.	114
Table 3.2: Table 1: Installation depth of sensors at active layer monitoring sites. Sensor type is indicated by an abbreviation in parentheses. Decagon 5TE (5TE) sensors measure volumetric water content and specific conductance, and thermocouples (TC) measure temperature. Sensors used in this study are shown in boldface font.	124
Table 4.1: Best-fit energy balance model parameters. Model parameters were manually calibrated to achieve the best fit to 10cm ground temperature observations	155
Table 4.2: Model fit metrics, Nash-Sutcliffe Efficiency (NSE) and Root Mean Squared Error (RMSE), quantifying the ability of the model to simulate ground temperature at 10cm depth.	155
Table 4.3: Summary metrics from control and scenario simulations. Metric values and absolute and relative changes from the control simulation are shown.	169

CHAPTER 1: Patterns of hydrologic connectivity in the McMurdo Dry Valleys, Antarctica: a synthesis of 20 years of hydrologic data

1.1 INTRODUCTION

The McMurdo Dry Valleys (MDVs) are characterized by a very cold and dry regional climate. Annual mean air temperature is -18°C [Doran *et al.*, 2002] and annual precipitation is <100 mm water equivalent [Keys, 1980; Bromley, 1985; Fountain *et al.*, 2010]. Despite the cold and dry climate, hydrologic reservoirs and their connections (glaciers, lakes, streams, permafrost, and soil moisture) supply the landscape with liquid water during the brief austral summer (November 1 – March 1), helping to sustain a cold desert ecosystem [Fountain *et al.*, 1999; Gooseff *et al.*, 2011]. Ecosystem productivity is largely regulated by the paucity of liquid water [Kennedy, 1993], which enhances the significance of hydrologic connectivity.

The main hydrologic connection in the MDVs is between glaciers, streams, and closed-basin lakes. Glaciers are the largest source of water to the MDVs. Glacier meltwater feeds streams, which flow into closed-basin lakes (Figure 1.1). The glacier energy balance is dominated by shortwave radiation, thus diurnal changes in the magnitude and incidence angle of shortwave radiation causes changes in streamflow at daily and hourly intervals [Hoffman *et al.*, 2008]. For example, streamflow can stop for several days during the summer, when cool and cloudy weather reduces energy fluxes to glacier surfaces. Because there is no rainfall in the MDVs and the landscape is underlain by continuous permafrost, much of the non-glaciated landscape is disconnected from stream networks.

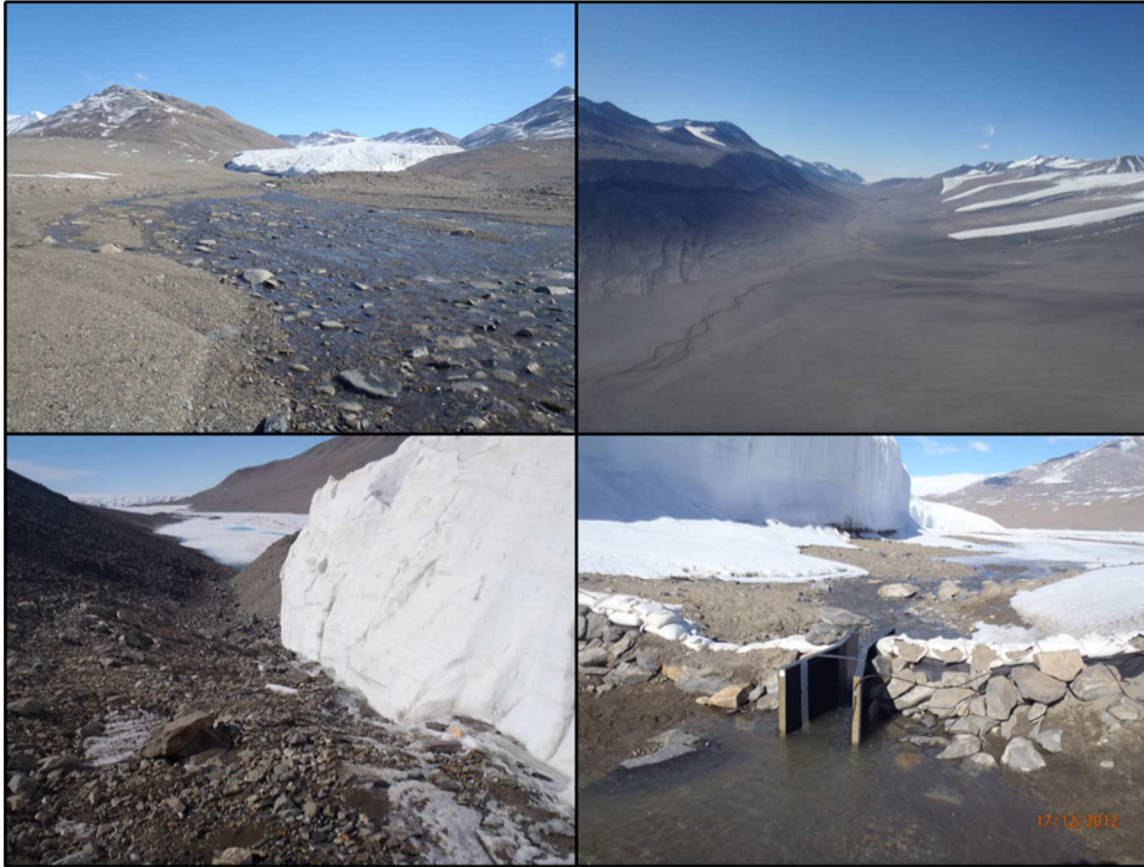


Figure 1.1: Select photos of glacial meltwater streams in the McMurdo Dry Valleys. (Top Left) Adams Stream flowing from Adams Glacier. (Top right) Eastward looking aerial view of the Onyx River flowing through Wright Valley. (Bottom left) Meltwater from the Sues Glacier flows through House Stream and into western Lake Hoare (a.k.a Lake Chad). (Bottom right) A Parshall flume at the gauge on Andersen Creek measures discharge entering the eastern end of Lake Hoare.

Patterns of glacier-stream-lake hydrologic connectivity in the MDVs occur across a broad spectrum of temporal scales. Inter-annual variability in climate (warmer v. cooler years; cloudier v. sunnier years) causes year-to-year variability in streamflow and the flux of solutes from streams into lakes [Doran *et al.*, 2008]. Annual (within a single summer) patterns of meltwater production are controlled by weather patterns. Cooler conditions during early and late summer limit meltwater production. Seasonal patterns of stream chemistry are indirectly controlled by weather because early summer flows are more concentrated than late summer season flows. At first, solutes that were excluded by freezing pore water and atmospheric salt deposits are rapidly

flushed by the first flows of the summer [Howard-Williams *et al.*, 1997]. Mid and late summer flows are therefore relatively dilute. On a daily timescale, the timing and magnitude of stream discharge and chemical fluxes are controlled by solar intensity and incidence angle on glacier terminal cliffs [Conovitz *et al.*, 1998].

The hydrology and ecology in the MDVs are tightly coupled. In the main channel and on the stream margins, streams harbor benthic microbial mats, consisting of cyanobacteria, heterotrophic bacteria, chlorophytes, diatoms, and microscopic invertebrates [McKnight *et al.*, 1999]. When streamflow ceases in the fall, the microbial mats become freeze-dried and then resume photosynthetic production within hours of becoming wetted with the initiation of flow the next summer [Niyogi *et al.*, 1997; McKnight *et al.*, 2007]. The distribution and abundance of microbial mats is controlled by habitat and long-term flow regime, with losses occurring due to scour during high flows and desiccation during prolonged periods of low flows (Cullis *et al.*, 2014; Kohler *et al.*, 2015). In turn, changes in mat abundance may alter nutrient loading to the lakes because the mats mediate in-stream nutrient cycling [McKnight *et al.*, 2004].

Furthermore, the long-term flow regime, especially flow intermittency and flood events, controls the community structure of the mats [Esposito *et al.*, 2006; Stanish *et al.*, 2011]. For example, Stanish *et al.*, (2012) observed the highest species diversity in moderately intermittent streams, while more persistent and highly intermittent streams had lower diatom diversity. Within a single stream, inter-annual variability in flow is associated with changes in diatom community composition [Esposito *et al.*, 2006; Stanish *et al.*, 2011]. Given the strong correlation of the community structure of the cyanobacteria and heterotrophic bacteria with diatom

community structure [Stanish *et al.*, 2013], flow regime is also likely to regulate the overall species composition of the mats.

The streams of the MDVs provide a natural laboratory for understanding the physical and chemical dynamics of hydrologic connections and their ecological consequences. The intention of this chapter is to analyze long-term data sets of stream discharge (Q), electrical conductance (EC), and water temperature (T) to assess contemporary and historical dynamics of glacier-stream-lake hydrologic connectivity. Three temporal perspectives are employed: annual, daily, and inter-annual to present a synthesis of stream dynamics in the MDVs. This study also provides a framework for understanding hydrologic connectivity in other watersheds.

1.2 STUDY SITE

The MDVs are a 22,700 km² region (4,500 km² of which are ice-free area) [Levy, 2013] located between McMurdo Sound and the Transantarctic Mountains, in southern Victoria Land, Antarctica (77.5°S, 163°E). Alpine and terminal glaciers, as well as perennial snowfields produce meltwater during the brief summer [Fountain *et al.*, 1999; Hoffman *et al.*, 2008; Gooseff *et al.*, 2011; Hoffman, 2011]. Meltwater moves through well established open channel networks [McKnight *et al.*, 1999] and shallow groundwater flowpaths (i.e. watertracks) [Levy *et al.*, 2011] into closed basin lakes and the Ross Sea. This study focuses on streams that have been the subject of long-term Q, EC, and T measurements (Table 1.1), in Taylor and Wright Valleys (Figure 1.2) by the McMurdo Dry Valleys Long-Term Ecological Research project (MCM-LTER).

Table 1.1: Stream length, gradient, and source glacier for all streams considered in this synthesis.

Drainage Basin	Stream	Total Length (km)	Length to Gauge (km)	Av. Gradient (m/m)	Source Glacier
Fryxell Basin & New Harbor	Canada	1.90	1.40	0.100	Canada Glacier
	Green	1.10	0.90	0.040	Canad Glacier
	Delta	9.50	9.40	0.050	Howard Glacier
	Crescent	12.80	12.50	0.060	Crescent Glacier
	Harnish	5.80	5.70	0.114	Kukri Hills
	Von Geurard	4.80	4.70	0.070	Kukri Hills
	Aiken	18.90	18.90	0.130	Kukri Hills
	Lost Seal	3.10	2.90	0.040	Commonwealth Glacier
	Huey	2.10	1.90	0.180	Aasgard Range
	Commonwealth	4.50	0.80	0.030	Commonwealth Glacier
Hoare Basin	House	0.40	0.40	0.220	Suess Glacier
	Andersen	1.40	1.10	0.090	Canada Galcier
Bonney Basin	Bohner	2.30	1.70	0.180	Sollas Glacier
	Priscu	2.80	2.70	0.016	Lacroix / Sollas Glaciers
	Lawson	0.40	0.40	0.190	Rhone Glacier
	Santa Fe	0.50	0.50	0.110	Taylor Galcier
Wright Valley	Onyx @ LWRT	31.80	2.00	0.006	Lower Wright Glacier
	Onyx @ Vanda	31.80	28.40	0.006	Lower Wright Glacier & others in Wright Valley

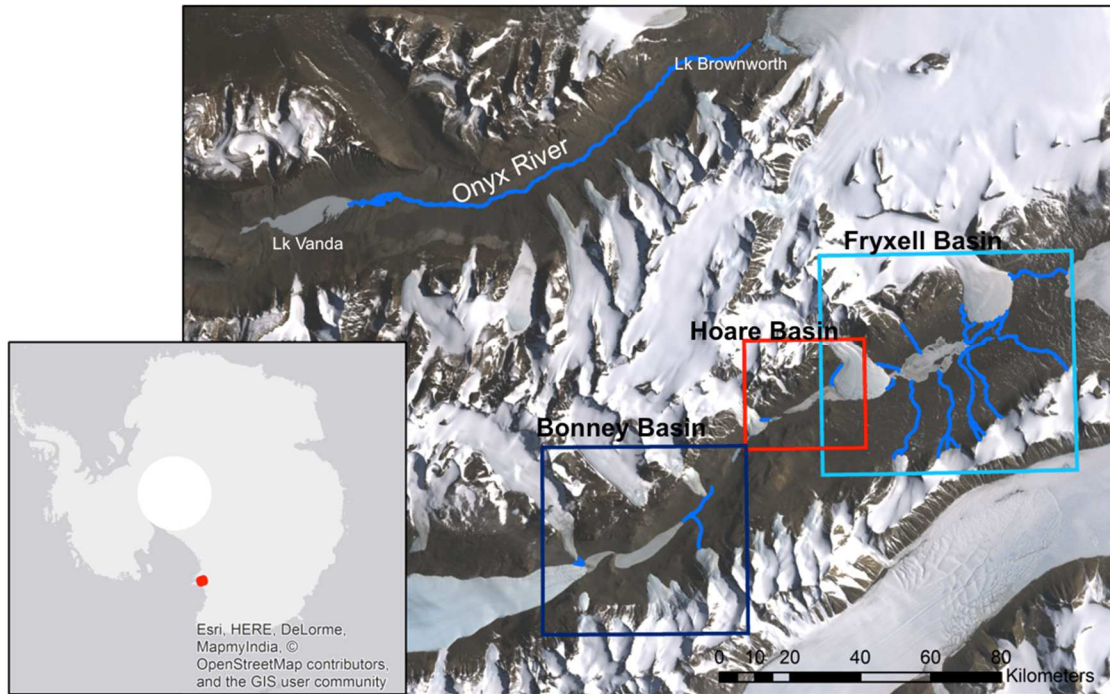


Figure 1.2: Site map showing gauged streams in the Taylor and Wright Valleys. The Onyx River flows through the Wright Valley from Lake Brownworth to Lake Vanda. The Taylor Valley has three primary lake drainages, which are shown in greater detail in Figures 1.3, 1.4, and 1.5.

1.2.1 Lake Fryxell Basin and New Harbor

Four perennially ice-covered lakes and the Ross Sea are the drainage termini for all gauged and un-gauged streams in the study area [Chinn, 1993]. Lake Fryxell is the eastern most lake basin in Taylor Valley, and receives meltwater inputs from thirteen streams (Figure 1.3), nine of which are gauged. The Commonwealth, Canada, Howard, Von Guerard, and Crescent Glaciers, plus several glaciers in the Kukri Hills, and perennial snowfields in the Aasgard Mountains provide meltwater to the basin. Several streams along the southern wall of the Fryxell basin flow into playa ponds before flowing into Lake Fryxell. Also, Aiken Creek flows into Many Glaciers Pond before continuing into Lake Fryxell. Because the Aiken Creek gauge is located below Many Glaciers Pond, and therefore the effect of MGP on flow, temperature and

chemistry must be considered. Commonwealth Stream, flowing from the Commonwealth Glacier, flows into the Ross Sea at New Harbor. This is the only gauged stream flowing into the Ross Sea (Figure 1.3).

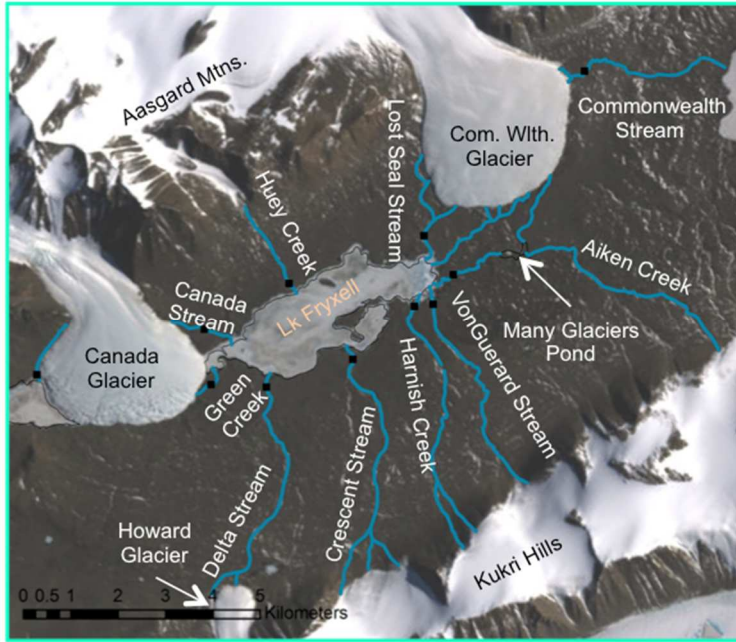


Figure 1.3: Gauged streams within the Fryxell and New Harbor basins. Gauge locations are shown as black squares along the blue stream path.

1.2.2 Lake Hoare Basin

The Hoare basin in the central Taylor Valley is separated from the Fryxell basin by Canada Glacier, and confined to the west by the Nuessbaum Riegel and Seuss Glacier (Figure 1.4). Recently Lake Hoare and Lake Chad have merged due to a rise in water level. The merged lake will hereinafter be referred to as Lake Hoare. Two of the four streams, Andersen and House, are currently or have been gauged. House Stream flows along the eastern edge of Seuss Glacier through an ice bound moraine into western Lake Hoare. Andersen flows into the eastern end of Lake Hoare along the western edge of the Canada Glacier. Several un-gauged watertracks seep into the south side of Lake Hoare and are estimated to contribute relatively low volumes of water

compared to streamflow, although their contribution to the solute budget may be more significant [Levy *et al.*, 2011].

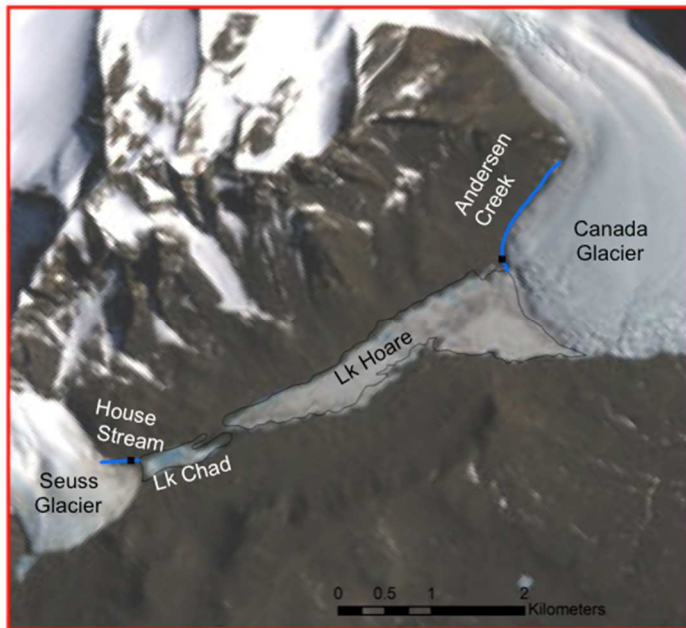


Figure 1.4: Gauged streams within the greater Lake Hoare basin.

1.2.3 Lake Bonney Basin

Lake Bonney is the western-most lake in Taylor Valley (Figure 1.5). The Neussbaum Reigel separates the eastern lobe of Lake Bonney from the Hoare Basin, and the terminus of the Taylor Glacier defines the western edge of the lake. Lake Bonney receives meltwater inflows from four streams, several watertracks, and an ephemeral stream known as Wormherder Creek [Nielsen *et al.*, 2012]. Three of the four streams in the basin are currently or have been gauged. Lawson Stream and Santa Fe Stream also flow into the western end of the lake. The gauge at Santa Fe Stream was decommissioned in 2000 due to rising lake levels. Bohner Stream is a tributary of Priscu Stream, which flows into the eastern end of the lake. Bohner Stream is currently gauged, but the gauge at Priscu was decommissioned in 2011 because rising lake levels

inundated the control structure. The gauge at Bohner Stream was constructed in lieu of the decommissioned gauge at Priscu. At the terminus of the Taylor Glacier, Blood Falls, a subglacial brine seepage, also flows into the western lobe of Lake Bonney [Mikucki and Priscu, 2007]. This seepage is un-gauged, but has been the subject of extensive previous and ongoing research [Mikucki *et al.*, 2004, 2009].



Figure 1.5: Gauged streams within the Lake Bonney Basin.

1.2.4 Lake Vanda Basin

Lake Vanda, in western Wright Valley, is the terminus of the Onyx River (Figure 1.2). The Onyx flows westward from Lake Brownworth into Lake Vanda. The primary meltwater source is the Lower Wright Glacier with contributions from numerous alpine glaciers along the Wright Valley. The Onyx River is the longest river in Antarctica and has been monitored collaboratively by the New Zealand and United States Antarctic Programs since 1972. Another

feature of the Onyx record is that upstream and downstream discharge measurements are made and Lower Wright (LWRT) and Vanda gauges, respectively.

1.3 METHODS

1.3.1 Measurement methods

The data analyzed here were collected with Campbell Scientific CR10X or CR1000 data loggers at 18 different stream sites in Taylor and Wright Valleys. Stream stage was measured at all sites, T at 15 sites, and EC at 14 sites. Data loggers collected data at 15-minute intervals.

Stream stage is measured using either PS-1/PS-2 Paroscientific or Accubar Sutron Corporation pressure transducers. PS-2 Paroscientific pressure transducers have 0.0001% measurement resolution and 0.02% accuracy within a range of 0 – 15 psi (0 – 34 ft. of water), and Accubar Sutron Corporation pressure transducers achieve measurement resolution of 0.0001 psi and an accuracy of 0.1% for readings above 4.4 psi and +/- 0.0044 psi for readings under 4.4 psi, within a measurement range of 0 – 22 psi (0-50 ft. of water). Rating relationships between stage Q measurements are developed using AQUATIC Informatics AQUARIUS® software. Ratings for each stream are updated at the end of each season and used to transform time-continuous stage observations into time-continuous Q estimates.

Stream temperature and EC are measured using Campbell Scientific CS547A conductivity and temperature probes through an A547 interface. Stream temperature

measurements have an accuracy of +/-0.4 C within a range of 0 – 50 °C. Specific conductance measurements have an accuracy of +/- 5% between 0.44 – 7 mS/cm and +/- 10% between 0.005 and 0.44 mS/cm.

1.3.2 Available Data

All data used in this study are publicly available. The Onyx River has a longer available record of stream discharge, beginning in 1969 at Vanda and 1972 at Lower Wright. Some combination of discharge, temperature, and specific conductance data are available for each site. Each site has a unique timeline of measurement history. Instrument malfunctions, catastrophic gauge loss during high flows, currently ongoing data revisions, and various other logistical constraints create gaps in the long-term records for each stream. A timeline of the measurements, or lack thereof, made at each site is presented in the Appendix (Table 1.A1).

1.3.3 Characterizing Connectivity on Annual Timescales

To determine the average duration of hydrologic connectivity during a flow season, the time of streamflow onset and cessation was calculated for each available year of record. Streamflow initiation was quantified as the time when 5% of the total annual observed flow passed a gauge, t_5 . Similarly, streamflow cessation was quantified as the time when 95% of the total annual observed flow passed a gauge, t_{95} . We used t_5 and t_{95} to estimate the start and end of the flow season because flow often exhibits on and off dynamics before and after these time points. Hence, t_5 and t_{95} provide a conservative estimate for the initiation and conclusion of

stream flow each year. Any years when the true beginning and end of the flow season are missing (i.e. sparse data sets, see Table 1A1) were removed from the analysis.

EC-Q relationships were used to investigate annual stream chemistry dynamics (EC is a surrogate for dissolved solutes). We plotted daily averaged EC data against daily averaged Q data in log-log space, following Godsey *et al.* [2009]. Data were then fit with a simple power law model (Equation 1.1)

$$EC = aQ^b \quad (1.1)$$

where, EC is specific electrical conductivity, normalized to 20°C ($\mu\text{S}/\text{cm}$), Q is discharge (L/sec), and a and b are best-fit empirical model parameters. In log-log space, b is the slope of the concentration-discharge relationship. A b parameter value of zero indicates purely chemostatic behavior; changes in Q correspond to no change in EC. On the other hand, a b parameter value of -1 indicates a pure dilution signal; EC varies inversely with Q. A pure dilution signal would reflect a constant mass flux of a solute source with variable discharge.

1.3.4 Characterizing Connectivity on Daily Timescales

Solar radiation, stream length, streambed roughness, and stream gradient control the timing and magnitude of daily peak flows [Conovitz *et al.*, 1998]. Therefore, each stream in the MDVs experiences higher flows and lower flows at consistent times of the day. Similarly, EC and T dynamics exhibit diurnal variations (Figure 1.6).

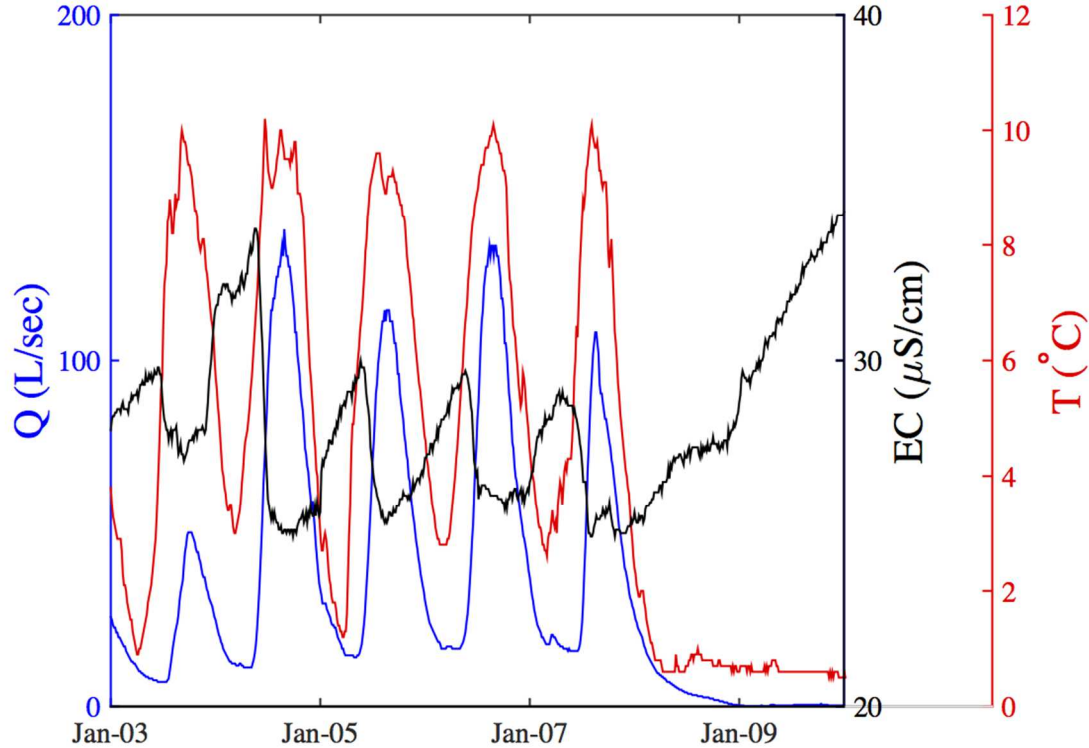


Figure 1. 6: Q (blue), EC (black) and T (red) data from a 7-day period on Canada Stream during January 1997. All variables exhibit diurnal variations. Similar diurnal variations are observed at all other gauge locations.

Long-term records are analyzed to determine average daily patterns of Q, EC, and T.

Fifteen-minute Q, EC, and T data are divided into hourly bins. Mean variable values are computed for each hourly bin to pull out the average 24-hour variable patterns for each stream.

1.3.5 Characterizing Connectivity on Inter-annual Timescales

Duration curves (or exceedence probability curves) provide a summary that characterizes Q, EC, and T dynamics from multiple years of record. Duration curves quantify the proportion of time that a variable equals or exceeds a given value as a cumulative exceedence probability (Equation 1.2),

$$P(Q, T, EC) = \int_{Q, T, EC}^{\infty} p(Q, T, EC) dx \quad (1.2)$$

where $p(Q, T, EC)$ is the probability density function of Q, T, or EC, and P is the cumulative exceedence probability for the variable of interest [Botter *et al.*, 2008]. Duration curves were generated with daily averaged observations from long-term records of Q, EC, and T.

The slope of a duration curve is an indication of inter-annual Q, T, or EC variability [Yadav *et al.*, 2007; Sawicz *et al.*, 2011]. The slope is computed between the 33rd and 66th percentiles of Q, T, or EC, which corresponds to the most linear portion of the duration curve in semi-log space. The slope of the flow duration curve (FDC) is modified slightly from Sawicz *et al.* [2011] to account for the common occurrence of zero-flow days during the summer for MDV streams, by computing slopes over the middle 1/3rd of the total range of observed exceedence probabilities (Equation 1.3)

$$Slope_{FDC} = \frac{\ln\left(\frac{Q_{P_{\max}/3}}{3}\right) - \ln\left(\frac{Q_{2P_{\max}/3}}{3}\right)}{P_{\max}/3} \quad (1.3)$$

where P_{\max} is the exceedence probability of 1×10^{-5} cms, the lowest discharge we are confident in reporting. The slope of the EC duration curve (CDC) is computed as (Equation 1.4)

$$Slope_{CDC} = \frac{\ln(EC_{0.33}) - \ln(EC_{0.66})}{0.66 - 0.33} \quad (1.4)$$

where $EC_{0.33}$ and $EC_{0.66}$ are EC values corresponding to 33% and 66% exceedence probabilities, respectively. Lastly, the slope of the stream temperature duration curve (TDC) is computed as (Equation 1.5)

$$Slope_{TDC} = \frac{T_{0.33} - T_{0.66}}{0.66 - 0.33} \quad (1.5)$$

where $T_{0.33}$ and $T_{0.66}$ are the temperatures corresponding to 33% and 66% exceedence probabilities, respectively. The natural logarithm of Q and EC values in Equations 1.3 and 1.4 account for linearity in the data when plotted on a semi-logarithmic axis. This transformation was not necessary in Equation 1.5 because TDCs appear linear between the 33% and 66% exceedence probabilities when plotted on linear scales.

Quantifying the total gauge-measured flow volumes for each year of record also interrogates inter-annual variability of glacier-stream-lake hydrologic connectivity. The Onyx River at Lake Vanda has the longest discharge record from MDVs region, with data available since 1969. Canada Stream has the most consistent and robust record from the Taylor Valley, with data available since 1990. Annual runoff volumes were computed for the Onyx River at Vanda and Canada Stream to display inter-annual variation in the magnitude of glacier-stream-lake connections. Annual runoff volumes were computed using a two-hour moving window trapezoidal numerical integration technique [Moin, 2010]. This approach avoids integrating between temporally disparate observations and provides a conservative estimate of annual flow volume.

The Onyx River and Canada Stream have the most robust and consistent records of discharge and serve as examples for inter-annual flow patterns. Further, annual flow volumes were computed for all streams within the Fryxell Basin to show inter-annual connection magnitude differences between streams.

1.4 RESULTS

1.4.1 Inter-annual Connectivity Dynamics

Flow duration curves for streams in the Fryxell basin are shown in Figure 1.7a, b. Curves are plotted on a semi-logarithmic axis to highlight variability in low-flow dynamics. The probability of daily average discharge exceeding 1 L/s varies greatly among streams. Daily average discharge on Harnish, Huey, Von Guerard, Crescent, and Delta exceed 1 L/s less than 60% of the time, due to the high number of zero flow days at these sites. Harnish, Huey, Von Guerard, and Crescent have all had zero-flow years, with no discharge observed at the gauge during the entire flow season (Supporting Information, Figure 1.A1). The greatest number of zero-flow years occurred at Harnish, where only 29% of daily average discharge observations exceeded 1 L/s. On Commonwealth Stream, daily average discharge observations exceed 1 L/s greater than 92% of the time. The median daily average discharge value is 20 L/s, the second highest median discharge value, next to Santa Fe, in the Taylor Valley.

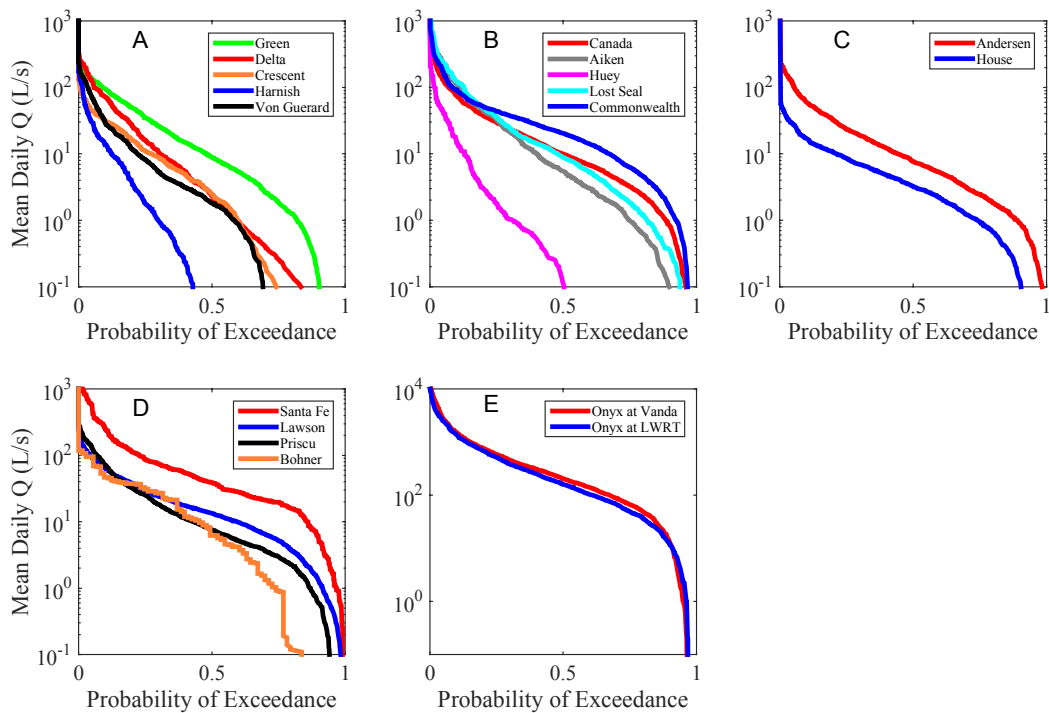


Figure 1.7: Flow duration curves for gauged streams draining into Lake Fryxell and the Ross Sea (A, B), Lake Hoare (C), Lake Bonney (D), and Lake Vanda in the Wright Valley (E). Note the larger y-axis range for duration curves for streams in the Wright Valley (E).

The most consistently flowing streams in the Fryxell basin are Canada, Green, Lost Seal, and Aiken, which exceed 1 L/s greater than 70% of the time and have flowed every year of the record (Figure 1.7a, b). These streams also have a greater probability of exceeding daily average flows higher than 100 L/s. Such high flows can scour benthic microbial mats [Cullis *et al.*, 2014]. Lower median daily average discharge values are observed at Crescent (2.5 L/s), Delta (2.3 L/s), Von Guerard (1.8 L/s), Huey (0 L/s), and Harnish 0 L/s. Streams with the greatest high flow exceedence probabilities are Aiken and Lost Seal, which are both fed by the Commonwealth Glacier. Canada is the most consistently flowing stream, overall, in the Fryxell basin.

The flow duration curve shapes for Andersen and House, draining into Lake Hoare, are very similar. However, the magnitudes are very different (Figure 1.7c). Namely, the exceedence probability of all discharge magnitudes is greater along Andersen, compared to House. The median observed daily discharges at House and Andersen are 3.27 L/s and 7.7 L/s, respectively.

In the Lake Bonney basin, Priscu and Lawson are the most consistently flowing streams (Figure 1.7d). Zero-flow observations during the flow season have rarely been made at these sites and daily average discharge observations exceed 1 L/s greater than 90% of the time. Santa-Fe has the greatest exceedence probabilities for all discharge magnitudes compared to all other gauged streams in Taylor Valley. Priscu and Lawson exhibit similar high flow probabilities, however Lawson is more likely to sustain lower flows than Priscu. The greatest number of daily average zero-flow observations was made at Bohner, where discharge exceeded 1 L/s 73% of the time. It should be noted, however, that only a single year of record is available at the Bohner gauge (Figure 1.A1).

The Onyx River, at both gauge locations, has the highest probability of encountering very high flows, relative to any Taylor Valley streams (Figure 1.7e). It should be noted that the y-axis scale limit for Figure 1.7e extends to 1×10^4 L/s. Median daily average discharge at Vanda and LWRT is 205.2 L/s and 161.5 L/s, respectively. The exceedence probability of daily average discharge values is generally greater at the Vanda gauge, compared to the LWRT gauge. However, the LWRT gauge has a greater probability of exceeding low daily average discharge values (>12.5 L/s). This may be evidence for net gains occurring along the extent of the Onyx River, where several alpine glaciers descending from the Asgard Range providing additional

runoff to the Onyx River. However, the hydraulic steepening of a flood pulse traveling from LWRT to Vanda or the release of stored water from the hyporheic zone may also explain the greater median daily average discharge at Vanda.

The slope of the most linear portion of the flow duration curve (Equation 1.3) is a quantification of the overall variability in seasonal discharge on a particular stream. The stream with the steepest flow duration curve slope, and thereby greatest variability in annual daily-average discharge, is Harnish (Figure 1.8). The stream with the shallowest flow duration curve slope, and thereby least variability in annual daily-average discharge, is Lawson. On the Onyx River, stream flow at LWRT is slightly more variable than at Vanda.

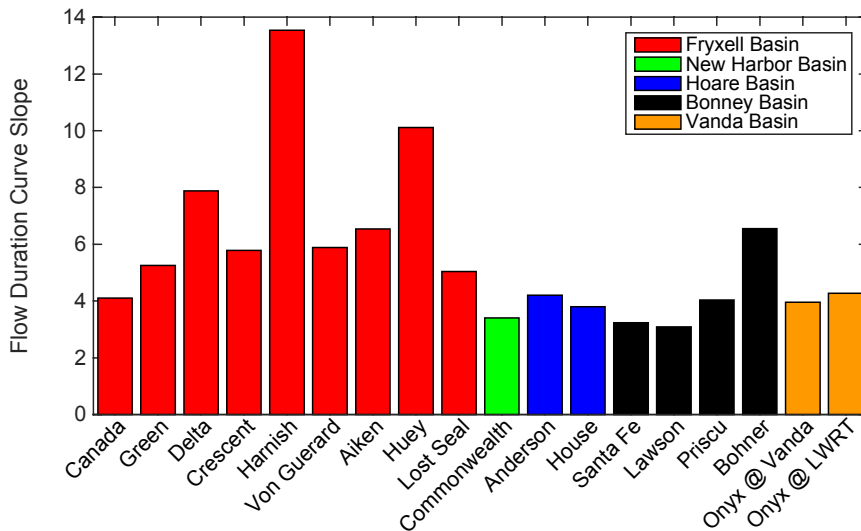


Figure 1. 8: Flow duration curve slopes for all gauged streams. Red bars show streams draining into Lake Fryxell, the green bar shows Commonwealth stream draining into the Ross Sea, blue bars show streams draining into Lake Hoare, black bars show streams draining into Lake Bonney, and orange bars show the Onyx at Vanda and LWRT.

In the Fryxell Basin, longer streams show a greater tendency to encounter very high EC values and have higher median annual daily-average EC values, relative to shorter streams

(Figure 1.9a, b). Specific conductance values greater than $14 \mu\text{S}/\text{cm}$ are more likely to be observed along Von Guerard, Harnish, Aiken, Crescent, Lost Seal, and Delta, compared to Canada and Green. The highest median daily average EC value occurred at Crescent ($177.5 \mu\text{S}/\text{cm}$). Median specific conductance observations at Canada ($26.5 \mu\text{S}/\text{cm}$) and Green ($33.7 \mu\text{S}/\text{cm}$) are much lower than those at the other streams ($72.1 - 177.5 \mu\text{S}/\text{cm}$). Specific conductance observations exceeding $100 \mu\text{S}/\text{cm}$ are more likely at Green than at Canada. Lost Seal shows the greatest EC variability in the Fryxell basin, and Crescent shows the lowest EC variability, as indicated by the CDC slope (Figure 1.10). Furthermore, relative to other basins in Taylor Valley, Fryxell basin streams have the least annual EC variability (Figure 1.10).

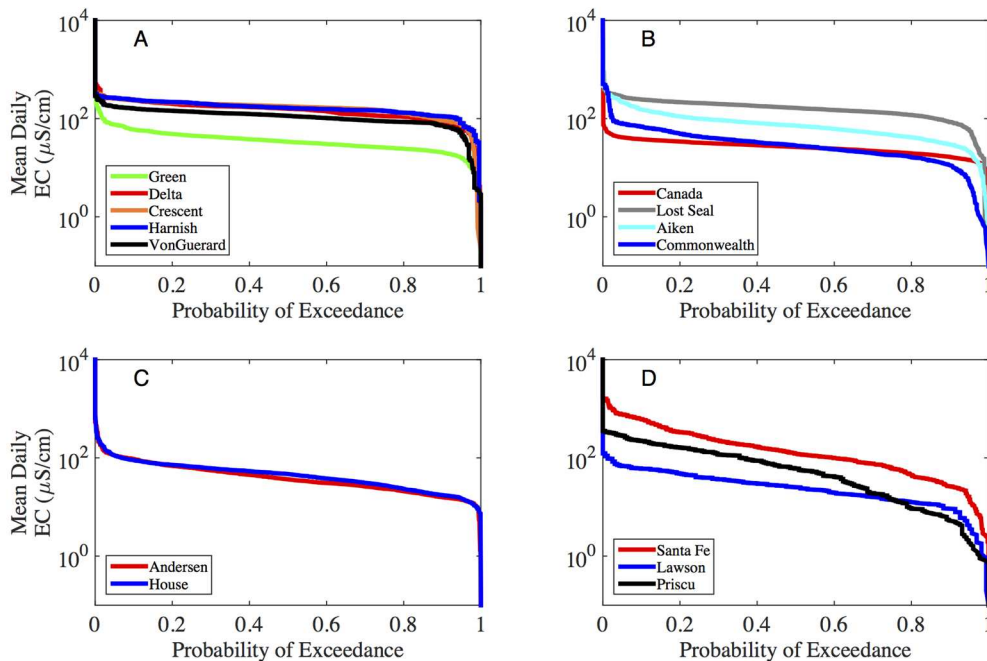


Figure 1.9: Specific conductance duration curves for EC-monitored streams draining into Lake Fryxell and the Ross Sea (A, B), Lake Hoare (C), and Lake Bonney (D).

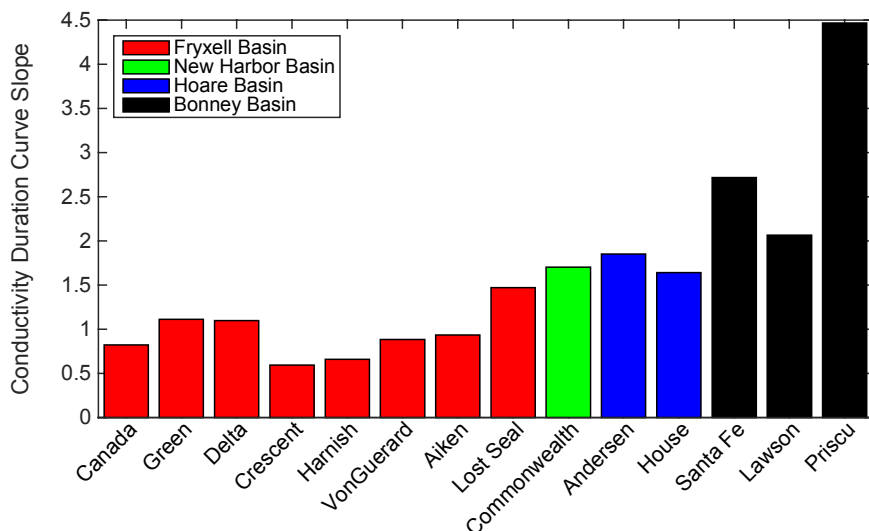


Figure 1.10: Conductivity duration curve slopes for streams in the Taylor Valley. Red bars show streams draining into Lake Fryxell, the green bar show Commonwealth Stream draining into the Ross Sea, blue bars show streams draining into Lake Hoare, and black bars show streams draining into Lake Bonney.

The median daily average EC magnitude at Commonwealth is 28.5 $\mu\text{S}/\text{cm}$ (Figure 1.9b), which is similar to that for Canada (26.5 $\mu\text{S}/\text{cm}$). However, relative to Canada, Commonwealth shows slightly greater overall variability in EC. Specific conductance measurements at Commonwealth exceed 10 $\mu\text{S}/\text{cm}$ 91% of the time, whereas those at Canada exceed 10 $\mu\text{S}/\text{cm}$ 98% of the time.

Streams in the Fryxell Basin with higher EC values tend to have a longer travel length from source-glacier to gauge locations (Table 1.1). Conversely, streams with lower EC values have a shorter travel length from source-glacier to gauge. However, Lost Seal, despite the short travel length from glacier to the gauge, sees higher EC compared to other shorter streams.

Andersen and House, in the Lake Hoare Basin, exhibit remarkably similar CDCs (Figure 1.9c). Median observed EC values are only slightly higher at House gauge (42 $\mu\text{S}/\text{cm}$) than at the Andersen gauge (36 $\mu\text{S}/\text{cm}$). Specific conductance measurements higher than 100 $\mu\text{S}/\text{cm}$ are slightly more likely at House than Andersen.

Streams in the Bonney basin exhibit distinct EC regimes (Figure 1.9d). The greatest exceedence probability at all EC magnitudes is observed at Santa Fe. Both Santa Fe and Priscu, which are second-order streams, exhibit higher median EC values, compared to Lawson, a first order stream. Priscu and Santa Fe show the greatest variability in EC, relative to other streams in the Taylor Valley, as indicated by the steep slope of the CDC curves (Figure 1.10). The shape and magnitude of the CDC for Lawson is similar to Canada and Green, however Lawson has a lower likelihood of exceeding very low EC magnitudes (5 $\mu\text{S}/\text{cm}$).

Within the Fryxell basin, Harnish has the highest median stream temperature of 4.1 $^{\circ}\text{C}$ (Figure 1.11a). Huey has the lowest median stream temperature of 1.5 $^{\circ}\text{C}$ (Figure 1.11b). Huey also exhibits the least variability in annual water temperature (Figure 1.12), and is the coolest stream in the basin. Von Guerard has the greatest probability of high water temperatures; in excess of 8 $^{\circ}\text{C}$. Longer streams in the Fryxell basin (Von Guerard, Aiken, Delta, Harnish, and Crescent) are more likely to exceed water temperatures of 5 $^{\circ}\text{C}$, compared to shorter streams. Relative to other streams in Taylor Valley, Fryxell basin streams exhibit the greatest annual variability of daily average stream temperatures (Figure 1.12). Commonwealth Stream has a median water temperature of 2.3 $^{\circ}\text{C}$, and the probability of daily average water temperature

exceeding 5 °C is only 1% (Figure 1.11b). The shape and magnitude the TDC observed at Commonwealth is most similar the TDC observed at Huey.

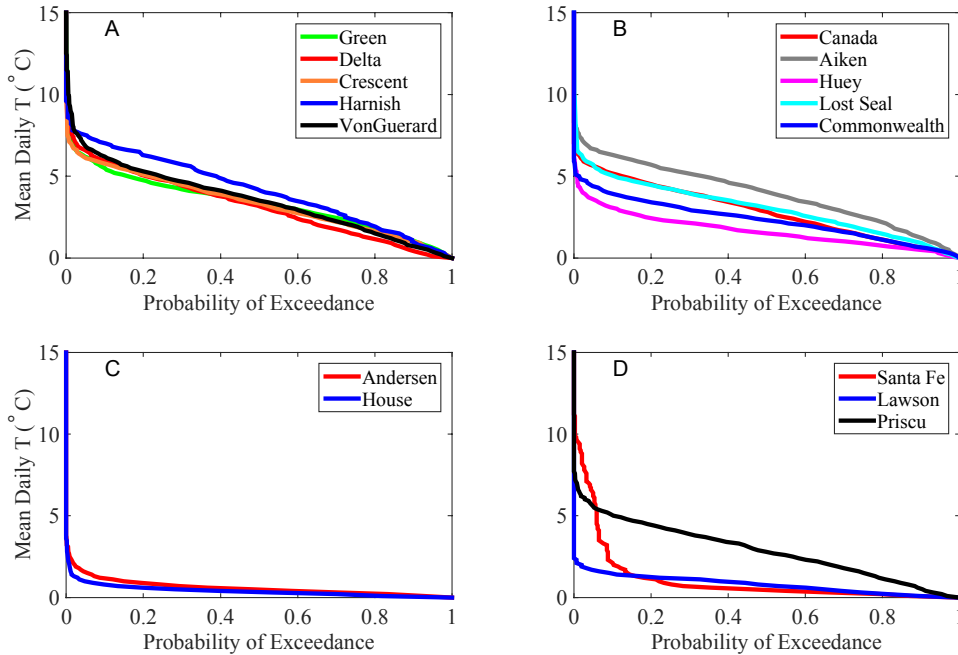


Figure 1.11: Water temperature duration curves for temperature monitored streams draining into Lake Fryxell and the Ross Sea (A, B), Lake Hoare (C), and Lake Bonney.

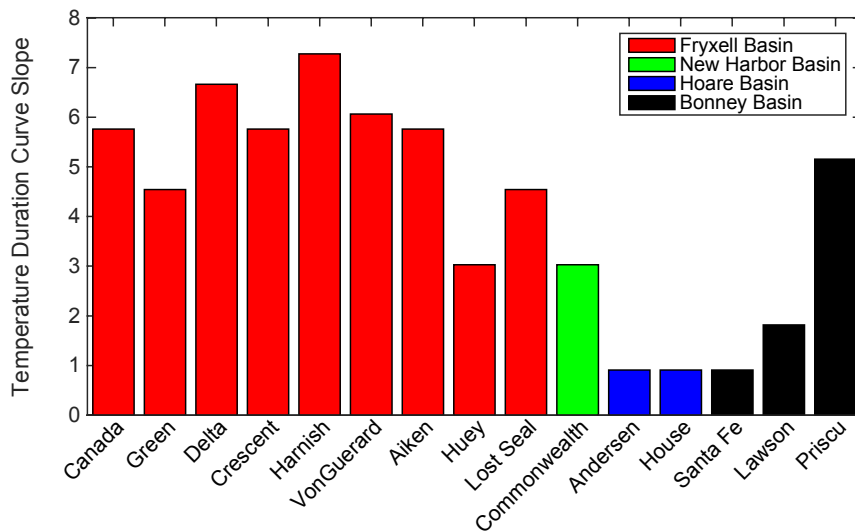


Figure 1.12: Temperature duration curve slopes for streams in the Taylor Valley. Red bars show streams draining into Lake Fryxell, the green bar shows Commonwealth Stream draining into the

Ross Sea, blue bars show streams draining into Lake Hoare, and black bars show streams draining into Lake Bonney.

Andersen and House Streams in the Hoare Basin are the coolest streams in Taylor Valley (Figure 1.11c). Median temperatures at Andersen and House are 0.5 °C and 0.3 °C, respectively. Both Andersen and House exhibit the least annual variability in water temperatures, compared to all other monitored streams in Taylor Valley (Figure 1.12).

Temperature duration curve shapes for streams in the Bonney basin show distinct patterns, as was seen for the EC regimes (Figure 1.11d). Santa Fe exhibits the most annual variability in daily average stream temperature (Figure 1.12). Also, the shape of the TDC for Santa Fe is highly non-linear. Santa Fe is most likely to encounter very warm water temperature, in excess of 10 °C, but also has the lowest median water temperature (0.6 °C). Priscu has the warmest median water temperature (2.8 °C). Lawson is consistently the coolest stream, where daily average temperatures have never exceeded 2.3 °C, and exhibits the least annual temperature variability (Figure 1.12).

The longer record for the Onyx provides a framework for evaluating the inter-annual flow variations in Taylor Valley streams. From 1970 to 1976 annual runoff on the Onyx River at Vanda shows a decreasing trend, followed by an increase from 1978 – 1986 (Figure 1.13). A sustained period of low flow lasted from 1994 through 2000. During the 1991/1992 season only $4.62 \times 10^4 \text{ m}^3$ of runoff was measured at the Vanda gauge, the lowest runoff season on record. The highest runoff year occurred during the 2001/2002 summer, when $1.62 \times 10^7 \text{ m}^3$ of melt water

passed the gauge at Vanda. Following the 2001/2002 high-flow season, annual discharge declined, before another high flow year in 2008.

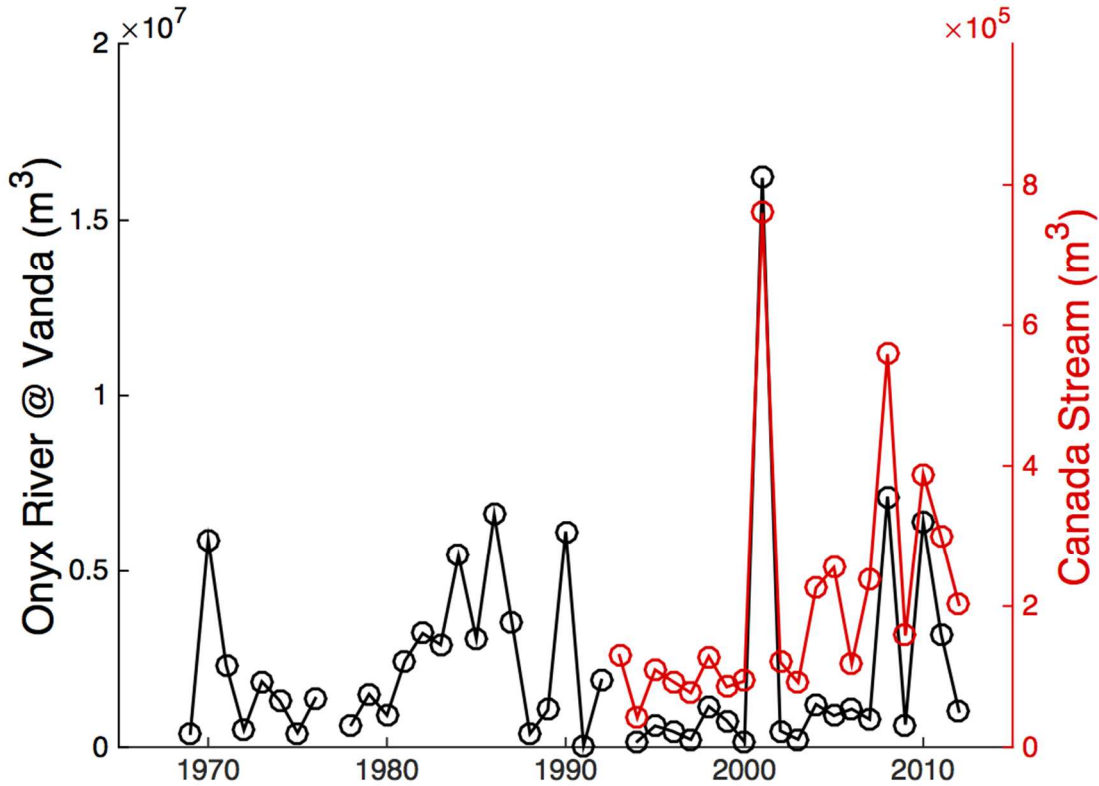


Figure 1.13: Historical runoff volumes for the Onyx River at the Vanda gauge (black) and Canada Stream at the Canada gauge (red).

The discharge record at Canada Stream mirrors the inter-annual dynamics of the Onyx River (Figure 1.13). The 2001/2002 and 2008/2009 seasons are the two highest flow seasons on record. Following the 2001/2002 season, annual discharge volumes have generally been higher with more inter-annual variability, compared to years before the high-flow year. For a more detailed discussion on the meteorology and hydrology of the 2001/2002 high-flow year, refer to Doran *et al.* [2008].

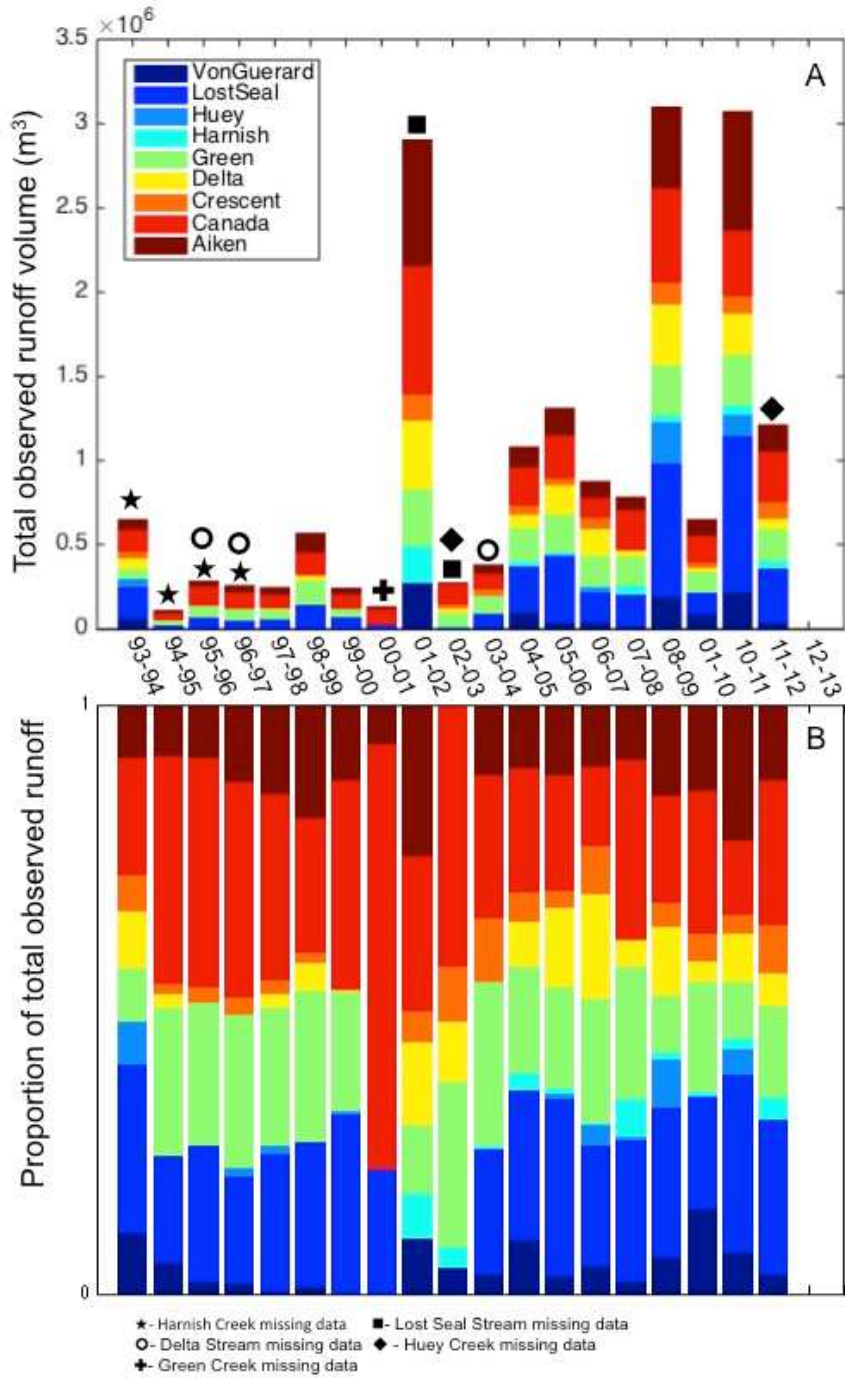


Figure 1.14: (A) Annual observed runoff entering Lake Fryxell and (B) stream-specific proportional contributions to annual observed runoff into Lake Fryxell. These data represent only the observed runoff measured at gauge locations. For each year, streams with missing records are indicated with symbols, see key at bottom of plot.

Total measured runoff volumes into the Lake Fryxell exhibit strong inter-annual variability (Figure 1.14a). The most runoff entering the Fryxell basin was observed during the 2008/2009 season, however incomplete records from the 2001/2002 season likely leads to an underestimate of the total runoff. Specifically, there was a catastrophic gauge failure on Lost Seal and no available record. The smallest amount of runoff entered Lake Fryxell during the 1994/1995 season.

Canada, Green, Lost Seal, and Aiken contribute the largest proportion of melt water to Lake Fryxell each year (Figure 1.14b). Therefore, melt from the Canada and Commonwealth glaciers compose the majority annual inflows to Lake Fryxell. Other glaciers in the Kukri Hills contribute a much smaller proportion of annual runoff. During lower flow years, such as the 2000/2001 and 1994/1995 seasons, flows on Canada Stream dominate the inflows into Lake Fryxell.

1.4.2 Annual Connectivity Dynamics

On average, glacier-stream-lake connectivity begins during December and ends in January (Figure 1.15). This period coincides with the timing of maximum annual air temperatures and incident shortwave solar radiation. The timing of connectivity varies greatly from year to year, as indicated by the error bars in Figure 1.15. The flow season lasts for an average of 4 – 9 weeks. Commonwealth has the longest flow season, averaging 8.3 weeks, and is also typically the first stream flow and last to cease. Aiken typically has the shortest flow season,

averaging 4.4 weeks. It is also typical for Crescent to be the last stream to begin flowing and for Lost Seal to be the first stream to cease flowing.

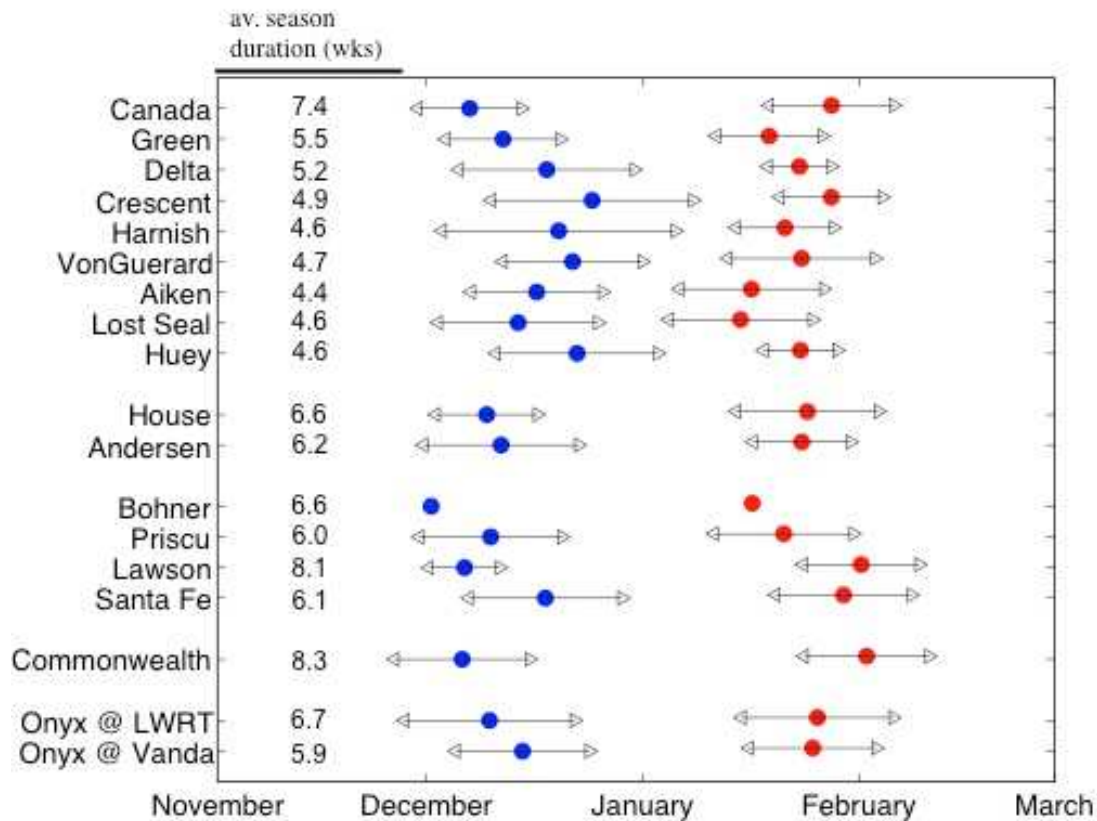


Figure 1.15: The mean t_5 (blue dots) and t_{95} (red dots) of annual streamflow for all gauged streams. Black error bars show +/- one standard deviation for start and end times. No error bars are shown for Bohner Stream because only a single year of record is currently available. Average flow season duration is listed for each stream.

Electrical Conductivity-discharge (EC-Q) relationships for all conductivity-gauged streams were analyzed in log-log space (Figure 1.A1). The slopes of the log-log EC-Q relationships (b) range from -0.22 on Commonwealth stream to 0.037 on House Stream (Figure 1.16). In general, these streams are dominated by chemostatic behavior, rather than pure dilution behavior. Longer streams, such as Von Guerard, Priscu, Lawson, Harnish, Delta, Crescent, and Aiken have slopes near zero. Shorter streams have more negative slopes, indicating a stronger

influence of dilution. Interestingly, House Stream is the only stream with a slope greater than zero. The chemostatic nature of these streams indicates that solute production and mobilization along the stream corridor proceeds at a similar pace to discharge of the open channel.

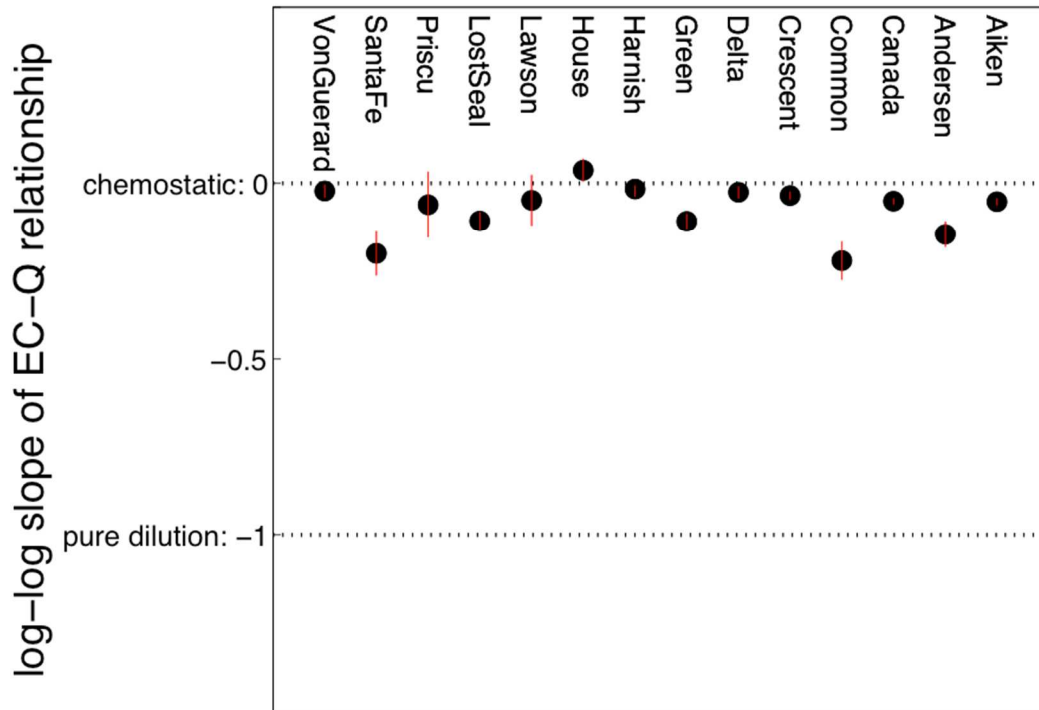


Figure 1.16: log-log slopes (b parameter) for EC-Q relationships. Red error bars show the 95% confidence interval of the best fitting b parameter.

The strength of EC-Q relationships is weakest on Santa Fe, Priscu, Commonwealth, and Lawson streams (Figure 1.A1). On these streams, there is a larger uncertainty in the log-log slope parameter, b (Figure 1.16). This is evidence that other variables, along with stream discharge, may exert a strong control on specific conductance variations.

1.4.3 Daily Connectivity Dynamics

Glacier-stream-lake connections follow a predictable diurnal cycle for all streams, typical of glacially-dominated catchments (Figure 1.17). The timing of peak daily discharge is characteristic for each stream because it is a combined function of glacier aspect, gradient, and stream length. Most streams encounter a single high-flow event in the day. However, Delta, Crescent, Bohner, and Santa Fe have more complicated daily connectivity patterns, in which discharge increases then decreases more than once during a single day. This more complicated connection is caused by multiple glacier source areas, that experience peak solar radiation at different times of the day [Conovitz *et al.*, 1998].

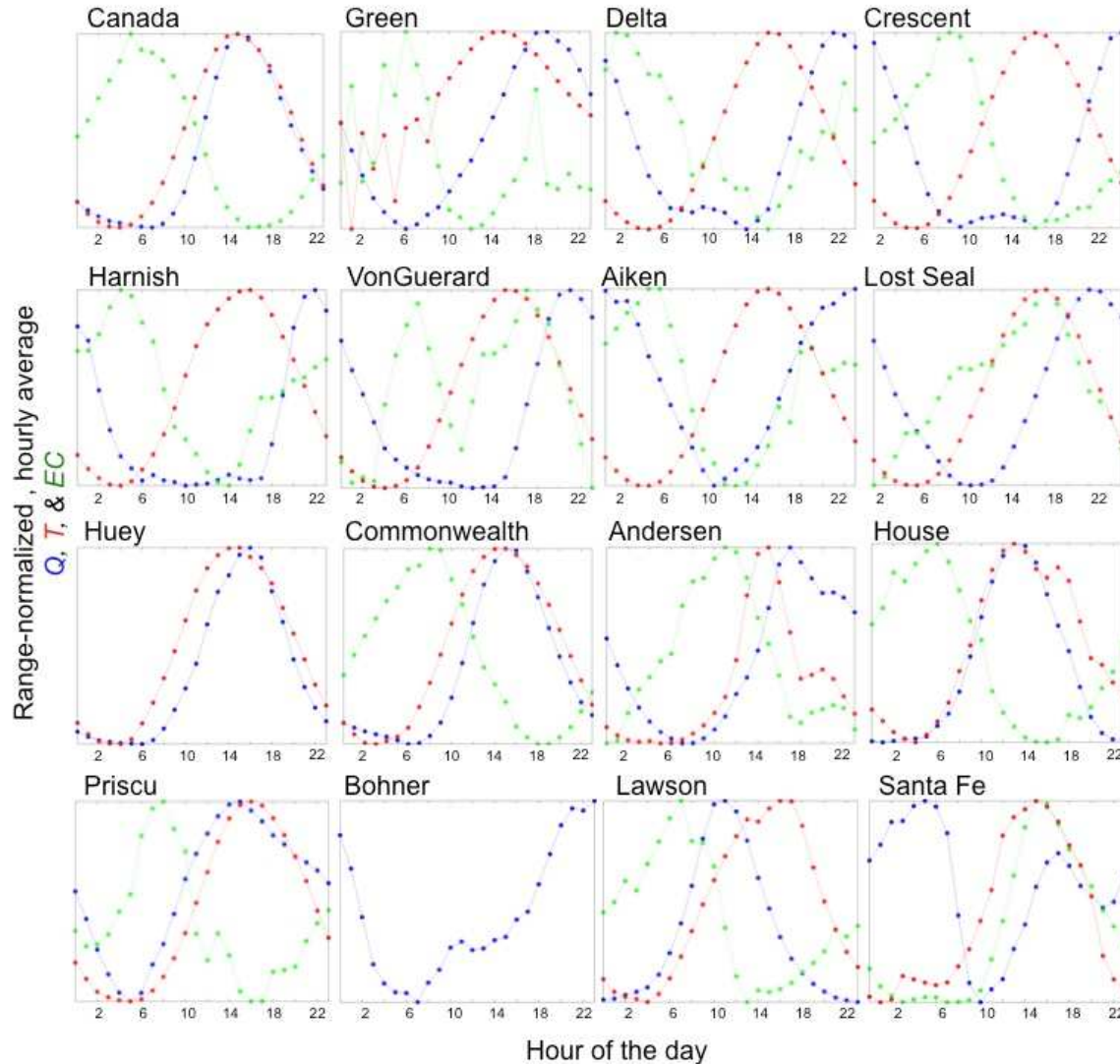


Figure 1.17: Average 24-hour Q, T, and EC patterns for streams within the Taylor Valley. Blue markers show hourly average discharge, red markers show hourly average water temperature, and green markers show hourly average specific conductance. The y-axis has been normalized over the observed range for each variable, such that daily maxima equal unity and daily minima equal zero.

Sub-daily stream temperature dynamics are consistent among all streams. Peak temperature occurs between 13:00 and 16:00, coincident with local solar noon during the austral summer. The coolest stream temperatures occur between 02:00 and 06:00. This dynamic reflects the importance of solar radiation on the stream water energy balance of all streams in the MDVs.

Specific conductance varies predictably over a 24-hour period as shown in Figure 1.17. Canada, Prisco, Commonwealth, and House Streams show clear dilution signals, as EC varies inversely with Q . However, dilution patterns are less clear in other streams, such as Aiken and Santa Fe, where EC exhibits a direct relationship with Q for many hours of the day. The complex relationship between EC and Q is a function of wave celerity, particle velocities, and surface-water groundwater connections along the stream corridor.

Over the course of an average day, the variability in EC is less than the 24-hour variability in Q for all streams (Figure 1.18). Despite the repeatable daily variation patterns in EC magnitude along each stream (Figure 1.17), on a 24-hour basis, these streams behave near chemostatically, similar to the annual behavior (Figure 1.16).

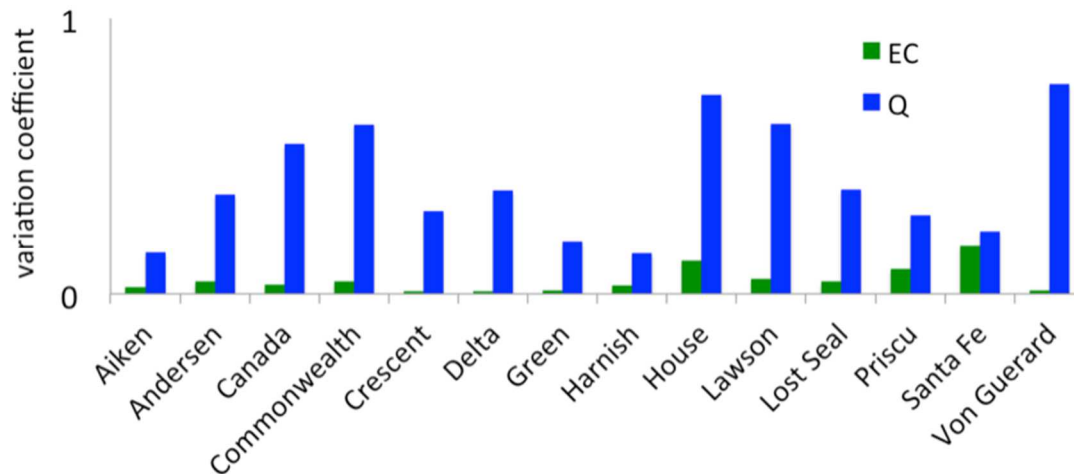


Figure 1.18: Variation coefficients of average 24-hour EC (green) and Q (blue) data. The daily average variation in EC is far less than the daily average variation in Q .

1.5 DISCUSSION

1.5.1 Annual electrical conductivity patterns infer differences in the connectivity of hyporheic zones

Streams of the Dry Valleys are dynamic and relatively simple systems, ideal for interrogating the influence of hyporheic exchange. Along the stream corridor, surface waters continuously exchange with shallow groundwaters in the hyporheic zone - the interstices of thawed sediments adjacent to and beneath stream channels [Runkel *et al.*, 1998]. Interestingly, hyporheic zones provide the main hydro-chemical connection between flowing stream waters and shallow groundwaters. Unlike temperate catchments, continuous permafrost prevents hydro-chemical connections with deep groundwater, and the lack of appreciable precipitation and high sublimation rates prohibit hydro-chemical connection between hillslopes and streams. Hyporheic connectivity is therefore chemically significant, because weathering reactions in hyporheic zones control stream solute loads (Gooseff *et al.*, 2002). Unlike in temperate catchments, the climate and geologic condition in the MDVs preclude hillslope processes from influencing stream chemistry.

Chemical weathering processes in the MDVs have been extensively investigated [Jones and Faure, 1978; Green *et al.*, 1988; Lyons and Mayewski, 1993; Gooseff *et al.*, 2002]. There are four primary sources of major ions found in stream and lake waters: (1) dissolution of marine derived salts and aerosols; (2) dissolution of calcite; (3) dissolution of thenardite (Na_2SO_4); and (4) hydrolysis of silicate materials. These processes require the presence of liquid water. Streams

and their hyporheic zones are the most consistently wetted portions of the landscape, and therefore are hotspots for chemical weathering. Measured weathering rates in the MDVs are equal to or greater than weathering in humid/temperate catchments, and weathering is believed to occur in hyporheic zones [Lyons *et al.*, 1997; Gooseff *et al.*, 2002].

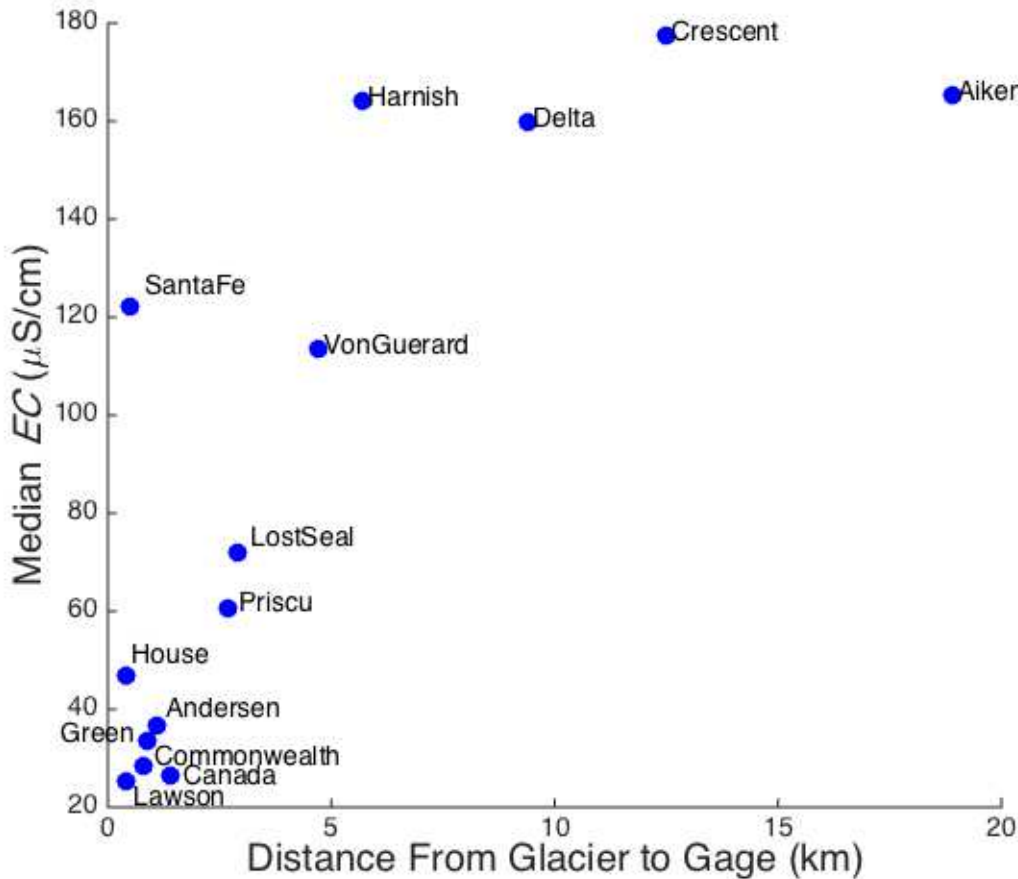


Figure 1.19: Median EC as a function of stream length, from glacier to gauge.

Long-term EC data in this study supports the interpretation that hydrologic connections between streams and hyporheic zones mediate solute loads in the MDV streams. Median EC generally increase with stream length (Figure 1.19), as corroborated by Welch *et al.* [2010].

Further, Gooseff *et al.* [2002] observed increases in Si, K, Mg, Na, Ca, and EC with increasing distance from the glacial source waters of Von Guerard Stream.

Landscape heterogeneity in the MDVs likely exerts a strong control on stream solute dynamics, specifically variations in water EC. For example, Santa Fe stream is an exception to the apparent relationship between stream length and median EC (Figure 1.19). It is only 0.5 km in length, but has a median EC of 122.1 $\mu\text{S}/\text{cm}$. Welch *et al.* [2010] and Foreman *et al.* [2004] reported anomalously high TDS and TSS loads from streams entering the west-lobe of Lake Bonney, including Santa Fe. Soil salinity increases from east to west in the Taylor Valley, where younger and wetter soils near the coast are less saline than older and drier soils near the polar plateau in the Bonney Basin [Bockheim, 1997].

We can understand inter-stream variation in stream-hyporheic connectivity through a simple conceptual model. If two identical volumes of meltwater are generated at the headwaters of Delta Stream (8.0 km length) and Canada Stream (1.5 km length), and we assume that the vertical and horizontal extent of hyporheic zones and hyporheic exchange rates are similar along both streams, then by virtue of stream length, melt water running through Delta Stream will be more connected to the hyporheic zone, spending a greater amount time within the hyporheic zone. If hyporheic residence time is a first order control on weathering reactions [Gooseff *et al.*, 2002], then over time longer streams will contribute more weathering products to lakes. However, the assumption that hyporheic zones have similar dimensions per unit length and similar exchange rates may not hold true. For example, Cozzetto *et al.* [2013] showed that the

effective volume of the hyporheic zone was much less than the volume of saturated sediments under and adjacent to Von Guerard Stream.

1.5.2 Biological implications of variability in annual flow connectivity

Longer streams exhibit more annually intermittent connections between glaciers and lakes, compared to shorter streams. This pattern is most evident in the Fryxell Basin (Figure 1.7a, b). In other words, shorter streams are more likely to sustain flow throughout the summer, whereas longer streams encounter more zero-flow days during the austral summer. Also, the initiation of flow occurs later for longer streams than shorter streams (Figure 1.15).

One possible explanation for this is differences in glacier contributing area elevation. The glacial contributing areas for longer streams are at higher elevations than those of shorter streams [Doran *et al.*, 2008]. Local summer lapse rates in the Taylor Valley have been estimated to be $6.5\text{ }^{\circ}\text{C km}^{-1}$ according to Hoffman [2011] and $9.8\text{ }^{\circ}\text{C km}^{-1}$ according to Doran *et al.* [2002]. It is reasonable to infer that on a given day air temperatures at lower elevations may be sufficient for meltwater generation, but are insufficient at higher elevations.

Alternatively, the role of hyporheic zones as storage reservoirs likely explain why longer streams exhibit more variability in hydrologic connection. The hyporheic zone immediately bordering the open channel must become saturated before channel flow is observed at the gauge. The volume of the hyporheic storage reservoir for longer streams is expected to be larger

compared shorter streams. Conovitz *et al.* [2006] demonstrated that volumes of water lost to hyporheic storage might be significant, particularly in low flow periods.

Evaporative losses from the open channel and hyporheic zones may also contribute to the intermittency of hydrologic connectivity observed in longer streams. Surface waters in longer streams are more isotopically enriched compared to shorter streams, indicating a strong evaporation signal [Gooseff *et al.*, 2006]. Evaporation losses occur in the open channel, at rates potentially as high as 6.17 mm dy^{-1} based on pan evaporation measurements by Gooseff *et al.* [2003]. However, in-channel evaporation does not completely explain lower flows in longer streams. Evaporation from hyporheic pore spaces at channel margins also occurs [Northcott *et al.*, 2009]; however, the net affect of this evaporation mechanism remains unknown.

In desert streams, annual hydrologic connectivity strongly influences stream benthic communities [Larned *et al.*, 2010] as is particularly evident in the polar desert of the MDVs. Anticipated climate change in the Dry Valleys [Turner *et al.*, 2009; Walsh, 2009] can be expected to alter hydrologic connections. Specifically, an increase in stream discharge and a decrease in flow intermittency are expected in the MDVs [Gooseff *et al.*, 2011]. Changes in hydrologic connectivity may create a less suitable habitat for diatom species adapted to functioning in highly intermittent environments (endemic species) [Stanish *et al.*, 2011, 2012]. In addition, because rates of mat regrowth are slow, with less than a 20% regrowth during one flow season following a scouring event [Kohler *et al.*, 2015b], increases in frequency of peak flows of 100 L/s that increase the likelihood of mat scouring may result in overall reductions in the mat abundance and change biogeochemical connectivity in the MDV.

1.5.3 The control of stream length and valley position on stream temperature dynamics

Longer streams have higher median surface water temperatures than shorter streams (Figure 1.20) and all streams in Taylor Valley experience peak daily average temperatures at nearly the same time, coincident with local solar noon (Figure 1.17). Cozzetto *et al.* [2006] also reported that the timing of peak water temperature for several streams in the Fryxell Basin was coincident with solar noon. Furthermore, Cozzetto *et al.* [2006] found that water temperatures at several sites along the channel of Von Guerard stream peaked at roughly the same time. This synthesis supports these conclusions by showing that the radiative energy balance and the connectivity with hyporheic zones likely control the timing and magnitude of stream temperatures.

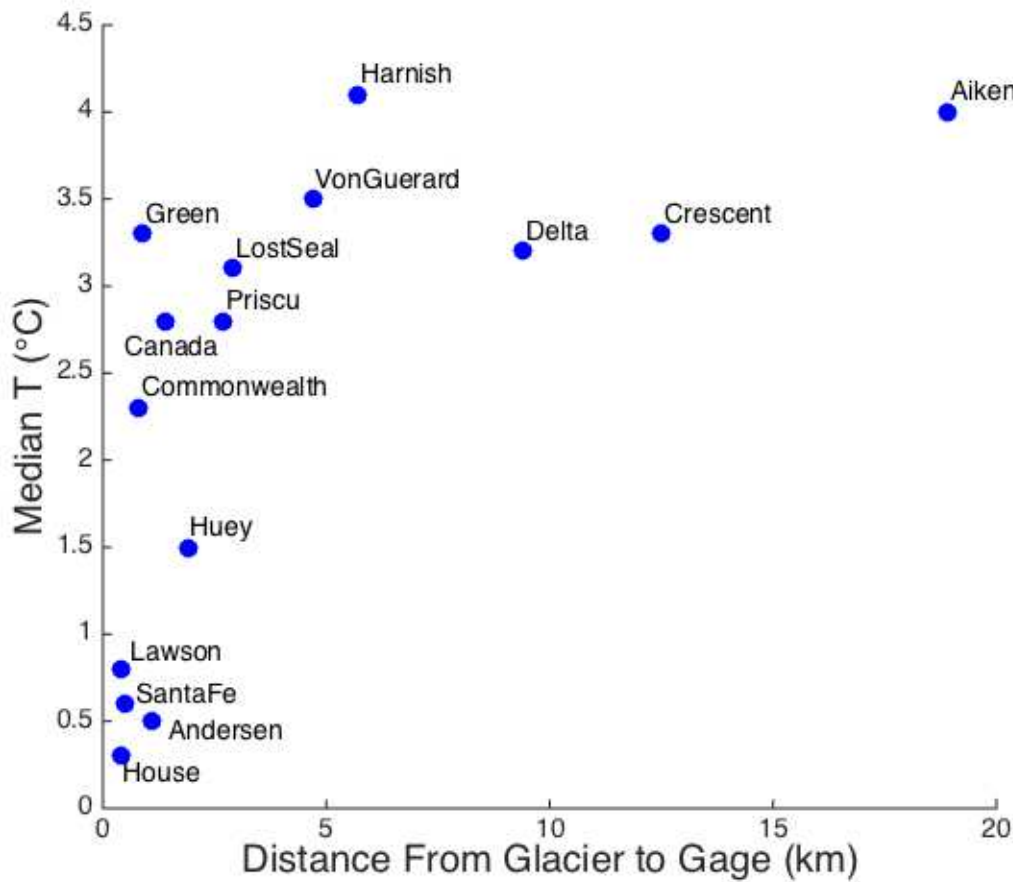


Figure 1.20: Median T as a function of stream length from glacier to gauge.

Santa Fe Stream exhibits the most dynamic thermal regime in Taylor Valley (Figure 1.11d). Because Santa Fe is a short stream that runs along the terminus of the Taylor Glacier, cool glacier water generated on high flow days is warmed little before reaching the gauge. Comparing this to Canada’s temperature-flow relationship, we see that daily average water temperatures show an increasing trend with increasing daily average discharge, until about 100 L/s when temperature begins to decrease with increasing daily flows (Appendix, Figure 1.A2).

Topographic shading differences within the Taylor Valley [Dana *et al.*, 1998] can also explain differences in temperature dynamics between streams. The coolest streams in the Taylor

Valley (House, Santa Fe, Andersen, and Lawson) all experience prolonged periods of daily topographic shading. These streams are located within the Bonney and Hoare basins, which are tightly confined by local topography. Streams with the warmest median temperatures are all located in the Fryxell Basin, which has a relatively wide valley floor.

1.5.4 Electrical Conductivity – discharge relationships

Chemostatic behavior of EC-Q relationships, at the annual and inter-annual timescale, was consistently observed for these streams (Figure 1.16). Relative to Q and T, the annual and inter annual variability in EC is small (Figure 1.9 & 10), corroborating the dominance of chemostasis. Similar chemostatic behavior has been observed in temperate catchments [Godsey *et al.*, 2009; Clow and Mast, 2010] and other glaciated catchments [Anderson *et al.*, 1997a; Anderson, 2005]. Previous work understanding the chemostatic catchment behavior in temperate catchments has focused on processes occurring along catchment hillslopes, such as the flushing of old hillslope water with newer water and changes in reactive mineral surface area due to changes in groundwater storage [Clow and Mast, 2010], neither of these occur in the relatively simple systems of the MDVs.

Chemostasis is caused a proportional and positive relationship between solute fluxes and water fluxes along the stream corridor. There are several explanations for chemostatic EC-Q relationships in MDV streams. First, it is possible that increases in discharge are complemented by an expansion of the hyporheic zone, and thereby an expansion of the reactive mineral surface area. This dynamic would increase the mass flux of solutes from hyporheic zones in proportion

with increased stream discharge, resulting in near-chemostatic behavior. This mechanism was eluded to by *Nezat et al.* [2001] as an explanation for the positive scaling of Si denudation rates with discharge. Second, an old-water hypothesis [*McDonnell*, 1990; *Kirchner et al.*, 2000; *Kirchner*, 2003], whereby daily flood pulses mobilize reacted water stored in the hyporheic zone from the previous flood events, could also maintain chemostasis. Third, the flushing of supraglacial aeolian dust deposited on glacier surfaces may increase reactive mineral surfaces and thereby weathering rates during high flow events [*Stumpf et al.*, 2012; *Marra et al.*, 2016]. This mechanism is somewhat analogous to the coupling between physical and chemical weathering in mid-latitude glaciated catchments, where the mobilization of physically abraded sub-glacial silt fuels high weathering rates along the stream corridor [*Anderson et al.*, 1997a; *Anderson*, 2005].

Chemostasis of EC in the MDVs may also be due to processes having little to do with chemical weathering. Many solutes in MDV streams are deposited by atmospheric deposition, given the proximity of the MDVs to the Ross Sea, rather than derived from the chemical weathering of minerals abundant in parent rock material [*Green and Canfield*, 1984]. Also, capillary wicking of stream water along the margin of stream channels [*Barrett et al.*, 2009] causes the development of salt crusts adjacent to the stream channel. An expansion of the wetted width of the stream channel during flood events may dissolve salt crusts, helping to maintain a chemostatic regime.

Future work on concentration-discharge relationships should consider solutes primarily derived from the weathering of primary and secondary minerals, such as dissolved silicon,

potassium, and bicarbonate. Understanding the relationship of rock-derived solutes with discharge will help elucidate the ability of the stream corridor to function as a geochemical filter and source between glaciers and lakes.

1.5.5 Climatic control on inter-annual flow variability

The long-term Q record shows high inter-annual variability in stream flow in the MDVs (Figures 14 & 15), where glacier melting generates the vast majority of streamflow observed at gauge locations. Therefore, similar to other glacially dominated catchments, inter-annual variations in stream flow are contingent upon prevailing climatic conditions and more specifically, inter-annual variations in the glacier surface energy balance. Thus, inter-annual stream flow variability is a manifestation of climate dynamics in the MDVs.

Several approaches have been used to model inter-annual flow volumes observed along streams in the MDVs. A simple temperature-index modeling approach [Hock, 2003] was used by Ebnet *et al.* [2005] to simulate runoff from select glaciers in the Taylor Valley. A modified melt model, accounting for spatial variations in solar radiation as well as air temperature, greatly improved model fits for north facing Howard glacier [Ebnet *et al.*, 2005]. Inter-annual variability in solar insolation likely plays a large role in controlling inter-annual runoff variability, particularly for streams emanating from north facing glaciers (Delta, Crescent, Von Guerard, Aiken, and Harnish). However, the influence of differences in snow coverage on glaciers from season to season is not yet well-quantified and could drastically change glacier surface albedo values.

Hoffman *et al.* [2008 & 2011] used a spatially distributed surface energy balance model to predict annual runoff volumes from the Canada Glacier. This more complicated modeling platform predicted runoff volumes reasonably well. However, the model performed poorly during lower flow years relative to higher flow years. This melt modeling effort did not account for in-stream processes, such as hyporheic storage and evaporative losses, which could be substantial during low-flow years. Coupling in-stream hydrologic and hydraulic models with glacier melt models is a potential venue for further research to better understand inter-annual runoff dynamics, particularly during anomalously high and low flow years.

1.6 CONCLUSIONS

Long-term stream gauge records allow for a robust understanding of the nature of glacier-stream-lake connectivity in the MDV. The extensive record of Q , EC , and T maintained by the MCM-LTER helps to elucidate hydro-ecological dynamics across various temporal (daily, annual, and inter-annual) and spatial (shorter streams v. longer streams, within and between basins) scales. 24-hour patterns of discharge, temperature, and specific conductivity are apparent across daily timescales. The timing of daily discharge differs between streams due to differences in glacier source area solar aspects. The timing of daily peak temperature is similar amongst all streams, coincident with the timing of solar noon. The daily relationship between EC and Q was unique amongst streams. Some, such as Canada, show a daily dilution dynamic, where Q and EC are inversely related. Other streams, such as Aiken, exhibit a flushing dynamic, where Q and EC are more directly related over the course of the day.

Although the timing and magnitude of annual flow connections are distinct among streams, in general, shorter streams were less intermittent and sustained higher flow magnitudes, compared to longer streams. Also, longer streams display higher mean annual specific conductance and exhibited more chemostatic EC-Q relationships, than shorter streams. This result suggests the enhanced influence of hyporheic zones along longer streams, compared to shorter streams.

The magnitude of glacier-stream-lake connections in the MDVs exhibits strong inter-annual variability. From 1969 – 2000 stream flow volumes show a decreasing trend. The highest observed flow season was 2001/2002. Following the 2001/2002 season, stream flow volumes have been greater and more variable compared to pre 2001/2002 years. Continuation of this higher inter-annual variability in the future is anticipated to drive ecosystem change. More frequent occurrence of peak flows may result in decreases in microbial mat abundance and community composition, for example.

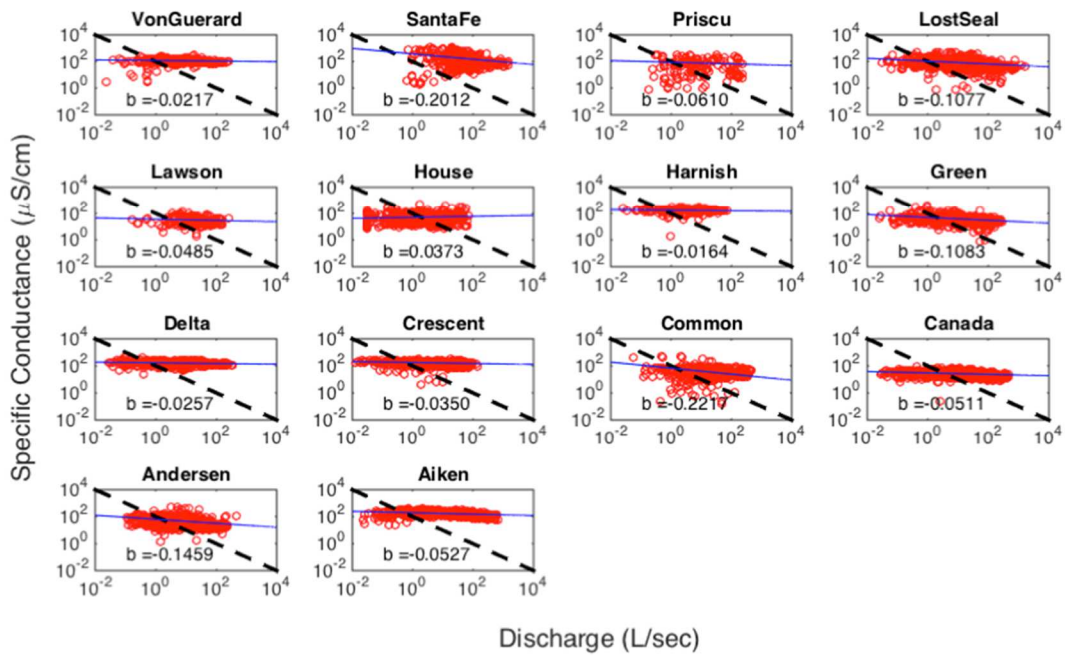


Figure 1.A1: log-log plots of EC-Q relationships for 14 streams within the Taylor Valley. Daily average values of Q and EC were used for this analysis. The blue line shows the best-fit slope of the relationship, and the black dashed lines shows a slope of -1, which indicates a pure dilution signal.

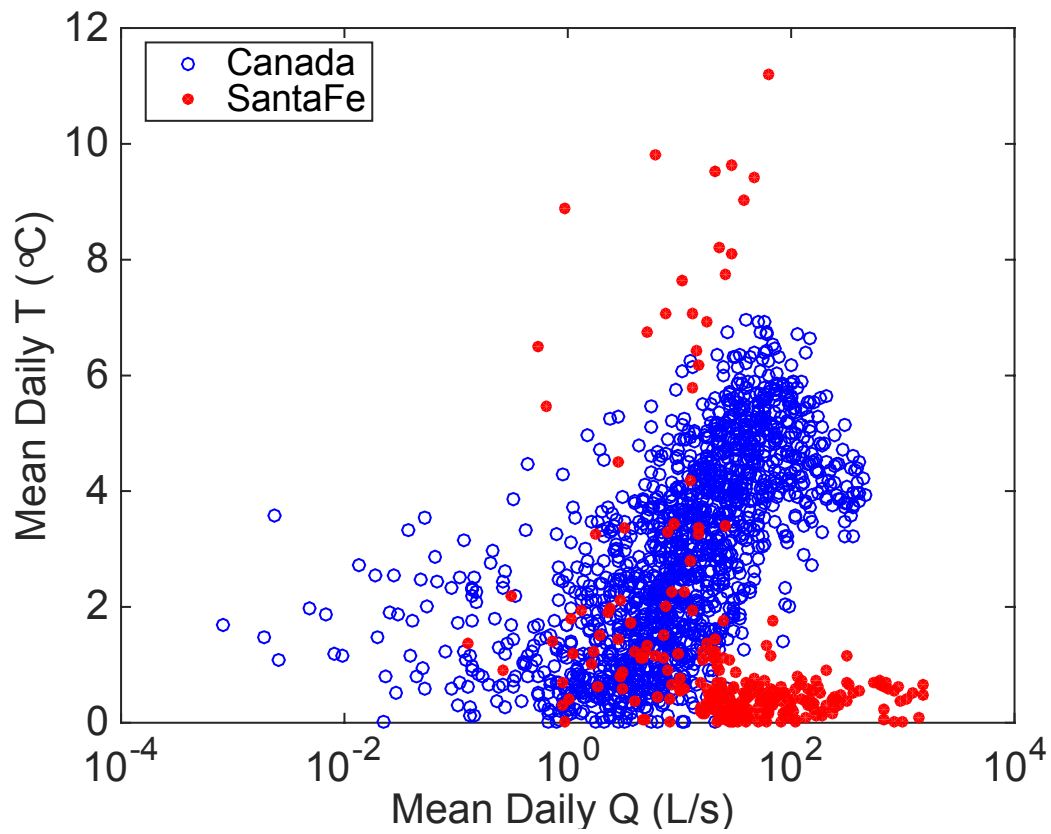


Figure 1.A2: Daily average T plotted as a function of daily average Q for Canada (blue open circles) and Santa Fe streams (closed red circles).

CHAPTER 2: Concentration–discharge relationships of weathering-derived solutes in streams of the McMurdo Dry Valleys, Antarctica

2.1 INTRODUCTION

2.1.1 Concentration discharge relationships and catchment function

Hydrologic and chemical connections within a watershed [Jencso *et al.*, 2009; Payn *et al.*, 2009, 2012; Covino *et al.*, 2011; EPA, 2014] control the nature of concentration-discharge (C-Q) relationships [Anderson *et al.*, 1997b]. As such, coincident discharge and water quality observations are useful for discerning patterns of source water connectivity within a watershed [Evans and Davies, 1998; Chanut *et al.*, 2002; McGlynn and McDonnell, 2003]. Chemostasis describes a dynamic where solute concentration remains relatively constant, while discharge may vary over orders of magnitude. Godsey *et al.* [2009] noted the chemostatic behavior of weathering-derived solutes in 59 catchments across North America. The ubiquity of chemostatic C-Q relationships implies that fluxes of weathering-derived solutes, such as dissolved silica, are primarily controlled by hydrologic fluxes, at the catchment scale, and that a shift in flowpaths or sources occur to keep a consistent C for wide ranges of Q. In temperate watersheds, the shifting sources of solutes that support chemostatic behavior are not clearly understood, and could include deep groundwater, shallow groundwater, soil water, differential source areas, etc.

Glacial meltwater streams of the McMurdo Dry Valleys (MDV) provide a useful natural laboratory for investigating the hydrologic and chemical connectivity of streams and hyporheic zones. Streams connect glaciers (source of streamflow) to closed-basin, ice-covered lakes while

maintaining connection to hyporheic zones along their length (Figure 2.1). Nearly all streamflow is derived from glacial meltwater, which fluctuates on a sub-daily basis due to solar aspect, resulting in diel pulses of streamflow [Conovitz *et al.*, 1998, Wlostowski *et al.*, 2016]. Stream channels are underlain and surrounded by hyporheic zones that are bounded at depth by permafrost, and thus typically thaw to maximum extent of less than 1m [Conovitz *et al.*, 2006]. Because there is no rainfall and most snowfall sublimates shortly after falling [Fountain *et al.*, 2010], stream channels remain hydrologically decoupled from adjacent hillslopes. The potential lateral extent of the hyporheic zone can be seen as a dark band of wetted soils at the margins of the stream channel [Northcott *et al.*, 2009]. The hydroclimatic setting of the MDVs provides an opportunity to elucidate chemical and hydrological controls on C-Q relationships, through a highly constrained conceptual model focused on streams and hyporheic zones. In this work we focus on the production and transport of weathering-derived solutes in Antarctic streams, with specific attention of dissolved silica (Si). The goal of this study is to understand how streams and hyporheic zones exert chemical and hydrologic controls on C-Q relationships of weathering derived solutes.

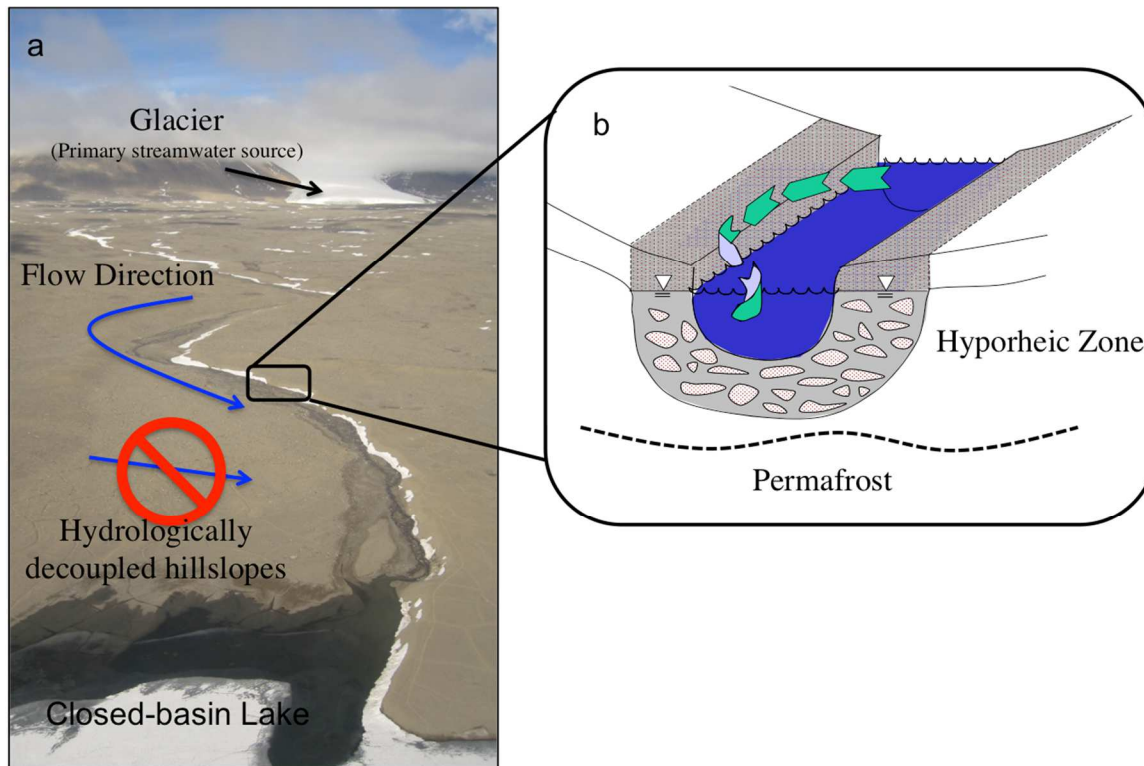


Figure 2.1: (a) An aerial image of a glacier-stream-lake hydrologic system (photo credit M. Gooseff). Along the stream corridor, waters exchange with shallow groundwaters in hyporheic zones (b). Unlike temperate catchments, hillslopes adjacent to stream channels are hydrologically decoupled.

2.1.2 Silicon cycle in Antarctic streams

Silicon is the second most abundant element in the earth's crust, accounting for over 28% of its composition. Si is found in crystalline, amorphous, and aqueous phases. The terrestrial Si cycle transports Si within and between various geochemical reservoirs by a suite of physical and chemical processes [Struyf *et al.*, 2010; Cornelis *et al.*, 2011]. At the base of the terrestrial Si cycle, physical and chemical weathering is responsible for the breakdown of primary silicate minerals. Si is then dissolved, transported and/or re-precipitated in a variety of organic and inorganic forms, before being ultimately deposited in oceans. The Si cycle is ecologically relevant because Si is biologically assimilated by plants and microorganisms, and climatically relevant because the weathering of primary silicates is a net sink of carbon dioxide.

Si is abundant as a solid in Antarctic streams and hyporheic zones, bound in the crystalline lattice of primary and secondary silicate minerals. XRD analysis of hyporheic sediments [Gooseff *et al.*, 2002; Marra *et al.*, 2016] reveals that feldspar, pyroxene and quartz are the most abundant primary minerals, while muscovite, illite, smectite, biotite, chlorite, and kaolinite are the most abundant secondary minerals. Amorphous Si is also present in Antarctic hyporheic zones. Diatoms assimilate dissolved Si from flowing stream waters to siliceous frustules, composed of polymerized amorphous silica [Lewin, 1961; Esposito *et al.*, 2008]. Amorphous Si species are also created when dissolved Si adsorbs to aluminum and iron oxides/hydroxides [Okamoto *et al.*, 1957; Huang, 1975; Pokrovski *et al.*, 2003]. Although this dynamic has not been directly reported in MDV streams, whole rock geochemical analysis shows that iron is abundant in stream sediments [Marra *et al.*, 2016] and iron oxides are known to exist in regional soils [Campbell *et al.*, 1998], indicating that silica-iron adsorption/desorption is likely to occur.

Chemical weathering of mineral surfaces and the dissolution of amorphous Si generates dissolved Si. Conventional theory on chemical weathering rates asserts that weathering is strongly controlled by climate [White and Blum, 1995]. That is, weathering rates are often positively correlated with temperature, precipitation, and runoff. The Arrhenius equation provides a fundamental linkage between environmental temperature geochemical reaction rates, justifying a correlation between climatic setting and chemical weathering rates [White *et al.*, 1999]. However, previous investigations provide evidence of moderate to high weathering rates occurring in MDV streams, despite the very cold and arid climate.

Early contributions of *Jones and Faure* (1978) showed that the strontium in Lake Vanda sediments was likely derived from the weathering of bedrock in Wright Valley. *Green and Canfield* (1984) concluded that dissolved calcium, magnesium, and bicarbonate in the Onyx River are likely sourced from the weathering of regional soils. *Green and Canfield* (1984) also noted that water in the Onyx River contains a progressively greater fraction of weathering-derived solutes along the 28-km length of the stream, a result replicated by *Green et al.* (2005). Later observations of dissolved Si in stream waters confirmed that chemical weathering of silicate minerals is occurring [*Green et al.*, 1988]. Furthermore, *Green et al.* (1988) noted a correlation between stream length and chemistry. Longer streams show more evidence of mineral weathering compared to shorter streams, where water chemistry appears to be dominated by atmospheric deposition. *Lyons et al.* (1997) quantified “catchment” average weathering rates for various streams in the Taylor Valley ($4 - 193 \times 10^3$ moles $\text{H}_2\text{SiO}_4 \text{ km}^{-2} \text{ yr}^{-1}$); these rates are similar to those calculated in humid/temperature catchments.

Because chemical weathering of silicate minerals requires rock-water interactions, the hyporheic zone is thought to be an important incubator of weathering in an otherwise parched landscape. *Nezat et al.* (2001) showed that annual Si denudation rates are similar in magnitude to other glaciated watersheds [*Anderson et al.*, 1997a], and are positively correlated with discharge. Based on these observations *Nezat et al.* concluded that higher streamflow years result in an expansion of the hyporheic zone, more rock-water interactions, and higher weathering rates. Moreover, *Gooseff et al.* (2002) showed that along-stream increases of Si and K^+ in Von Guerard Stream may be explained by high chemical weathering rates and rapid hyporheic exchange rates.

Field-estimated geometric weathering rates from *Gooseff et al.* (2002) ranged from 6.4×10^{-13} - 4.5×10^{-12} moles Si $m^{-2} \text{ sec}^{-1}$. These rates are comparable to other field-based geometric weathering rates estimates in temperate humid catchments observed by *Velbel* (1985) and *Swoboda-Colberg and Drever* (1993). Furthermore, *Maurice et al.* (2002) observed the formation of etch pits on mica slides embedded in the hyporheic zone after 39 days during the austral summer. Based on etch pit geometry, a weathering rate of 8.3×10^{-14} moles mica $m^{-2} \text{ sec}^{-1}$ was calculated.

The stream corridor is hypothesized to be a major source of Si because glacier waters contain relatively low Si concentrations. Atmospheric deposition of Si on glacier surfaces is very low [*Mayewski and Lyons*, 1982]. The concentration of Si in supraglacial melt streams is also low. *Fortner et al.* (2005) observed an average Si concentration of 0.08 mg L^{-1} in supraglacial streams on Canada Glacier, whereas proglacial Canada Stream (a short stream on the east side of the Canada Glacier) displayed an average Si concentration of 0.85 mg L^{-1} during the 1995-1996 flow season. Although Si concentrations in proglacial streams are low, cryoconite holes present isolated Si hot spots. *Tranter et al.* (2004) measured Si concentrations as high as 1.85 mg L^{-1} in cryoconite holes (locations of preferential melt on the surface of glaciers containing significant sediment) atop Canada Glacier. The net affect of cryoconite holes on the chemistry of meltwaters entering proglacial channel heads remains unknown.

2.1.3 Chapter goals and hypotheses

The goal of this chapter is to address the hypothesis that hyporheic exchange and high rates of chemical weathering control the nature of C-Q relationships for weathering-derived

solutes in glacial catchments. This goal will be addressed by first analyzing long-term stream geochemical records to characterize the nature of C-Q relationships for weathering-derived solutes and infer the relative importance of chemical weathering among eight different streams in the eastern Taylor Valley. Second, a series of numerical solute transport models will be used to simulate long-term Si concentrations in Von Guerard stream. Transport models, which simulate hyporheic exchange and chemical weathering, are used to test the hypothesis that hyporheic exchange and rapid chemical weathering control Si chemistry.

2.2 STUDY SITE

The MDVs (Figure 2.2) cover a 22,700 km² area of East Antarctica, 4,500 km² of which are ice-free [Levy, 2013]. Mean annual temperature is -18°C [Doran *et al.*, 2002] and annual precipitation is <10 mm water equivalent [Keys, 1980; Bromley, 1985; Fountain *et al.*, 2010]. Despite the cold and dry climate, seasonal melting of glacier ice generates ephemeral stream flow during the austral summer (November – February) [Lewis *et al.*, 1998; Ebnet *et al.*, 2005; Hoffman *et al.*, 2008]. The brief flow season generally lasts between 4.4 and 8.3 weeks, beginning by mid December, and concluding by early February [Wlostowski *et al.*, 2016]. Detailed reviews of physical hydrology in the MDVs have been provided by Conovitz *et al.*, [1998], Fountain *et al.*, [1999] Doran *et al.*, [2008], Gooseff *et al.*, [2011], and Wlostowski *et al.* [2016].



Figure 2.2: Location map of the McMurdo Dry Valleys. The Taylor Valley, the research hub of the McMurdo Dry Valleys LTER, is indicated. Cartographic credit: Brad Herried, Polar Geospatial Center, University of Minnesota.

Flow in MDV streams varies greatly over daily, annual, and inter annual time scales. Daily variations in flow are caused by diel variations of glacier melt rates, which are largely controlled by diel variations in shortwave radiation fluxes and solar aspect on the top and steep sides of MDV glaciers [Conovitz *et al.*, 1998; Lewis *et al.*, 1998] (Figure 2.3, a). Over annual and inter annual time periods, climatic variability controls the magnitude of daily flood pulses and total annual streamflow volumes [Doran *et al.*, 2008; Hoffman, 2011] (Figure 2.3, b). Warm and sunny austral summers, such as the 2001/02 summer, can cause 10 times more runoff compared to cooler and cloudier austral summers, such as the 2000/01 summer.

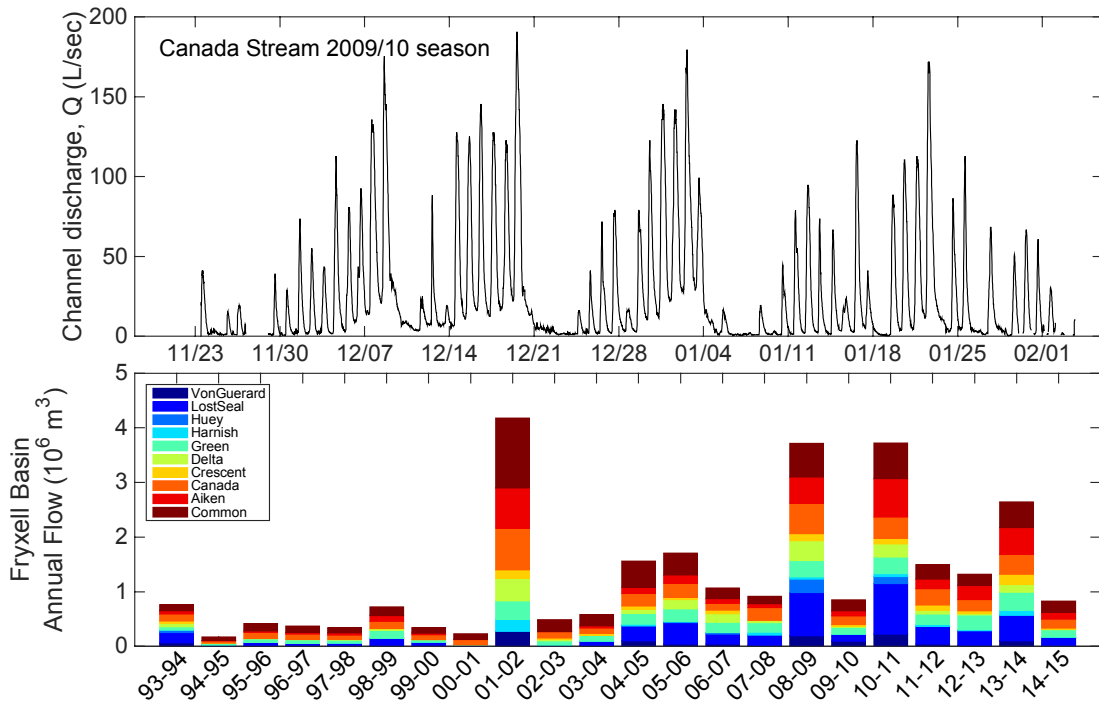


Figure 2.3: (a) Streamflow record at Canada Stream during the 2009/10 austral summer, and (b) the long-term record of total annual streamflow volumes from all gauged streams in the Lake Fryxell Basin (b).

This study considers eight streams in the Lake Fryxell and Ross Sea basins of eastern Taylor Valley (Figure 2.4, Table 2.1). Delta Stream, Crescent Stream, and Von Guerard Stream flow from the Kukri Hills into the southern side of Lake Fryxell, and are among the longest streams in the basin. Green Creek and Canada Stream flow from the Canada Glacier into the western end of Lake Fryxell, and are among the shortest streams in the basin. Aiken Creek and Lost Seal Stream flow into the eastern end of Lake Fryxell. Lost Seal is sourced by meltwater from the Commonwealth Glacier, while Aiken Creek is sourced from glaciers in the Kukri Hills and the Commonwealth Glacier. Aiken Creek is by far the longest stream in the Fryxell Basin and flows through Many Glaciers Pond near its entrance into Lake Fryxell. Commonwealth

stream is sourced by meltwater from the Commonwealth Glacier, and flows into the Ross Sea at New Harbour.

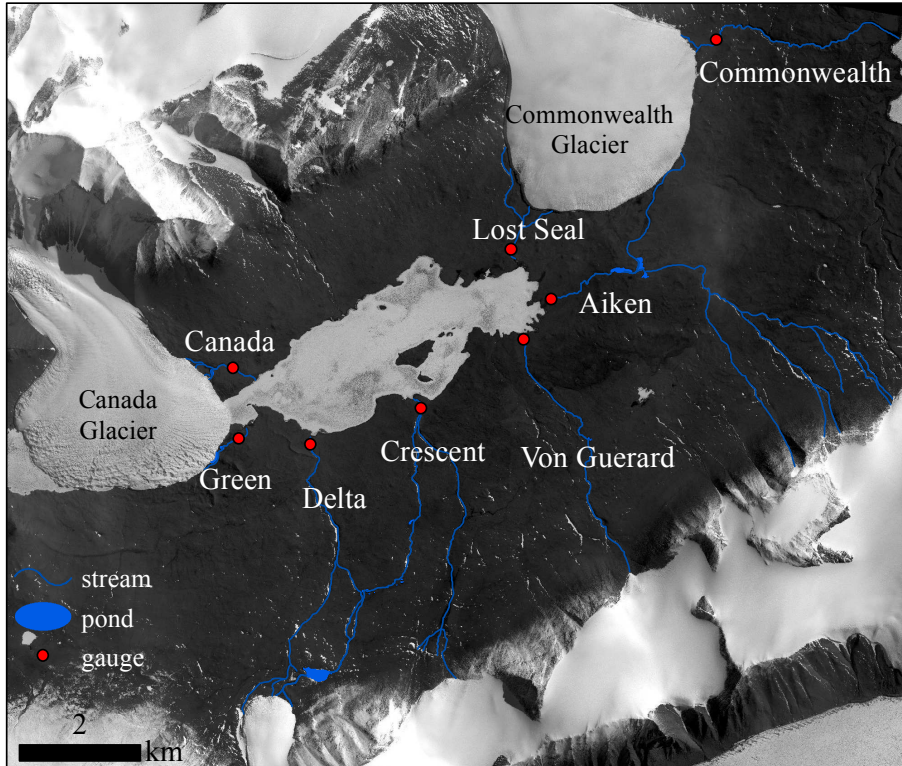


Figure 2.4: Eight streams in eastern Taylor Valley considered in this study. WorldView3 Imagery courtesy of Polar Geospatial Center, University of Minnesota.

Table 2.1: Length and gradient of the eight streams in eastern Taylor Valley. The number of LTER water samples collected on each stream between 1990 and 2015 is also listed (data available from the McMurdo LTER online database, <http://www.mcmlter.org>).

Stream	Length, total (km)	Length, to gauge (km)	Gradient (m/m)	# of samples collected
Aiken	18.9	18.9	0.13	95
Crescent	12.8	12.5	0.06	77
Delta	9.5	9.4	0.05	75
Von Guerard	4.8	4.7	0.07	96
Commonwealth	4.5	0.8	0.03	87
Lost Seal	3.1	2.9	0.04	103
Canada	1.9	1.4	0.1	131
Green	1.1	0.9	0.04	124

Streams in eastern Taylor Valley flow through sandy valley-bottom soils with interspersed cobbles and boulders. Soils in this region were deposited by the Ross Sea drift and

show evidence of strong cryoturbation [*Bockheim and McLeod, 2008*]. Soil parent material is a mixture of granite, gneiss, dolerite, and sandstone [*Péwé, 1960; Doran et al., 1994; Bockheim, 1997*]. Streambeds are composed of jumbled rocks and larger boulders along steeper gradient reaches. Along lower gradient reaches, water flows over a stone pavement developed by the long-term persistence of periglacial processes [*McKnight et al., 1999*].

2.3 METHODS

2.3.1 Long-term stream geochemical sampling and analysis

The Taylor Valley has been the primary research site for the McMurdo Long-Term Ecological Research (MCM-LTER) Project since 1993. As part of the long-term monitoring effort, a network of stream gauges was established and has been maintained throughout the region. Stream gauges monitor the discharge, water temperature, and specific conductance at 15-minute intervals during flow seasons. A more detailed account of stream gauging procedures can be found in Chapter 1 of this dissertation or [*Wlostowski et al., 2016*].

Between 1993 and 2014, as part of the ongoing LTER project, water samples were collected near gauge locations. Samples were collected irregularly during each flow season. Between 75 and 124 total samples were collected over the record period on each stream (Table 2.1). Although water samples are analyzed for many different solutes, this study will focus only on cations, bicarbonate, and dissolved Si. Within 24 hours of collection, samples were filtered through 0.4 μm Nucleopore polycarbonate membrane filters. Cation and Si samples were filtered

into DI rinsed HDPE bottles. Cation and Si samples were stored at 4°C until analysis, following the methods of *Welch et al.*, [2010]. Alkalinity was determined by titration, and titration alkalinities are assumed to be primarily bicarbonate [*Welch et al.*, 2010].

Dissolved Si is measured colorimetrically following the methods of *Mullin and Riley*, 1955. In natural waters at pH < 9, dissolved Si is primarily present as silicic acid, H₄SiO₄ [*McKeague and Cline*, 1962]. Other polymerized silicon species may also be present in solution. However, these compounds are not detectable by colorimetric methods. Hereinafter we will use the term ‘silica’ or simply ‘Si’ in reference to colorimetrically detected dissolved silicon species, likely H₄SiO₄.

To objectively test for chemostasis, concentration-discharge relationships of Ca⁺, K⁺, HCO₃⁻, and Si are fit with a power-law model:

$$C = aQ^b \quad (2.1)$$

where C is concentration of a dissolved constituent (mg/L), Q is daily average discharge (L/sec), b is a scaling parameter that approximates the slope of the concentration-discharge relationship on a logarithmic axis, and a is a constant. Following the logic of *Godsey et al.* (2009), b indicates the degree of dilution occurring in the system. A b value of -1 describes a pure dilution system, where the rate of solute mobilization remains constant as discharge increases and decreases. A b value of 0 (horizontal line in log-log space) describes a purely chemostatic system. That is, as discharge increases, the rate of solute mobilization increases in the same proportion, resulting in similar solute concentrations at all discharge conditions. Lastly, a b value greater than 0 indicates a concentrating system, where concentration increases as flow increases.

In addition to long-term geochemical sampling, a more intensive sampling campaign was conducted on Von Guerard Stream between January 9th and January 21st, 2016. During this time, water samples were collected from both the stream channel and 9 hyporheic mini-piezometers. Mini-piezometers were designed and installed to sample mobile hyporheic pore space at discrete depths. Mini-piezometers were installed to a depth of 20 – 35 cm beneath the stream surface. Samples were collected at least once per day during the monitoring period, and were filtered and analyzed for dissolved Si and oxygen stable isotopes. $\delta^{18}\text{O}$ of water samples was analyzed with a Picarro L1102-I instrument, and reported relative to V-SMOW.

2.3.2 Numerical weathering and transport model

To address the hypothesis that hyporheic exchange and high rates of chemical weathering control the nature of C-Q relationships, a 1-dimensional unsteady and non-uniform transient storage model is used to simulate hyporheic exchange, Si transport and Si weathering in Von Guerard Stream. The transport model is based on the One Dimensional Transport with Inflow and Storage (OTIS) Model [Runkel, 1998]. Model equations are modified to allow the hyporheic zone area (A_S in OTIS; there is very little in-channel storage in MDV streams) to change as a function of time. The Si mass and water balance of the stream channel is expressed as:

$$\frac{\partial C}{\partial t} = -\frac{Q}{A} \frac{\partial C}{\partial x} + \frac{1}{A} \frac{\partial}{\partial x} \left(AD \frac{\partial C}{\partial x} \right) + \alpha (C_{HZ} - C) \quad (2.2)$$

where t is time (sec), x is channel distance (m), C is the main-channel Si concentration (mg/L), Q is the flow rate of water in the channel (m^3/sec), A is the cross sectional area of flow in the

stream channel (m^2), D is a dispersion coefficient (m^2/sec), α is the stream channel – hyporheic zone exchange rate (1/sec), and C_{HZ} is the Si concentration in the hyporheic zone (mg/L).

The hyporheic zone is conceptualized as a series of well-mixed reservoirs (or dead-zones) that dynamically exchange water and solutes with the open channel. While water and solutes can move into and out of the hyporheic zone, the model assumes that no downstream or upstream advection or dispersion occurs in the hyporheic zone [Thackston and Schnelle, 1970]. The Si mass and water balance of the hyporheic zone is expressed as

$$\frac{dC_{HZ}}{dt} = \alpha \frac{A}{A_{HZ}} (C - C_{HZ}) + \frac{1}{A_{HZ}} \frac{dA_{HZ}}{dt} (C' - C_{HZ}) + \lambda (\hat{C} - C_{HZ}) \quad (2.3)$$

where A_{HZ} is the cross-sectional area of the hyporheic zone (m^2), \hat{C} is the equilibrium concentration of Si in the hyporheic zone (mg/L), λ is a first-order weathering rate coefficient (1/sec), and C' is a Si concentration (mg/L) dependent on whether or not the hyporheic zone is expanding or contracting with time. A_{HZ} is controlled by thaw depth beneath the stream channel, $z_{thaw}(t)$ (m), channel width, w_c (m), wetted margin half-width, w_m (m), and porosity, ϕ as:

$$A_{HZ}(t) = z_{thaw}(t) \times (w_c + 2w_m) \times \phi \quad (2.4)$$

When the hyporheic zone is expanding (i.e., $dA_{HZ}/dt > 0$), $C' = C_{thaw}$ (Equation 2.5), where C_{thaw} is the Si concentration of newly thawed interstitial pore waters enveloped by the expansion of the hyporheic zone. Conversely, when the hyporheic zone is contracting (i.e., $dA_{HZ}/dt \leq 0$), $C' = C_{HZ}$ (Equation 2.5), and second term on the right hand side of Equation 2.3 goes to zero. The time rate of change in C_{HZ} is not affected by the contraction of the A_{HZ} , because the removal of fluid from a well-mixed reservoir does not alter the concentration of the remaining fluid in the reservoir.

$$C' = \begin{cases} C_{thaw} & ; \frac{dA_{HZ}}{dt} > 0 \\ C_{HZ} & ; \frac{dA_{HZ}}{dt} \leq 0 \end{cases} \quad (2.5)$$

A Crank-Nicolson implicit numerical scheme is used to solve the system of coupled equations (Equations 2.2 and 2.3) [Runkel and Chapra, 1993].

Sub-channel thaw depth is estimated with the University of Alaska Fairbanks Geophysical Institute Permafrost Laboratory (GIPL2) model [Shiklomanov *et al.*, 2007; Jafarov *et al.*, 2012, 2013]. The model numerically solves the Stefan Problem [Stefan, 1891] with phase change, to approximate the temperature of sub-channel soils (Equation 2.6).

$$c_e \frac{\partial T}{\partial t} = \frac{\partial}{\partial z} \left[k \frac{\partial T}{\partial z} \right] \quad (2.6)$$

where c_e is the effective volumetric heat capacity of the soil ($\text{J m}^{-3} \text{K}^{-1}$), k is the soil thermal conductivity ($\text{W m}^{-1} \text{K}^{-1}$), T is soil temperature (K), z is depth (m), and t is time (seconds). The effective soil heat capacity is defined as:

$$c_e = c_b + L_f \frac{d\theta_l(T)}{dT} \quad (2.7)$$

where c_b is the bulk volumetric heat capacity of the soil ($\text{J m}^{-3} \text{K}^{-1}$), L_f is the volumetric latent heat of fusion (J m^{-3}), and θ_l is the unfrozen water content ($\text{m}^3 \text{m}^{-3}$). $\theta_l(T)$ is assumed to be a differentiable function describing liquid water content as a function of temperature

$$\theta_l(T) = \begin{cases} \theta & T \geq T_f \\ \tau|T|^n & T < T_f \end{cases} \quad (2.8)$$

where, τ and n are empirical constants [Lovell, 1957]. The depth of thaw is estimated at each time-step by approximating the location of the zero-degree isotherm. The GIPL model uses a Crank-Nicolson implicit numerical routine.

Spatially and temporally continuous Q estimates are required to run the Si transport model. Discharge is continuously approximated with a 1-dimensional flood routing model. The routing model employs a kinematic wave simplification of the momentum equation (Equation 2.9), which assumes that dynamic terms in the momentum equations are negligible. Therefore, the friction slope is simply equal to the bed slope and discharge can be described as a function of flow depth (Equation 2.10).

$$\frac{\partial A}{\partial t} + \frac{\partial Q}{\partial x} = q_l \quad (2.9)$$

$$Q = \sigma A^m \quad (2.10)$$

where q_l is a lateral inflow rate (m^2/sec), and σ and m are kinematic wave parameters for a particular cross sectional shape, slope, and channel roughness. For wide and shallow rectangular channels σ and m are defined as:

$$\sigma = \frac{\sqrt{S_o}}{n} w^{-2/3} \quad (2.11)$$

$$m = \frac{5}{3} \quad (2.12)$$

where, S_o is the channel slope (m/m) and n is the Manning's roughness coefficient . Kinematic wave equations are numerically solved with a backwards-time backwards-space implicit finite difference technique.

2.3.3 Model parameterization

We assume a uniform channel width, w_c , of 5 m based on personal observations and the work of *Alger* (1997). Furthermore, we assumed a uniform wetted margin half width, w_m , of 2 m, based on the observations of *Northcott et al.* (2009) , which show that within 2 m of the stream edge, soil moisture dropped below 10% by volume. Porosity, ϕ , is set to 0.4, typical for a sandy gravel substrate as also used by *Koch et al.* (2011). The average slope and length Von Guerard stream were estimated to be 0.07 m/m and 4.7 km, respectively by terrain analysis with GIS software. Manning's roughness was set to 0.1, based on values used by *Runkel et al.* (1998) for flood routing along Huey Creek, another Fryxell Basin stream.

The routing model was driven at the upstream boundary by approximate daily melt pulses. Previous work shows that melt production follows a diel pattern, where the timing and magnitude of peak melt is controlled by solar insolation on glacier cliffs [*Conovitz et al.*, 1998]. As such, daily upstream melt pulses (q_{melt}) are assumed to have a Gaussian shape with respect to time:

$$q_{melt}(t) = q_{pk} e^{-\frac{1}{2} \left(\frac{t-t_{pk}}{\sigma} \right)^2} \quad (2.13)$$

where q_{pk} is the peakflow magnitude of the upstream pulse (m^3/sec), t_{pk} is the hour of the day when peak melt occurs, and σ is the standard deviation of the melt distribution. It is assumed that t_{pk} on Von Guerard glacier occurs at the same time every day ($t_{pk} = 12:00$) and $\sigma = 2$ hours, such that 95% of daily glacier melt is assumed to occur within 4 hours of 12:00 every day. The magnitude of the upstream melt pulse was optimized to match daily peak flow magnitudes observed at downstream gauge locations between October 2004 and February 2013.

Transport and weathering parameters were constrained by previous solute transport investigations of MDV streams. The stream channel dispersion coefficient, D , was set to $0.5 \text{ m}^2/\text{sec}$, a value also used by *Runkel et al.* [1998] and *Gooseff et al.* [2002]. The equilibrium concentration of Si in the hyporheic zone, \hat{C} , was set to 5.7 mg/L , stemming from the observations of *Gooseff et al.* [2002]. The Si concentration of newly thawed hyporheic sediments was set to 2.35 mg/L , the median Si concentration observed in Von Guerard stream between 2004 and 2013.

Exchange rate, α , and weathering rate, λ , parameters were selected by choosing the best performing parameter set (lowest mean absolute error, MAE) from 1000 Monte-Carlo simulations. Monte-Carlo simulations considered randomly selected parameter combinations from a log-normally distributed parameter range of $[3.5 \times 10^{-5} - 4 \times 10^{-2}] \text{ 1/sec}$ for α and $[4 \times 10^{-7} - 5 \times 10^{-5}] \text{ 1/sec}$ for λ . The sampled range of α considers the published range of α from all OTIS studies on MDV streams. The bottom value was published by *Gooseff et al.* [2003], while the upper boundary was published by *Gooseff et al.* [2004]. The sampled range of λ considers the range of λ published by *Gooseff et al.* [2002]. The range was extended upwards to an upper

boundary of 5×10^{-5} 1/sec to account for a vague positive correlation between discharge and λ noticed in that study (Figure 2.5) and because that study only considered relatively low-flow conditions ($Q < 0.015$ m³/sec), whereas the discharge on Von Guerard between 2004 – 2013 frequently exceeded 0.015 m³/sec.

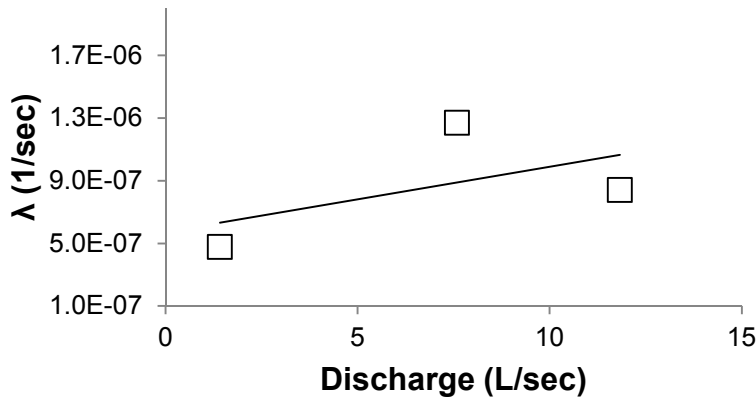


Figure 2.5: Optimal weathering rate constant values, λ , from *Gooseff et al.* (2002) plotted as a function of Discharge. A vague positive correlation is evident and the range of discharge values considered in this study is all < 14 L/sec. The linear relationship is insignificant at the 5% level.

Hyporheic thaw depth was estimated from GIPL simulations that ran from June 1, 2004 – June 1, 2013. The 1-D model domain extended 10 meters beneath the streambed, and the domain was discretized into 1 cm layers. The model is forced by a Dirichlet type upper boundary condition:

$$T(0, t) = T_{surface} \quad (2.14)$$

The upper boundary condition was informed by stream temperature when stream temperature data was available, and air temperature during periods when the stream was not flowing and/or stream temperature data was not available. A time series of forcing data is shown in (Figure 2.6).

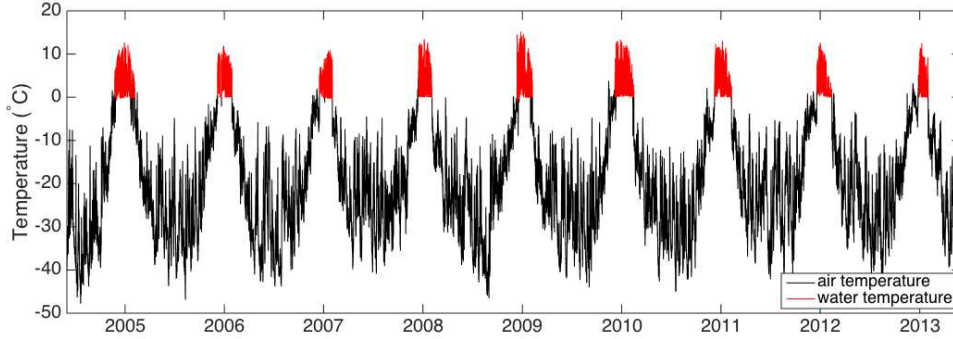


Figure 2.6: Upper boundary forcing data used to drive the GIPL heat transfer model, which is used to approximate thaw depth beneath the streambed of Von Guerard Stream.

A Neuman boundary condition was used at the lower boundary:

$$\frac{\partial T(z_{\max}, t)}{\partial z} = G \quad (2.15)$$

where G is a geothermal heat flux. The initial model temperature was assumed to be -30°C at all depths, and it was assumed that hyporheic sediments remained fully saturated at all times.

Bulk volumetric heat capacity is estimated as the sum the frozen (c_{frozen}) and thawed (c_{thaw}) soil heat capacities, weighted by the fraction of unfrozen soil water (θ_l/θ).

$$c_b = c_{\text{thaw}} \cdot \left(\frac{\theta_l}{\theta}\right) + c_{\text{frozen}} \cdot \left(1 - \frac{\theta_l}{\theta}\right) \quad (2.16)$$

Thawed soil heat capacity is calculated as:

$$c_{\text{thaw}} = c_s(1 - \phi) + c_{\text{water}}(\theta) + c_{\text{air}}(\phi - \theta) \quad (2.17)$$

and frozen soil heat capacity is calculated as:

$$c_{\text{frozen}} = c_s(1 - \phi) + c_{\text{ice}}(\theta) + c_{\text{air}}(\phi - \theta) \quad (2.18)$$

where c_s is the heat capacity of soil mineral grains ($\text{J m}^{-3} \text{K}^{-1}$), c_{water} is the heat capacity of water ($4.188 \times 10^6 \text{ J m}^{-3} \text{K}^{-1}$), c_{ice} is the heat capacity of ice ($1.9415 \times 10^6 \text{ J m}^{-3} \text{K}^{-1}$), and c_{air} is the heat

capacity of air ($1.23 \times 10^3 \text{ J m}^{-3} \text{ K}^{-1}$). The heat capacity of soil mineral grains was empirically determined following *Oleson et al.* [2010].

$$c_s = \left(\frac{2.128(\%sand) + 2.385(\%clay)}{(\%sand) + (\%clay)} \right) \times 10^6 \quad (2.19)$$

Bulk thermal conductivity is computed as the weighted product of thawed (k_{thaw}) and frozen (k_{frozen}) soil thermal conductivity [*Farouki*, 1981].

$$k = k_{thaw}^{\left(\frac{\theta_t}{\theta}\right)} k_{frozen}^{\left(\frac{1-\theta_t}{\theta}\right)} \quad (2.20)$$

Thawed thermal conductivity is calculated as:

$$k_{thaw} = k_s^{(1-\phi)} k_{water}^{(\theta)} k_{air}^{(\phi-\theta)} \quad (2.21)$$

and frozen thermal conductivity is calculated as:

$$k_{frozen} = k_s^{(1-\phi)} k_{ice}^{(\theta)} k_{air}^{(\phi-\theta)} \quad (2.22)$$

where k_s is the thermal conductivity of soil minerals, k_{water} is the thermal conductivity of water ($0.6 \text{ W m}^{-1} \text{ K}^{-1}$), k_{ice} is the thermal conductivity of ice ($2.29 \text{ W m}^{-1} \text{ K}^{-1}$), and k_{air} is the thermal conductivity of air ($0.023 \text{ W m}^{-1} \text{ K}^{-1}$). The thermal conductivity of soil minerals is computed using the methods of [*Oleson et al.*, 2010].

$$k_s = \frac{8.80(\%sand) + 2.92(\%clay)}{(\%sand) + (\%clay)} \quad (2.23)$$

Unfrozen water parameters (τ and n in Equation 2.8) were approximated by fitting Equation 2.8 to the observed soil water phase composition curve observed at 15cm depth in Von Guerard Stream. A Decagon 5TE sensor was positioned at 15 cm depth in the bed of Von Guerard Stream to measure volumetric water content and temperature. These observations were

part of an ongoing active layer monitoring campaign, described extensively in the methods of Chapters 3. Here, water content and temperature data from a single location are used to inform a soil water phase composition curve [Lovell, 1957; Outcalt *et al.*, 1990] and estimate unfrozen water parameters τ and n in Equation 2.8 (Figure 2.7). Hyporheic pore water is observed to freeze rapidly, once temperatures drop below the freezing point. As such, unfrozen water parameters from Equation 2.8 are $\tau = 0.09$ and $n = -0.04$ ($R^2=0.77$).

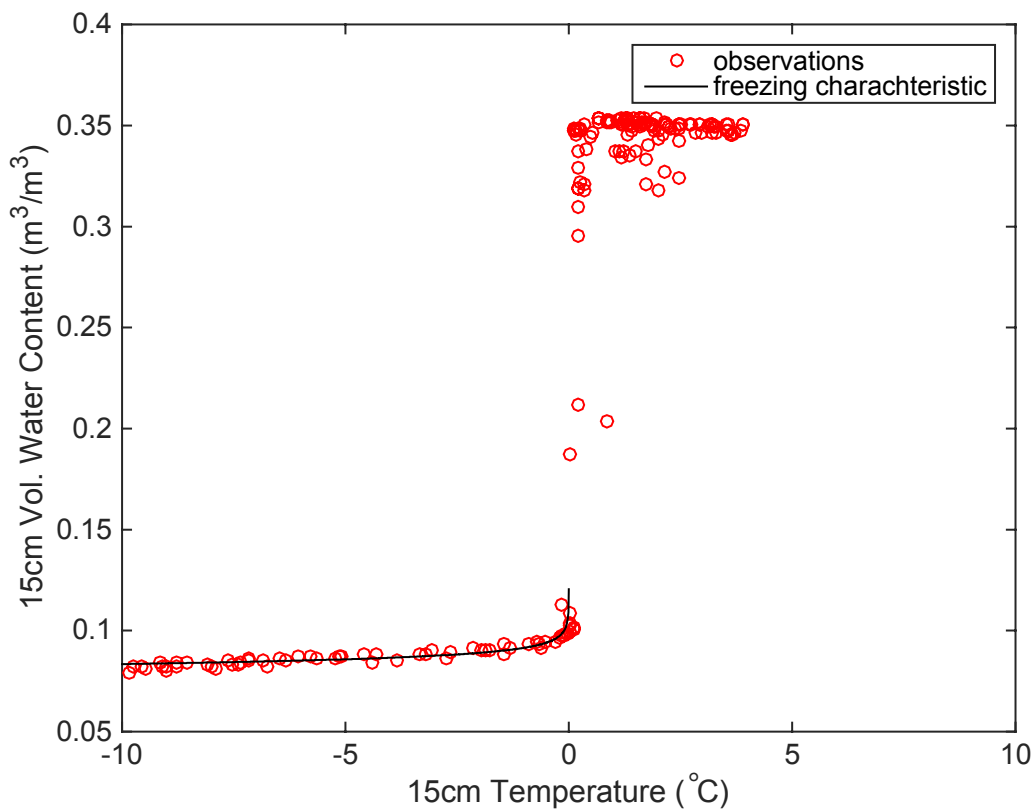


Figure 2.7: Soil water phase composition curve from 15cm depth in the hyporheic zone of Von Guerard Stream. The abrupt drop in soil moisture content at below freezing temperatures shows that the hyporheic zone freezes rapidly. The freezing characteristic curve is fit with the power law model of Equation 2.8.

2.3.4 Model simulations

Three weathering and transport models are developed to simulate observed Si concentrations in Von Guerard Stream (Table 2.2). Model 1 is the “classic” OTIS model [Runkel, 1998], where A_{HZ} , α and λ do not change through time. In Model 1, the second term on the right hand side of Equation 2.3, which accounts for changes in A_{HZ} , is removed. The hyporheic zone area, A_{HZ} , in Model 1 is determined for each flow season as the average of $A_{HZ}(t)$ computed by Equation 2.4. Model 2 allows A_{HZ} to change through time according to Equation 2.4, where α and λ remain constant. Finally, Model 3 allows A_{HZ} and λ to change through time, while α remains constant. In model 3, λ is assumed to be a linearly increasing function of Q :

$$\lambda = 3.9 \times 10^{-5}(Q) + 3.6 \times 10^{-7} \quad (2.24)$$

Equation 2.24 was developed based on the observed increase in λ as a function of Q in *Gooseff et al.* [2002] (Figure 2.5).

Table 2.2: Parameterization of weathering and transport models 1, 2 and 3

	A_{HZ} (m ²)	α (sec ⁻¹)	λ (sec ⁻¹)
Model 1	Constant, mean of seasonal A_{HZ} variations	constant	constant
Model 2	Dynamic, according to (4)	constant	constant
Model 3	Dynamic, according to (4)	constant	Dynamic, according to (Eq. 24)

The Monte-Carlo optimization of α and λ was conducted for Model 2. Near optimal α and λ values were also used in Model 1 and Model 3. Each model was initialized at $C = C_{HZ} = 2$ mg/L at the beginning of the 2004/05 flow season. End of season C and C_{HZ} values were used as initial conditions for the subsequent flow season.

2.4 RESULTS

2.4.1 Long-term geochemical observations

Dissolved Si is derived from the chemical weathering of primary and secondary minerals and the dissolution of amorphous species. Concentrations of Si in streams range from 0.1 – 4.5 mg/L (Figure 2.8). Longer streams in southern Fryxell Basin (Delta, Crescent, and Von Guerard) exhibit the highest median Si concentrations. Lost Seal and Aiken exhibit moderate median Si concentrations, relative to the low median concentrations observed in shorter streams (Canada, Green, and Commonwealth). Delta and Aiken disrupt the apparent correlation between stream length and median Si concentration, suggesting that ponds along the stream corridor of these streams may be sinks for dissolved Si.

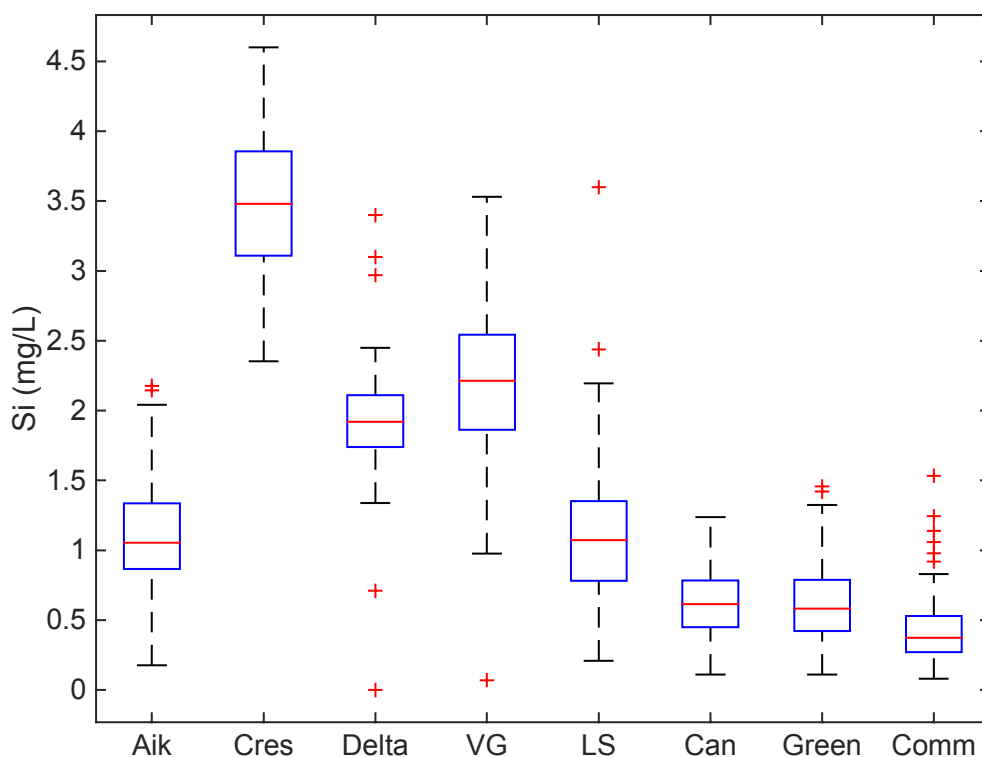


Figure 2.8: The distribution of dissolved silicon in water samples from eight streams in the Fryxell Basin. Boxplots are arranged from left to right in order of decreasing stream length.

Besides Si, relative concentrations of other solutes provide evidence of chemical weathering occurring in stream channels. Sodium is assumed to be primarily derived from marine aerosol deposition, with minimal contributions from chemical weathering [Welch *et al.*, 2010]. Conversely, Ca^+ and K^+ are rock-derived solutes, common by products of primary and secondary mineral weathering. As such, Na:Ca and Na:K ratios are helpful metrics for identifying the occurrence of chemical weathering [Gibbs, 1970; Green and Canfield, 1984; Green *et al.*, 1988]. Na:Ca and Na:K ratios decrease between glaciers and stream gauges on all streams in the eastern Taylor Valley (Figure 2.9). The relative enrichment of Ca^+ and K^+ along the stream corridor is evidence that chemical weathering is occurring in streams and hyporheic zones. The source glacier ratios for Aiken Stream are not shown in Figure 2.9 because the melt

water source of Aiken Stream is split between glaciers in the Kukri Hills and Commonwealth Glacier. Also, Many Glaciers Pond should be acknowledged as a complicating factor to the chemistry of Aiken Stream.

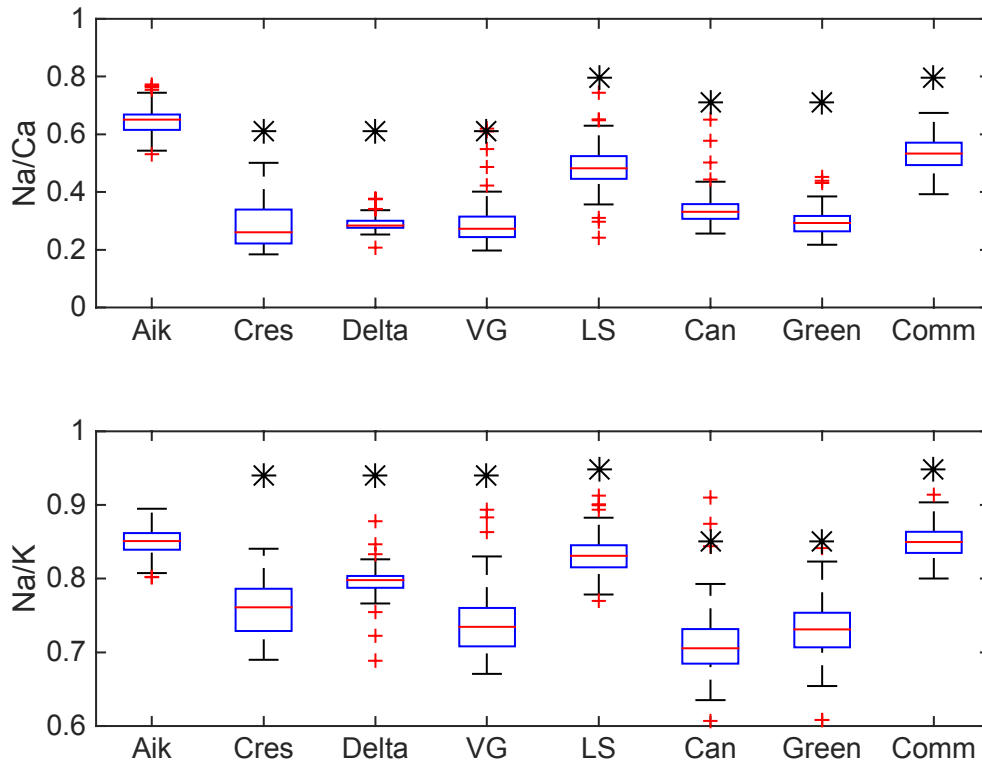


Figure 2.9: Stream water Na:Ca and Na:K ratios for eight streams in the Fryxell Basin are shown as box plots. Black asterisk symbols indicate the Na:Ca and Na:K ratios of glacier ice in the ablation zone of source glaciers for each stream (data from Lyons et al., 2003).

Concentration–discharge relationships show that Si , Ca^+ , K^+ , and HCO_3^- concentrations vary only slightly, relative to a 4-order of magnitude variation in daily average discharge (Figure 2.10). In general, C-Q relationships for Si , Ca^+ , K^+ , and HCO_3^- are similar at any one stream; however, variability of C-Q relationships is observed among streams. A power-law model (Equation 2.1) is used to describe C-Q relationships at each stream, where the power scaling parameter, b , describes the degree to which the relationship is affected by dilution. The power

scaling parameter, b , is much closer to 0 than -1 for all streams and all solutes, indicating a generally chemostatic relationship (Figure 2.11). However, the value of b for all solutes tends to be more negative on shorter streams, compared to longer streams. The chemostatic behavior of weathering-derived solutes in these streams suggests that rates of solute mobilization and production are nearly proportional to discharge rates over intra- and inter-annual timescales.

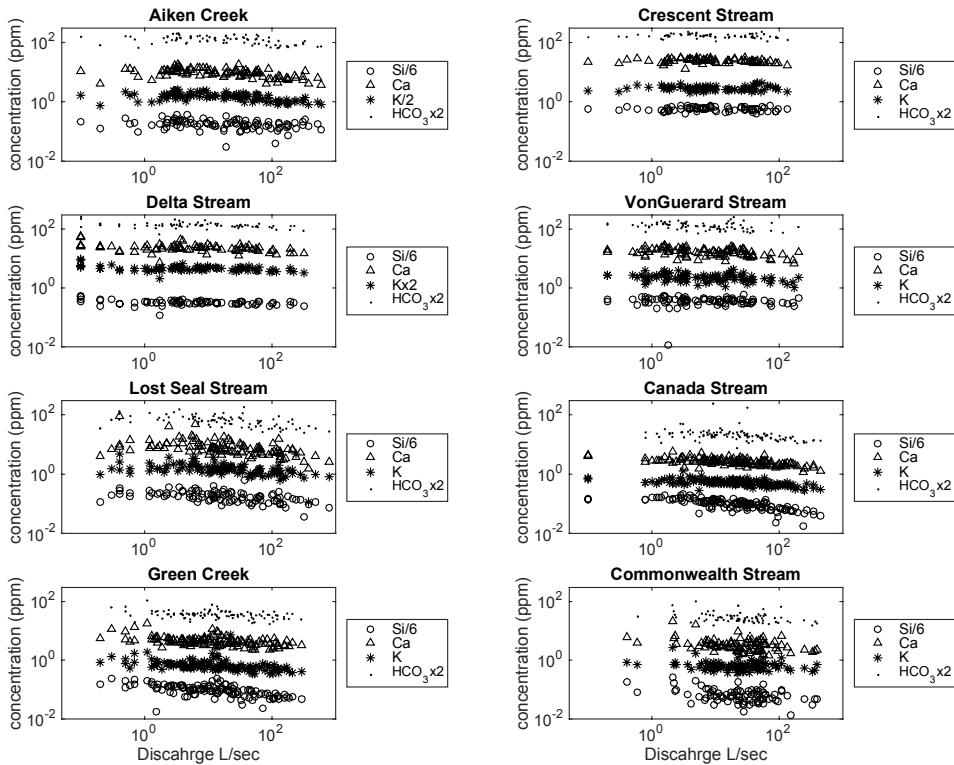


Figure 2.10: Concentration-discharge relationships of weathering derived solutes (Si, Ca⁺, K⁺, and HCO₃⁻) for eight streams in eastern Taylor Valley. Concentration magnitudes of some solutes are scaled to optimize presentation in log-log space. Scaling y-axis magnitudes does not affect the apparent log-log slope in these plots.

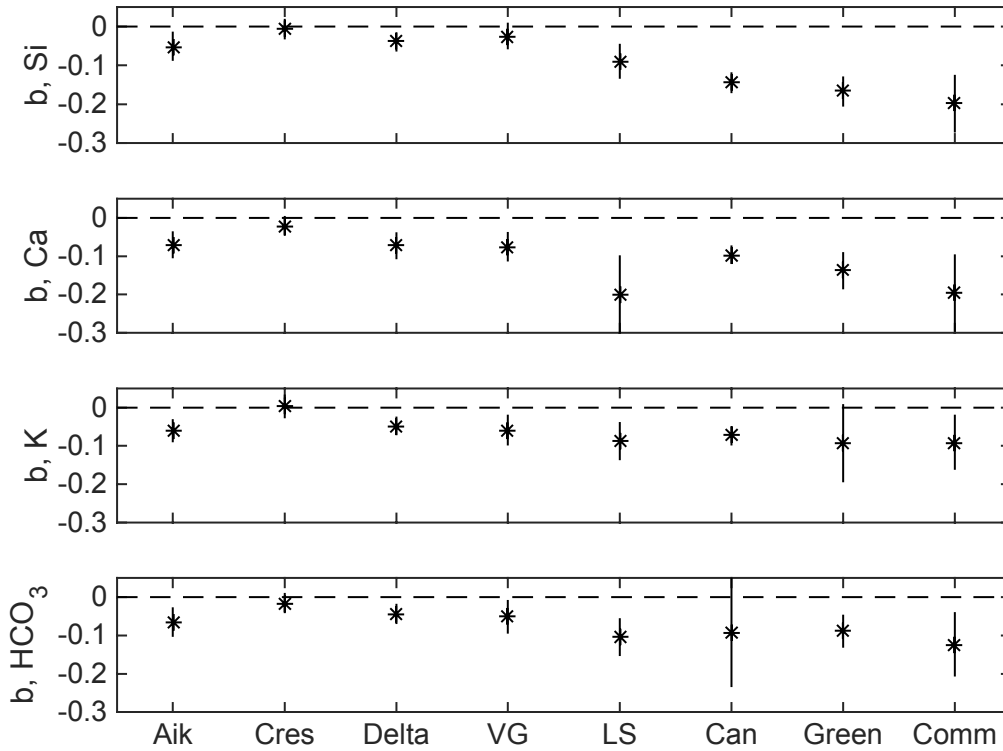


Figure 2.11: Optimal b parameter values and 95% confidence intervals from power law regression of concentration-discharge relationships. A b parameter value equal to 0 indicates a purely chemostatic regime, whereas a b parameter value of -1 indicates a dilution dominated regime. All streams exhibit near-chemostatic behavior.

Annual Si denudation rates (D_{Si}) quantify the annual flux of Si exported from a catchment. Si denudation rates are computed as

$$D_{Si} = \frac{C_{Si} \int Q(t) dt}{A_c} \quad (2.25)$$

where, C_{Si} is the annual average Si concentration [M/L^3], Q is streamflow [L^3/T], t is time [T], and A_c is the surface area of the “catchment”. Catchment surface area, A_c , is calculated as the product of stream length and total average wetted channel width

$$A_c = (w_c + 2w_m) * L \quad (2.26)$$

where, L is stream length [L]. By assuming a stream channel width, w_c , of 5 m and a margin half-width w_m of 2 m, Si denudation rates were calculated for all available record years for streams in the eastern Taylor Valley (Figure 2.12). Annual denudation rates scale positively with annual specific discharge in all streams. Furthermore, denudation rates observed in eastern Taylor Valley streams are comparable to denudation rates observed in other glacier-covered catchments across the world [Anderson et al., 1997a]. Nezat et al. [2001] first made this observation, however this work (Figure 2.12) incorporates many more years of geochemical and hydrologic data to more clearly present the proportional scaling of denudation rate (flux) with discharge and display a more complete range of denudation rates.

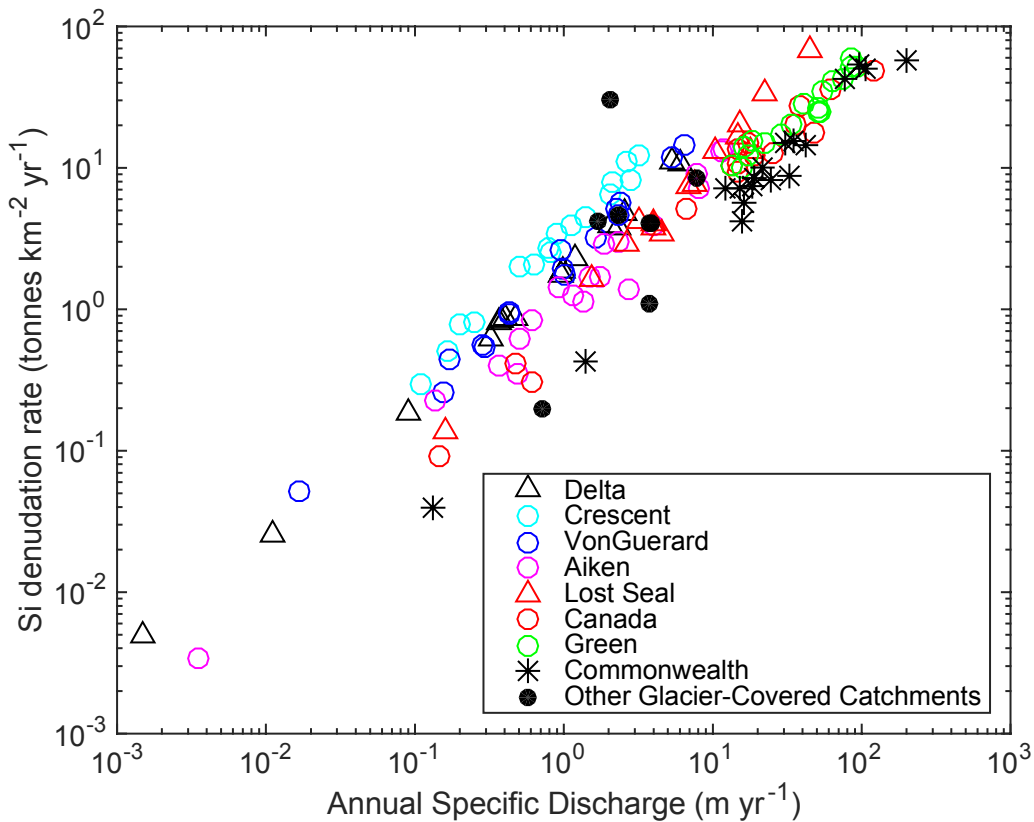


Figure 2.12: Silica denudation rates plotted as a function of annual specific discharge for streams in the eastern Taylor Valley. Si denudation rates for other glacier-covered catchments across the world are also shown (data from Anderson et al. [1997a]).

2.4.2 Short-term Stream Channel and Hyporheic Si and $\delta^{18}\text{O}$ Observations

Daily water samples from Von Guerard Stream channel and hyporheic zone show that the hyporheic zone is more enriched in Si, relative to stream channel water at all times (Figure 2.13). Following the onset of higher stream flow events on January 13th, Si concentrations of channel water show a progressive dilution from 3 – 2 mg/L, whereas the concentration of hyporheic water always remains > 2.5 mg/L. On January 12th samples were collected during two separate sampling events. The first sampling event was conducted immediately before the daily peak flow, while the second event was conducted during the daily peak flow. Little change was observed in hyporheic Si concentration from before to during the flood. However, channel water Si concentration appears diluted by the onset of the daily peak flow.

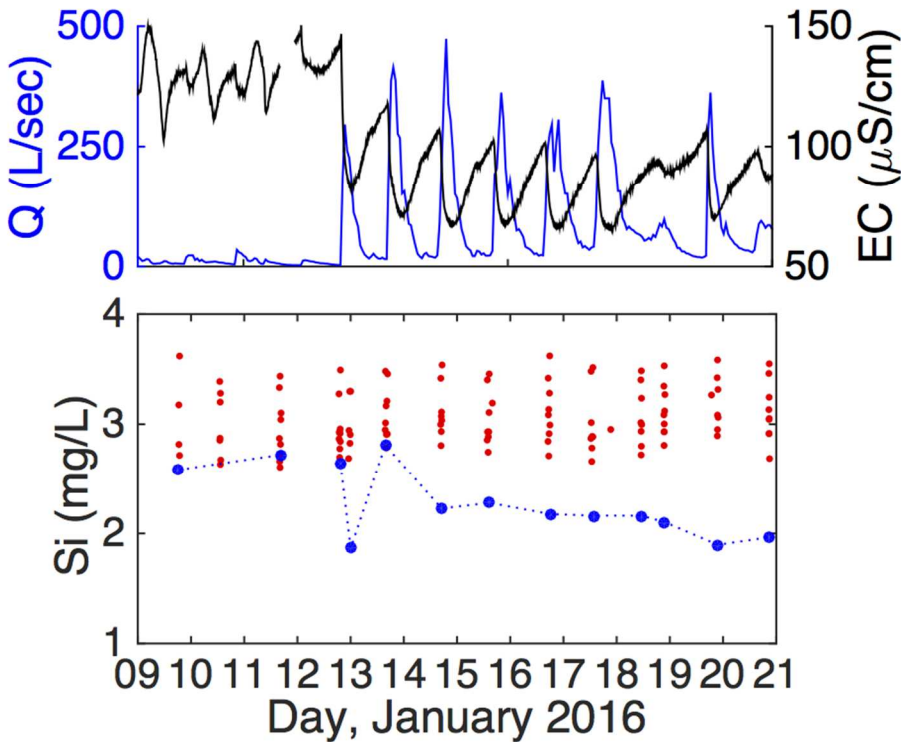


Figure 2.13: Daily Si samples on Von Guerard stream during January 2016. The top panel shows discharge and electrical conductivity (EC) observed during this period, and the bottom panel shows Si concentrations observed in the stream channel (blue dots) and hyporheic zone (red dots).

From January 9th – 13th, $\delta^{18}\text{O}$ signatures of channel and hyporheic waters ranged from -26.5 to -22.4 permil (Figure 2.14). All samples were relatively enriched, compared to the average $\delta^{18}\text{O}$ signature of glacier ice, -27.52 permil. Prior to the onset of higher flows on January 13th, channel and hyporheic $\delta^{18}\text{O}$ exhibits a general upward trend or progressive enrichment. Prior to January 13th, channel water is relatively enriched in $\delta^{18}\text{O}$, compared to hyporheic water. After the onset of high flows on January 13th, channel water and hyporheic water show a downward trend of progressively more negative $\delta^{18}\text{O}$ signatures. Also during this time, $\delta^{18}\text{O}$ signatures of channel water and hyporheic water become progressively more homogeneous. Isotopic homogenization

indicates that hyporheic water and channel water are well mixed. However, the coincident stratification of Si concentrations between the channel and hyporheic zone (Figure 2.13) indicates that the hyporheic zone remains geochemically distinct from channel water, and Si dissolution rates may be more rapid than exchange rates.

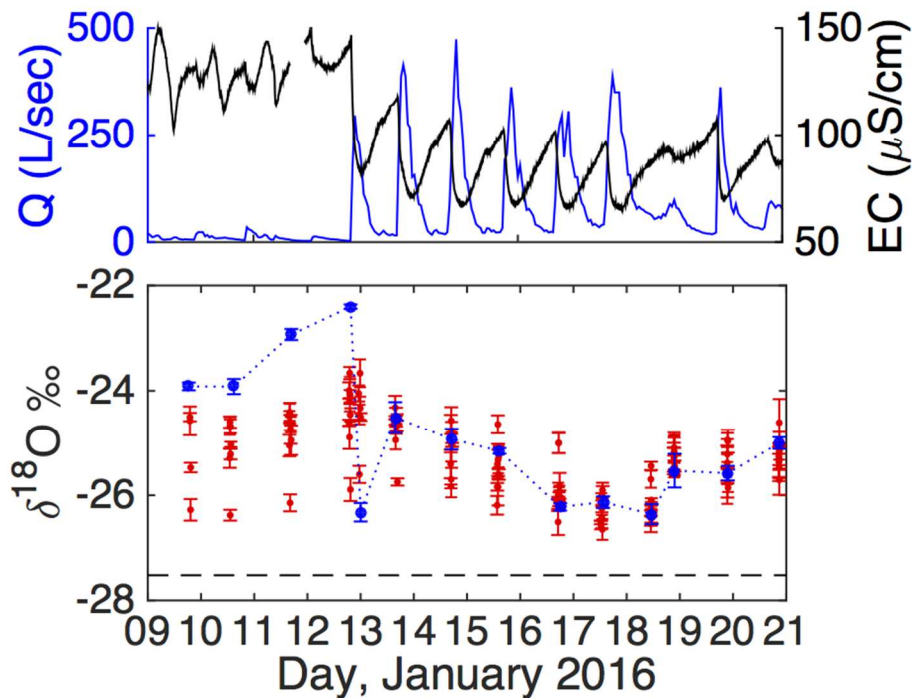


Figure 2.14: High-resolution $\delta^{18}\text{O}$ samples from Von Guerard Stream during January 2016. The top panel shows discharge and EC observed during this period, and the bottom panel shows $\delta^{18}\text{O}$ observed in the stream channel (blue dots) and hyporheic zone (red dots).

2.4.3 Numerical Model Simulations of Si weathering and transport in Von Guerard Stream

The unsteady transport weathering and transport model requires spatially and temporally continuous Q and A estimates. Q and A is estimated along the length of Von Guerard Stream for

2004/05 through 2013/14 flow seasons with a kinematic wave flood routing model forced by idealized flood pulses at the upstream boundary. The routing model is more capable of simulating observed flows during low flow years, compared to high flow years (Figure 2.15). Examples of simulated and observed hydrographs from a one low flow and one high flow year (Figure 2.16) show that routing the model is capable of accurately simulating observed peak flow magnitudes and diel variability. However, because the routing scheme does not account for baseflow transience, the model under-predicts observed baseflow during high flow years.

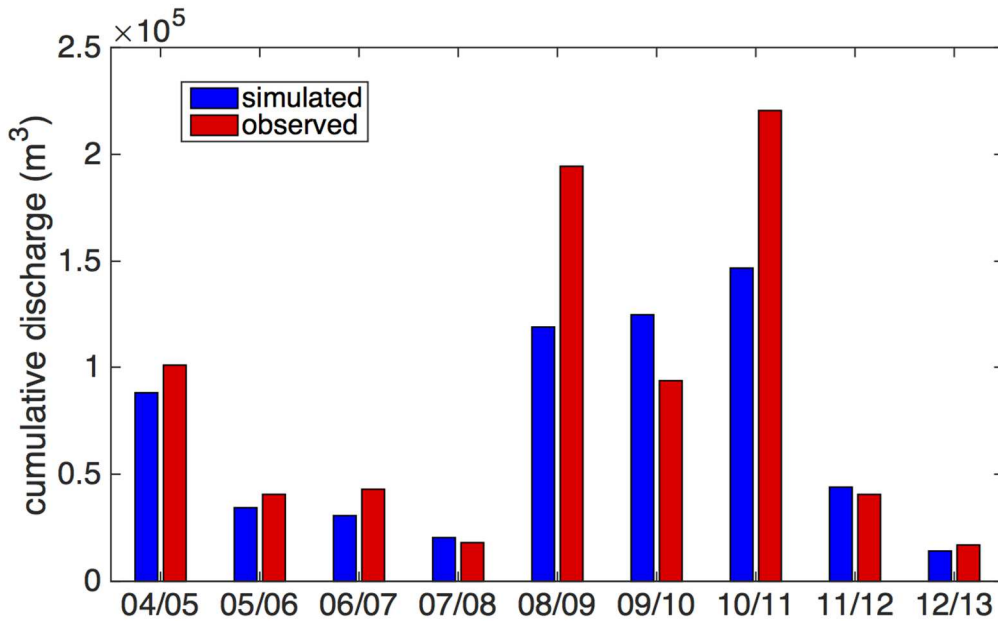


Figure 2.15: Simulated and observed annual cumulative discharge for all flow seasons between 2004/05 and 2012/13.

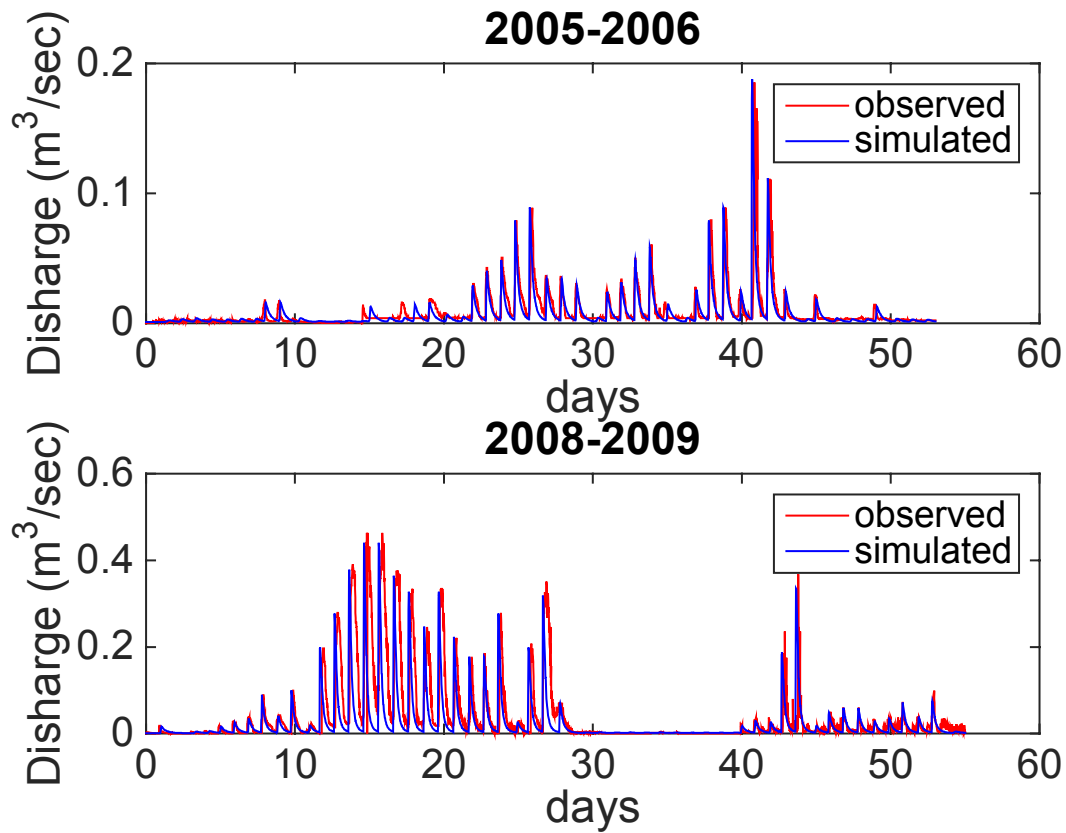


Figure 2.16: Simulated and observed hydrographs for a low flow year (2005/06) and a high flow year (2008/09). Generally, the flood routing model was better able to simulate low-flow years than high flow years. This discrepancy is attributed to the inability of the simple flood routing scheme to simulate baseflow dynamics.

Sub-channel thaw depth, which is used to estimate $A_{HZ}(t)$ according to Equation 2.4, is estimated with the GIPL heat-transfer model. The model simulates maximum seasonal thaw depths between 40 and 55 cm beneath the channel bed (Figure 2.17). Model results show a seasonal pattern of progressive thaw deepening, followed by a rapid freeze up. Although we lack continuous thaw depth observations, simulated maximum thaw depths agree with measurements of late January thaw depth on Von Guerard between 55 – 60 cm reported by *Conovitz et al.* [2006].

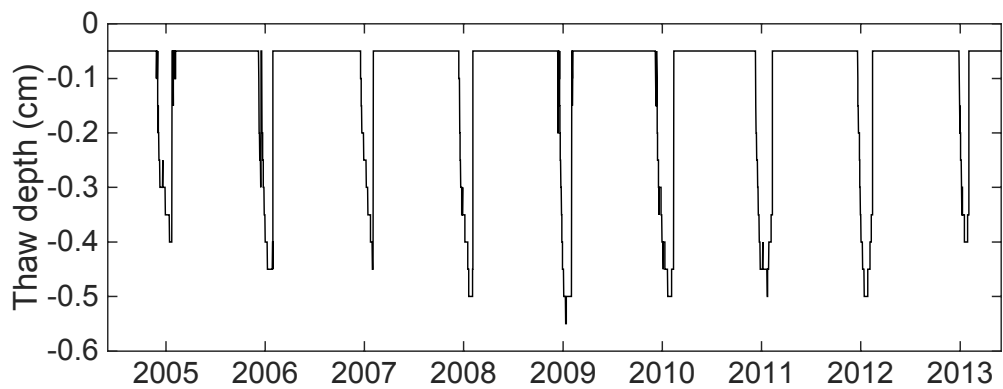


Figure 2.17: Thaw depth simulated by GIPL between July 2004 and July 2006.

A Monte-Carlo optimization approach was used to estimate λ and α parameters in model 2. After 1000 simulations of randomly generated parameter combinations, the best performing simulation (MAE = 0.99 mg/L) was used to identify near-optimal values of α (7.9×10^{-5} 1/sec) and λ (1.1×10^{-6} 1/sec) (Figure 2.18). Near-optimal α and λ values were then used to parameterize Model 1 and Model 3.

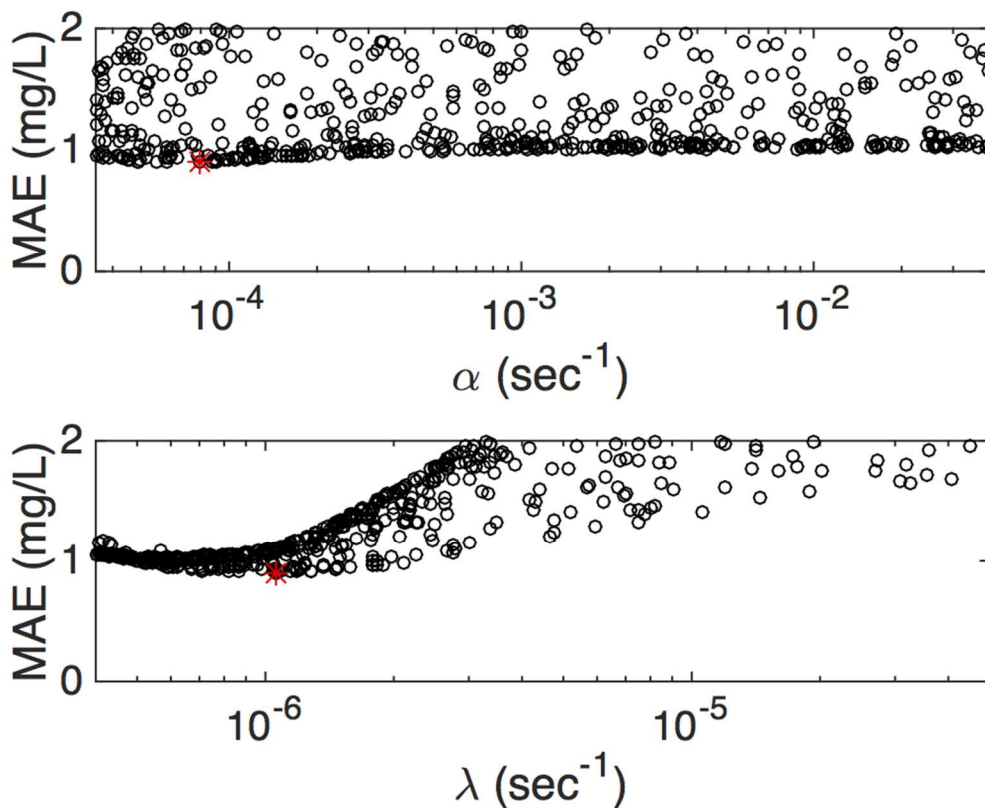


Figure 2.18: Model 2 Monte-Carlo simulation results for α and λ . Red markers indicate the best performing parameter set. Simulations resulting in Mean Absolute Error (MAE) values above 2 mg/L are not shown.

Model 3 is the best performing model of the ensemble, with respect to MAE (Figure 2.19 and Figure 2.20). Not only does Model 3 provide the best objective fit to the observations, but the range of Si simulated by Model 3 more closely matches the observed range Si concentrations (Figure 2.21) and Model 3 best reproduces the observed C-Q relationships (Figure 2.22).

Although Model 3 is the most objectively plausible model, all models fail to fully capture observed C-Q dynamics. All of the models under-predict Si concentration at high flows, while over-predicting Si at low flows (Figure 2.22).

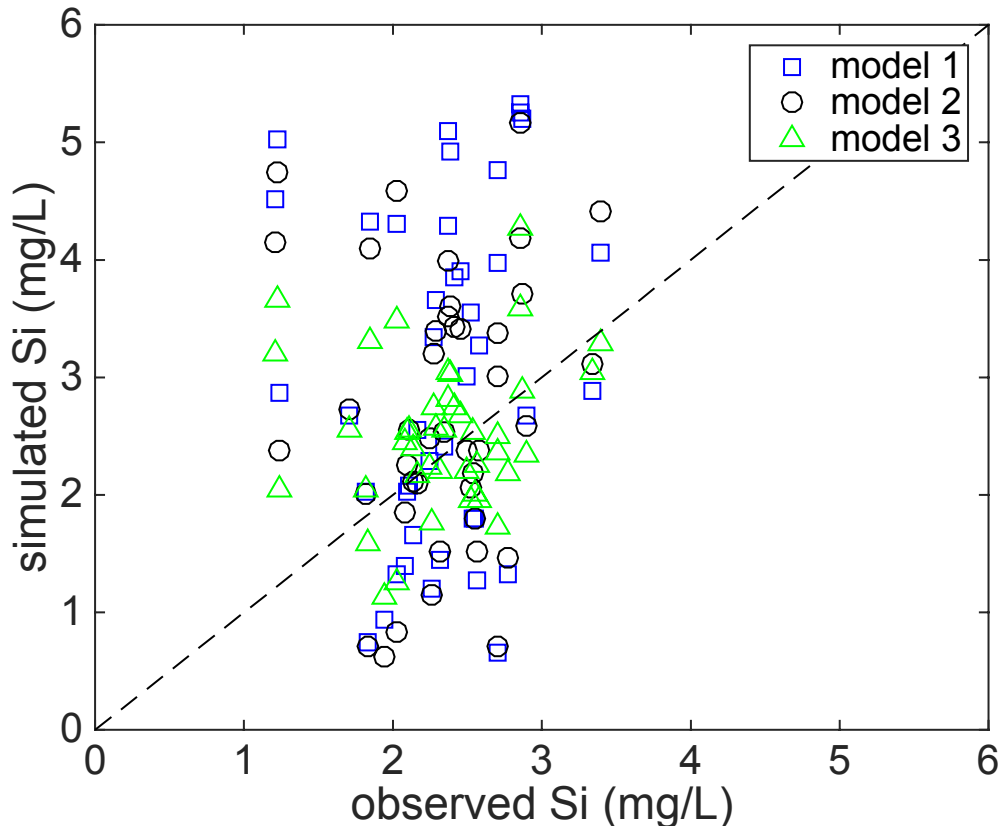


Figure 2. 19: Simulated Si concentrations plotted against observed Si concentrations for each of the three models.

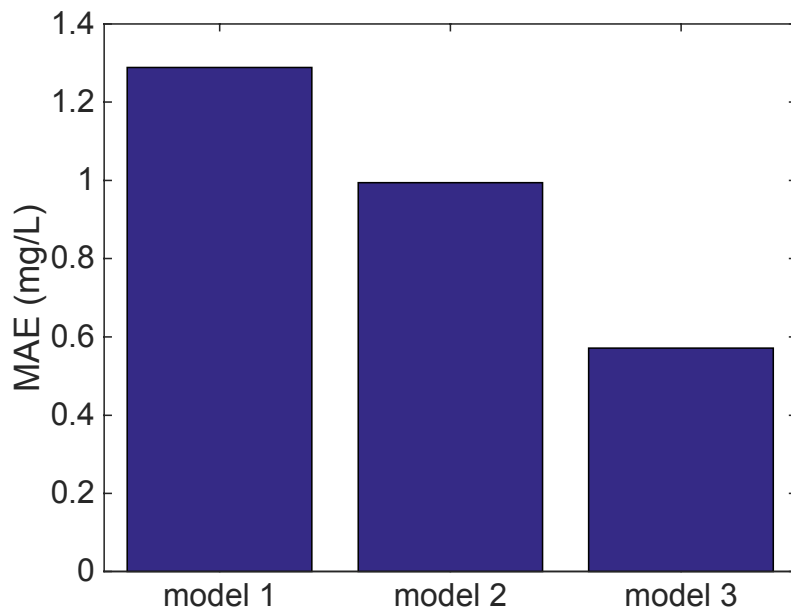


Figure 2. 20: Mean absolute error (MAE) of each of the three models. The best performing model is OTIS-mdv with λ as a function of Q .

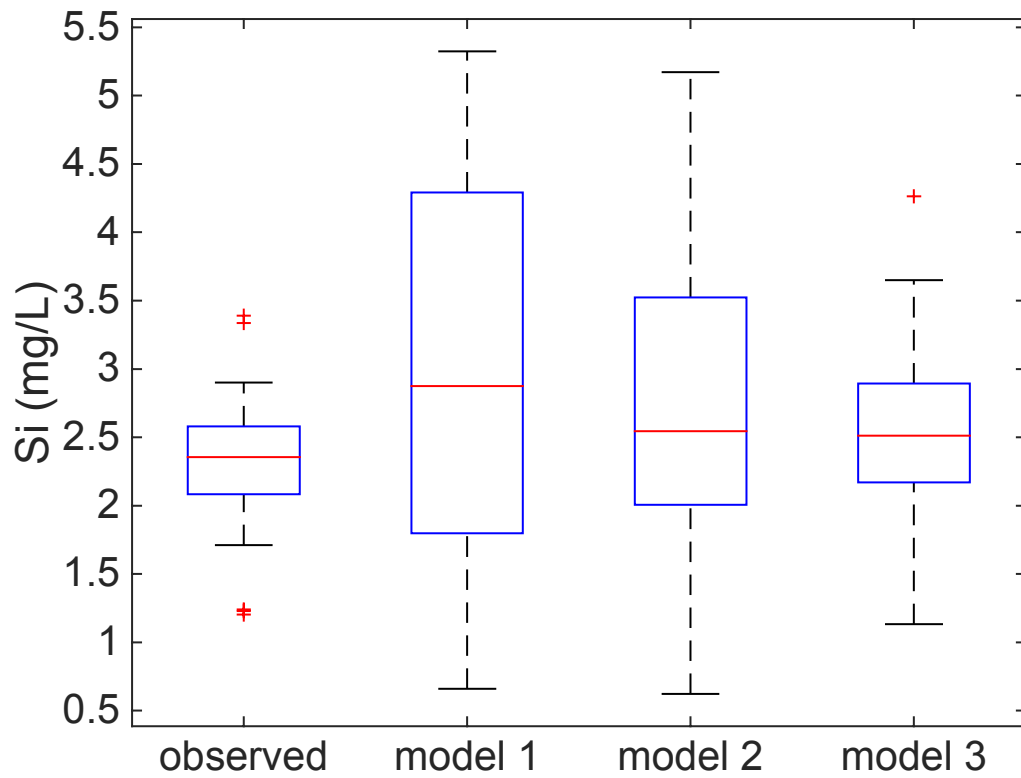


Figure 2.21: Observed and simulated Si distributions. Simulated Si distributions include only simulated Si concentrations at times when observations were made.

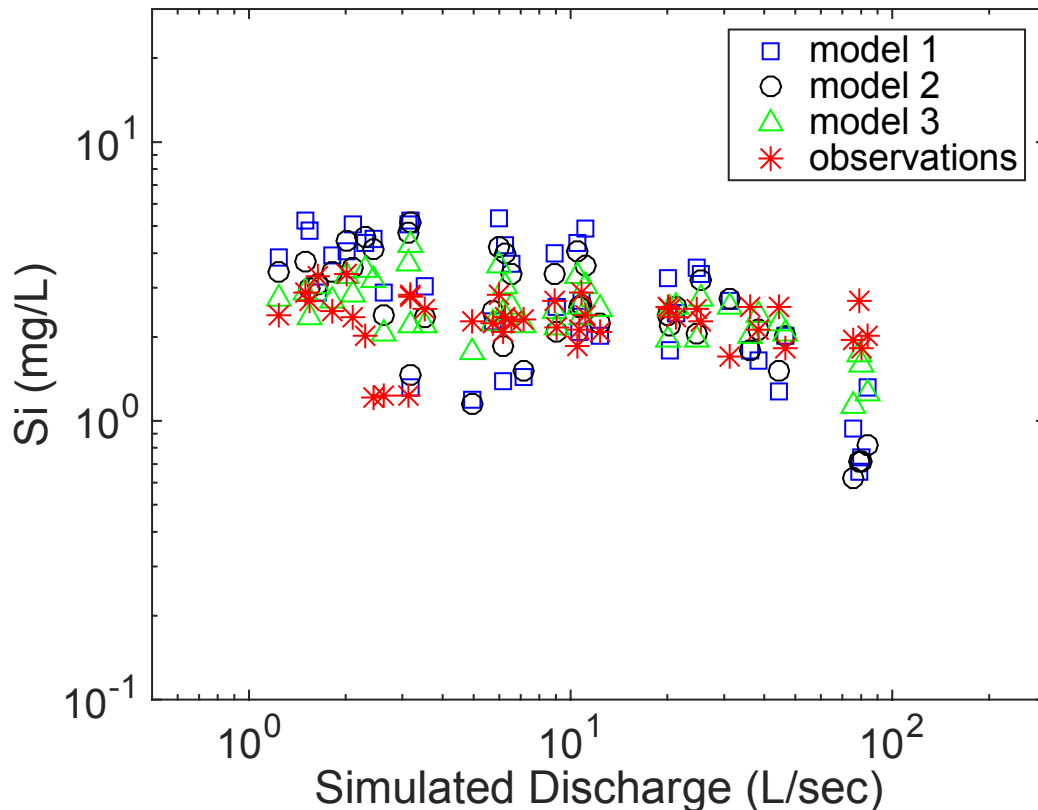


Figure 2.22: Observed and simulated Si-Q relationships. All models over predict Si concentrations at low flows and under predict Si concentrations at high flows. However, the best performing model is the OTIS-mdv with λ as a function of Q.

Select high flow and low flow years are used to illustrate sub-annual, and sub-daily model dynamics (Figure 2.23 and Figure 2.24). Periods of sustained high flow result in the dilution of simulated C and C_{HZ} . Subsequent periods of sustained low flow result a progressive enrichment of simulated C and C_{HZ} . Model 1 is less sensitive to changes in stream flow when A_{HZ} (black line in the bottom panels of Figure 2.23 and Figure 2.24) is less than the seasonal average A_{HZ} (red dashed line in the bottom panels of Figure 2.23 and Figure 2.24), such as during the beginning and end of each flow season. Conversely, Model 1 is more sensitive to changes in flow when A_{HZ} is greater than the seasonal average A_{HZ} . In Models 1 and 2, simulated C and C_{HZ} exhibit greater rates of change during high flows (dilution) and low flows (enrichment). On the

other hand, Model 3 simulated C and C_{HZ} exhibit smaller rates of change during high flow (dilution) and low flows (enrichment). For example, high flows during December of 2010 (Figure 2.23) dilute Models 1 and 2 well below observed Si concentrations. However, Model 3 more closely matches observed Si concentrations due to the ability of λ to increase as Q increases. All models simulate a daily dilution of C at the onset of daily peak flows, while C_{HZ} is relatively unaffected by the abrupt increase in daily channel flow.

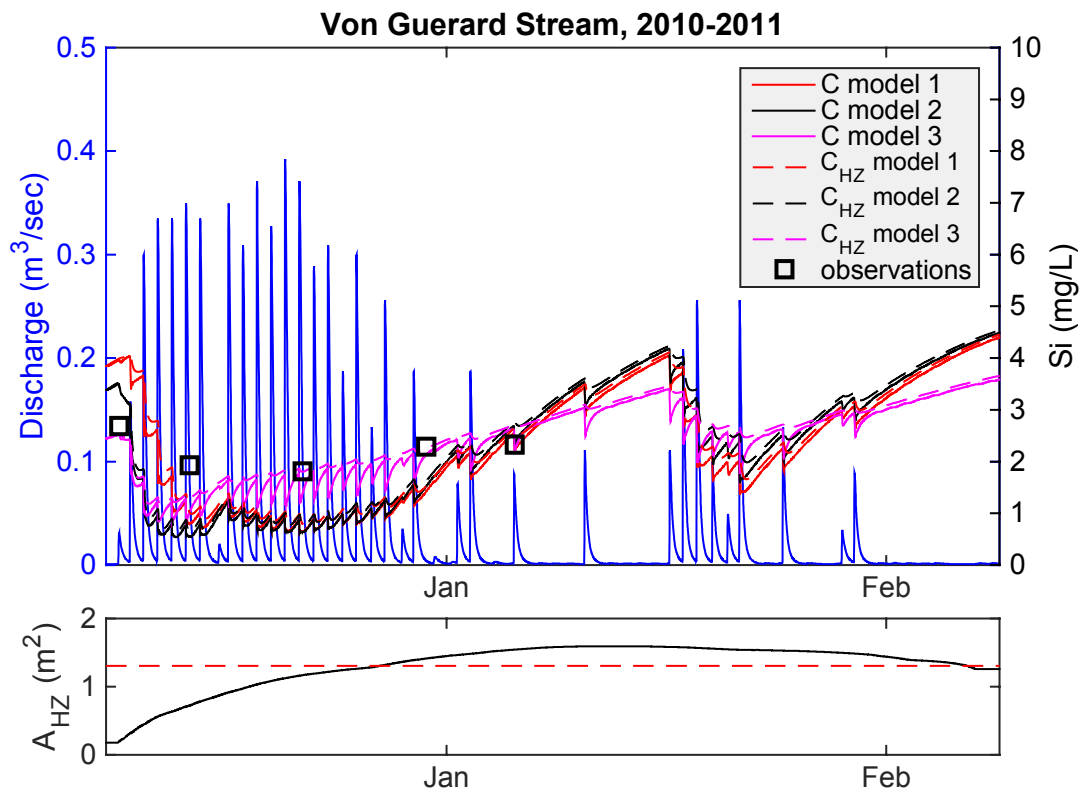


Figure 2.23: Simulation results from the 2010/11 season, a high flow year. The top panel shows simulated discharge, main channel concentration, storage zone concentration, and observations. Resultant concentration time series from all three models are shown with different colors. The bottom panel shows storage zone area for model 1 (red) and models 2 and 3 (black line).

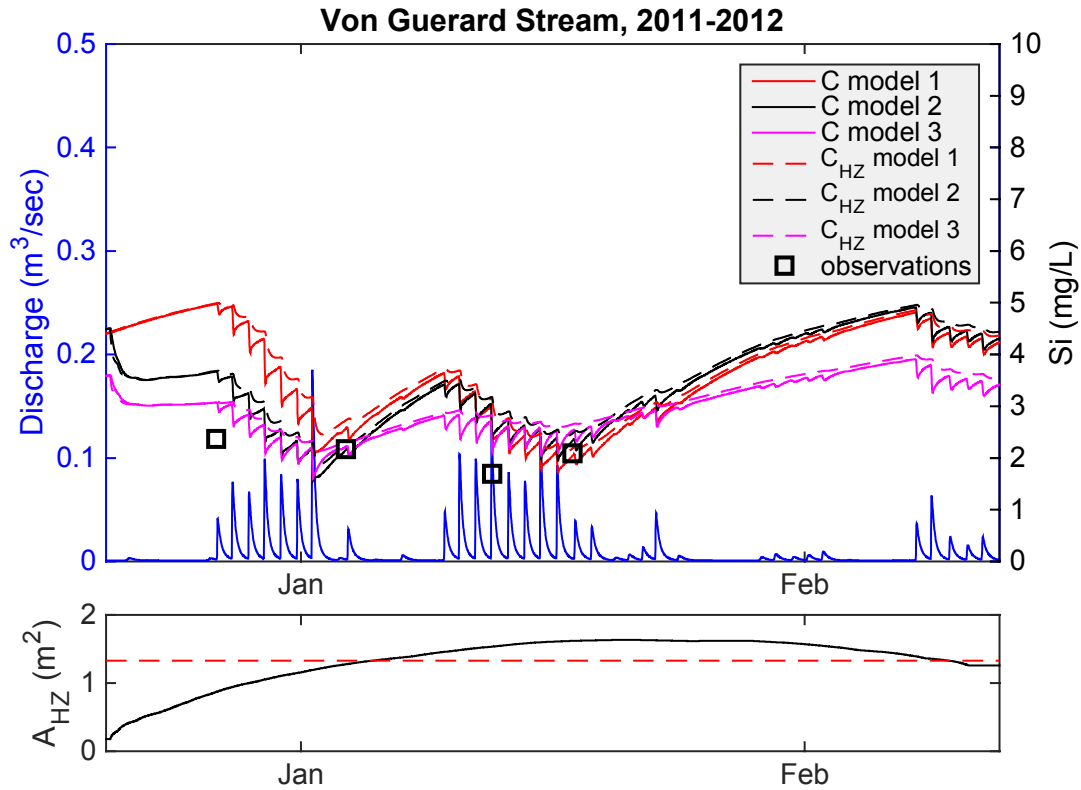


Figure 2.24: Simulation results from the 2011/12 season, a low flow year. The top panel shows simulated discharge, main channel concentration (C), hyporheic zone concentration (C_{HZ}), and observations. Resultant concentration time series from all three models are shown with different colors. The bottom panel shows storage zone area for model 1 (red) and models 2 and 3 (black line).

Ultimately, Model 3 performs better than Models 1 and 2, and Model 2 outperforms Model 1. Model 3 is objectively the best performing model because λ scales positively with Q . Models 1 and 2, where λ is constant, severely overpredict observed concentrations during periods of sustained low flow and underpredict observed concentrations during periods of sustained high flow (Figure 24). Model 1 is the worst performing model, which indicates that the seasonal expansion and contraction of A_{HZ} is likely to be an important process controlling the storage of water and solutes in the hyporheic zone. Overall, numerical modeling results show that constant high weathering rates and hyporheic exchange (Models 1 and 2) cannot fully

explain observed Si-Q relationships (chemostasis) in MDV streams. However, *variable* weathering rates (Model 3) and hyporheic exchange can to more closely explain observed Si-Q relationships (minimizing MAE).

2.5 DISCUSSION

The MDV streams behave near-chemostatically with respect to Si, Ca⁺, K⁺, and HCO₃⁻, though shorter streams are more affected by dilution than longer streams (Figure 2.10 and Figure 2.11). Chemostasis implies that solute production and exchange rates are proportional to runoff rates. Chemostasis of weathering derived solutes has been previously observed in a variety of mid-latitude catchments [Hall, 1970; Godsey *et al.*, 2009; Clow and Mast, 2010; Herndon *et al.*, 2015]. The climatic and hydrologic setting of the MDVs (Figure 2.1), suggest that geochemical and hydrologic processes occurring along the stream corridor control the chemostatic behavior of glacial melt streams. Stream geochemical data presented in this study provide additional evidence of high chemical weathering rates, an important geochemical control on C-Q relationships. Furthermore, numerical solute transport modeling illustrates how hydrologic processes (hyporheic exchange) must operate in tandem with geochemical processes (weathering) to simulate observed C-Q dynamics.

2.5.1 Chemical weathering in Antarctic streams and hyporheic zones

Based on the available data, the Si concentration of glacial runoff entering the proglacial channel head is relatively low compared to stream water, suggesting streams and hyporheic

zones are a net source of dissolved Si in the MDVs. In this study, we show that median stream water Si concentrations (1.53 – 3.48 mg/L) (Figure 2.8) are over an order of magnitude greater than supraglacial runoff Si concentrations (0.1 mg/L) [Fortner *et al.*, 2005]. The enrichment of Si along the stream channel has also been documented by Gooseff *et al.* [2002] and Stumpf *et al.* [2012]. The source of Si to flowing stream waters has widely been attributed to chemical weathering of primary and secondary minerals [Lyons *et al.*, 1997; Nezat *et al.*, 2001; Gooseff *et al.*, 2002; Maurice *et al.*, 2002; Stumpf *et al.*, 2012; Marra *et al.*, 2016].

The enrichment of Ca^+ and K^+ in stream water, relative to glacier ice, is also observed in these streams. Na:Ca and Na:K ratios decrease between glacier ice and stream gauges (Figure 2.9). Because K^+ and Ca^+ are rock-derived solutes from aluminosilicate weathering and Na^+ is largely derived from atmospheric deposition, decreasing Na:K and Na:Ca ratios are evidence of chemical weathering occurring in stream channels. This result and the subsequent interpretation is corroborated by Green *et al.*, [1988], Gooseff *et al.* [2002], Lyons *et al.* [2003], and Stumpf *et al.*, [2012]. This result justifies the structure of the weathering and transport model used in this study, where the enrichment of dissolved Si occurs along the stream corridor while concentration of glacial waters entering the proglacial channel head remain constant.

At an annual timescale, Si denudation rates scale positively with specific discharge and denudation rates are comparable to those observed in other glaciated catchments (Figure 2.12). This result was first published by Nezat *et al.* [2001], however our study has added over 20 years of geochemical data to the analysis, which more clearly illustrates a positive scaling relationship and confirms the magnitude of Si denudation rates in MDV streams. Chemostatic C-Q

relationships (Figure 2.10) suggest that solute flux (production and mobilization) scales proportionately with channel discharge. The positive proportional scaling of Si denudation rates with specific discharge confirms this interpretation of chemostasis at a broader timescale.

At the daily timescale, 12 days of coincident isotopic and Si observations from the hyporheic zone and stream channel suggest that dissolution rates may be greater than exchange rates. During this brief period, hyporheic Si concentrations were consistently greater than channel water concentrations. Contrarily, the isotopic composition of channel and hyporheic water was indistinguishable following the onset of higher flows on January 13th. Based on these data, the hyporheic zone and stream channel are hydrologically well mixed, but the hyporheic zone is geochemically distinct from channel water. This result supports the notion of high rates of Si dissolution occurring in Antarctic hyporheic zones and suggests that dissolution rates may out-pace hydrologic exchange rates.

2.5.2 Dynamic hydrologic controls on C-Q relationships

Hyporheic exchange is an important hydrologic control on C-Q relationships in MDV streams. Hyporheic exchange mobilizes reacted water from the hyporheic zone to the main channel. In the absence of hyporheic exchange, reacted water in the hyporheic zone would not mix with channel water, resulting in lower than observed stream water Si concentrations. This dynamic is illustrated by reducing α by two orders of magnitude in Model 1 from the optimal α (7.9×10^{-5} 1/sec). Simulated main channel concentration remains < 1 mg/L, whereas hyporheic zone concentration continuously increases, approaching solubility \hat{C} (Figure 2.25). This suggests

that annual and inter-annual C-Q dynamics are very sensitive to a lower threshold of α and that hyporheic zones rapidly exchange with main channel waters in MDV streams.

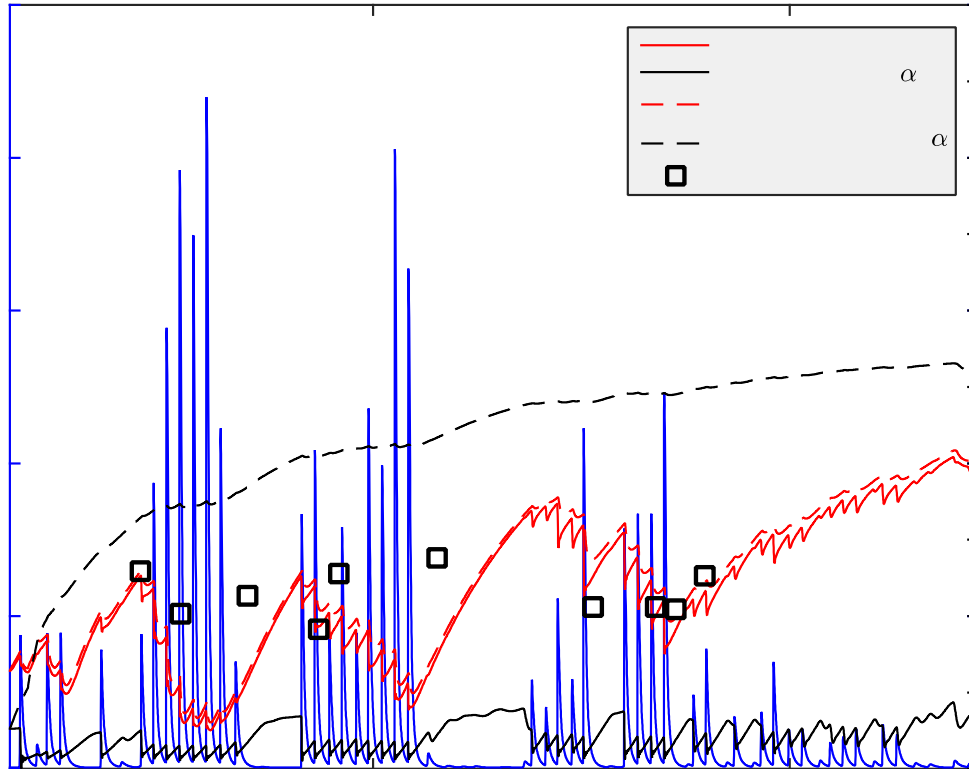


Figure 2.25: Model 2 results for the 2009/10 flow season under two different exchange rate scenarios. Red lines show model results for the optimal α value (7.9×10^{-5} 1/sec), whereas the black lines show model results for an unrealistically low α value (7.9×10^{-7} 1/sec).

The volume of the hyporheic zone is also an important hydrologic control on C - Q dynamics. Hyporheic volume controls the sensitivity of C and C_{HZ} to changes in stream flow. Differences between Model 1, where A_{HZ} is constant, and Model 2, where A_{HZ} is dynamic, illustrates this point (Figure 2.23 and Figure 2.24). When A_{HZ} of Model 1 is greater than A_{HZ} of Model 2, Model 1 is less sensitive to changes in flow than model 2. On the other hand, when A_{HZ} of Model 1 is less than A_{HZ} of Model 2, Model 1 is more sensitive to changes in flow than model

2. Furthermore, the lower MAE of Model 2 compared to Model 1 suggests that seasonal changes in the size of the hyporheic zone is an important control on C-Q relationships.

Other studies have attributed chemostatic C-Q relationships to the periodic flushing of hydrologic storage reservoirs. The ‘old’ water paradox [Kirchner, 2003] states that stream flow responds rapidly to hydrologic forcings (e.g. rainfall, snowmelt, or glacier melt) while the concentrations of passive tracers exhibit extremely damped responses [e.g., Kirchner *et al.*, 2000]. It logically follows that catchments must displace ‘old’ water during storm events, as opposed to rapidly transporting ‘new’ event water to the stream. The ‘old’ water paradox has been considered to be a key mechanism controlling C-Q relationships in other catchments [e.g. Pearce *et al.*, 1986; Sklash *et al.*, 1986; Clow and Mast, 2010]. However, in the MDV hydrologic system, the ‘old’ water hypothesis is not plausible due to the relative scarcity of storage volume and consequently rapid hydrologic turnover times.

Hydrologic turnover of the hyporheic zone is co-limited by the hyporheic zone volume and hyporheic flow rates. Hydrologic turnover time may be quantified as the duration of time required for a 90% reduction in storage zone concentration from an initial concentration at the beginning of a flow season. Hydrologic turnover time is computed for each season using model 1 with λ set to zero (i.e. weathering turned off). Thaw depth is assumed to be 60 cm at all times, providing a generous estimate of A_{HZ} and conservative estimate of turnover time. Hydrologic turnover of the hyporheic zone was achieved during 7 of 9 flow seasons (Figure 2.26). The 2007/08 and 2012/13 seasons did not experience enough streamflow to reduce storage zone concentrations by 90% of the initial concentration. Hydrologic turnover time was negatively

related with annual flow (Figure 2.27), and ranged from 8.74 – 30.69 days. Based on these model results, the ‘old’ water paradox cannot explain chemostasis in MDV streams because there is simply not enough storage to allow the accumulation of ‘old’ water. Although hydrologic processes are important, they are unable to fully explain C-Q dynamics, alone.

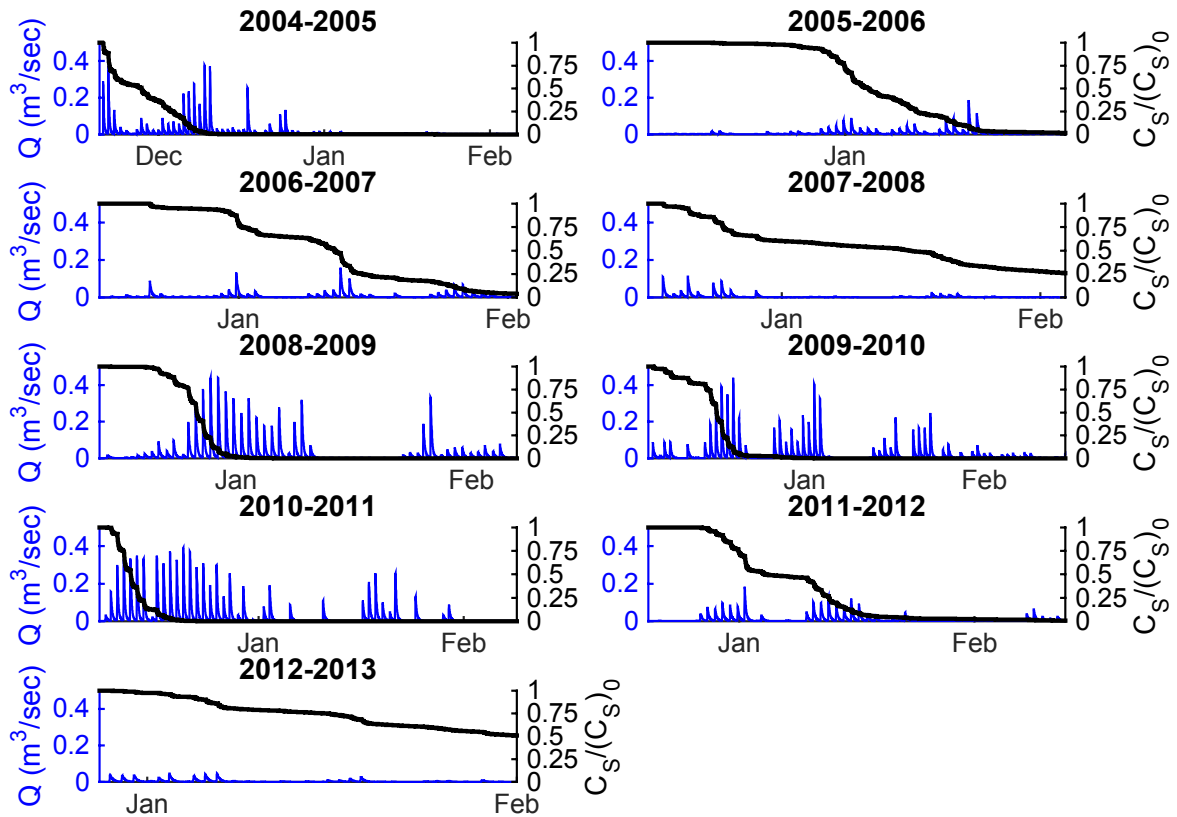


Figure 2. 26: Progressive hydrologic turnover of the hyporheic zone for nine flow seasons on Von Guerard Stream. Complete hydrologic turnover is defined here as the time for required for hyporheic zone concentrations to achieve a 90% reduction from an initial concentration.

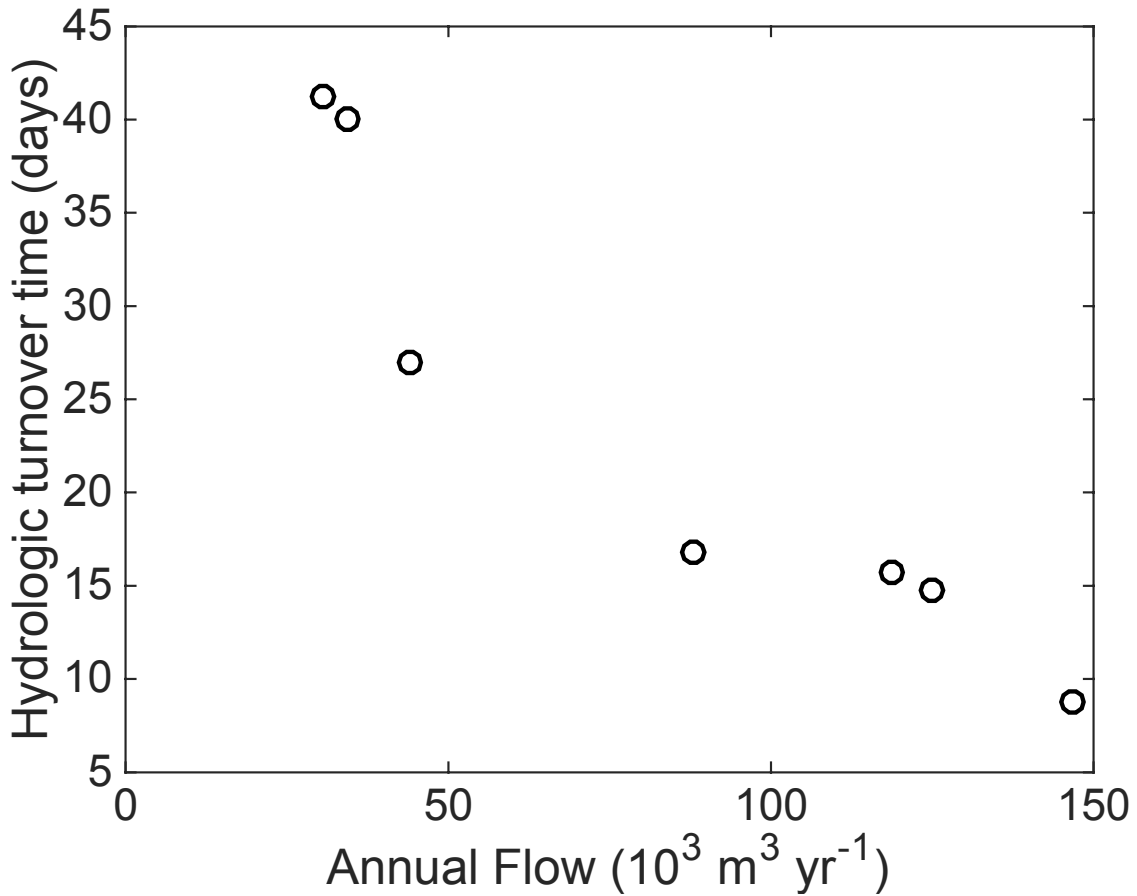


Figure 2.27: Hydrologic turnover time plotted as a function of annual flow for seasons when complete hydrologic turnover was achieved.

2.5.3 Dynamic Geochemical Controls on C-Q relationships

Models 1 and 2 were unable to explain observed C-Q dynamics. These models over-predict Si concentration at low flows, and under-predict Si concentrations at high flows (Figure 2.22). On the other hand, Model 3 produced the best objective fit to observed data and more closely simulated observed C-Q dynamics. This observation raises an important question about the structure of Model 3: What physical mechanisms may cause λ to scale positively with Q ?

Glaciers and streams trap aeolian dust mobilized from regional drifts by winter storms. In eastern Taylor Valley, aeolian sediment fluxes range from $0.26 - 27.87 \text{ g m}^{-2} \text{ yr}^{-1}$ [Lancaster, 2002]. Much of the wind-blown material is silt and clay sized. On glacier surfaces, dust accumulates in cryoconite holes. Aeolian dust can be released into proglacial streams during certain flow events. *Stumpf et al.* [2012] and *Marra et al.* [2014, 2016] hypothesize that aeolian dust is released from glacier surfaces during large melt events and is easily weathered along the stream corridor. Dust is believed to be easily weathered in the stream channel because of its very high surface area [Marra et al., 2016] and the “fresh” nature of mineral faces [Deuerling et al., 2014].

The flushing of aeolian deposited fine grain material from glacier surfaces to proglacial streams during significant melt events provides a plausible explanation for the relative success of Model 3. Unlike Models 1 and 2, the first-order rate of weathering, λ , is assumed to be a linearly increasing function of Q . The mobilization of aeolian dust during high flows would tend to increase mineral surface area, allowing weathering rates to scale positively with Q . A similar mechanism has been proposed for glaciated catchments in lower latitudes, whereby physical subglacial erosion produces new reactive mineral surfaces and increases chemical weathering rates [Anderson, 2005]. At the moment, the flushing of aeolian dust from glaciers during high flow events is only a hypothesis for explaining why weathering rates may scale positively with discharge. More detailed observations of suspended sediment loads in streams, ice-bound sediment concentrations in glaciers, and the function of supraglacial drainage networks are needed to rigorously test this hypothesis.

2.6 CONCLUSION

Hydrologic and geochemical observations show that chemical weathering is occurring along the stream corridor (Figure 2.8 - Figure 2.9), weathering derived solutes behave chemostatically (Figure 2.10 and Figure 2.11), annual Si denudation rates scale positively with specific discharge (Figure 2.12), and rates of Si production may outpace rates of hyporheic exchange (Figure 2.13 and Figure 2.14). Given the relatively simple nature of the MDV hydrologic system, rates of solute production and mobilization occurring along the stream corridor scale proportionately with streamflow rates.

It was hypothesized that hyporheic exchange and high rates of chemical weathering control the nature of C-Q relationships. An unsteady numerical weathering and transport model was developed to test this hypothesis. The model shows that hyporheic exchange is a critical hydrologic process controlling Si-Q relationships. However, a hyporheic ‘old’ water hypothesis, whereby ‘old’ water from the hyporheic zone is mobilized during high flows to buffer changes in stream geochemistry, does not apply in MDV streams due to a lack of significant storage. Furthermore, models with constant weathering rates were unable to simulate observed Si-Q dynamics. However, a variable weathering rate model more closely matches observed Si-Q patterns (Figure 2.21 and Figure 2.22). This result suggests that Si weathering rates increase with increasing discharge in MDV streams and hyporheic zones.

This work contributes to an ongoing discussion regarding chemical weathering rates in glaciated catchments. Study findings support the hypotheses of *Anderson [2005]*, *Stumpf et al.*

[2012], and *Marra et al.* [2014, 2016], which suggest that weathering rates increase with increasing discharge in glaciated catchments. Future work should focus on investigating the processes controlling weathering rate variability in glaciated systems, including quantification of the timing and magnitude of suspended sediment fluxes from cold-based glaciers in the MDVs.

2.7 APPENDIX

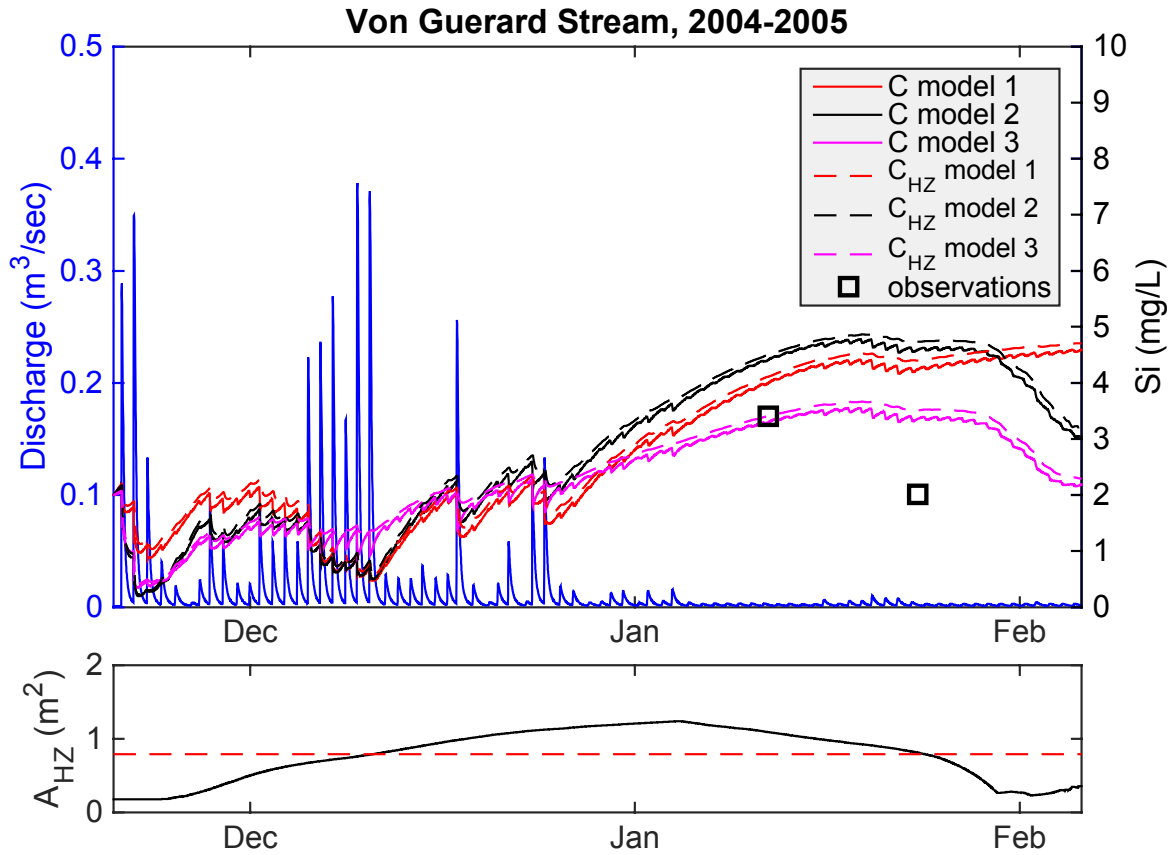


Figure 2.A1: Simulation results from the 2004/05 season. The top panel shows simulated discharge, main channel concentration (C), hyporheic zone concentration (C_{HZ}), and observations. Resultant concentration time series from all three models are shown with different colors. The bottom panel shows storage zone area for model 1 (red) and models 2 and 3 (black line).

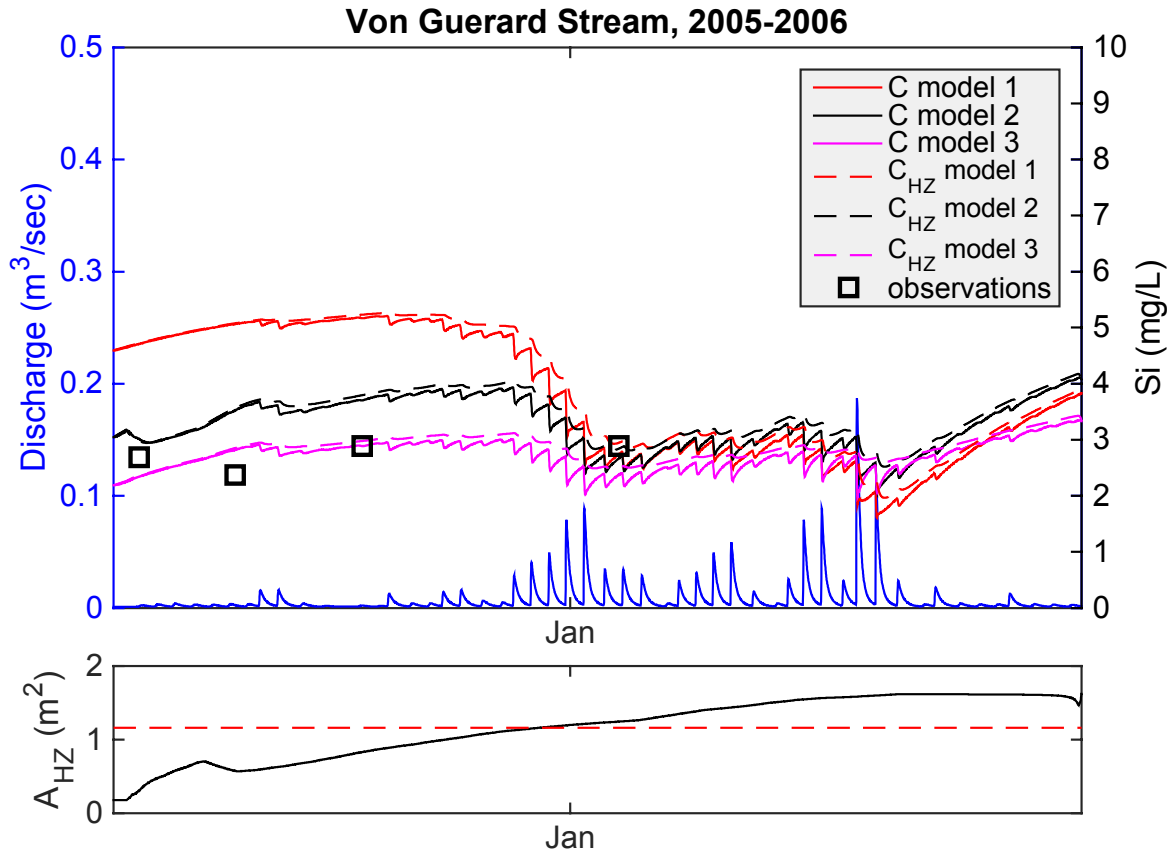


Figure 2.A2: Simulation results from the 2005/06 season. The top panel shows simulated discharge, main channel concentration (C), hyporheic zone concentration (C_{HZ}), and observations. Resultant concentration time series from all three models are shown with different colors. The bottom panel shows storage zone area for model 1 (red) and models 2 and 3 (black line).

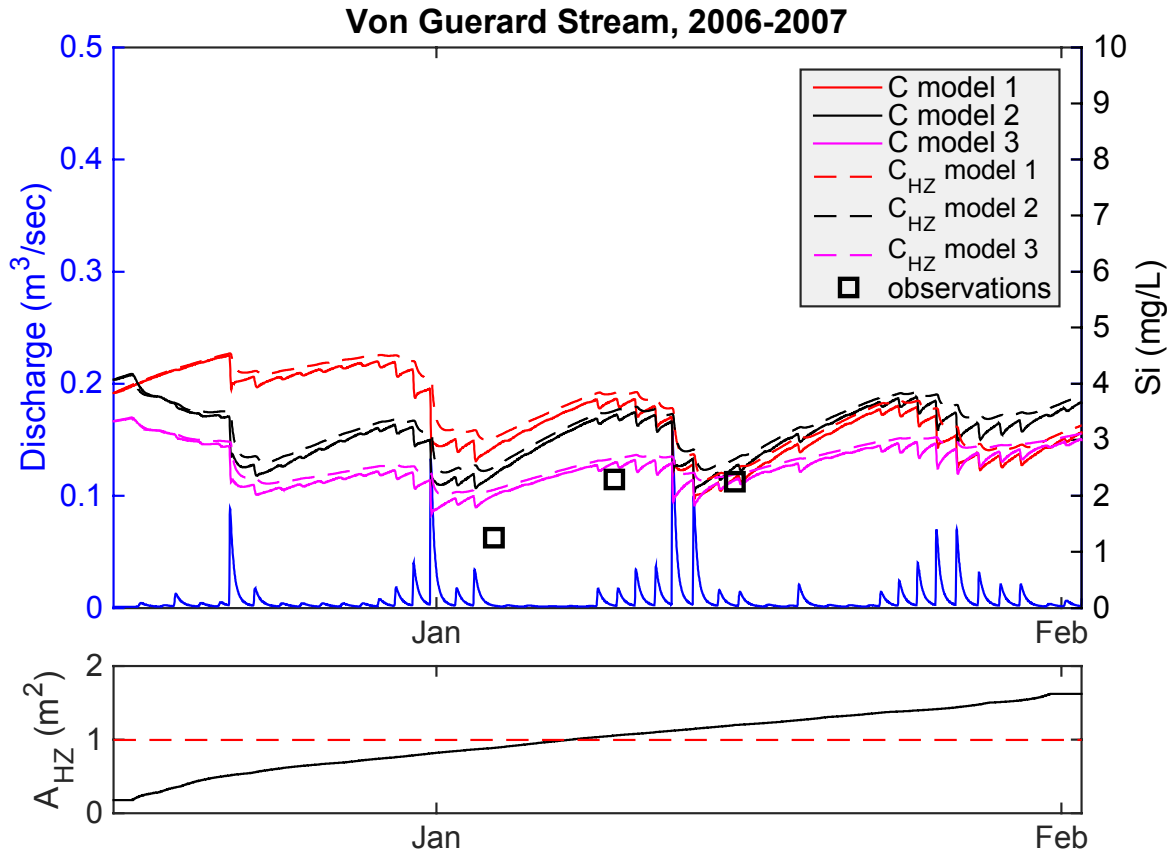


Figure 2.A3: Simulation results from the 2006/07 season. The top panel shows simulated discharge, main channel concentration (C), hyporheic zone concentration (C_{HZ}), and observations. Resultant concentration time series from all three models are shown with different colors. The bottom panel shows storage zone area for model 1 (red) and models 2 and 3 (black line).

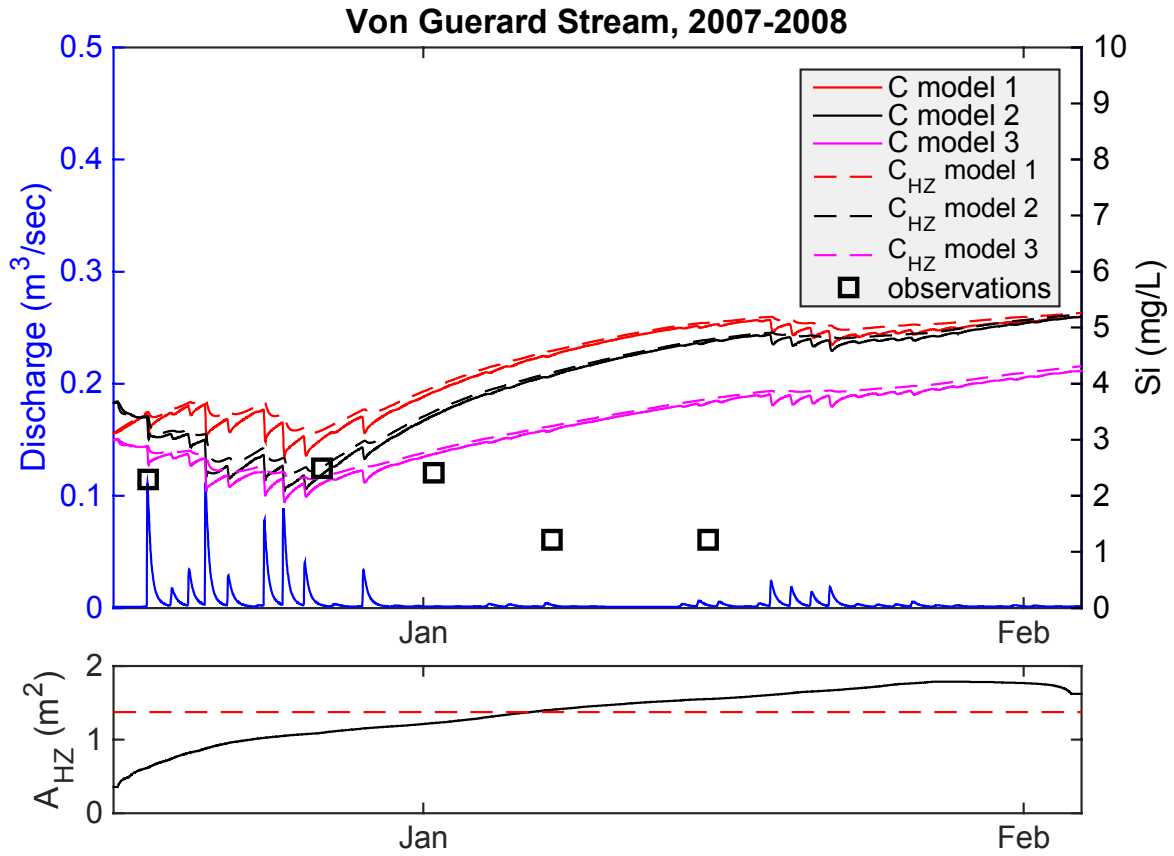


Figure 2.A4: A1: Simulation results from the 2007/08 season. The top panel shows simulated discharge, main channel concentration (C), hyporheic zone concentration (C_{HZ}), and observations. Resultant concentration time series from all three models are shown with different colors. The bottom panel shows storage zone area for model 1 (red) and models 2 and 3 (black line).

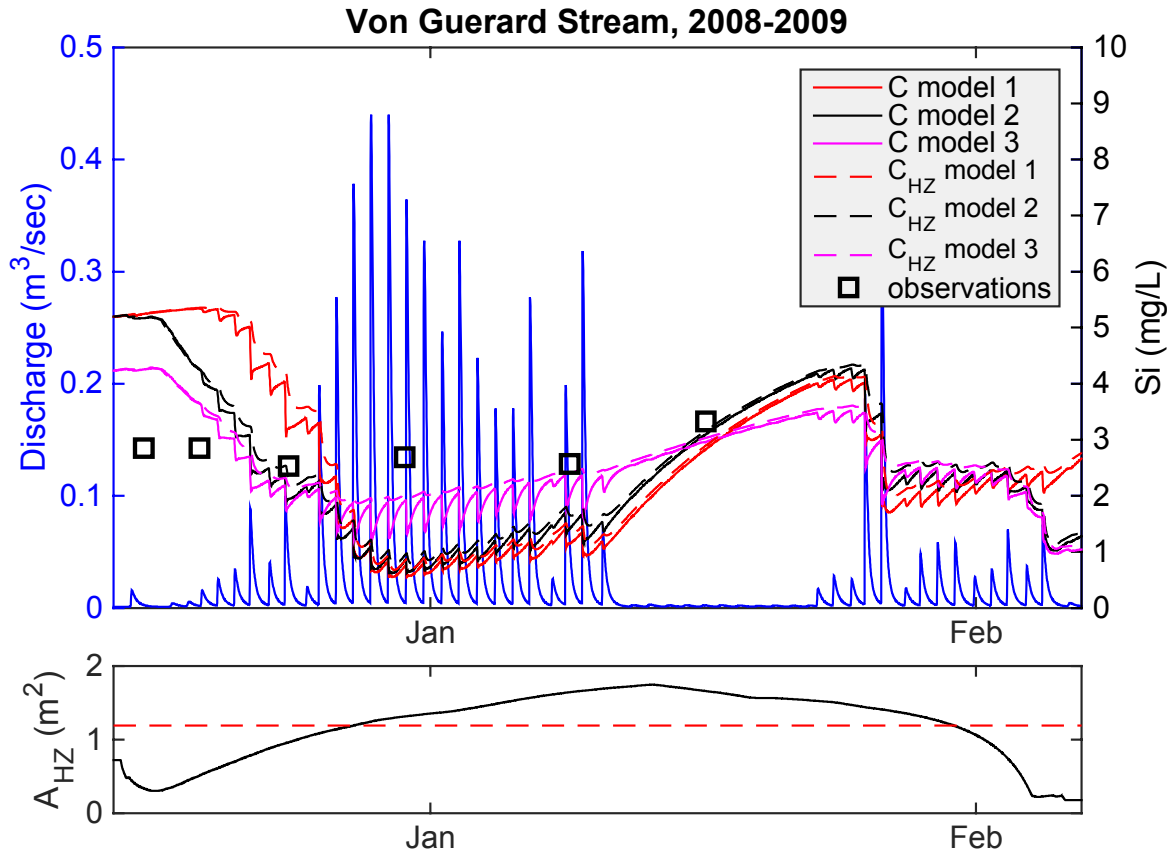


Figure 2.A5: Simulation results from the 2008/09 season. The top panel shows simulated discharge, main channel concentration (C), hyporheic zone concentration (C_{HZ}), and observations. Resultant concentration time series from all three models are shown with different colors. The bottom panel shows storage zone area for model 1 (red) and models 2 and 3 (black line).

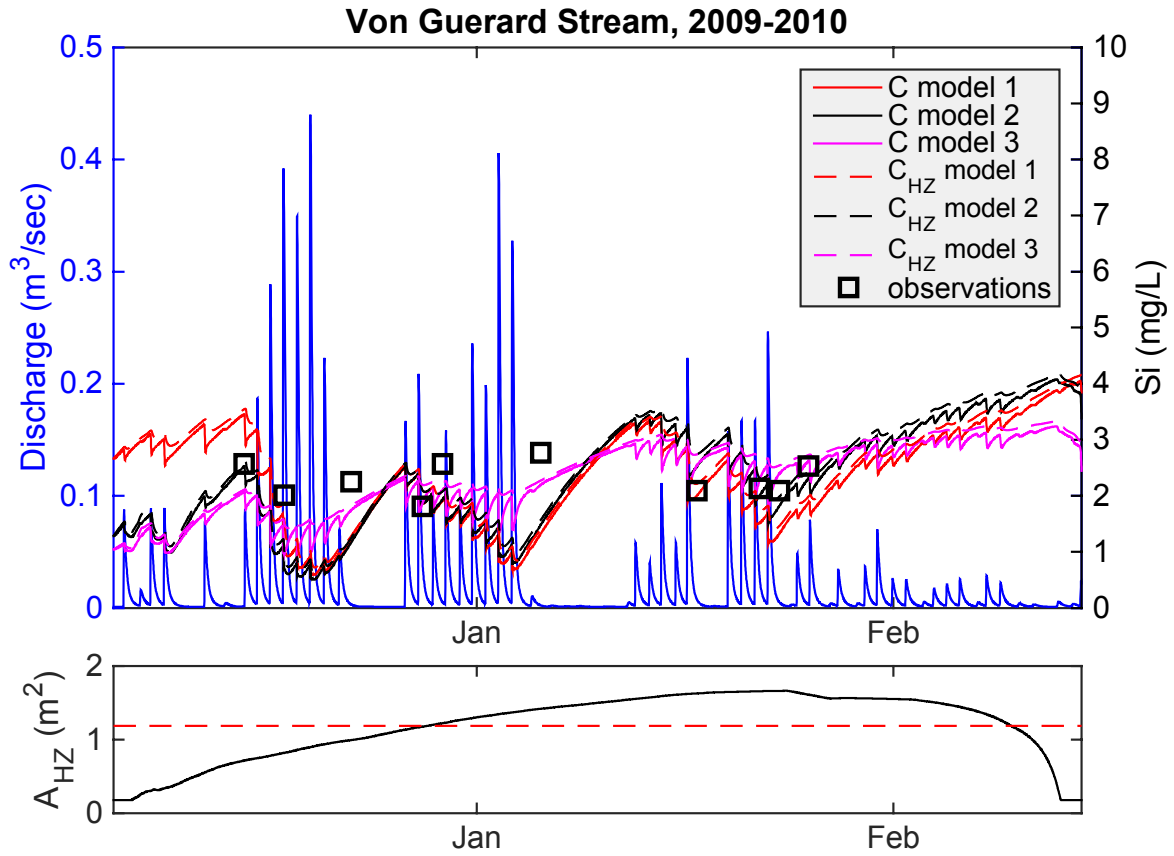


Figure 2.A6: Simulation results from the 2009/10 season. The top panel shows simulated discharge, main channel concentration (C), hyporheic zone concentration (C_{HZ}), and observations. Resultant concentration time series from all three models are shown with different colors. The bottom panel shows storage zone area for model 1 (red) and models 2 and 3 (black line).

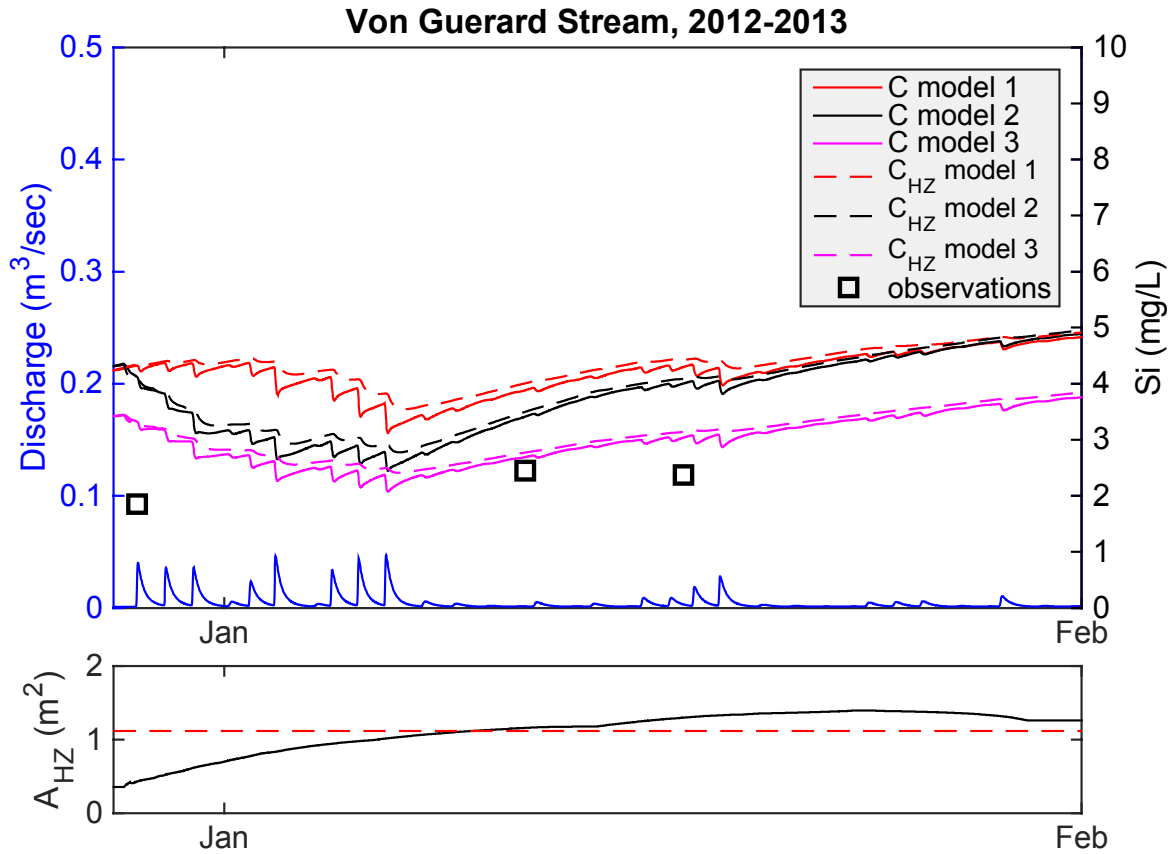


Figure 2.A7: Simulation results from the 2012/13 season. The top panel shows simulated discharge, main channel concentration (C), hyporheic zone concentration (C_{HZ}), and observations. Resultant concentration time series from all three models are shown with different colors. The bottom panel shows storage zone area for model 1 (red) and models 2 and 3 (black line).

CHAPTER 3: The control of soil moisture on the frequency and rate of freezing events in shallow active layer soils in the McMurdo Dry Valleys, Antarctica

3.1 INTRODUCTION

The McMurdo Dry Valleys (MDVs) of Antarctica are one of the coldest and driest environments on earth. Despite extreme cold and aridity, valley-bottom soils harbor an ecosystem composed of invertebrates and microbial flora. Nematodes are the most abundant invertebrates found in the Dry Valleys soils and occupy the highest trophic level of a relatively simple soil food-chain [Cary *et al.*, 2010]. Only three species of nematode are found in these soils: *Plectus antarcticus (murrayi)*, *Eudorylaimus antarcticus*, and *Scottinema lindsayae*. As Antarctic soil ecosystems lack invertebrate diversity and trophic redundancy [Adams *et al.*, 2006], the soil ecosystem is particularly vulnerable to the loss or decline of a single nematode species brought about by environmental change. The dual simplicity and vulnerability of Antarctic soil food webs has prompted long-term observations and experimentation to understand how environmental change might affect the structure and function of such soil ecosystems.

Due a gradual recovery of the Antarctic ozone hole [Yang *et al.*, 2005] and greenhouse warming, climate models predict a gradual warming of East Antarctic and the greater MDV region [Chapman and Walsh, 2007; Walsh, 2009]. Warming is expected to progress at approximately 0.3 °C/decade, resulting in an increase of summer air temperatures by 2 °C by 2100 [Chapman and Walsh, 2007]. Anticipated near-surface warming is likely to increase soil moisture across the landscape. Several warming-induced processes will increase soil moisture at

local and regional spatial scales. Warmer surface temperatures will favor melt during the hydrologic partitioning of snow patches [Gooseff *et al.*, 2003b], enhance rates of ground ice and permafrost thaw [Fountain *et al.*, 2014], and expand wetted margins adjacent to lakes and streams [Gooseff *et al.*, 2007; Northcott *et al.*, 2009].

In the relatively desiccated MDV landscape, active layer soil moisture (specifically liquid) exerts direct control on invertebrate species diversity and abundance. Soil moisture dynamics are controlled by local shallow groundwater flow (e.g. infiltration), and phase change (e.g. evaporation and freezing). Because, pore water chemistry is partially controlled by the same processes, soil moisture strongly controls the biogeochemical environment of active layer ecosystems. For example, in wetted margins adjacent to stream channels, drier distal soils tend to be saltier and contain less organic matter than wetter soils closer to the stream channel [Treonis *et al.*, 1999; Barrett *et al.*, 2009; Northcott *et al.*, 2009]. Higher osmotic stress and the lack of organic carbon causes dry distal soils to be a relatively harsh habitat, compared to wet near-stream soils. As such, invertebrate abundance [Treonis *et al.*, 1999], nutrient cycling rates [Barrett *et al.*, 2002; Gooseff *et al.*, 2003b] and microbial activity [Zeglin *et al.*, 2009; Van Horn *et al.*, 2014], tend to be positively correlated with soil moisture.

Soil moisture also fundamentally controls soil thermodynamics [Farouki, 1981]. Thermal diffusivity tends to increase with increasing soil saturation, as the thermal conductivity of water is much greater than that of air. Also, latent heat content increases as a function of soil moisture. Due to the release of latent of fusion, wet soils tend to freeze more gradually than dry soils. This

results in a so-called “zero-curtain effect”, where soil temperature remains isothermal at the freezing point while the majority of pore water changes phase to ice [Outcalt *et al.*, 1990].

Nematodes in Antarctic soils are exposed to a suite of freezing and desiccation stresses each year. A variety of physiological responses allow nematodes to withstand extreme environmental stresses, and the relative success of physiological stress tolerance strategies are limited by soil environmental conditions. For example, the success of stress tolerance mechanisms is controlled by soil freezing rate, which is mediated by latent heat release (soil moisture) and the rate of energy transfer through the soil (thermal characteristics) [Holmstrup *et al.*, 2002; Wharton *et al.*, 2002]. In gradually freezing soils, organisms either employ cryoprotective dehydration or are capable of surviving innoculative freezing [Wharton, 2003]. In very dry rapidly freezing soils, organisms employ anhydrobiosis to avoid desiccation stress [Treonis *et al.*, 2000]. During anhydrobiosis, animals evacuate much of the water from their body cavity and avoid the fatal consequences of innoculative crystallization. If higher soil moisture content slows freezing rates, nematode species capable of cryoprotective dehydration and innoculative freezing may gain a physiological advantage over anhydrobiosis specialists.

Low-temperature survival mechanisms employed by nematodes incur a metabolic cost and limit opportunity for growth and reproduction [Adhikari *et al.*, 2010; Knox *et al.*, 2015]. Long-term *S. Lindsayae* abundance data show that during years with a high number of freeze events, their development is limited and reproductive success is inhibited [Knox *et al.*, 2015]. Therefore, if higher soil moisture decreases freeze-event frequency, invertebrate abundance may increase due to a reduction in physiological stress.

The goal of this research is to elucidate the physical controls on freezing dynamics in soils of the McMurdo Dry Valleys. Given an anticipated increase in soil moisture across the Dry Valleys with regional warming, it is useful to understand how future climate conditions may affect the abiotic soil environment, specifically the frequency and rate of freezing events in the shallow active layer. I hypothesize that increased soil moisture will lower the frequency and rate of freeze-events in Dry Valley soils.

3.2 STUDY SITE

The McMurdo Dry Valleys (MDVs) encompass a 22,700 km² area of East Antarctica between the East Antarctic Ice Sheet and Ross Sea. 4,500 km² of the MDVs are ice-free. This study will focus on several sites within the Taylor Valley. Long-term (1993 – 2014) weather observations from eight meteorological stations in Taylor Valley illustrate the extremely dry and cold nature of the climate (Figure 3.1 and Table 3.1). Mean annual air temperature is -18°C. Average austral spring/summer (November - February) air temperature is -6°C and average winter (March - October) air temperature is -24°C. There are an average of 17 degree-days above freezing per year, always occurring between November 1 and March 1. Mean annual relative humidity is 66%. The valley experiences continuous sunlight during austral summer and continuous darkness during the austral winter. Summertime solar noon radiation is between 470 – 515 W/m² [Doran *et al.*, 2002]. There is a general east-west oriented climate gradient within Taylor Valley. Western Taylor Valley tends to be warmer, drier and windier than eastern Taylor Valley [Doran *et al.*, 2002]. The three month period between December 1 – March 1 is the

period of greatest biological activity. Continuous solar radiation and relatively warm air temperatures can increase the soil habitat temperatures above freezing.

Table 3.1: Summary of long-term meteorological observations (1994-2014) from eight sites in the Taylor Valley.

	Taylor Glacier (TARM)	Lake Bonney (BOYM)	Lake Hoare (HOEM)	Howard Glacier (HODM)	Canada Glacier (CAAM)	Lake Fryxell (FRLM)	Cmwth. Glacier (COHM)	Explorers Cove (EXEM)
distance from coast (km)	39	25	15	17	15	9	6	4
elevation (m asl)	334.13	64.43	77.11	472.49	264.43	19	290.24	25.75
Air Temperature (°C)								
avg mean annual	-16.95	-17.16	-17.91	-17.25	-17.49	-20.21	-17.8	-19.34
max mean annual	-15.52	-14.41	-16.21	-15.9	-16.93	-18.13	-16.3	-17.59
min mean annual	-18.97	-19.06	-19.78	-18.54	-19.51	-22.45	-19.14	-21.32
avg mean summer	-5.92	-3.85	-5.04	-7.49	-6.31	-5.08	-7.39	-5.92
max mean summer	-4.95	-3.24	-3.72	-5.99	-5.66	-4.29	-6.96	-5.25
min mean summer	-6.93	-4.48	-5.81	-8.44	-7.25	-5.82	-8.19	-6.51
avg mean winter	-22.28	-23.83	-24.12	-22.04	-22.74	-27.67	-22.87	-25.71
max mean winter	-20.29	-21.16	-21.74	-20.15	-22.1	-24.63	-20.79	-23.49
min mean winter	-24.5	-26.51	-27.05	-24.04	-24.42	-31.05	-25.12	-29.08
DDAF (°C-d)								
avg mean annual	13.05	47.04	20.5	5.42	9.55	19.36	3.94	15.15
max mean annual	25.91	80.63	38.84	11.61	21.26	34.7	12.47	30.04
min mean annual	2.34	10.46	4.74	0.01	0.74	5.07	0.04	1.43
Relative Humidity (%)								
avg mean annual	59.8	63.18	68.58	61.9	60.98	75.46	67.93	75.68
Wind Speed (m/sec)								
avg mean annual	5.18	3.84	2.67	3.15	3.19	3	3.92	2.78
absolute max	29.12	25.92	21.88	27.9	31.43	30.98	26.07	25.82
Shortwave Radiation (W/m²)								
avg mean annual	104.12	103.81	89.87	97.12	100.53	106.65	108.34	105.9
max mean annual	121.76	164.36	97.15	104.5	109.98	112.37	114.56	115.79
min mean annual	86.3	84.24	80.67	88.3	93.29	96.47	101.15	88.97



Figure 3.1: Location map of the Taylor Valley. Met stations and Active Layer Monitoring Sites (ALMS) within the valley are shown.

Soils in Taylor Valley are coarsely textured, containing small amounts of silt and clay, and lack significant cohesion or structural development [*Campbell et al.*, 1998]. Soil parent materials are primarily granitic glacial tills and dolerite sandstones, remnants of multiple glaciations [*Prentice et al.*, 1998]. Soil organic material is minimal because vascular vegetation across the landscape is non-existent. Eastern Taylor Valley soils are underlain by ice-cemented permafrost, showing evidence of active cryoturbation, while western Taylor Valley soils are underlain by dry-frozen permafrost and lack evidence of cryoturbation [*Bockheim et al.*, 2007]. Spatial differences in permafrost characteristics are related by differences in moisture sources and vapor pressure gradients throughout the region [*McKay et al.*, 1998]. A detailed mapping of soil and permafrost characteristics in the Taylor Valley can be found in *Bockheim and McLeod* (2008).

Soil moisture content is an important control on the thermal properties of soils in the MDVs [*Ikard et al.*, 2009]. In general, valley bottom soils have very low moisture contents, averaging approximately 1% water by volume in the upper 3 cm of the soil horizon [*Campbell et al.*, 1998]. However, the proximity of soils to hydrologic reservoirs, such as snow, streams, and lakes, is an important spatial control on soil moisture. Open bodies of water, such as lakes and streams, are surrounded by a wetted margin. Wetted margins are created by the capillary wicking of moisture through soil pore spaces [*Gooseff et al.*, 2007]. Wetted margins can have a width of 2 – 35 m [*Barrett et al.*, 2009] and soil moisture content generally decreases with increasing distance from the open water source [*Northcott et al.*, 2009]. Similarly, snow patches are a source of moisture for subnivian and adjacent soils [*Campbell et al.*, 1998; *Gooseff et al.*,

2003b]. *Gooseff et al.*, [2003b] observed subnivian soils to be 20 times more moist than exposed soils.

Spatially discrete “wet patches” are also commonly observed in Taylor Valley. Wet patches are visibly moist soils, appearing darker than drier adjacent soils. There are two primary mechanisms forming wet patches: (1) direct condensation of atmospheric water vapor into saline surficial soil pore spaces (i.e., deliquescence) [*Levy et al.*, 2012] (2) the sub-surface routing of melt water through watertracks [*Levy et al.*, 2011]. Watertracks are sourced by snowmelt or melting ground ice and route meltwater down gradient above the ice-table. Interstitial watertrack water is very salty relative to stream waters. *Levy et al.* [2011] referred to watertracks as “solute superhighways”, reporting solute concentrations over an order of magnitude greater than are typically observed in streams. High solute concentrations in watertracks are attributed to very long transit times, atmospheric salt accumulation, and evaporative concentration. Wet patch locations were investigated by *Langford* [2013], who found that topography and regional microclimates govern their spatial distribution. Watertracks are located along linear flow paths coincident with regions of high topographic flow accumulation [*Levy et al.*, 2011].

Four sites were selected to intensively monitor thermal and hydrologic active layer dynamics (Figure 3.1). Two sites are located adjacent to streams in the Lake Fryxell Basin - Von Guerard (VG) (Figure 3.2) and Green Creek (GC) (Figure 3.3). The remaining two sites are located adjacent to watertracks, Watertrack B (WTB) (Figure 3.4) and Wormherder Creek (WHC) (Figure 3.5).

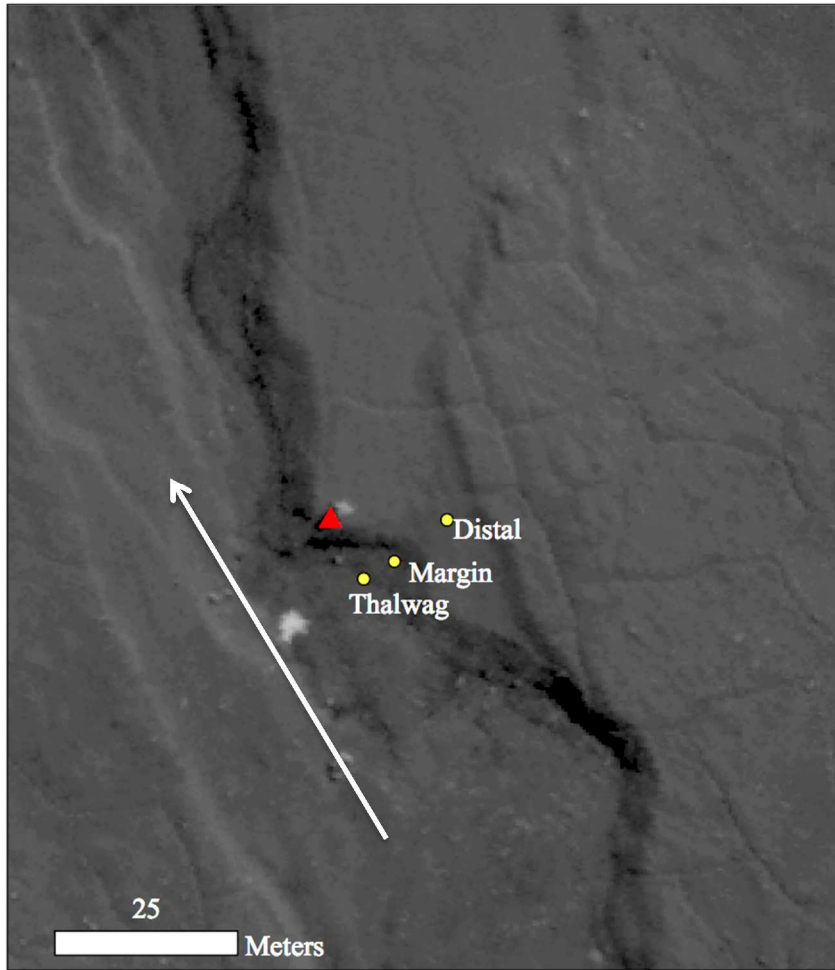


Figure 3.2: Aerial image of Von Guerard ALMS. Yellow markers show the position of vertical sensor arrays in the channel thalweg, wetter margin, and dry distal soils. Stream flow is oriented from the bottom of the image towards the top of the image. WorldView3 imagery provided by the University of Minnesota Polar Geospatial Center.

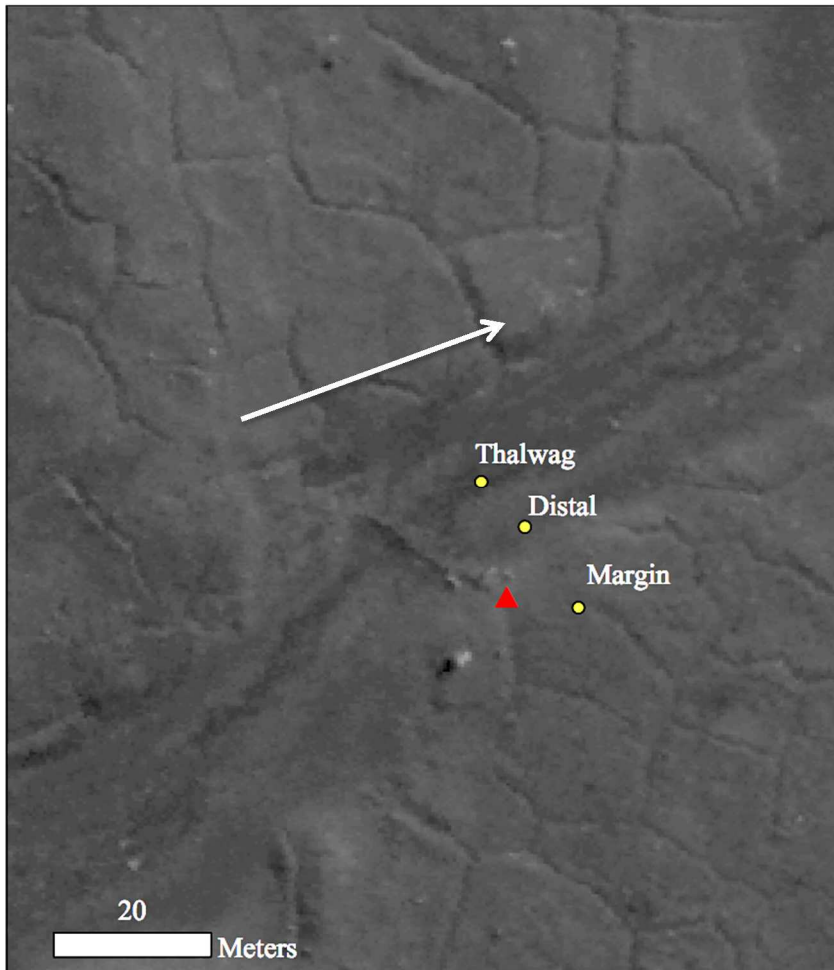


Figure 3.3: Aerial image of Green Creek ALMS. Yellow markers show the position of vertical sensor arrays in the channel thalweg, wetter margin, and dry distal soils. Stream flow is oriented from left to right in the image. WorldView3 imagery provided by the University of Minnesota Polar Geospatial Center.

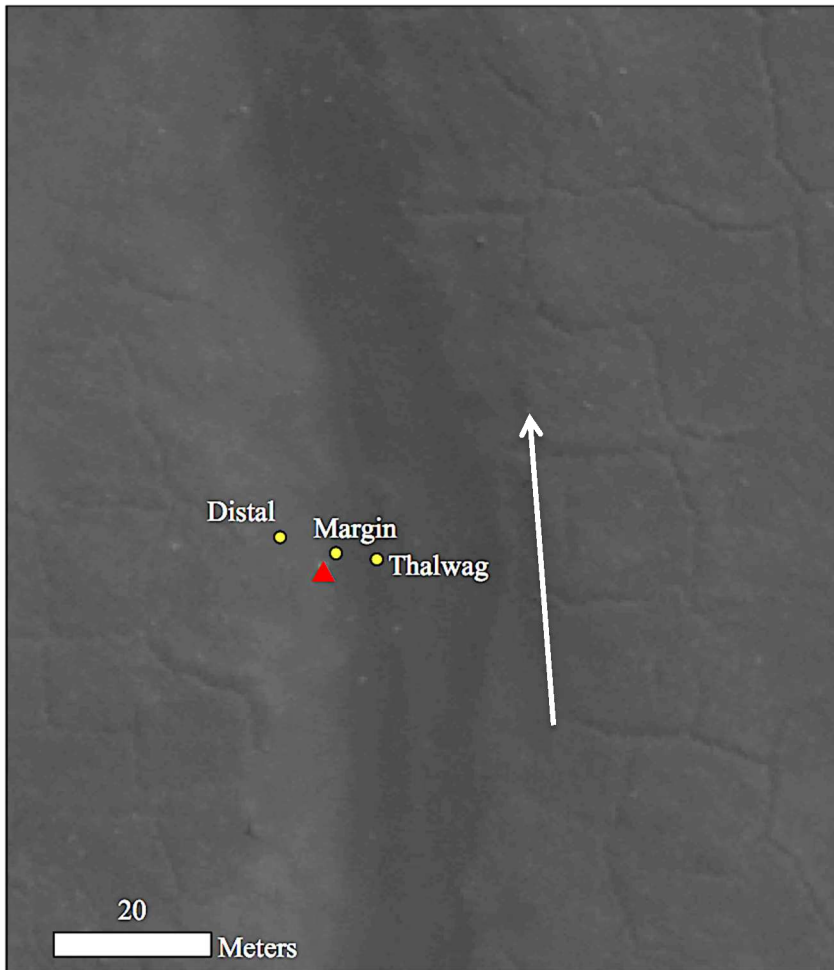


Figure 3.4: Aerial image of Watertrack B ALMS. Yellow markers show the position of vertical sensor arrays in the channel thalweg, wetter margin, and dry distal soils. Flow is oriented from the bottom to top of the image. WorldView3 imagery provided by the University of Minnesota Polar Geospatial Center.

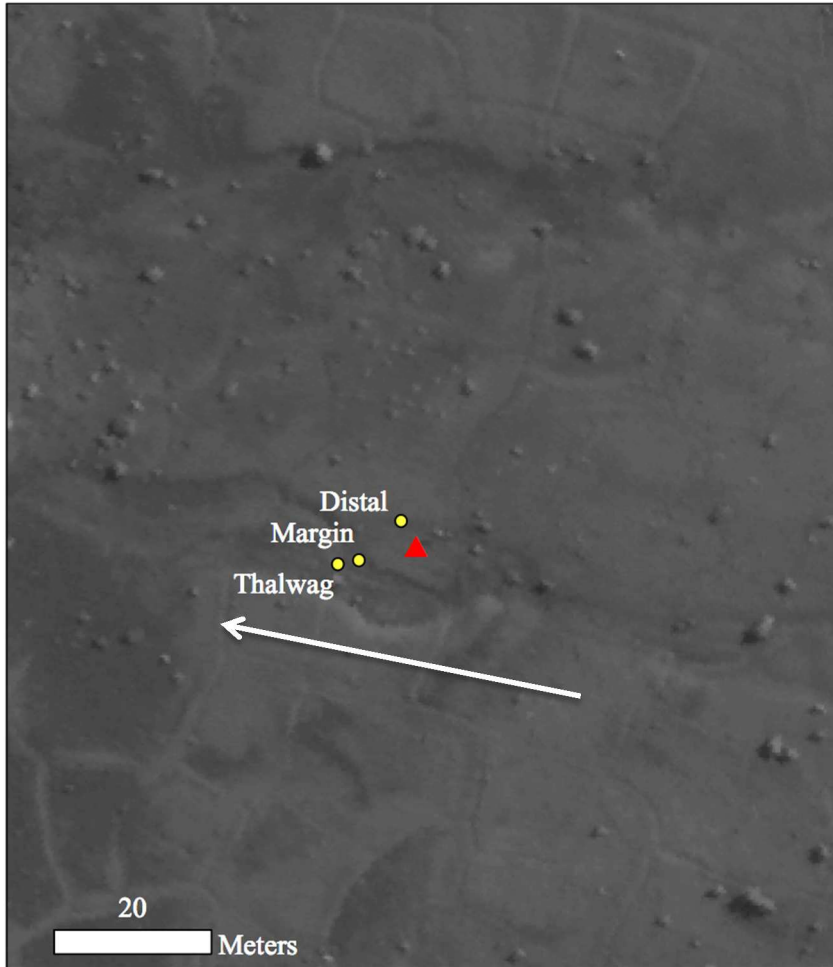


Figure 3.5: Aerial image of Wormherder Creek ALMS. Yellow markers show the position of vertical sensor arrays in the channel thalweg, wetter margin, and dry distal soils. Flow is oriented from right to left in the image. WorldView3 imagery provided by the University of Minnesota Polar Geospatial Center.

3.3 METHODS

Active layer monitoring stations (ALMSs) are developed to measure temperature, soil moisture, and pore water specific conductance along natural moisture gradients at each study site. K-Type, Duplex Insulated Omega® Thermocouple Wire was cut and insulated at one end to measure soil temperature at discrete depths. Thermocouples are wired into a Campbell

Scientific® AM25T 25-Channel Solid-State Thermocouple Multiplexor, connected to a CR1000 Measurement and Control Datalogger. Thermocouples measure temperature within a range of -250 to +250°C, at an accuracy of 2% below freezing and 0.75% above freezing, and a precision of 0.001°C.

Decagon® 5TE sensors are used to measure soil temperature, volumetric water content and electrical conductivity. Each 5TE sensor is wired into a Campbell Scientific AM16/32B 16-Channel Relay Multiplexor, which is also connected to a CR1000. Soil moisture is measured by time-domain reflectometry (TDR), where the Topp Equation for mineral soil [Topp *et al.*, 1980] is used to infer volumetric soil moisture from direct observations of the Apparent Dielectric Permittivity of the soil.

Apparent Dielectric Permittivity is measured with an accuracy of +/- 1 [unitless], and a resolution of 0.1. Using the Topp equation, soil moisture is estimated with an accuracy of 0.03 m³/m³ and a resolution of 0.001 m³/m³. Topp equation parameters were not adjusted (calibrated) prior to installation. Pore water specific electrical conductivity is measured with an accuracy of 10% and resolution of 0.01 dS/m.

Sensors were installed at known depths along 1-dimensional vertical array within several excavated pits. Sensor installation depths below the ground surface are reported in (Table 3.2). After sensor installation, each pit was backfilled by replacing sediments in same order they were excavated, making the best effort to restore soils to a nearly undisturbed state. At each site, a pit was dug and instrumented in the channel thalweg, wetted margin, and dry distal soils. Thalweg

pits were dug in the middle of the drainage feature. Wetted margin pits were dug at the transition between visibly wet and/or inundated soils and distal soils, located far from the fluvial feature.

Table 3.2: Table 1: Installation depth of sensors at active layer monitoring sites. Sensor type is indicated by an abbreviation in parentheses. Decagon 5TE (5TE) sensors measure volumetric water content and specific conductance, and thermocouples (TC) measure temperature. Sensors used in this study are shown in boldface font.

	Von Guerard (VG)			Green Creek (GC)			Watertrack B (WTB)			Wormherder Creek (WHC)		
	Thalwag	Margin	Distal	Thalwag	Margin	Distal	Thalwag	Margin	Distal	Thalwag	Margin	Distal
sensor depth, cm (sensor type)	1 (TC)	1 (TC)	5 (5TE)	1 (TC)	1 (TC)	1 (TC)	1 (TC)	1 (TC)	1 (TC)	1 (TC)	1 (TC)	1 (TC)
	5 (5TE)	5 (5TE)	10 (TC)	5 (5TE)	5 (5TE)	5 (5TE)	5 (5TE)	5 (5TE)	5 (5TE)	5 (5TE)	5 (5TE)	5 (5TE)
	10 (TC)	10 (TC)	15 (5TE)	10 (TC)	10 (TC)	10 (TC)	10 (TC)	10 (TC)	10 (TC)	10 (TC)	10 (TC)	10 (TC)
	15 (5TE)	15 (5TE)	25 (5TE)	15 (5TE)	15 (5TE)	15 (5TE)	15 (5TE)	15 (5TE)	15 (5TE)	15 (5TE)	15 (5TE)	15 (5TE)
	25 (TC)	25 (TC)	30 (TC)	20 (TC)	20 (TC)	20 (TC)	20 (TC)	20 (TC)	20 (TC)	20 (TC)	20 (TC)	20 (TC)
	30 (TC)	30 (TC)	40 (TC)	25 (TC)	25 (TC)	25 (TC)	25 (5TE)	25 (5TE)	25 (5TE)	25 (TC)	25 (TC)	25 (TC)
	35 (5TE)	35 (5TE)	50 (TC)	30 (TC)	30 (TC)	30 (TC)	30 (TC)	30 (TC)	30 (TC)	33 (5TE)	30 (TC)	30 (TC)
	40 (TC)	40 (TC)	60 (TC)	35 (5TE)	35 (5TE)	35 (5TE)	35 (5TE)	32 (5TE)	35 (5TE)		35 (5TE)	35 (5TE)
					45 (TC)	45 (TC)	40 (TC)				45 (TC)	45 (TC)
										55 (TC)		

Given the importance of freezing events on the active layer habitat [Knox *et al.*, 2015], shallow soil moisture and temperature data, between 0 – 15 cm depth, are analyzed to characterize the frequency and rate of freezing events at each site. Shallow data are used because the invertebrate habitat typically does not extend below 15 cm. The protocol for collecting LTER soil biology samples is to excavate soils between 0 and 10 cm depth [Freckman and Virginia, 1997]. At each site, soil moisture, temperature, and specific conductance are measured at 15 cm and temperature is measured at 10 cm. Data from sensors at 10 and 15 cm are analyzed in this chapter.

When ground temperatures approach the freezing point of liquid water, interstitial soil moisture does not freeze immediately and abruptly. Rather, the freezing of soil water occurs gradually across a “freezing window” and unfrozen water can exist at temperatures well below freezing [Anderson and Tice, 1973; Romanovsky and Osterkamp, 2000]. This work uses phase composition curves at 15 cm to quantify the freezing window at each site. Phase composition curves relate coincidentally observed volumetric soil moisture to ground temperature (Figure 3.6). It is assumed that TDR volumetric soil moisture measurements are sensitive to the unfrozen liquid water fraction of soil moisture. This is a reasonable expectation because the relative dielectric constant of water is much higher than that of ice. The upper boundary of the freezing window is defined as the temperature at which the steepest decline in soil moisture is observed on the phase composition curve (Figure 3.6). The lower boundary of the freezing window is defined as the temperature at which soil moisture has declined by 90% of the observed soil moisture range (Figure 3.6).

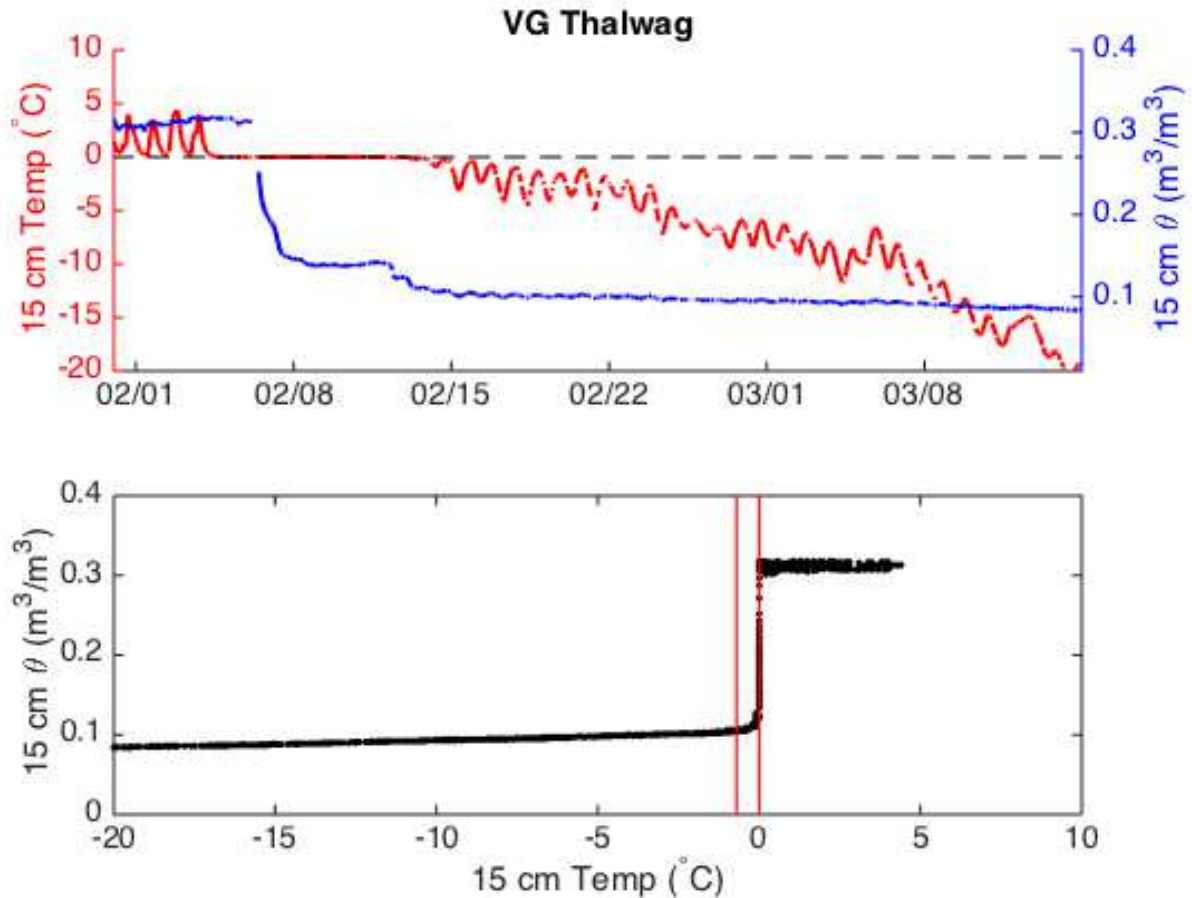


Figure 3.6: Coincidentally observe temperature and volumetric soil moisture content (θ) at 15 cm depth between February 1, 2015 and March 15, 2015 (top panel) are used to create soil moisture phase composition curves (bottom panel). The freezing window is illustrated on the soil moisture phase composition curve (bottom panel) by two vertical red lines.

Freeze events occur when ground temperature at 10 cm depth passes from above to below the freezing window. The total number of freezing events for a given period of record is computed by counting the total number of freezing window crossings. In the work of *Knox et al.* (2015), the frequency of freeze-thaw cycles is calculated. Here we diverge slightly by only calculating freeze events (i.e. whenever temperature drops from above to below the freezing window), because it is the process of freezing that exerts a physiological stress response from

soil biota. For each freeze-event, the freezing rate is also quantified as the rate of change in temperature with respect to time as soil temperature decreases across the freezing window.

$$freeze\ rate = \frac{[T_{upper} - T_{lower}]}{[t_{T_{upper}} - t_{T_{lower}}]} \quad (3.1)$$

where T_{upper} and T_{lower} are the upper and lower boundaries of the freezing window, respectively, and $t_{T_{upper}}$ and $t_{T_{lower}}$ are the times when ground temperature crosses the upper and lower freezing window boundaries, respectively.

3.4 RESULTS

Active layer temperature at 10 cm, volumetric water content (VWC) at 15 cm, and specific conductance (SpC) at 15 cm were measured from mid January 2014 through early February 2016 (Appendix, Figure A1 – Figure A4). Active layer soils are subjected to a wide range of temperatures. The lowest temperature (-46.6°C) was observed in distal soils at VG, and the highest temperature (10.8°C) was observed in margin soils at WHC. Between January 2014 and February 2016, active layer soils at 10 cm depth were above freezing for 100 – 180 total days (Figure 3.7, A), or 13 – 24% of the observation duration (Figure 3.7, B). Active layer soils at VG spent the fewest number of days above freezing, while soils at WHC spent the greatest number of days above freezing. At VG and WTB, the number of days above freezing increased with increasing distance from the thalwag. At WHC and GC, the greatest number of days above freezing was observed at margin and thalwag sites, respectively.

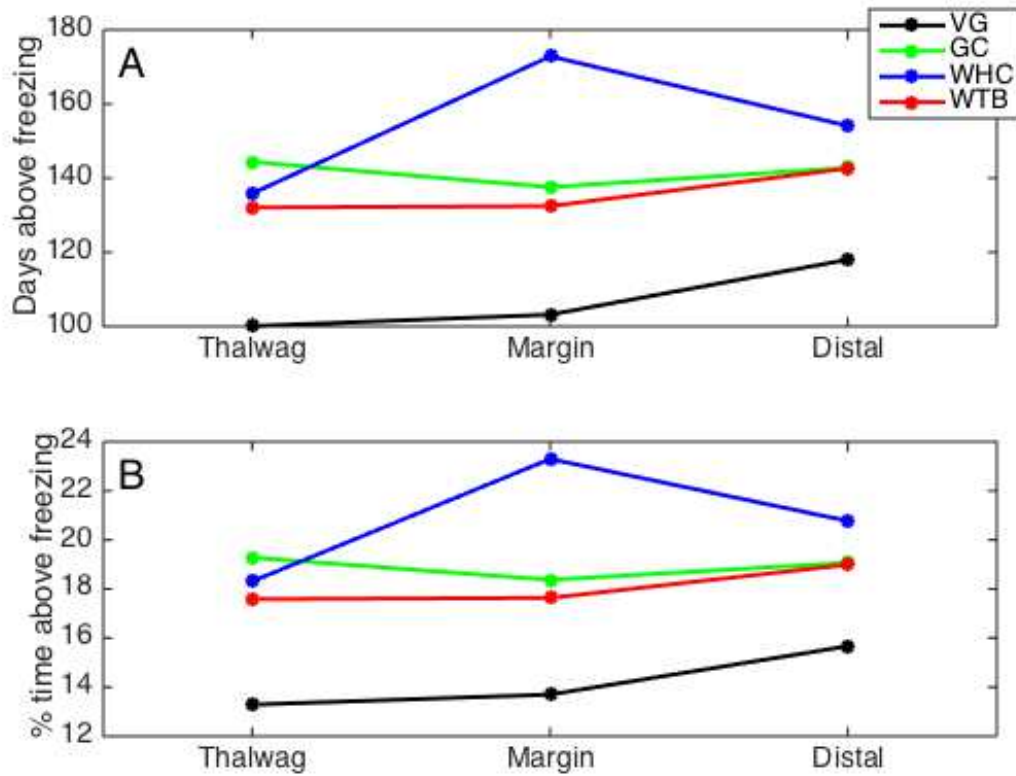


Figure 3.7: The number of days above freezing (A) and the percentage of observed time above freezing (B) at 10cm depth at each active layer monitoring site. The percentage of time above freezing is the percent of total observation time that ground temperature at 10 cm was above freezing.

Average summer (December - February) 10 cm active layer temperature ranged from 1.8°C to 4.17°C. Mean temperatures at thalwag, margin, and distal locations were not significantly different from each other, as indicated by non-overlapping error bars (Figure 3.8, A). At all active layer stations, VWC was highest at thalwag locations, and decreased from margin to distal locations (Figure 3.8, B). Volumetric water content at distal locations was consistently below 0.1 m³/m³, with the exception of GC where the distal site had a mean VWC of 0.13 m³/m³. The range of SpC observations spanned over an order of magnitude between active layer sites, from 0.111 – 3.145 mS/cm. Conductivity was lower at stream sites (GC and

VG) compared to watertracks (WHC and WTB) (Figure 3.8, C). At GC, VG, and WTB, SpC was greater at margin locations than thalweg locations. However, at WHC, wetted margin SpC was greater than in the thalweg. Distal soils were too dry to make reliable SpC measurements.

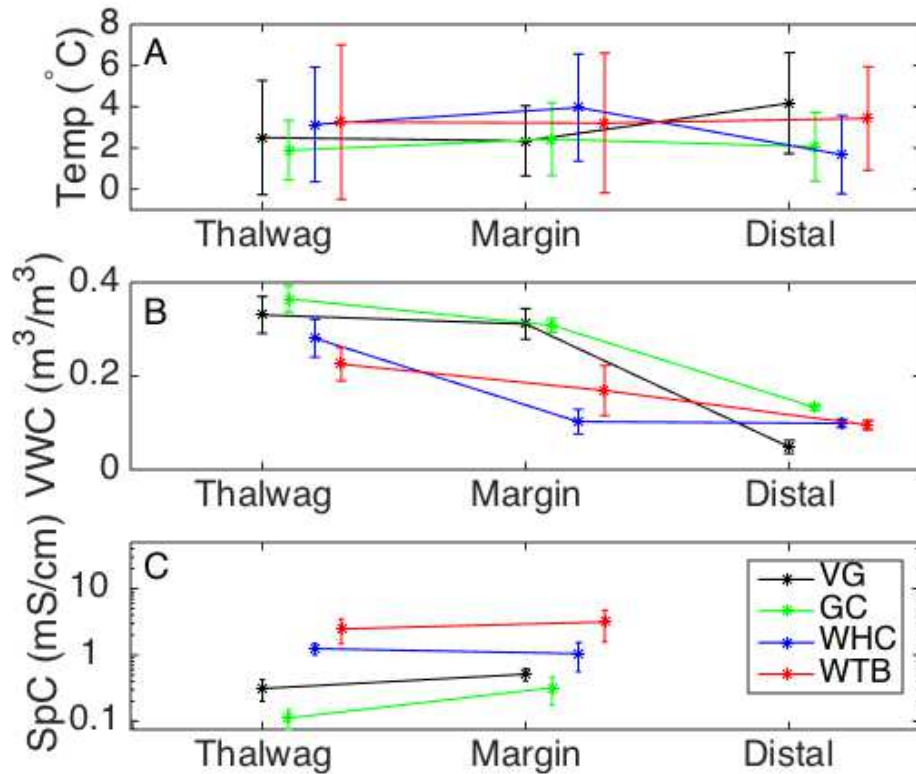


Figure 3.8: Summer (December - February) mean 10 cm temperature (A), 15 cm volumetric water content (B), and 15 cm specific conductance (C) at active layer monitoring sites.

The width of the freezing window, as calculated from soil moisture phase composition curves, is unique at each ALMS location (Figure 3.9). The smallest freezing window is observed at the VG margin location, where freezing initiates at $-0.1\text{ }^{\circ}\text{C}$ and ends at $-0.4\text{ }^{\circ}\text{C}$. The widest freezing window is observed at WTB margin, where freezing initiates at $0\text{ }^{\circ}\text{C}$ and continues to $-2.7\text{ }^{\circ}\text{C}$. On average, the freezing window begins at $0\text{ }^{\circ}\text{C}$ and extends to $-0.8\text{ }^{\circ}\text{C}$. For subsequent quantifications of freeze event frequency and freezing rate, we define the freezing window as 0C to -0.8 C , based on these observations.

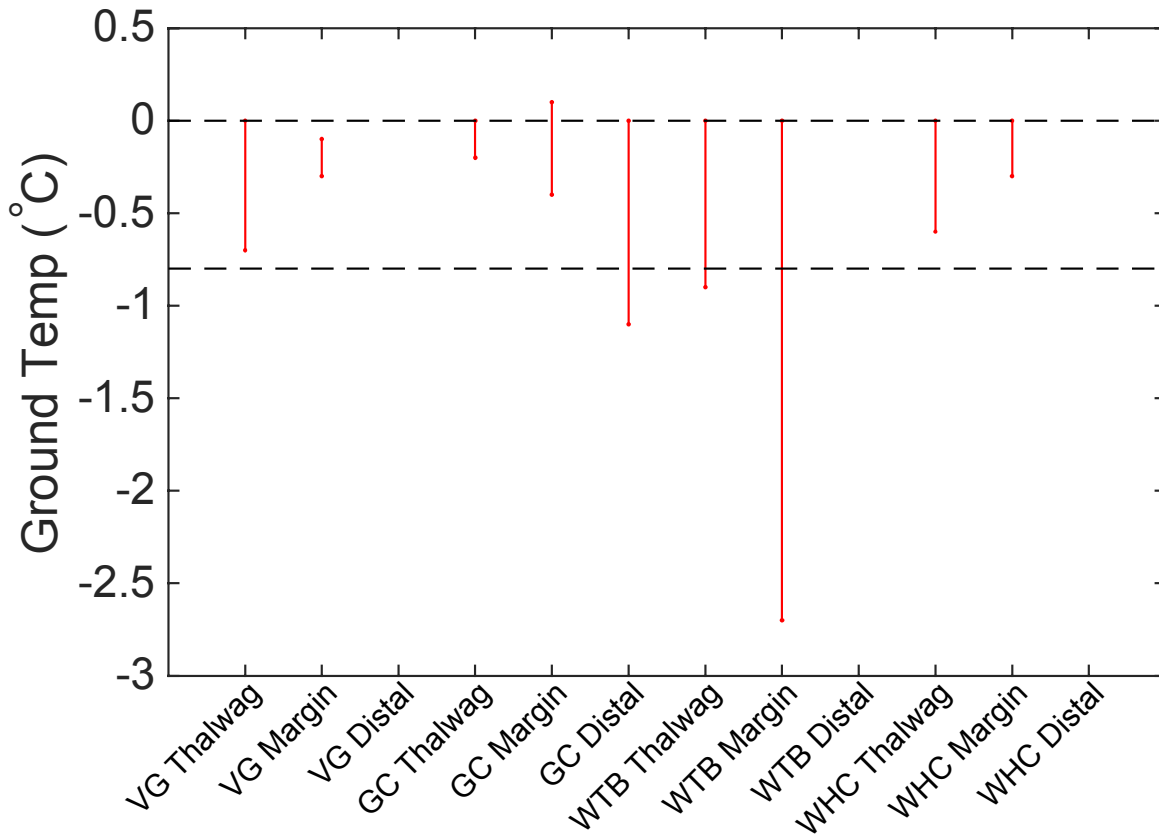


Figure 3.9: Freezing windows at all ALMS locations calculated by moisture phase composition curve thresholds. Red lines show the width of the thermal window at specific ALMS sites, whereas black dashed lines show the average width of the freezing window among all sites. The freezing window was not calculated at several distal sites because soil moisture was too low to generate soil moisture phase composition curves.

Between 2 and 41 freeze-events were observed at active layer sites during the period of observation (Figure 3.10). With the exception of GC and VG, the number of freeze-events increased across the thalweg, margin, distal transect. The frequency of freeze-events at a location is negatively related to the average VWC of that location (Figure 3.11). The frequency of freeze-events is also sensitive to a threshold VWC of $0.1 \text{ m}^3/\text{m}^3$. The number of freeze-events increases abruptly at sites where the average summer water content is below $0.1 \text{ m}^3/\text{m}^3$.

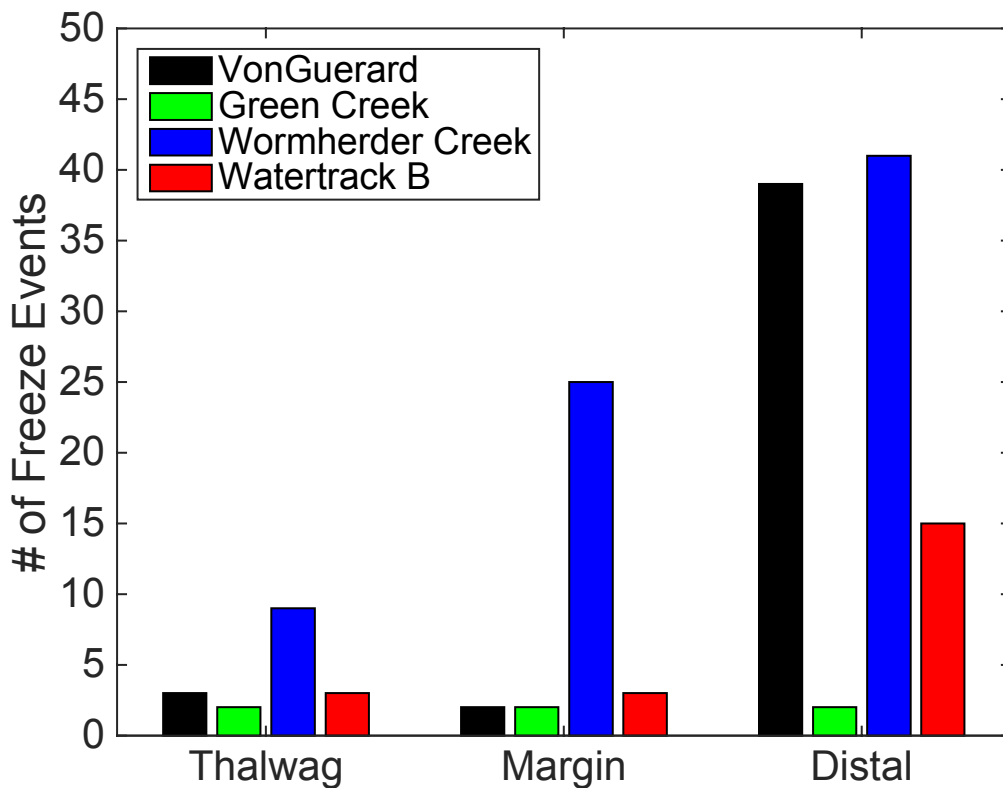


Figure 3.10: Number of freeze events recorded between January 2014 and February 2016 at active layer monitoring sites.

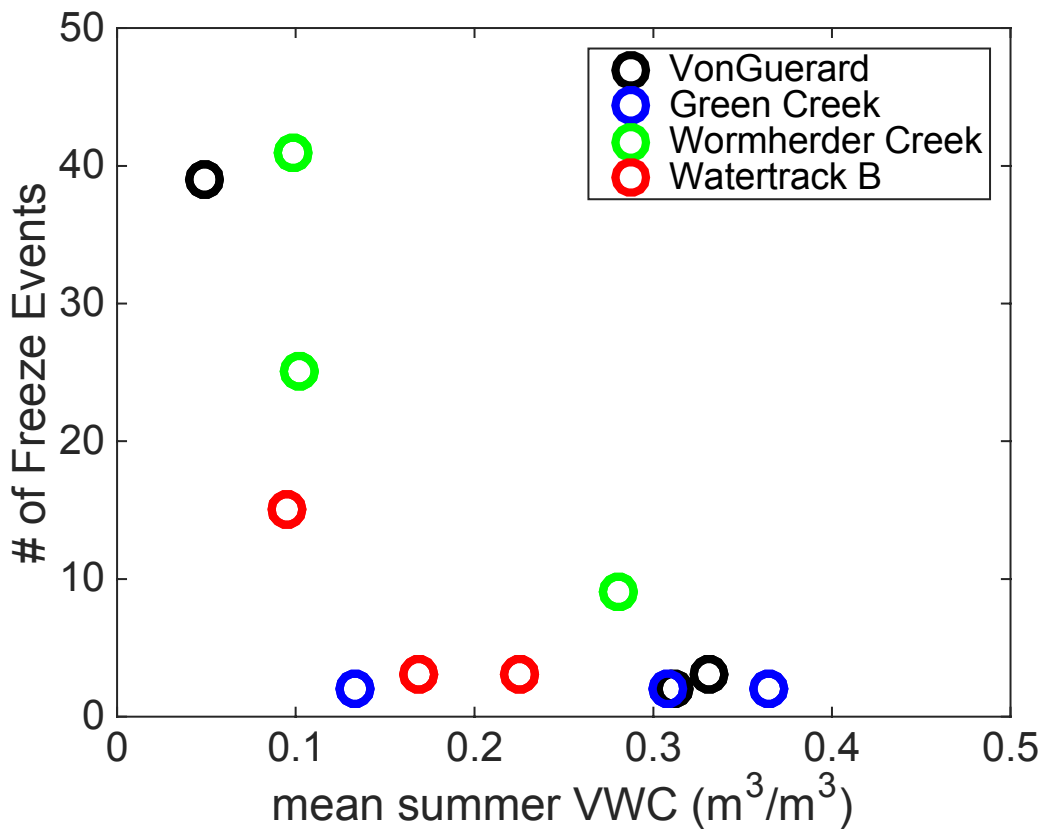


Figure 3.11: Number of freeze-events at 10cm as a function of mean austral summer (December – February) volumetric water content at 15 cm.

Among all ALMSs and all 3 locations, active layer freezing rates (Equation 3.1) ranged from 0.002 – 1.131 °C/hr (Figure 3.12). Freezing rate is negatively related to average 5-day antecedent VWC. Wetter soils freeze more gradually than dry soils. However a VWC threshold is also apparent a 0.1 m³/m³. Below volumetric water contents of 0.1 m³/m³, freezing rates increase abruptly.

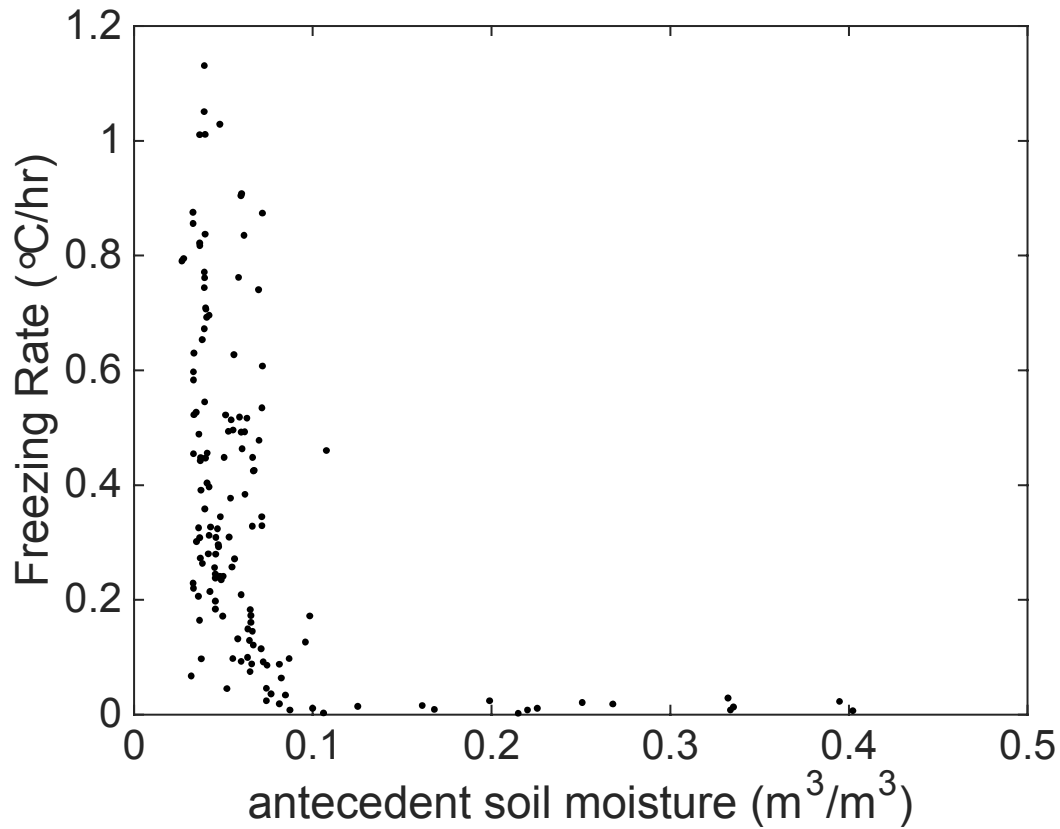


Figure 3.12: 10 cm Freezing rate plotted as a function of 15 cm antecedent soil moisture

3.5 DISCUSSION

Incremental climate warming in the McMurdo Dry Valleys can result in a disproportionately large increase in the abundance of liquid water across the landscape, due to glacier melt [Doran *et al.*, 2008], snowmelt [Gooseff *et al.*, 2003b] and permafrost degradation [Levy *et al.*, 2013]. As such, warmer air temperatures tend to increase soil moisture content across the landscape. This was illustrated by a sustained multi-year increase in soil moisture following an anomalously warm summer (December 2001 – January 2002) in the MDVs, which caused record amounts of glacier melt [Barrett *et al.*, 2008].

In order to understand the thermodynamic consequence of higher soil moisture under a warmer climate, I analyzed here active layer temperature and soil moisture data across natural wetness gradients adjacent to streams and watertracks. I hypothesized in the introduction of this chapter, that increased soil moisture will lower the frequency and rate of freeze-events in Dry Valley soils. Based on our results, we are unable to refute the hypothesis. Active layer data show that soil moisture has a strong influence on the frequency and rate of freeze-events. Freeze frequency and freezing rate are highly sensitive to a VWC threshold of $0.1 \text{ m}^3/\text{m}^3$. At $\text{VWC} < 0.1 \text{ m}^3/\text{m}^3$, the frequency and rate of freeze-events increases abruptly, However at $\text{VWC} > 0.1 \text{ m}^3/\text{m}^3$ soils are less likely to experience more than one freeze event per year and freeze gradually ($<0.03 \text{ }^\circ\text{C/hr}$).

The $0.1 \text{ m}^3/\text{m}^3$ soil moisture threshold separating frequently and rapidly freezing soils from seldom and gradually freezing soils may be explained by the soil latent heat content, which

is to soil moisture. A zero curtain effect, where soil temperatures at multiple depths remain near 0 °C for a prolonged duration of time as latent heat is released/consumed during freezing/thawing [Outcalt *et al.*, 1990], is observed in wetter soils and not observed in the driest soils at ALMSs. For example, at VG ALMS during February 2015, a pronounced zero curtain is observed at the margin site, but not detected at the distal site (Figure 3.13). The soil moisture, and thereby latent heat content, at the margin site is 7 times greater than at the distal site prior to this specific freeze event. The presence of a zero curtain drastically reduces freezing rate, because temperature changes are slight (the width of the freezing window), relative to the duration of time required to release the latent heat of fusion. Dry soils lack enough latent heat content to exhibit zero curtain dynamics, and therefore freeze much more rapidly than wet soils. Similarly, freeze frequency is much lower at $VWC > 0.1 \text{ m}^3/\text{m}^3$ because the release of latent heat buffers soil temperature from energy fluxes at the soil surface. As latent heat is released, the soil profile remains isothermal, which suppresses vertical conductive heat transfer. Conversely, in the absence of latent heat release, variability in surface energy fluxes may force ground temperature to repeatedly cycle above and below the freezing window limits.

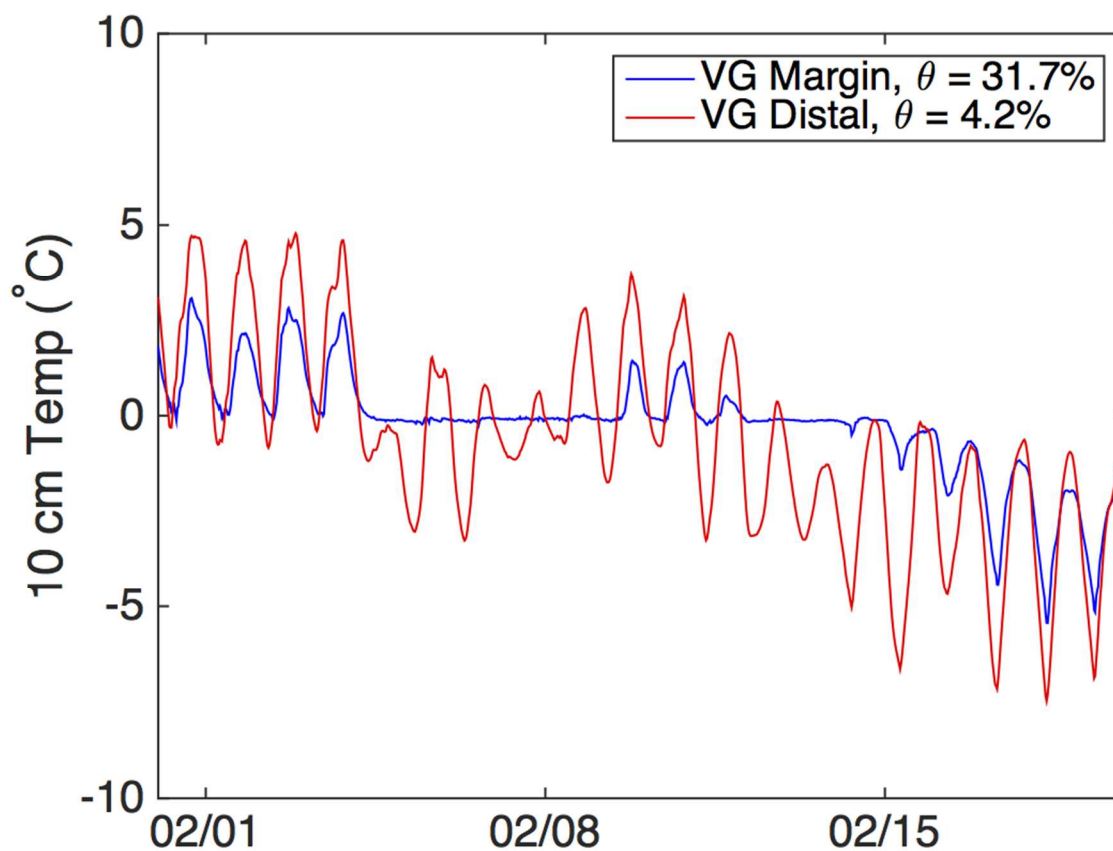


Figure 3.13: A pronounced “zero-curtain”, where ground temperature remains nearly constant at 0 C for an extended duration of time, is apparent at VG margin but not detected at VG distal. Zero-curtains are caused by the release of latent heat. Dry soils lack sufficient moisture to exhibit a zero-curtain dynamic, and therefore freeze more frequently and more rapidly than wet soils.

The frequency of freeze events is known to influence life cycle and population dynamics of *S. lindsayae* [Knox *et al.*, 2015]. In particular, a high annual frequency of freeze-events results in prolonged periods of stunted growth and decreased reproductive success. Knox *et al.* (2015) hypothesized that freeze tolerance/avoidance strategies have a metabolic opportunity cost of growth and reproduction. Freeze tolerance and avoidance strategies mandate the enhanced transcription of stress-related genes to facilitate the production of stress-tolerance proteins [Adhikari *et al.*, 2010]. Active layer temperature and soil moisture data in this study show that marginal increases in soil moisture can drastically alter the frequency of freeze-events. This

result indicates that higher soil moisture will reduce metabolic costs on soil invertebrates, favoring higher growth rates and enhanced reproductive success.

However, the ecological benefits of increased soil moisture are likely to be species specific. Although all nematode species may benefit from a reduced frequency of freeze-stress, certain species are more likely than others to thrive in a wetter environment. Long term observations of nematode abundance and diversity show that *S. lindsayae* prefers dry soils, whereas *P. antarcticus* and *E. antarcticus* prefer wetter soils [Treonis *et al.*, 1999; Barrett *et al.*, 2008; Simmons *et al.*, 2009]. Therefore, *P. antarcticus* and *E. antarcticus* may benefit more from an increase of soil moisture than *S. lindsayae*. However, the results of this study also show that slight increases in soil moisture from below to above $0.1 \text{ m}^3/\text{m}^3$ are needed to drastically lower the frequency of freeze events. It is possible that this VWC threshold is low enough to sustain *S. lindsayae* populations, while also reducing the frequency of freeze-events.

The results of this study also show that freezing rate exhibits a threshold response to soil moisture (Figure 3.10). At $\text{VWC} > 0.1 \text{ m}^3/\text{m}^3$, freezing rates are more gradual than at $\text{VWC} < 0.1 \text{ m}^3/\text{m}^3$. Freezing rate is believed to favor different physiological strategies for dealing with freeze-stress [Wharton *et al.*, 2002; Wharton, 2003]. In gradually freezing soils, cryoprotective dehydration is favored. During cryoprotective dehydration, organisms surrounded by ice dehydrate rather than freeze [Holmstrup *et al.*, 2002]. Dehydration is driven by vapor pressure gradients between super cooled water inside the body cavity and surrounding ice. However, in more rapidly freezing soils with sufficient water, inoculative freezing may be unavoidable. In this case, anti-freeze and recrystallization inhibiting proteins are needed to prevent the fatal

growth of ice crystals within the body cavity. In very dry soils, which also freeze very rapidly, desiccation stress triggers anhydrobiosis.

Results of this study show that the nature of freeze stress on the soil habitat may vary over small spatial scales. For example, at VG the distal location was subjected to 25 total freeze events and an average freezing rate of 0.5 °C/hr, compared to two total freeze events and an average freezing rate of 0.02 °C/hr at margin and thalweg locations (Figure 3.8 and Figure 3.10). Coincident with a drastic change in habitat freeze dynamics over a scale of several tens of meters, ecosystem diversity and abundance also changes. *Treonis et al.*, (1999) showed that nematode communities shifted from *P. antarcticus* and *E. antarcticus* dominated to *S. lindsayae* dominated across a 32 m transect between a stream thalweg and distal soils. This shift in community composition may be linked to differences in physiological stress tolerance mechanisms employed by each nematode species.

Laboratory and field evidence show that hydrophilic nematodes, *P. antarcticus* and *E. antarcticus*, are capable of anhydrobiosis as well as other freeze-tolerance strategies, such as the creation of anti-freeze and recrystallization inhibiting proteins. However, the hydrophobic nematode, *S. lindsayae*, is believed to employ anhydrobiosis extensively. Different freezing rates between wet and dry soils shown in this study may explain why *S. lindsayae* is more commonly found in dry soils. Very dry and rapidly freezing soils may favor anhydrobiosis because desiccation stress precedes freezing stress. Conversely, gradually freezing wet soils require organisms to either cryoprotectively dehydrate or survive inoculative freezing. *P. antarcticus* and *E. antarcticus* are perhaps better physiologically suited to deal with freezing stress in wetter

soils, than *S. lindsayae*. Results of this work show that freezing rate is tightly coupled to soil moisture and exhibits a threshold at $0.1 \text{ m}^3/\text{m}^3$. Therefore, future changes in soil moisture anticipated under a warmer climate will be an important characteristic affecting species distribution. Physiologically versatile organisms, such as *P. antarcticus* and *E. antarcticus* may be better suited for survival in a wetter soil habitat.

3.6 CONCLUSION

An increase in soil moisture is anticipated as a consequence of climate warming in the MDVs. To understand how an increase in soil moisture will alter soil thermodynamics, I analyzed active layer temperature, soil moisture, and specific conductance data along natural wetness gradients adjacent to fluvial features. Observations show soil moisture has little influence on mean temperature or the duration of time spent above freezing. However, soil moisture exerts a strong control on the frequency and rate of freeze-events. Over a two-year period, soils at $\text{VWC} < 0.1 \text{ m}^3/\text{m}^3$ experienced between 15 and 41 freeze-events, compared to soils at $\text{VWC} > 0.1 \text{ m}^3/\text{m}^3$ that experienced between 2 and 9 freeze-events (Figure 3.11). Similarly, soil moisture plays a strong control on freezing rate. These data show that dry soils freeze more rapidly than wet soils. Soils at $\text{VWC} < 0.1 \text{ m}^3/\text{m}^3$ experienced freezing rates of $0.007 - 1.131 \text{ }^\circ\text{C}/\text{hr}$, whereas soils at $\text{VWC} > 0.1 \text{ m}^3/\text{m}^3$ experienced freezing $< 0.029 \text{ }^\circ\text{C}/\text{hr}$ (Figure 3.12). Threshold soil moisture content of $0.1 \text{ m}^3/\text{m}^3$ is an important control on both freeze-frequency and freezing rate.

The frequency and rate of freeze events is a known control on nematode lifecycle and population dynamics. Furthermore, soil moisture is a strong control on invertebrate species diversity in MDV soils. Wetter soils, which freeze less frequently and more gradually than dry soils, may favor hydrophilic nematode species capable of cryoprotective dehydration and surviving inoculative freezing (*P. antarcticus* and *E. antarcticus*) over hydrophobic nematode species that are thought to rely heavily upon anhydrobiosis specialists (*S. lindsayae*).

3.7 APPENDIX

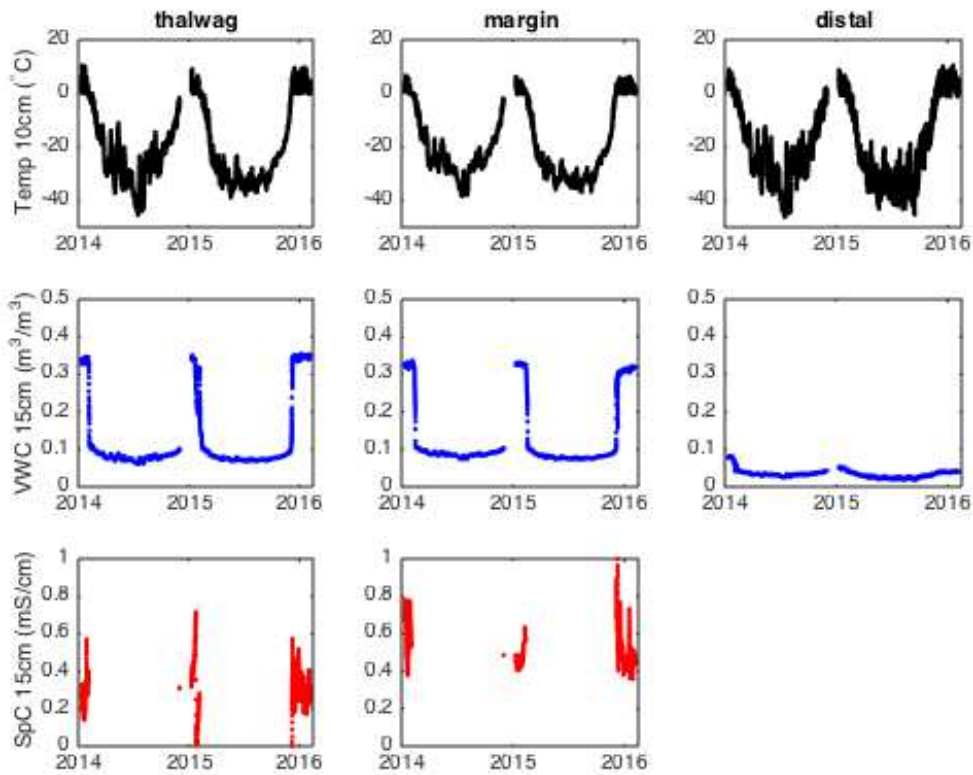


Figure 3.A1: 10cm temperature, and 15 cm specific conductance and volumetric water content data at Von Guerard Stream between January 12, 2014 and February 4, 2016 (753 days).

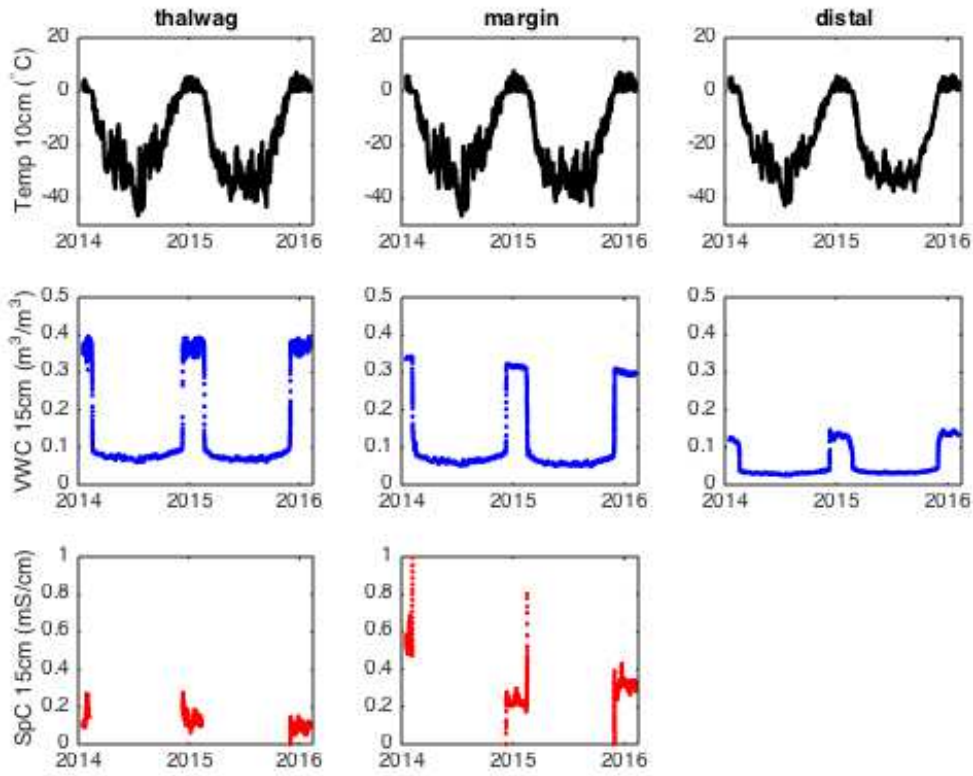


Figure 3.A2: 10cm temperature, and 15 cm specific conductance and volumetric water content data at Green Creek between January 16, 2014 and February 4, 2016 (748 days).

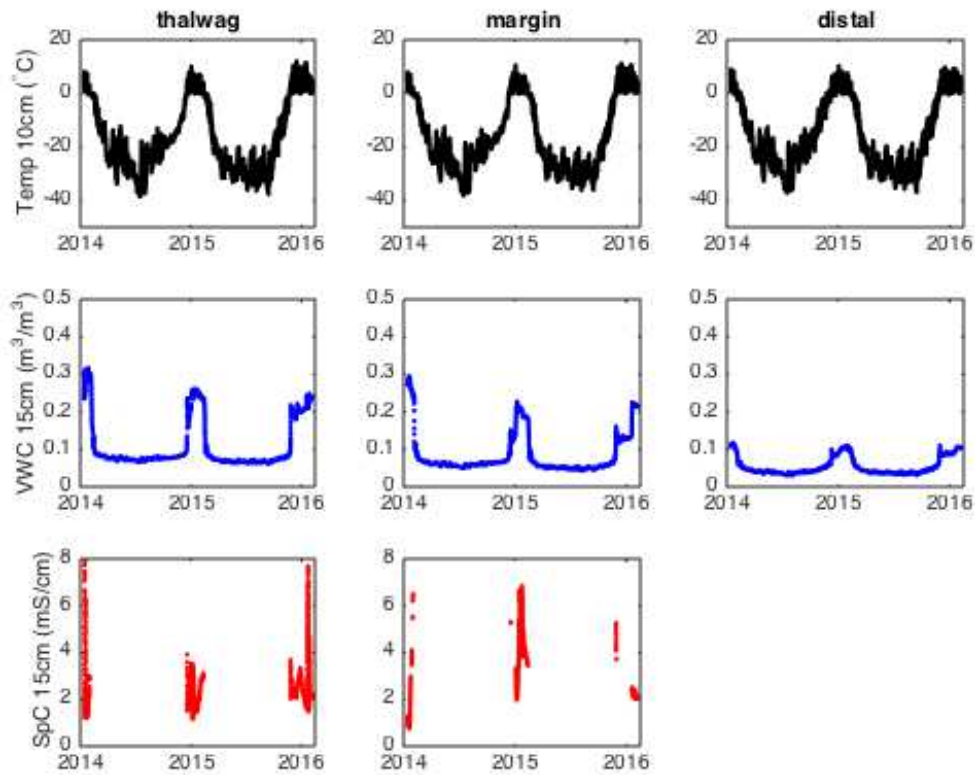


Figure 3.A3: 10cm temperature, and 15 cm specific conductance and volumetric water content data at Watertrack B between January 14, 2014 and February 4, 2016 (751 days).

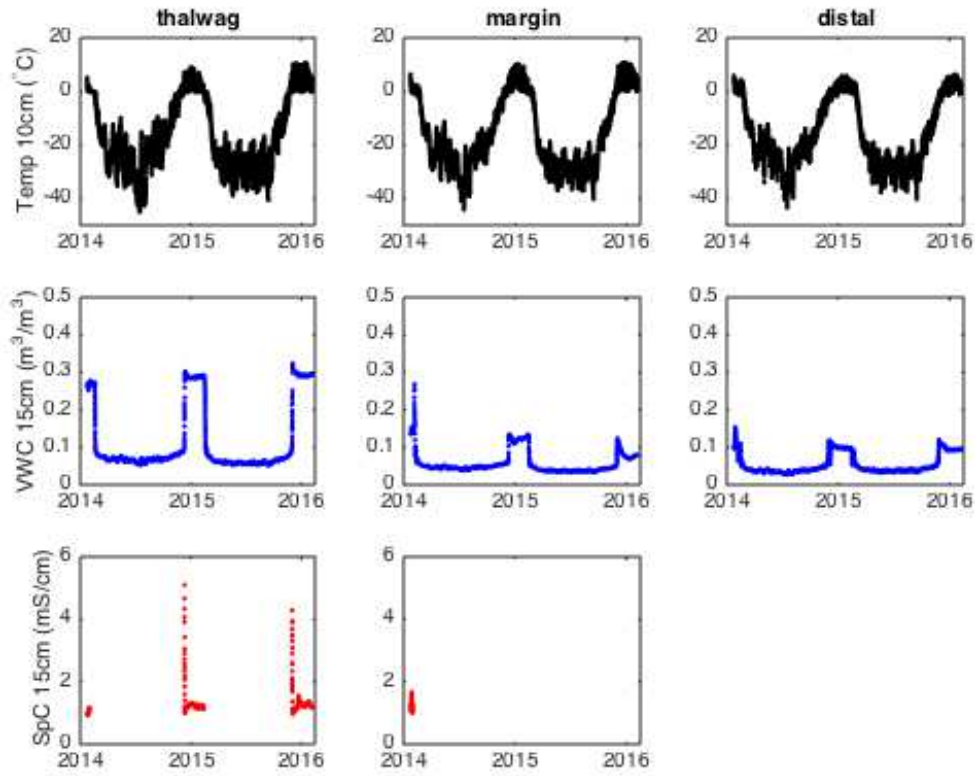


Figure 3.A4: 10cm temperature, and 15 cm specific conductance and volumetric water content data at Wormherder Creek between January 23, 2014 and February 4, 2016 (741 days).

CHAPTER 4: The thermodynamic regime of Antarctic soils under a warmer and wetter future

4.1 INTRODUCTION

The McMurdo Dry Valleys (MDVs) ecosystem is particularly sensitive to small variations in climate, specifically air temperature. Because summer air temperatures are near the freezing point of water, slight increases in air temperature cause disproportionately large increases in the abundance of liquid water across the landscape [*Kennedy, 1993; Fountain et al., 1999; Doran et al., 2008*]. Warming air temperatures can increase glacial melt and streamflow, contribute to rising lake levels, and degrade ice-rich permafrost [*Barrett et al., 2008; Doran et al., 2008; Fountain et al., 2014*]. As such, soil habitats adjacent to lakes, ponds and streams, and above ice-rich permafrost are likely to experience an increase in soil moisture under a warmer climate regime.

In Chapter 3, I investigated the effect of soil moisture on the freezing regime of habitable soils. Observations of soil temperature and volumetric moisture content supported the hypothesis that wetter soils freeze less frequently and more gradually than drier soils. However, the data and analyses conducted in Chapter 3 were largely focused on the sub-surface. That is, sub-surface temperature dynamics were empirically explained as a function of soil moisture. A significant question still remains: How does the combination of soil moisture *and* land-atmosphere energy fluxes control the thermal regime of active layer soils? To understand how the thermal regime of

the active layer habitat will change in the future, it is necessary to acknowledge both surface and sub-surface dynamics.

In this chapter I use a numerical modeling approach to interrogate the combined influence of land-atmosphere energy fluxes and soil moisture on the thermal regime of the soil habitat. Chapter 3 did not develop a physically-based explanation of how soil moisture and energy fluxes at the soil surface control the active layer thermal regime. I here employ a numerical model is used to provide a mechanistic explanation of how soil moisture affects the thermal regime of the habitable soil zone (0 – 15 cm) and the depth of active layer soils. I use numerical simulations to explicitly test how the combination of warmer air temperatures and wetter soils, expected under future climate scenarios, will alter the thermal regime of active layer soils.

4.2 METHODS & STUDY SITE

4.2.1 Surface energy budget and subsurface thermal models

One-dimensional surface energy budget and subsurface thermal models are used to simulate active layer ground temperature. The surface energy budget is assumed to be a balance between radiation, sensible heat, and conduction

$$Q_h + (1 - \alpha)Q_{SW}^\downarrow + Q_{LW}^\downarrow - \sigma T_{sur}^4 = Q_c \quad (4.1)$$

where Q_h is the sensible heat flux (W/m^2), Q_{SW} is incident shortwave radiation (W/m^2), T_{sur} is the ground surface temperature (K), Q_{LW} is downwelling long wave radiation (W/m^2), σ is the

Stefan-Boltzmann constant ($\text{W/m}^2/\text{K}^4$), α is the albedo of the ground surface, and Q_c is the conductive heat flux (W/m^2).

Sensible heat flux is calculated through measurements of wind speed and the temperature gradient between the ground surface and near-surface air [Hinzman *et al.*, 1998; Ling and Zhang, 2004] as

$$Q_h = c_{air} \rho_{air} D_h (T_a - T_{sur}) \quad (4.2)$$

where c_{air} is the specific heat of air at constant pressure (J/kg/K), ρ_a is the density of air (kg/m^3), T_a is the air temperature (K) at height z_i (m) above the ground surface. The heat exchange coefficient, D_h , is calculated as

$$D_h = \frac{u \lambda^2}{\left[\ln \left(\frac{z_i}{z_0} \right) \right]^2} \quad (4.3)$$

where, u_z is wind speed (m/sec) and height z_i (m) above the ground surface, λ is the von Karman constant, 0.41, and z_0 is a surface roughness coefficient. We assume constantly neutral atmospheric conditions which allows (3) to hold at all times.

Ground heat conduction, Q_c , is governed by Fourier's Law as

$$Q_c = -k \frac{\partial T}{\partial z} \quad (4.4)$$

where z is depth below the ground surface (m), T is ground temperature (K) at depth z below the ground surface, k is thermal conductivity of the soil (W/m/K). The rate of change in ground temperature with time is governed by a conservation of heat

$$\frac{\partial T}{\partial t} = -\frac{1}{C} \frac{\partial Q_c}{\partial z} \quad (4.5)$$

where, C is the bulk volumetric heat capacity of the soil ($\text{J}/\text{m}^3/\text{K}$).

It is assumed that soil water freezes within a discrete temperature window, DT (K) [Anderson *et al.*, 2013]. As such, bulk thermal conductivity, k , and bulk volumetric heat capacity, C , depend on the phase of water in the soil matrix and therefore soil temperature. Thermal conductivity is expressed as

$$k = \begin{cases} k_f & T < T_f - DT \\ k_f + \frac{k_u - k_f}{DT} [T - (T_f - DT)] & T_f - DT < T < T_f \\ k_u & T > T_f \end{cases} \quad (4.6)$$

where, T_f is the upper limit of the freezing window (K), k_f is the thermal conductivity of a completely frozen soil, and k_u is the thermal conductivity of a completely thawed soil. Similarly, C is expressed as

$$C = \begin{cases} C_f & T < T_f - DT \\ C_f + L \left(\frac{\theta}{DT} \right) & T_f - DT < T < T_f \\ C_u & T > T_f \end{cases} \quad (4.7)$$

where, C_f is the volumetric heat capacity of a completely frozen soil, C_u is the volumetric heat capacity of a completely thawed soil, L is the latent heat of fusion ($3.337 \times 10^5 \text{ J}/\text{kg}$), and θ is the volumetric water content of the soil (m^3/m^3).

Frozen and thawed thermal bulk conductivity, k , and volumetric heat capacity, C , depend on the volumetric fractions of soil, water (liquid or ice), and air [Kersten, 1949]. Thawed or

frozen k is computed as a geometric mean of the conductivity of solid and ice/liquid volume fractions

$$k_{f/u} = k_{i/l}^\theta k_s^{(1-\phi)} k_a^{(\phi-\theta)} \quad (4.8)$$

where $k_{i/l}$ is the thermal conductivity of ice or water, k_a is the thermal conductivity of air, and ϕ is soil porosity (m^3/m^3). Thawed and frozen C is computed as a weighted sum of the heat capacity of solid and ice/liquid volume fractions

$$C_{f/u} = C_{i/l}(\theta) + C_s(1-\phi) + C_a(\phi-\theta) \quad (4.9)$$

where $C_{i/l}$ is the heat capacity of ice or liquid and C_a is the heat capacity of air.

4.2.2 Meteorological Forcing Data

Eight meteorological stations in the Taylor Valley measure air temperature, wind speed, incident shortwave (SW) radiation, and incident long wave (LW) radiation. These data are needed to inform the surface energy budget. Because met data is not collected at ALMs, MicroMet [Liston and Elder, 2006], a quasi-physically based meteorological interpolation model, is used to estimate forcing data at each ALMS. MicroMet uses a Barnes interpolation scheme [Barnes, 1964] and a 250 meter DEM to interpolate observations between met stations, and account for topographic influences on air temperature and SW radiation (i.e. lapse rate and topographic shading). MicroMet has been used previously to interpolate met observations in the Taylor Valley by Hoffman *et al.* [2008 and 2016] and a detailed methodological review of MicroMet is provided by Liston and Elder [2006].

4.2.3 Study Site

The surface energy budget model is used to simulate ground temperature at margin and distal locations of Von Guerard ALMS (VG), Green Creek ALMS (GC), Watertrack B ALMS (WTB), and Wormherder Creek ALMS (WHC) (Figure 3.1 – Figure 3.5). A more detailed description of ALMSs, and Taylor Valley soil characteristics can be found in Chapter 3. Ground temperature at thalweg sites is not simulated because heat advection is likely to occur in stream and water track channels and heat advection is not accounted for in this ground temperature model.

4.3 RESULTS

4.3.1 Meteorological Data

MicroMet is used to estimate air temperature, SW and LW radiation, and wind speed at ALMSs. MicroMet outputs are shown for VG (Figure 4.1), and the output for other sites can be found in the Appendix (Figures 4.A1 – 4.A3). Air temperature follows a seasonal cycle, where maximum temperature occurs between December and January (3 – 8 °C) and minimum temperature occurs sometime between June and August (-40 - -45 °C) (Figure 4.1A). Air temperature is more variable during winter months, relative to summer months, due the influence of adiabatically warmed air masses sweeping through Taylor Valley during katabatic wind storms [Marshall and Turner, 1997; Nylén et al., 2004; Speirs et al., 2010]. Incident shortwave radiation shows a strong seasonal cycle (Figure 4.1B). From September through April, the sun is

above the horizon, and SW radiation fluxes are greater than zero. Between late October and early March, the sun is constantly above the local horizon and SW radiation flux is consistently greater than zero. Peak radiation ($\sim 700 - 800 \text{ W/m}^2$, depending on the site) occurs in late December. Between late April and early September, incident SW radiation is zero because the sun remains below the local horizon. Incident LW radiation ranges from $100 - 300 \text{ W/m}^2$ and is highest during the austral summer, when air temperature is warmest (Figure 4.1B). Wind speed is highly variable, but generally highest during the austral winter (Figure 4.1C). Katabatic storm events can increase wind speeds $> 20 \text{ m/sec}$ for shorter periods of time and these events usually occur during winter months.

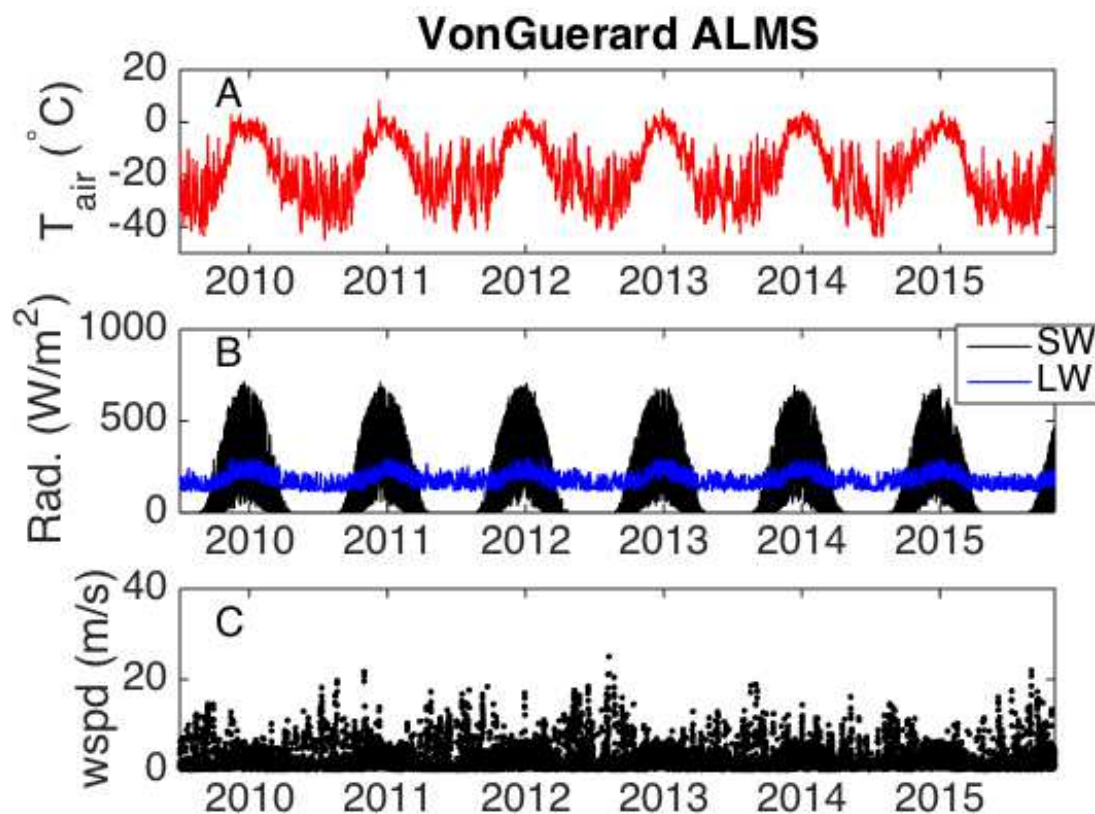


Figure 4.1: MicroMet simulated air temperature (A), SW and LW incident radiation (B), and wind speed (C) at Von Guerard ALMS. These data are needed to inform the surface energy budget model.

A Degree-day is a temporally integrative measure of above freezing air temperatures. At ALMSs, between 5.12 – 71.61 annual degree-days above freezing are observed over the period of record considered in this study (Figure 4.2). Each site exhibits strong inter-annual variability in degree-days above freezing. 2014/2015 was the coolest year, while 2014 was the warmest year. Between sites, a consistent pattern is observed, where degree-days above freezing at WHC > GC > VG > WTB.

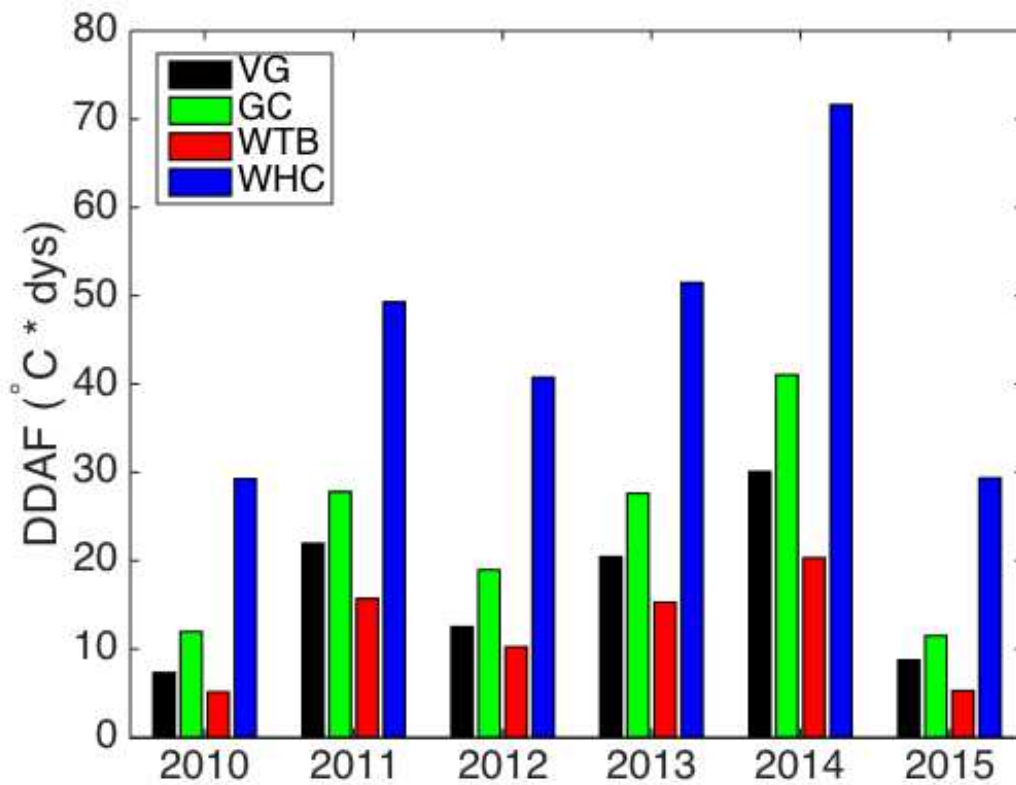


Figure 4.2: Air temperature degree-days above freezing (DDAF) at ALMSs. Continuous air temperature data was estimated at ALMSs with MicroMet.

Strong between-site variability of annual cumulative SW radiation is observed at ALMSs between 2009 and 2015 (Figure 4.3). For all years except 2013 and 2015, VG is the sunniest site. This may be due to its location in the middle of Fryxell Basin where topographic shading is

minimal [Dana *et al.*, 1998]. Inter annual variability in SW radiation is due to the influence of cloud cover. The most pronounced inter-annual variability is observed at WHC. WHC received the least incident SW between 2010 and 2012, however between 2013 and 2015 WHC was one of the sunniest sites. This indicates that WHC may be more affected by inter-annual variability in cloud cover than other sites.

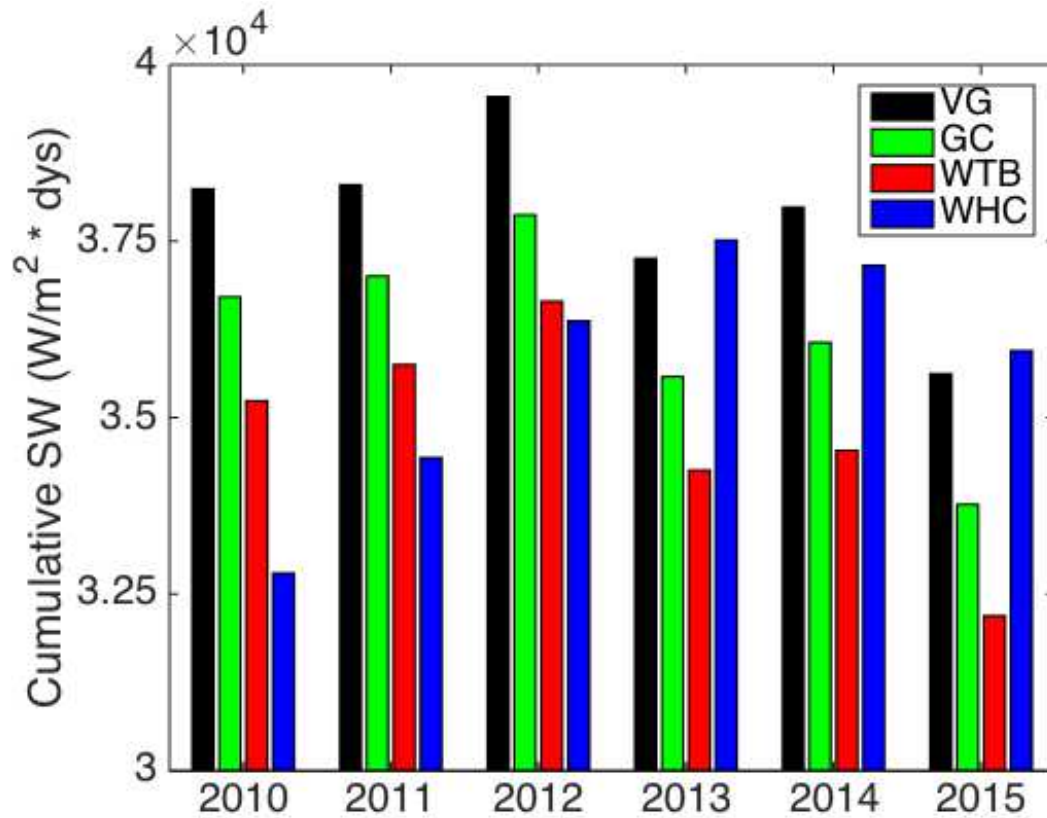


Figure 4.3: Cumulative annual solar radiation at ALMSs, as computed from MicroMet estimates.

The distribution of wind speed among ALMSs shows that wind speeds between 0 – 1 m/sec are most common, while progressively higher wind speeds are less common (Figure 4.4). GC and VG are the calmest sites, while WTB and WHC are windier. The probability of high wind events >5 m/sec is highest at WHC and WTB, as indicated by heavy PDF tails and low PDF peaks, relative to GC and VG. WHC is by far the windiest site. At WHC, wind speed

exhibits a slightly bimodal distribution with a primary peak at 0.9 m/sec and a secondary peak at 5.2 m/sec.

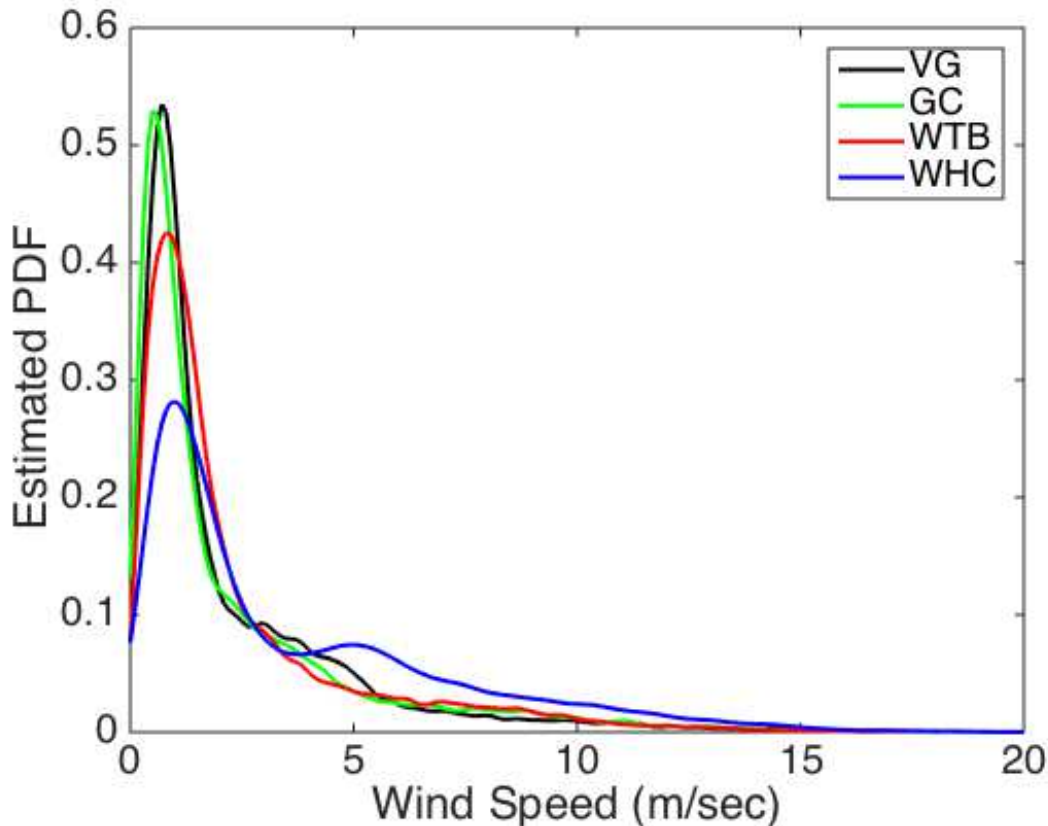


Figure 4.4: Estimated PDF of wind speed at ALMSs. “Estimated”, indicates that PDFs were generated with a kernel smoothing function applied to all available wind speed data between July 1, 2009 and July 1, 2015. Wind speed was approximated at each station using MicroMet.

4.3.2 Ground temperature modeling results

Albedo, α , and surface roughness, z_0 , were manually adjusted to achieve the best visual fit to observed ground temperature at 10cm (Table 4.1). Best-fit α ranged from 0.01 – 0.03 and best-fit z_0 ranged from 0.01 – 0.02 m. Thermal conductivity of soil solids, k_s was set equal to 3 W/m/K at all sites, a value slightly higher than is typical for bedrock (2.2 W/m/K), according to *Lunardini* [1981]. Porosity, ϕ_0 , was set to the maximum volumetric soil moisture observed at

corresponding ALMS thalweg locations (Figure 3.A1 – Figure 3.A4). It is assumed that maximum soil moisture at thalweg locations represents a near saturated condition, and is therefore a good estimate of porosity. Further, this mandates the assumption that porosity is similar among thalweg, margin, and distal locations at each ALMS. Soil moisture, θ , was fixed at the maximum soil moisture observed at each location (distal and margin). However, at VG distal, θ was set to $0.01 \text{ m}^3/\text{m}^3$, lower than the observed soil moisture range of $0.04 - 0.08 \text{ m}^3/\text{m}^3$. At VG distal, a lower soil moisture value produced a much better fit to observed data. Objective quantifications of model fit indicate satisfactory model performance at all sites. Nash Sutcliffe Efficiency (NSE) ranged from $0.92 - 0.98$ and RMSE ranged from $2.21 - 3.60 \text{ }^\circ\text{C}$ (Table 4.2).

Table 4.1: Best-fit energy balance model parameters. Model parameters were manually calibrated to achieve the best fit to 10cm ground temperature observations

ALMS	location	α	z_0 (m)	k_s (W/m/K)	θ (m^3/m^3)	ϕ_0 (m^3/m^3)
VG	margin	0.01	0.01	3	0.35	0.35
	distal	0.01	0.01	3	0.01	0.35
GC	margin	0.03	0.018	3	0.25	0.25
	distal	0.03	0.015	3	0.12	0.25
WTB	margin	0.01	0.01	3	0.18	0.25
	distal	0.01	0.01	3	0.10	0.25
WHC	margin	0.01	0.02	3	0.25	0.35
	distal	0.03	0.02	3	0.16	0.35

Table 4.2: Model fit metrics, Nash-Sutcliffe Efficiency (NSE) and Root Mean Squared Error (RMSE), quantifying the ability of the model to simulate ground temperature at 10cm depth.

ALMS	location	NSE	RMSE ($^\circ\text{C}$)
VG	margin	0.92	3.61
	distal	0.98	2.21
GC	margin	0.96	2.75
	distal	0.94	3.27
WTB	margin	0.95	2.65
	distal	0.95	2.72
WHC	margin	0.96	2.56
	distal	0.94	2.97

Simulated and observed ground temperature for the 2014/2015 austral summer (November 1 – March 1) is shown for VG ALMS (Figure 4.5 and Figure 4.7). Simulated versus observed ground temperature data for GC, WBT, and WHC are shown in the Appendix (Figure 4.A4– Figure 4.A9). At VG, model predictions over estimate ground temperature during the November and early December. The over-prediction of early summer ground temperature is more severe at the margin site, compared to the distal site (Figure 4.6 and Figure 4.8). This is likely due to the insulating influence of snow [Gooseff *et al.*, 2003b], which is not accounted for in the surface energy balance model used here. During January, and February, model predictions more closely match observed ground temperature.

At VG margin, a distinct zero-curtain is observed at 10cm, where ground temperature remains isothermal near 0 °C as soil pore water freezes (Figure 4.5). The model is capable of capturing this dynamic by releasing latent heat within the freezing window. Conversely, at the drier distal site, no zero curtain is observed (Figure 4.7). The model is equally capable of capturing more rapid and frequent freeze dynamics at the drier VG distal site, where the lack of liquid water limits the release of latent heat. However, θ at VG distal needed to be lowered below observed soil moisture at this site in order to best match observations. Higher θ values at VG distal resulted in a pronounced zero curtain, which is not observed in observed 10 cm ground temperatures.

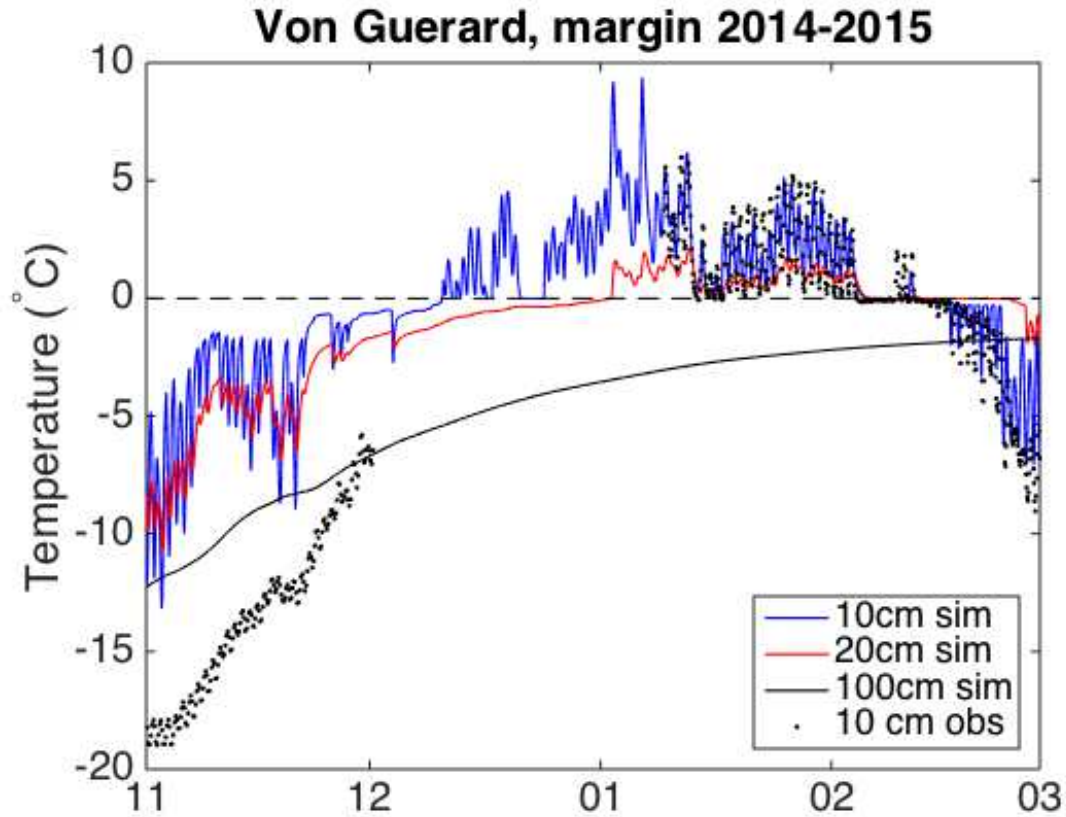


Figure 4.5: Simulated and observed ground temperature at VG ALMS margin site between November 2014 and March 2015. No observations are available between December and mid January due to a sensor malfunction.

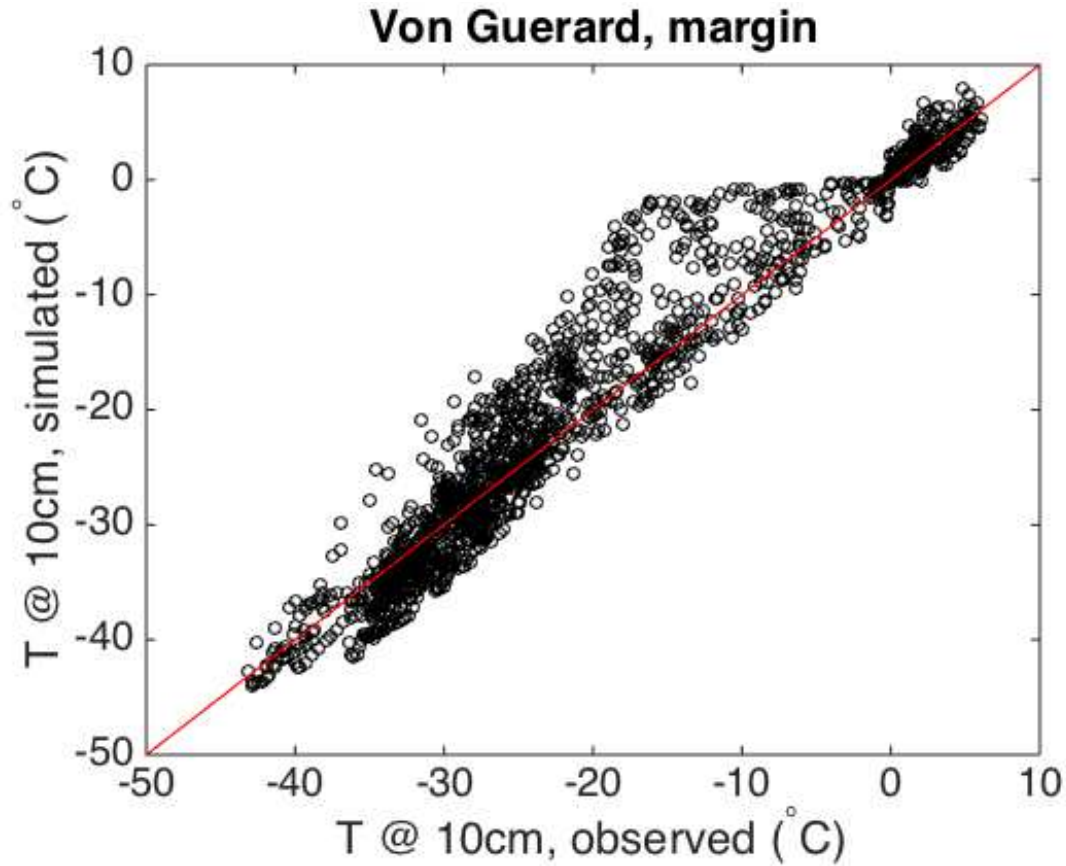


Figure 4.6: Simulated and observed 10cm ground temperature at VonGuerard margin site. All available ground temperature observations are used and the 1:1 line is shown in red. Simulations over predict observed temperatures between -20 and 0 °C. This over prediction corresponds to spring and early austral summer months (October, November, early December), when snow cover likely insulates shallow ground temperatures.

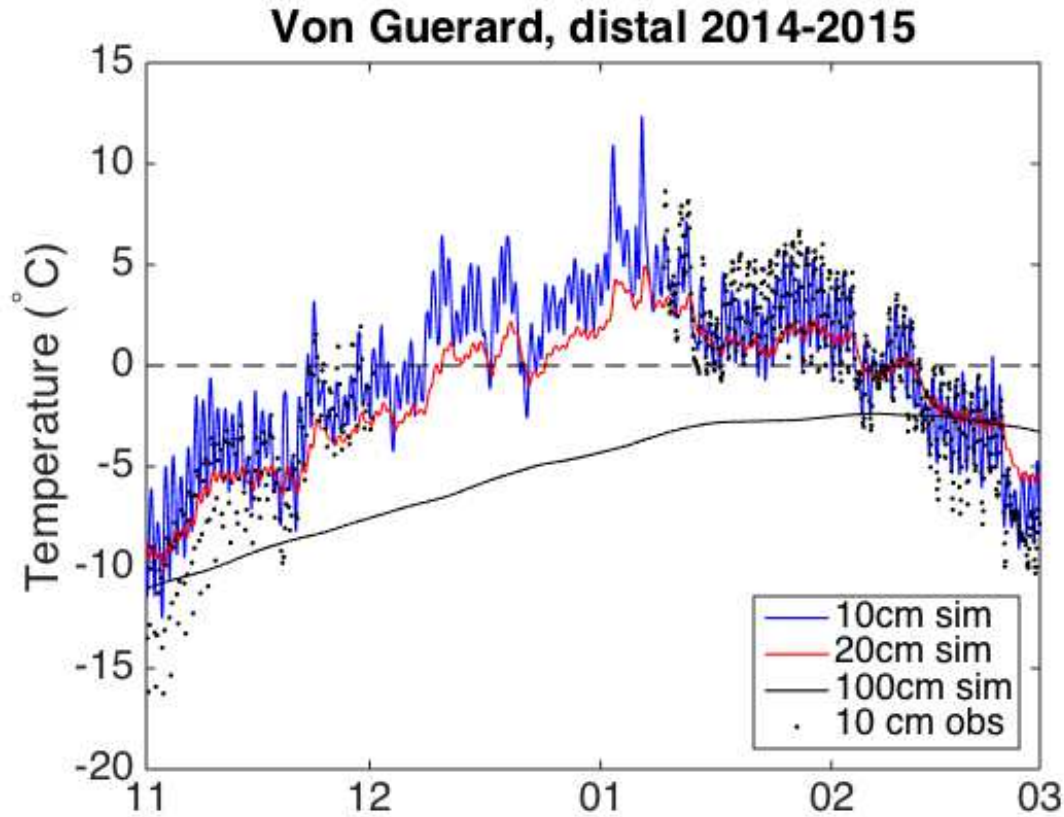


Figure 4.7: Simulated and observed ground temperature at Von Guerard ALMS distal site between November 2014 and March 2015. No observations are available between December and mid January due to a sensor malfunction. Best fitting soil moisture at this site was $0.01 \text{ m}^3/\text{m}^3$, which was less than the maximum observed 15 cm soil moisture at this site.

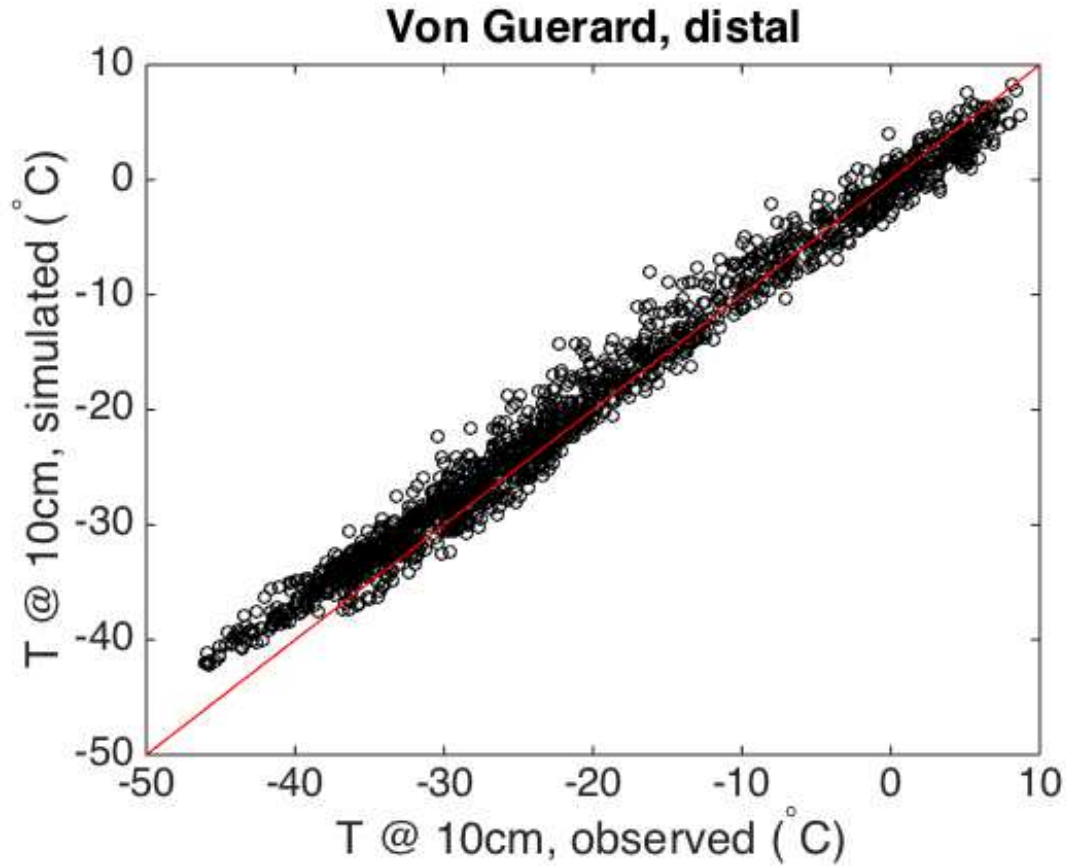


Figure 4.8: Simulated and observed 10cm ground temperature at VonGuerard distal site. All available ground temperature observations are used and the 1:1 line is shown in red.

Habitat temperature is partially controlled by energy fluxes between the ground surface and atmosphere. Surface energy fluxes for 2014/2015 at VG are presented in (Figure 4.9) and (Figure 4.10). Surface energy fluxes for remaining sites are shown in the Appendix (Figure 4.A10 –Figure 4.A15). A positive energy flux indicates energy transfer from the atmosphere to the ground and tends to warm the ground surface, while a negative energy flux indicates energy transfer from the ground to the atmosphere and tend to cool the ground surface.

At VG, net SW radiation is the largest positive energy flux during the austral summer, ranging from 0 to 750 W/m² (Figure 4.9 and Figure 4.10). During the austral winter, when the sun remains below the local horizon, net SW flux is consistently zero and sensible heat is the

largest positive flux. Conversely, during the austral summer, sensible heat is the most negative surface energy flux as the ground surface is warmer than overlying air. Sensible heat flux ranges from -450 to 210 W/m² throughout the year. Net LW radiation is mostly negative throughout the year, acting to cool the ground surface, although brief periods of net positive LW flux occur during the austral summer. Net LW radiation ranges between -300 to 15 W/m². Ground conduction oscillates between positive and negative on a daily basis during the austral summer. Ground conduction at VG ranges between -250 and 250 W/m². Conductive flux variability is greater at margin (Figure 4.9) sites than drier distal sites (Figure 4.10) due to the higher thermal conductivity of wet soils relative to drier soils.

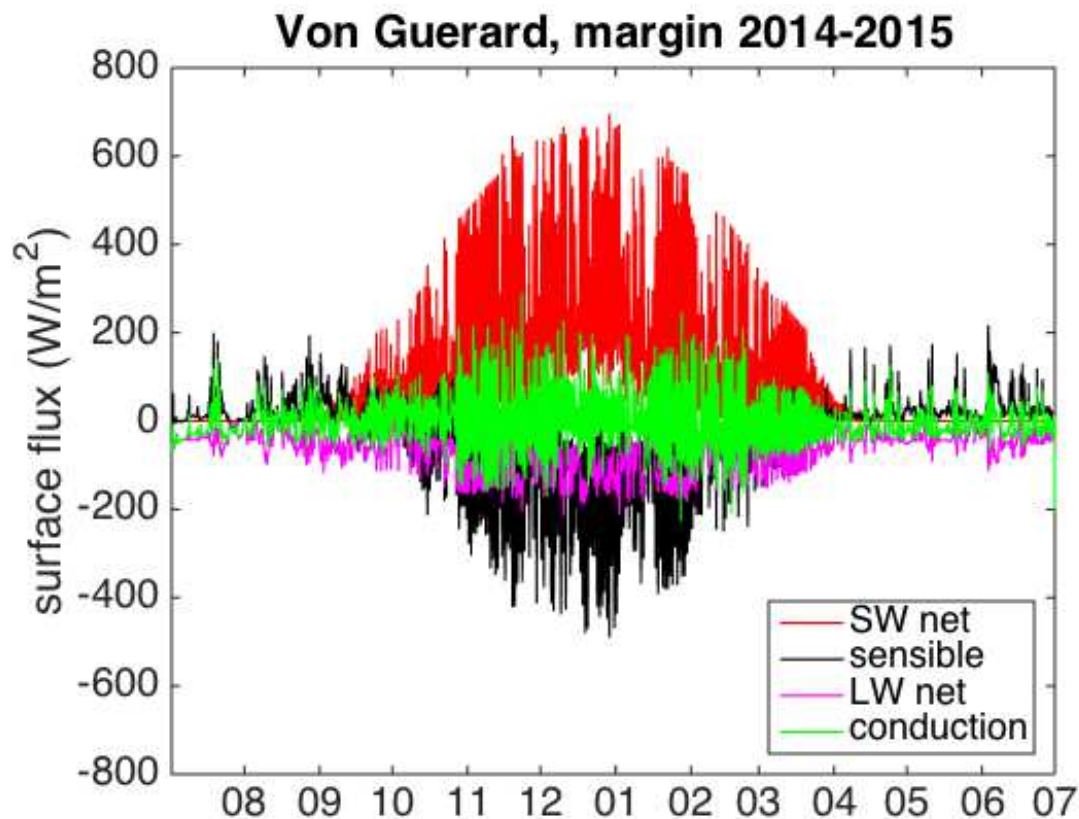


Figure 4.9: Surface energy fluxes at VG ALMS margin location between July 2014 and July 2015. Positive values indicate energy transfer into the ground surface from the atmosphere, and negative values indicate energy transfer from the ground surface to the atmosphere.

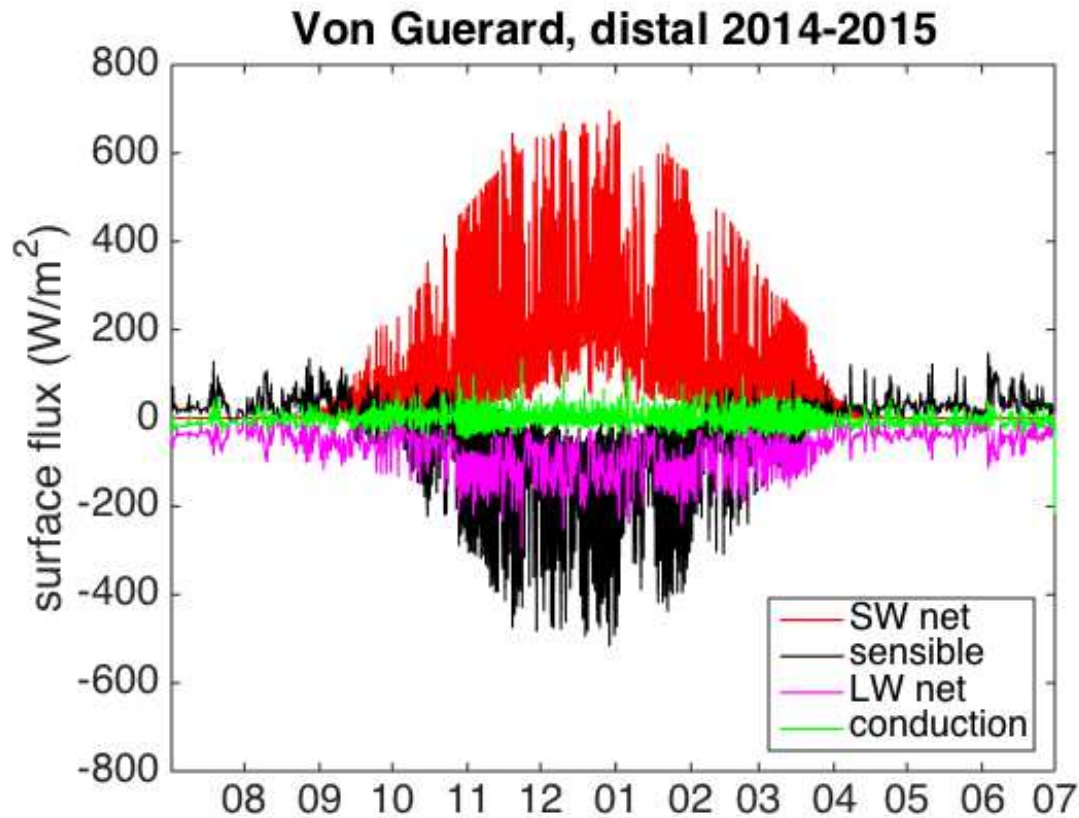


Figure 4.10: Surface energy fluxes at VG ALMS distal location between July 2014 and July 2015. Positive values indicate energy transfer into the ground surface from the atmosphere, and negative values indicate energy transfer from the ground surface to the atmosphere.

Daily average conductive flux, the sum of daily sensible and radiative fluxes, exhibits an asymmetrical seasonal dynamic. This dynamic is observed at all ALMSs, and is best illustrated at VG margin between the August 1, 2014 and July 1, 2015 (Figure 4.11). During spring and early summer, between September and December, daily conductive flux gradually increases at an approximate rate of $0.3 \text{ W/m}^2/\text{dy}$. Also, during this time daily conductive fluxes are both positive (warming) and negative (cooling). During late summer and through the fall, between December and March, daily conductive flux rapidly declines at an approximate rate of $0.6 \text{ W/m}^2/\text{dy}$. During February and March the daily average conductive flux is always negative, which continuously

cools the active layer. The asymmetry in seasonal conductive flux shows that active layer soils cool more rapidly during the fall than they warm in the spring.

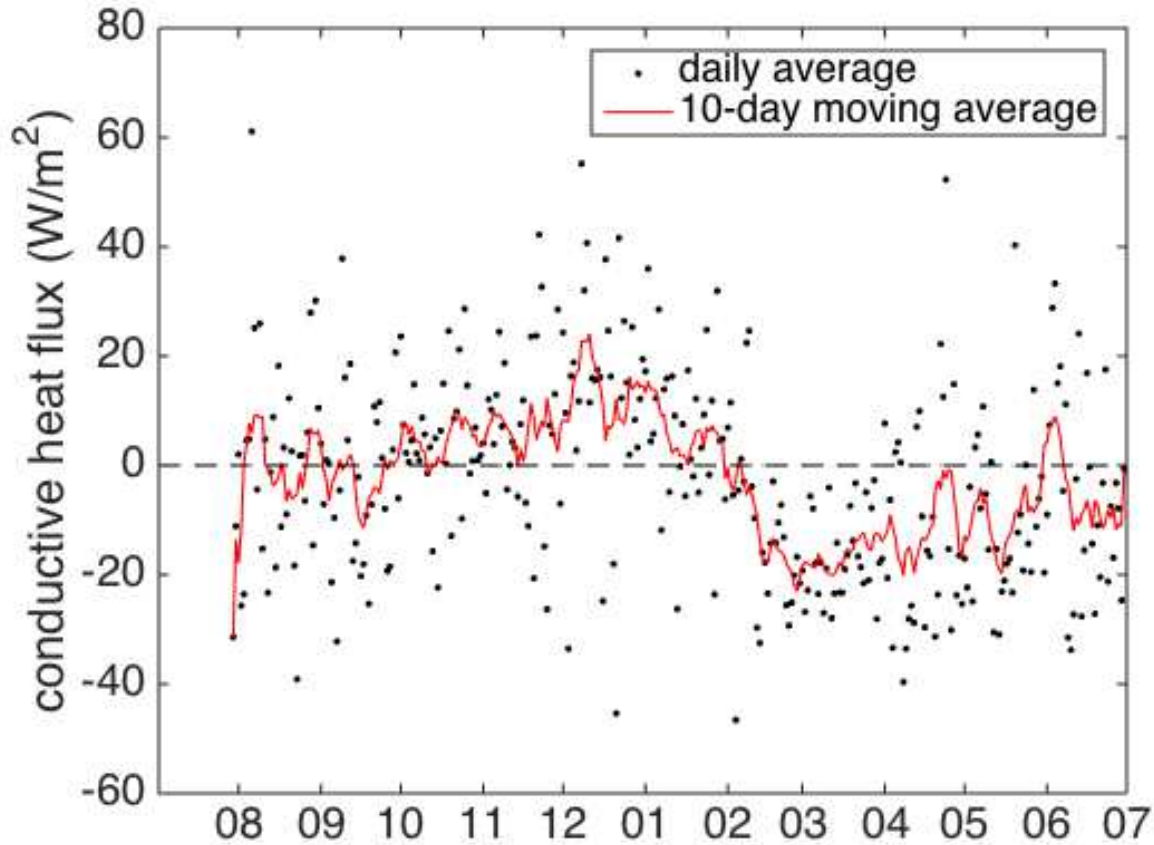


Figure 4.11: Daily average conductive flux and 10-day moving average of daily conductive flux at the VG margin site between August 2014 and July 2015. The conductive flux at the soil surface rapidly decreases between December and March. During February and March, the conductive flux is consistently negative which rapidly cools the active layer.

Cumulative summer conductive flux for 2014/2015 is greater at margin locations than drier distal locations (Figure 4.12). There is little difference between net radiation (SW and LW) and sensible heat exchange between distal and margin locations. WHC exhibits the largest magnitude net radiation and sensible heat fluxes, but the smallest conductive flux at margin locations. The smallest conductive flux is observed at the VG distal site.

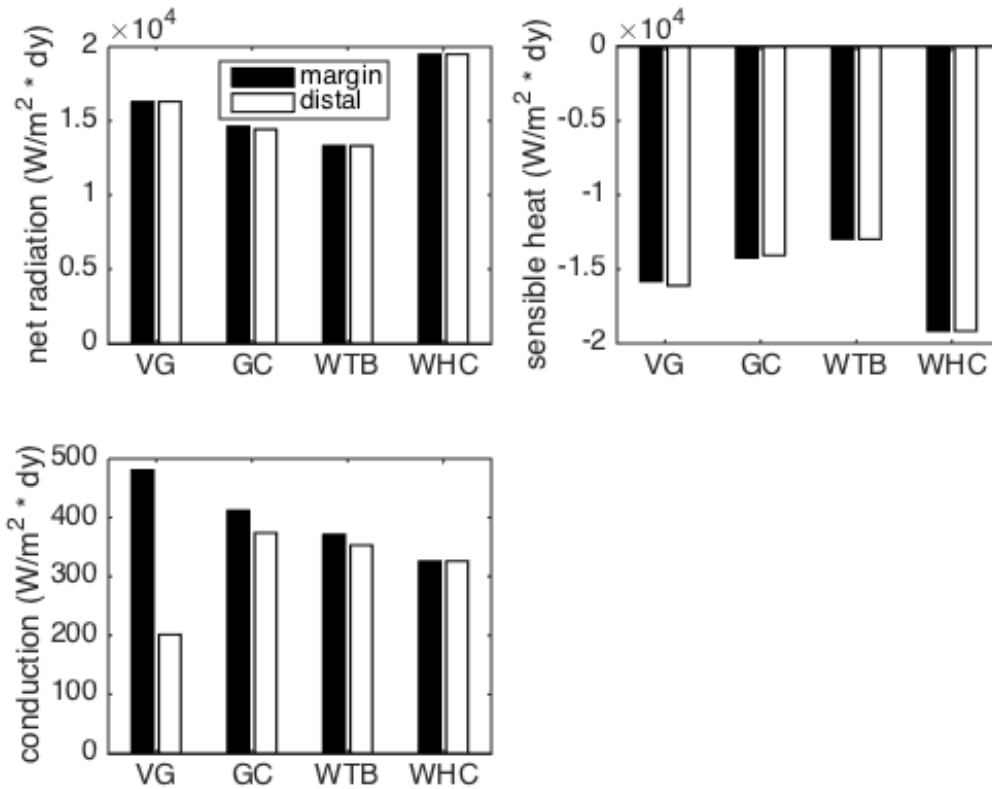


Figure 4.12: Cumulative summer (Nov, Dec, Jan, and Feb) surface energy fluxes during the 2014/2015 season at each ALMS.

Simulated active layer depth at VG increases gradually between November and February, before rapidly contracting between February and March (Figure 4.13 and Figure 4.14). Profiles for other ALMSs can be found in the Appendix (Figure 4.A16 – Figure 4.A18). The more rapid contraction in active layer depth is due to a consistently negative conductive heat flux at the soil surface throughout February and March (Figure 4.11). Annual maximum active layer depth ranges between 0.57 and 0.35 m. At VG, the distal location thaws deeper than the margin location each year. However, at other ALMSs, the margin location thaws deeper than the distal location each year. At all sites drier distal locations thaw more rapidly and than wetter margin locations. Also, drier sites exhibit greater within season variability in active layer depth, relative

to wetter margin sites. Active layer depth at distal sites tends to expand and contract more rapidly than at the margin sites.

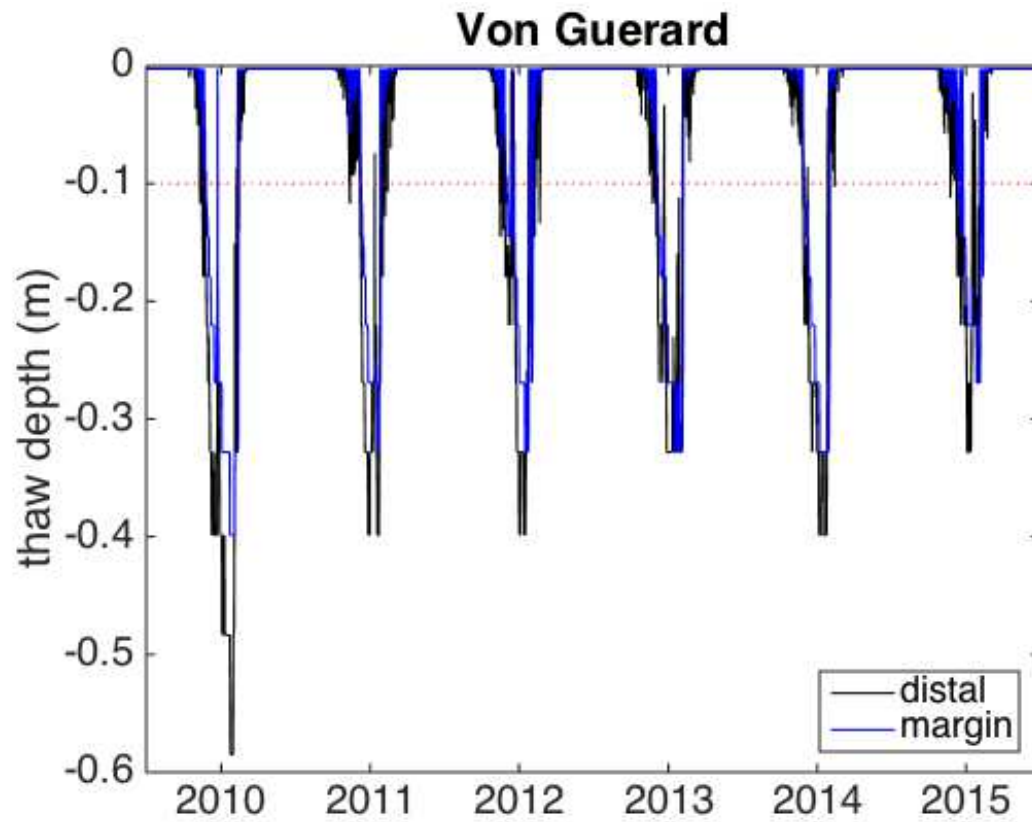


Figure 4.13: Simulated thaw depth at VG ALMS between July 2009 and July 2015.

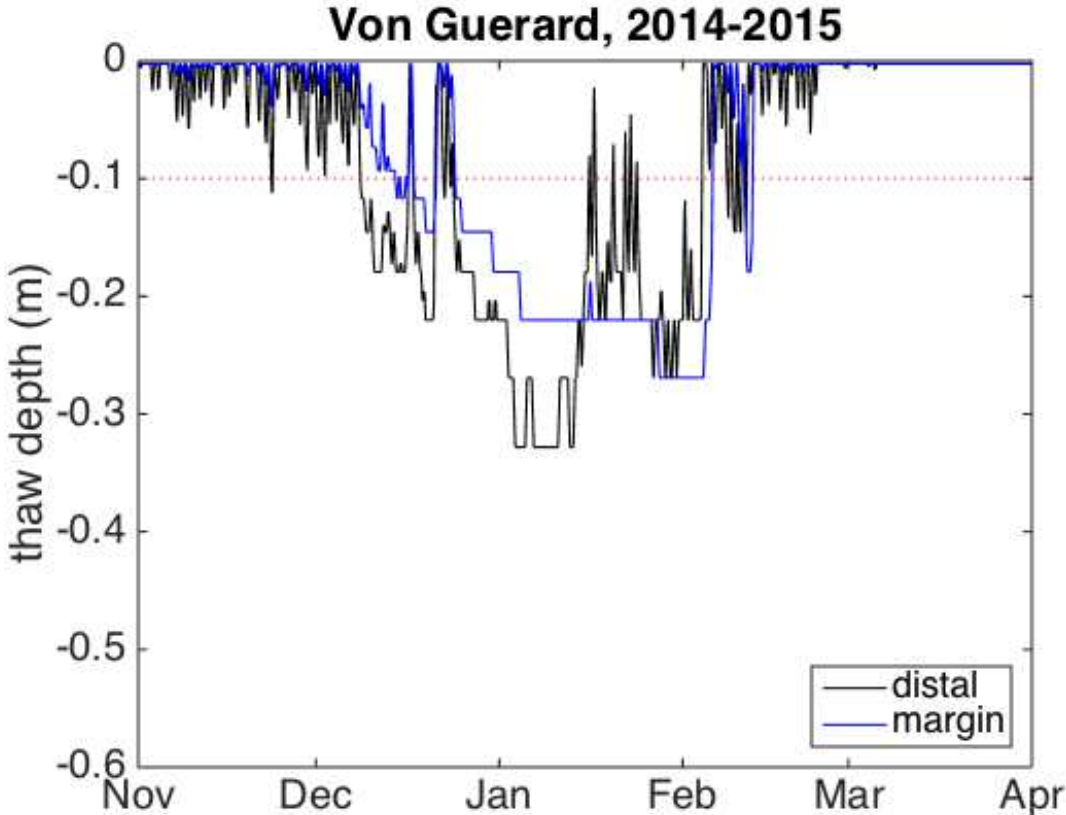


Figure 4. 14: Simulated thaw depth at Von Guerard ALMS between November 2014 and April 2015. The progression of active layer thaw depth shows a similar seasonal trend to other seasons, where soils thaw gradually and freeze rapidly.

4.3.3 Scenario analysis

Scenario analysis is used to infer how anticipated warming air temperature and increased soil moisture may affect the thermodynamic regime of the active layer habitat (0 – 15 cm below the ground surface). Scenario analysis is only performed at a single site, VG distal, where the energy balance model produced the best objective fit to observed ground temperature data (Table 2). Also, VG distal is the driest of all ALMS sites ($\theta = 0.01$) and provides the best opportunity to perturb θ across a wide range of plausible future scenarios. Scenario analyses only consider the 2015/2015 seasons.

Soil moisture and air temperature are perturbed in a series of scenarios (S1 – S5). Simulated ground temperature from each scenario simulation is compared against a base-case “control” (C) parameterization (Table 4.1). Four scenarios are tested (Table 4.3): S1) a +2°C change in air temperature, and no change in soil moisture; S2) a +0.1 m³/m³ change in soil moisture, and no change in air temperature; S3) saturated soil moisture conditions, and no change in air temperature; S4) a +0.1 m³/m³ change in soil moisture, and +2°C change in air temperature; S5) saturated soil moisture conditions, and a +2°C change in air temperature.

Scenario 1 (S1), increased air temperatures but no change in soil moisture, caused substantial changes to the thermal regime of the active layer habitat (Figure 4.15 and Table 4.3). Average 10 cm active layer temperature increased by 1.48 °C, an 1138% increase from the control simulation. The number of days spent above freezing at 10 cm increased by 15 days. Furthermore, warmer air temperatures alone also caused a 60% increase in the number of freeze events and a 20% increase in freezing rate.

Scenario 2 (S2), a +0.1 m³/m³ change in soil moisture but no change in air temperature, resulted in a cooling of the active layer habitat, a reduction in active layer depth, and a reduction in the frequency and rate of freeze events (Figure 4.15 and Table 4.3). Average summer ground temperature at 10cm decreased by 133% from the control simulation. Maximum thaw extent decreased by 44% and the duration of time above freezing at 10cm depth decreased by 10%. Furthermore, the modest increase in soil moisture in S2 resulted in a 90% reduction in the frequency of freeze events and a 95% reduction in the rate of freeze events. Only 1 freezing event occurred during the season at the transition from austral summer to austral winter.

Increasing soil moisture to saturation without any change in air temperature, as simulated by scenario 3 (S3), caused a warming of the active layer habitat, a reduction in thaw depth, and a reduction in the frequency and rate of freezing (Figure 4.15 and Table 4.3). Summer ground temperature at 10 cm increased by 40%, but thaw depth decreased by 32% and the time above freezing decreased by 11%, relative to the control simulation. Saturated soil conditions also resulted in a 90% reduction in freeze frequency and a 95 % reduction in freezing rate. Similar to S2, only 1 freeze event occurred at the transition from austral summer to austral winter.

Increased soil moisture and warmer air temperatures, as simulated by scenarios 4 (S4) and 5 (S5), caused a warming of the active layer habitat, a reduction in thaw depth, and reductions in the frequency and rate of freezing events (Figure 4.15 and Table 4.3). Modest (+0.1 m³/m³), substantial (saturation) increases in soil moisture with warmer air temperatures caused similar increases in average summer ground temperature at 10 cm (800 – 1030% increase) and the duration of time above freezing at 10 cm (9 – 10% increase). S4 and S5 both resulted in a 17% reduction in active layer depth, a 90% reduction in freeze frequency and 98% reduction in freezing rate. In these scenarios only 1 freeze event occurred at the transition from summer to winter.

Table 4.3: Summary metrics from control and scenario simulations. Metric values and absolute and relative changes from the control simulation are shown.

Scenario	av. 10cm T (°C)	av. 10cm summer T (°C)	max thaw depth (m)	10cm days above freezing (dys)	# 10cm freeze events	av freeze rate (°C/hr)
Control (C)	-16.70	-0.13	0.48	62.05	20	0.39
+2°C T _{air} (S1)	-15.34	1.35	0.59	76.93	16	0.47
+10% θ (S2)	-16.82	-0.30	0.27	55.91	1	0.02
Saturation (S3)	-17.26	-0.08	0.33	54.99	1	0.02
+10% θ , +2°C T _{air} (S4)	-15.45	1.01	0.40	68.00	1	0.01
saturation, +2°C T _{air} (S5)	-15.82	1.22	0.40	68.23	1	0.01
	Δ av. 10cm T (°C)	Δ av. 10cm summer T (°C)	Δ max thaw depth (m)	Δ 10cm days above freezing (dys)	Δ # 10cm freeze events	Δ av freeze rate (°C/hr)
+2°C T _{air} (S1)	1.36	1.48	0.11	14.88	-4	0.08
+10% θ (S2)	-0.12	-0.17	-0.21	-6.14	-19	-0.37
Saturation (S3)	-0.56	0.05	-0.15	-7.06	-19	-0.37
+10% θ , +2°C T _{air} (S4)	1.25	1.14	-0.08	5.95	-19	-0.38
saturation, +2°C T _{air} (S5)	0.88	1.35	-0.08	6.18	-19	-0.38
	% Δ av. 10cm T	% Δ av. 10cm summer T	% Δ max thaw depth	% Δ 10cm days above freezing	% Δ # 10cm freeze events	% Δ av freeze rate
+2°C T _{air} (S1)	8.14	1138.46	22.92	23.98	-20	20.05
+10% θ (S2)	-0.72	-133.69	-43.92	-9.90	-95	-95.13
Saturation (S3)	-3.36	39.27	-31.65	-11.37	-95	-94.67
+10% θ , +2°C T _{air} (S4)	7.48	878.71	-16.94	9.58	-95	-97.85
saturation, +2°C T _{air} (S5)	5.27	1037.69	-16.94	9.96	-95	-97.71

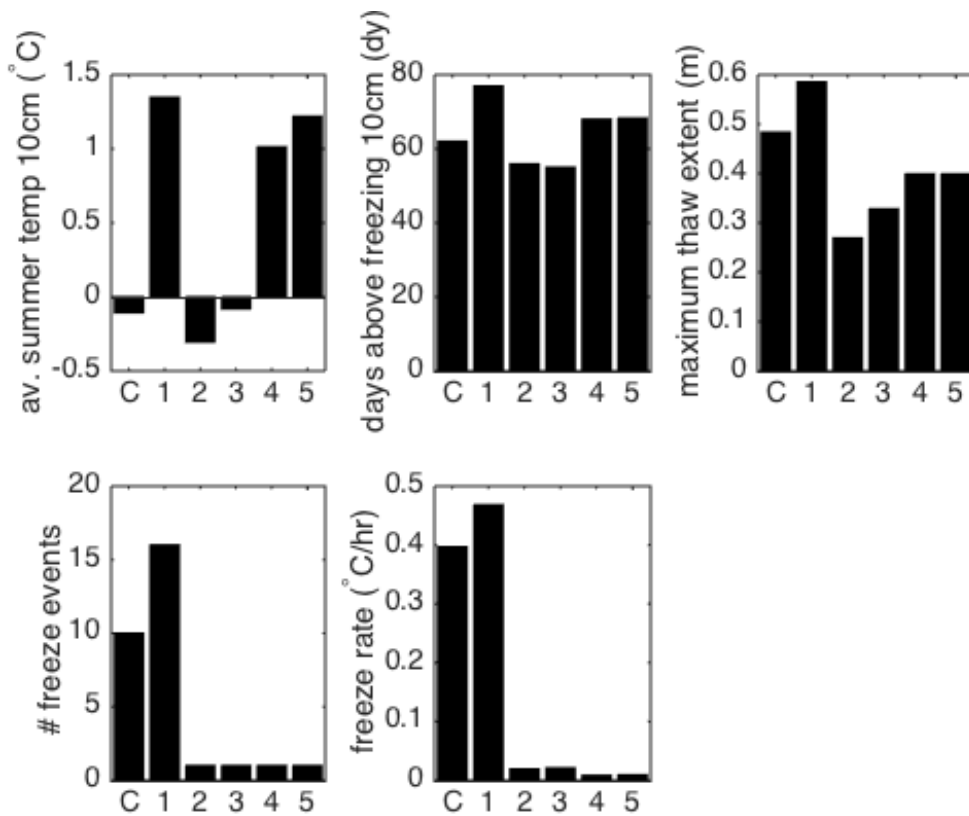


Figure 4.15: Thermodynamic metrics from control (C) and scenario (S1 – S5) simulations at VG distal location. S1 is +2°C change in air temperature and no change in soil moisture, S2 is +0.1 m³/m³ change in soil moisture and no change in air temperature, S3 is an increase in soil moisture to saturation and no change in air temperature, S4 is a +0.1 m³/m³ change in soil moisture and a +2°C change in air temperature, and S5 is an increase in soil moisture to saturation and a +2°C change in air temperature.

4.4 DISCUSSION

The thermal regime of the soil habitat (0 – 15 cm depth) in the McMurdo Dry Valleys is controlled by energy fluxes at the soil-atmosphere boundary, conductive fluxes within the active layer, the release/consumption of latent heat, and physical properties of active layer soils. Under future climate scenarios, the MDV region is likely to experience warmer air temperatures and a subsequent increase in soil moisture [Barrett *et al.*, 2008; Gooseff *et al.*, 2011]. Increases in soil moisture are likely to arise from the melting of ice-rich permafrost and ground ice, and the expansion of wetted margins adjacent to lakes, streams, and ponds. Soil moisture and air temperature are important controls on the thermal regime of soils because air temperature gradients drive sensible heat exchange and soil moisture affects the soil thermal diffusivity and latent heat content. In this study, a numerical surface energy balance and ground heat transfer model is developed to simulate the combined influence of air temperature and soil moisture on the thermodynamic regime of active layer habitats. Model results reveal how plausible changes in air temperature and/or soil moisture may affect habitat temperature, the annual duration of time the soil habitat spends above freezing, active layer thaw depth, and annual freeze frequency and rate.

The simple soil energy balance model employed in this study is capable of simulating much of the observed variability in shallow ground temperature at ALMSs. Model NSE was > 0.9 and RMSE < 3.7 °C at all sites. The satisfactory objective performance of this model shows that radiation, sensible heat exchange, conduction, and the latent heat of fusion are the dominant

heat transfer mechanisms controlling soil habitat temperature. Other surface energy budget and heat transfer models employed in the MDVs have considered latent heat exchange at the soil surface (evaporation/condensation) and the insulating influence of snow cover [McKay, 2009; Hunt *et al.*, 2010]. Although this work ignored the role of vapor exchange within and above the soil surface, the model was capable of simulating 10 cm ground temperatures with a similar skill (RMSE = 2.21 – 3.61 °C) as the model of Hunt *et al.*, 2010 (RMSE 1.44 – 2.8 °C), which considered vapor exchanges.

A critical shortcoming of the simple model used in this work is the lack of an algorithm to account for the affects of snow. Snow accumulation insulates subnival soils, keep the subnival soils cooler than exposed soils during the austral spring [Hardy *et al.*, 2001; Gooseff *et al.*, 2003b]. The Taylor Valley receives very little precipitation because it sits within the precipitation shadow of the Trans Antarctic Mountains [Fountain *et al.*, 2010]. Much of the snow accumulation in the Taylor Valley is sourced from blown snow off the East Antarctic Ice sheet. Blown snow tends to accumulate in topographic depressions, such as stream channels. The spatial distribution of early summer snow cover is patchy [Eveland *et al.*, 2013]. The greatest difference between simulated and observed 10 cm temperature is observed during the austral spring, when ALMS sites are likely covered in snow. This dynamic is particularly evident at the VG ALMS, margin location (Figure 4.5 and Figure 4.6). Future work with this energy balance model should incorporate a simple snow component capable of simulating soil insulation due to snow cover.

The annual duration of time the active layer habitat spends above freezing is dependent on soil moisture. This is observed at ALMs, as the fraction of time above freezing shows a generally negative relationship with mean austral summer soil moisture (Figure 4.16). Model scenarios 2 ($\theta=0.1$) and 3 (θ_{sat}), in which soil moisture is increased but air temperature is not changed, exhibited 9-11% reduction in days above freezing at 10 cm relative to the control simulation ($\theta<0.01$). The decrease in days above freezing in wetter soils is due to the release of latent heat as wetter soils thaw during early summer. Snow cover likely influences inter-site variability in observed time above freezing (Figure 4.16). Because the model used in this study does not consider snow cover, model scenario analyses isolate the potential role of soil moisture to alter the duration of time soil at 10 cm depth spend above freezing.

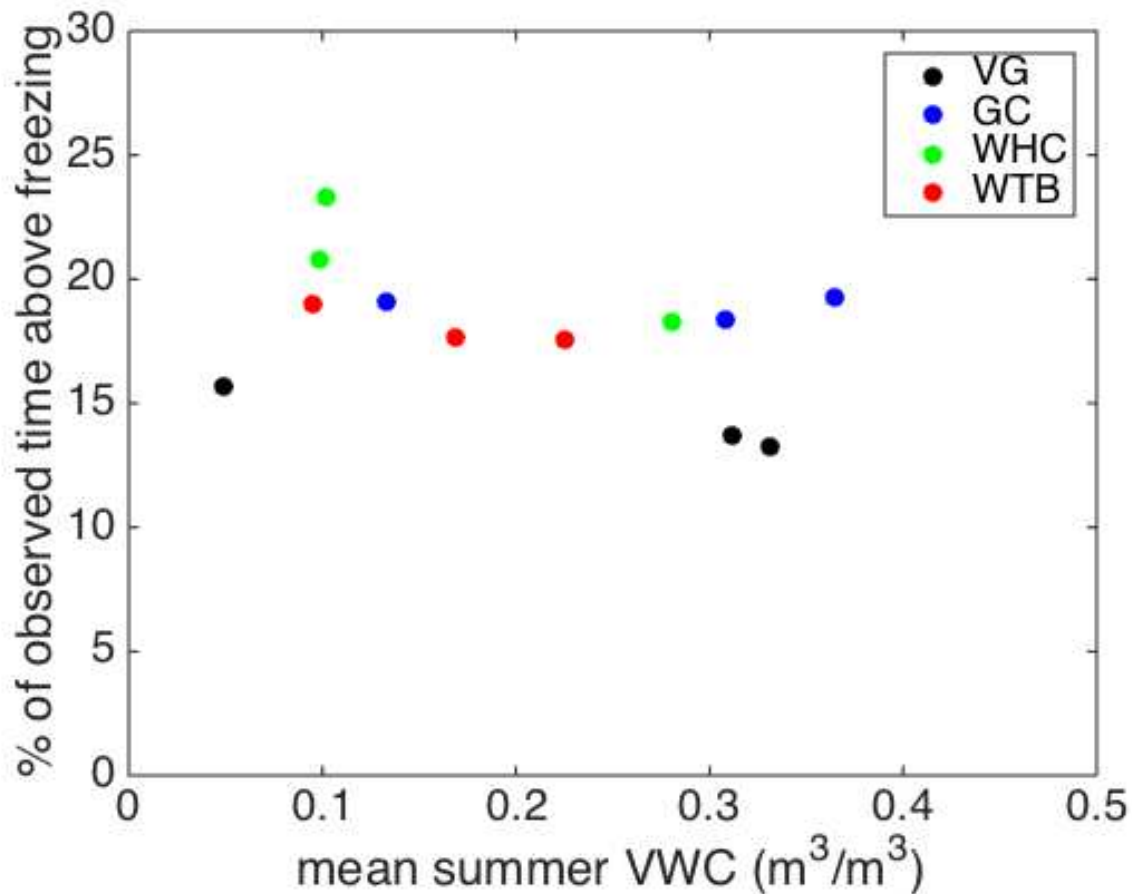


Figure 4.16: The percentage of observed time that soils at 10 cm spend above freezing, plotted as a function of mean austral summer (Dec, Jan, Feb) soil moisture at 15 cm depth. A generally negative trend is observed, where wetter soils spend less time above freezing than drier soils.

Empirical evidence and model simulations also show that wetter soils freeze less frequently and more gradually than drier soils. ALMS observations discussed in Chapter 3 indicate that a soil moisture threshold exists at $0.1 \text{ m}^3/\text{m}^3$. Dry soils, $\theta < 0.1 \text{ m}^3/\text{m}^3$, freeze more frequently and more rapidly than wet soils, $\theta > 0.1 \text{ m}^3/\text{m}^3$. The model scenario analysis in this study revealed a similar dynamic. When soil moisture was increased from 0.01 to $0.1 \text{ m}^3/\text{m}^3$, annual freeze frequency reduced from 10 to 1 and freezing rate decreased from $0.39 \text{ }^\circ\text{C}/\text{hr}$ to $0.01 \text{ }^\circ\text{C}/\text{hr}$ (Table 4.3). Also, warmer air temperatures and very dry soil conditions (S1) resulted

in both an increase in the frequency and rate of freezing events. Conversely, warmer air temperatures with moderate and very wet soil moisture conditions (S4 and S5) yielded a strong reduction in the frequency and rate of freezing, relative to the control scenario. These results illustrate that under a warmer climate, drier soil habitats may encounter additional freeze stresses, whereas wetter habitats may be buffered from repeated annual freezing events.

The potential transition from a drier to wetter soil habitat may pose a tradeoff between time above freezing and the intensity of freeze stress. According to the results of this study, wetter soils are subjected to fewer and more gradual freeze events, but spend less time above freezing (Figure 4.15). Because freeze events demand fewer metabolic resources from soil organisms, more energy may be allocated to reproduction and growth in wetter soils where freeze stress is greatly diminished [Adhikari *et al.*, 2010; Knox *et al.*, 2015]. Conversely, because the total time above freezing is suppressed in wetter soils and time window that organisms have to reproduce and grow each summer will be restricted. Under a warmer and wetter climate (S4 and S5), total time above freezing is increased and freeze stress is decreased. As such, a wet and warm scenario may result in increased growth and reproduction rates for certain hydrophilic organisms, such as *P. antarcticus* and *E. antarcticus*.

In model scenarios in which soil moisture is increased (S2, S3, S4 and S5), active layer depth decreased between 16 – 44% from the control simulation (Table 3), in which $\theta = 0.01$. The reduction in active layer depth from the control simulation is more extreme for a minor increase in soil moisture (S2, -44%), compared to a large increase in soil moisture (S3, -32%). This may

be due to a non-linear change in thermal diffusivity as a function of soil moisture. Thermal diffusivity is the quotient of bulk thermal conductivity and bulk volumetric heat capacity. Thermal diffusivity controls the rate at which energy can propagate through soils. For a hypothetical coarse-grained soil ($\phi=0.35$), thermal diffusivity decreases between $\theta = 0$ and $\theta = 0.10$ (Figure 4.17). However, thermal diffusivity increases from $\theta = 0.10$ to $\theta_{sat} = 0.35$. A slight increase in soil moisture in the driest portions of the landscape may decrease active layer depths, whereas an increase of soil moisture in moderately wet portions of the landscape will deepen thaw depth. *Ikard et al.* [2009] observed higher thermal diffusivities in wetter soils, compared drier soils, along the wetted margin of Lake Fryxell. Modeling results in this study corroborate *Ikard et al.* [2009] when $\theta > 0.1$, but contradict results when $\theta < 0.1$. Because soil moisture is highly variable over small spatial scales in the Taylor Valley, soil moisture is an important consideration for understanding which regions are most vulnerable to permafrost degradation and thermokarst development under a warmer climate [*Levy et al.*, 2013; *Fountain et al.*, 2014; *Sudman et al.*, 2017]. Heat transfer models that do not account for spatial variability in soil moisture, and thereby spatial variability in thermal diffusivity and latent heat content, will insufficiently simulate contemporary and future active layer depths.

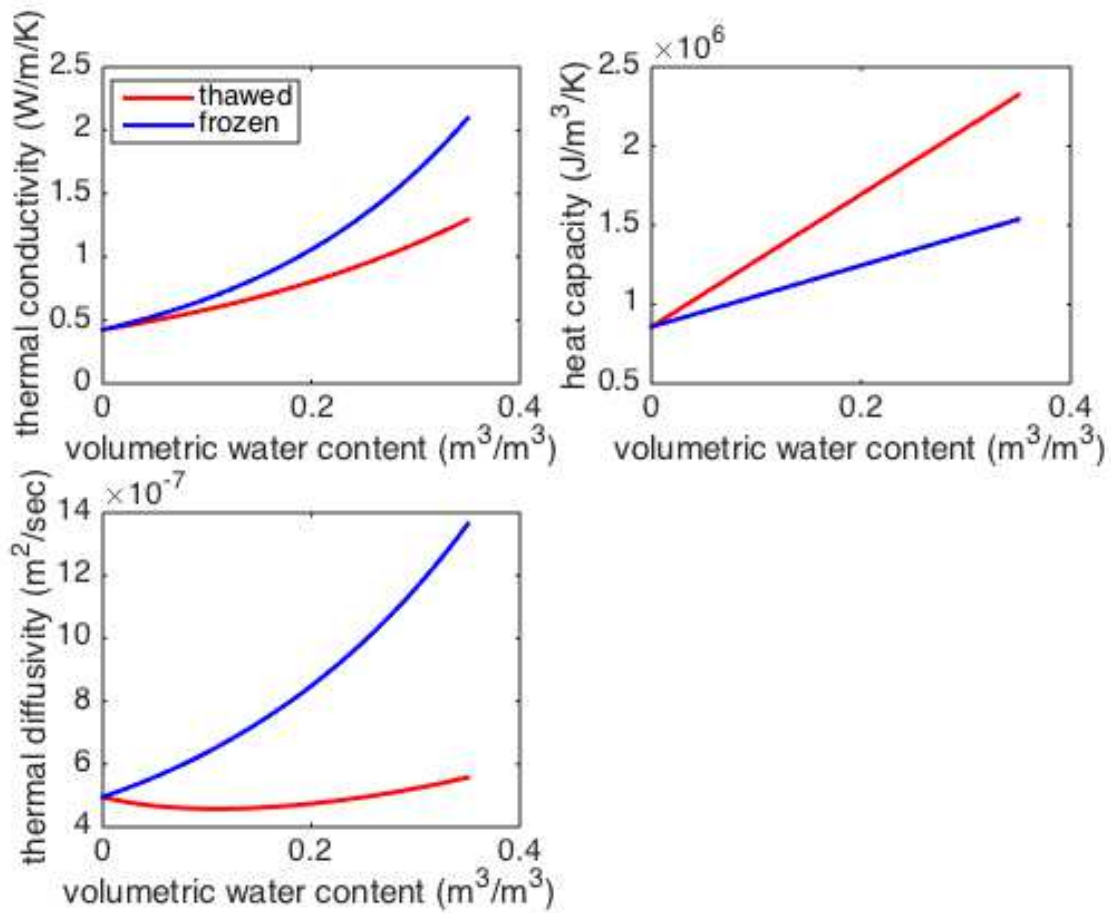


Figure 4.17: Thermal conductivity, volumetric heat capacity, and thermal diffusivity as a function of volumetric water content for thawed and frozen soils. Soil porosity is assumed to be 0.35.

4.5 CONCLUSION

In this study, numerical surface energy balance and soil heat transfer models are used to simulate active layer thermodynamics in the MDVs. The model(s), which considered radiation, sensible heat exchange, conduction, and freeze/thaw of soil water, were capable of accurately simulating observed 10 cm ground temperature. The largest model misfit to data is observed during spring and early summer months, when snow cover likely insulates shallow active layer temperatures. Scenario analyses were used to consider how potential changes in air temperature and soil moisture will alter active layer thermodynamics in the driest portions of the landscape. Results show that higher air temperatures and increased soil moisture result in warmer average summer temperatures at 10 cm depth, an increase in the duration of annual time above freezing at 10 cm depth, and a decrease in the frequency and rate of freeze events at 10 cm depth. Overall, results of this study confirm that soil moisture exerts strong control on active layer thermodynamics in the MDVs. Moreover, models suggest that future changes in air temperature and soil moisture will likely result in significant changes to the thermal regime of active layer habitats in the MDVs.

4.6 APPENDIX

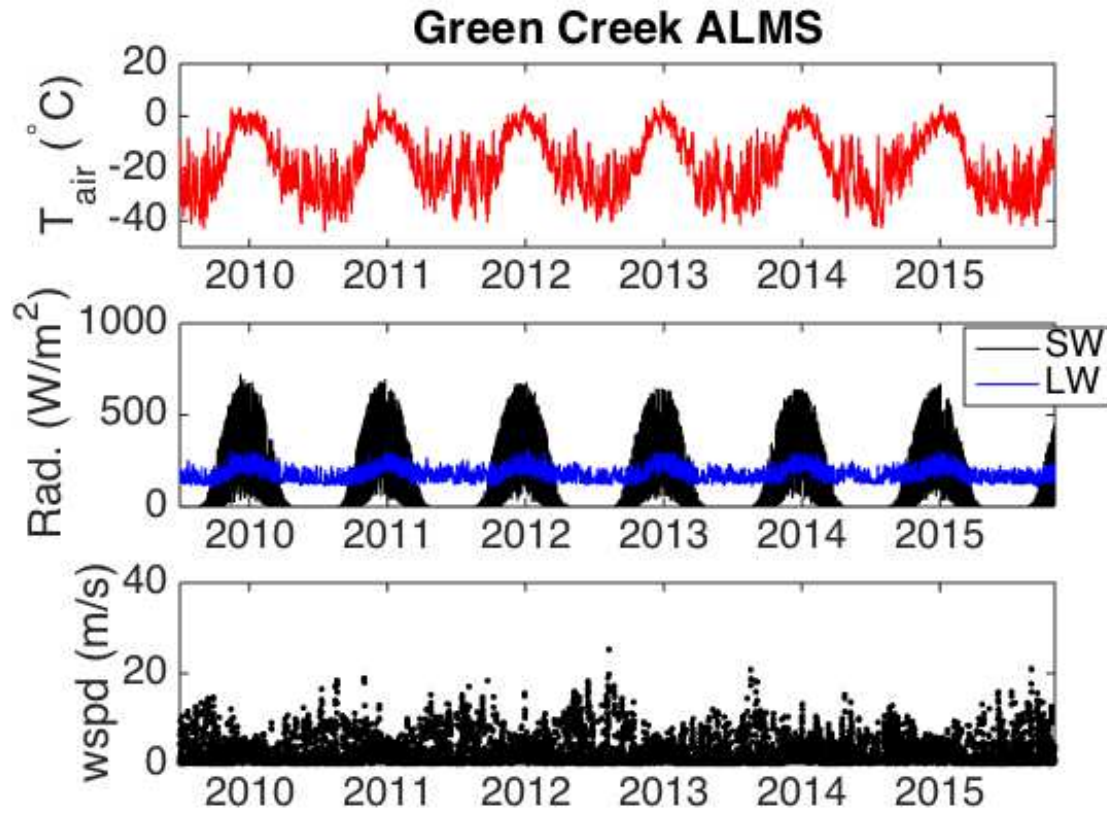


Figure 4.A1: MicroMet simulated meteorological data at Green Creek ALMS. (Top panel) Air temperature (T_{air}), (middle panel) SW and LW radiation (Rad), and (bottom panel) wind speed (wspd) are shown.

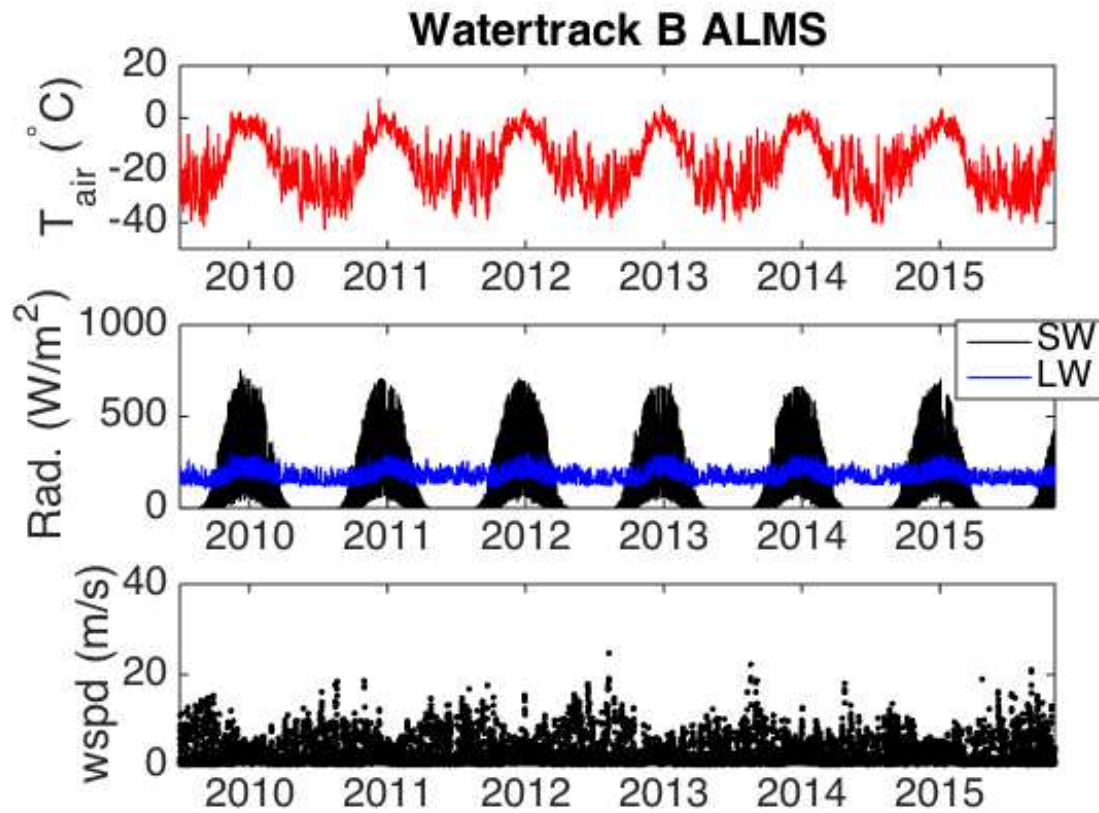


Figure 4.A2: MicroMet simulated meteorological data at Watertrack B ALMS. (Top panel) Air temperature (T_{air}), (middle panel) SW and LW radiation (Rad), and (bottom panel) wind speed (wspd) are shown.

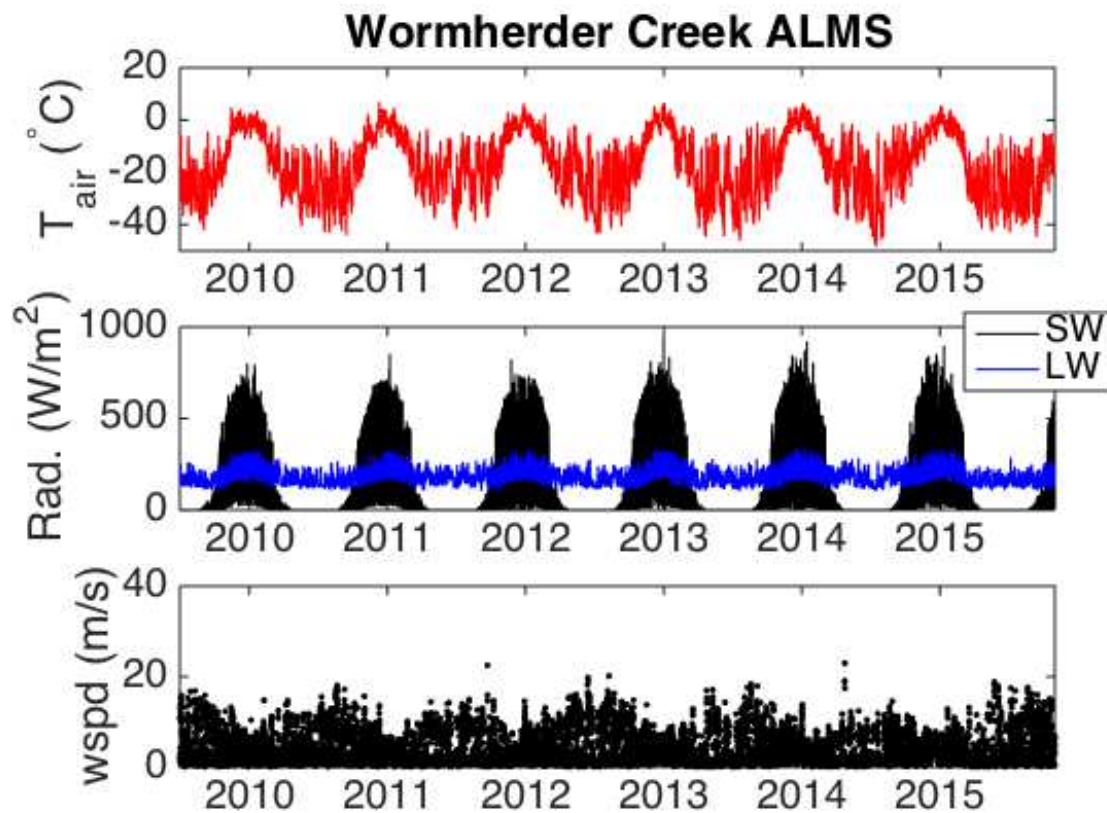


Figure 4.A3: MicroMet simulated meteorological data at Green Creek ALMS. (Top panel) Air temperature (T_{air}), (middle panel) SW and LW radiation (Rad), and (bottom panel) wind speed (wspd) are shown.

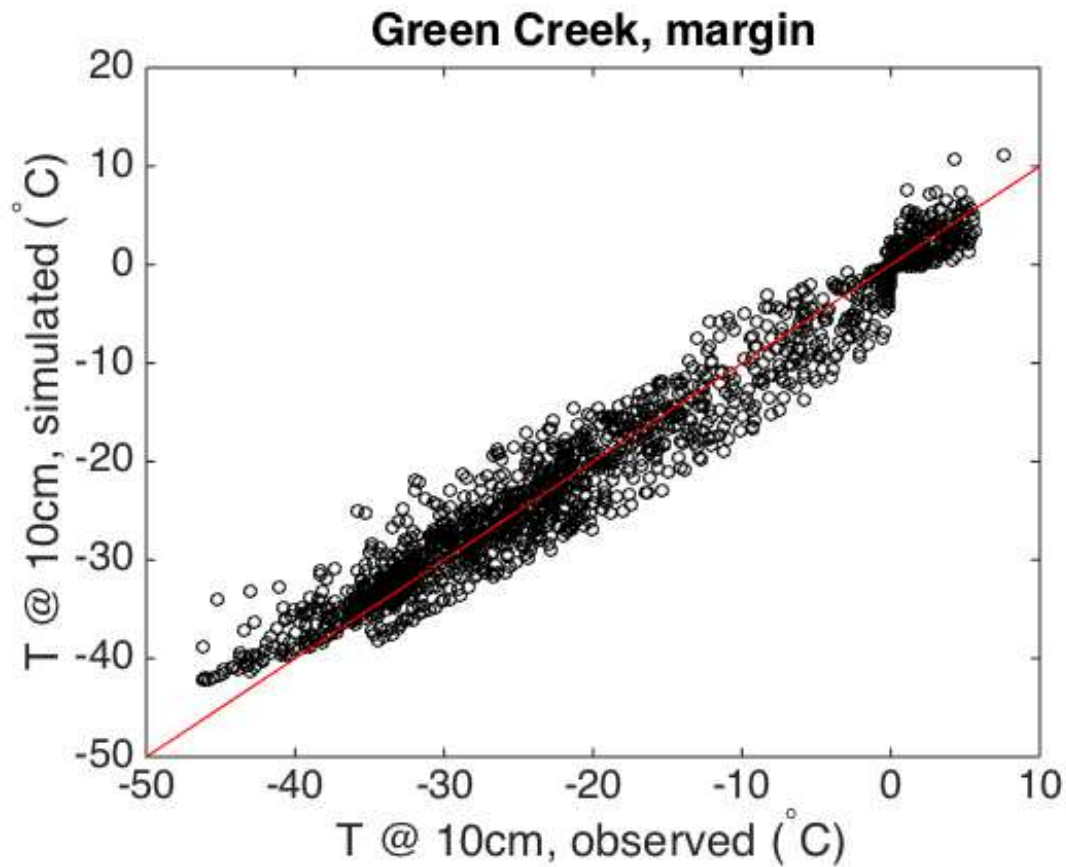


Figure 4.A4: Simulated and observed 10cm ground temperature at Green Creek margin site. All available ground temperature observations are used and the 1:1 line is shown in red.

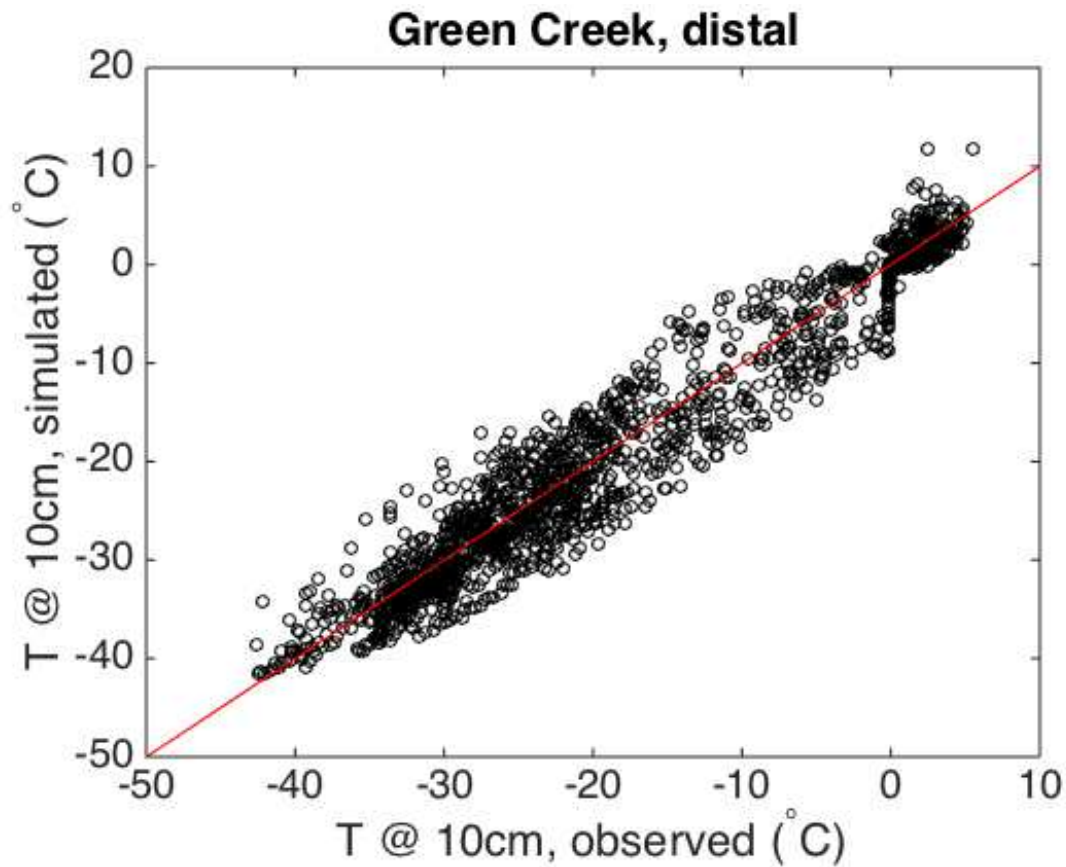


Figure 4.A5: Simulated and observed 10cm ground temperature at Green Creek distal site. All available ground temperature observations are used and the 1:1 line is shown in red.

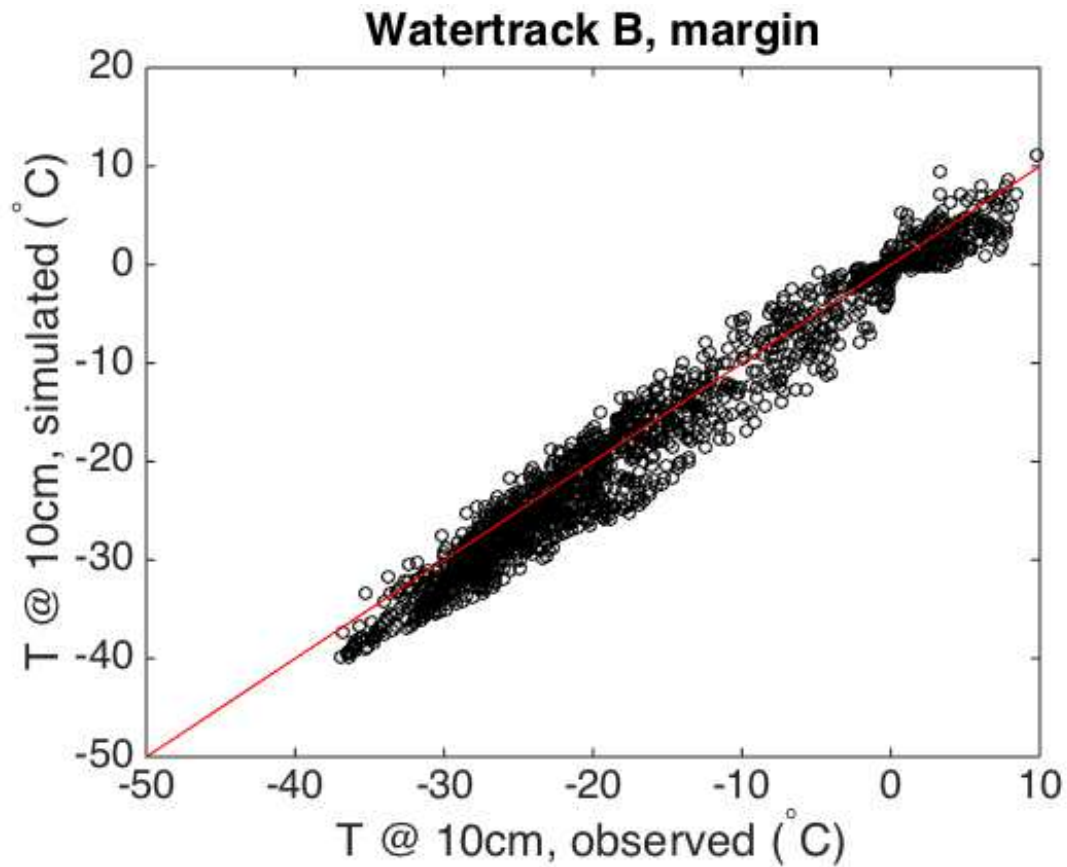


Figure 4.A6: Simulated and observed 10cm ground temperature at Watertrack B margin site. All available ground temperature observations are used and the 1:1 line is shown in red.

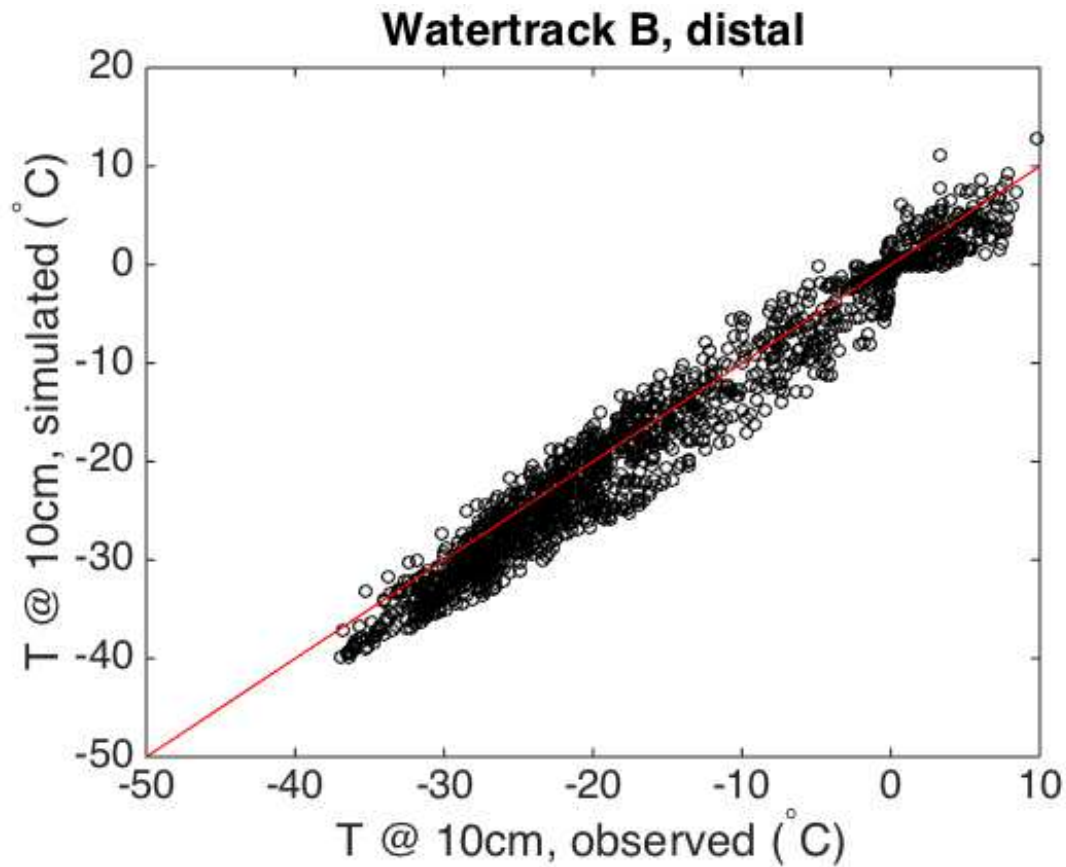


Figure 4.A7: Simulated and observed 10cm ground temperature at Watertrack B distal site. All available ground temperature observations are used and the 1:1 line is shown in red.

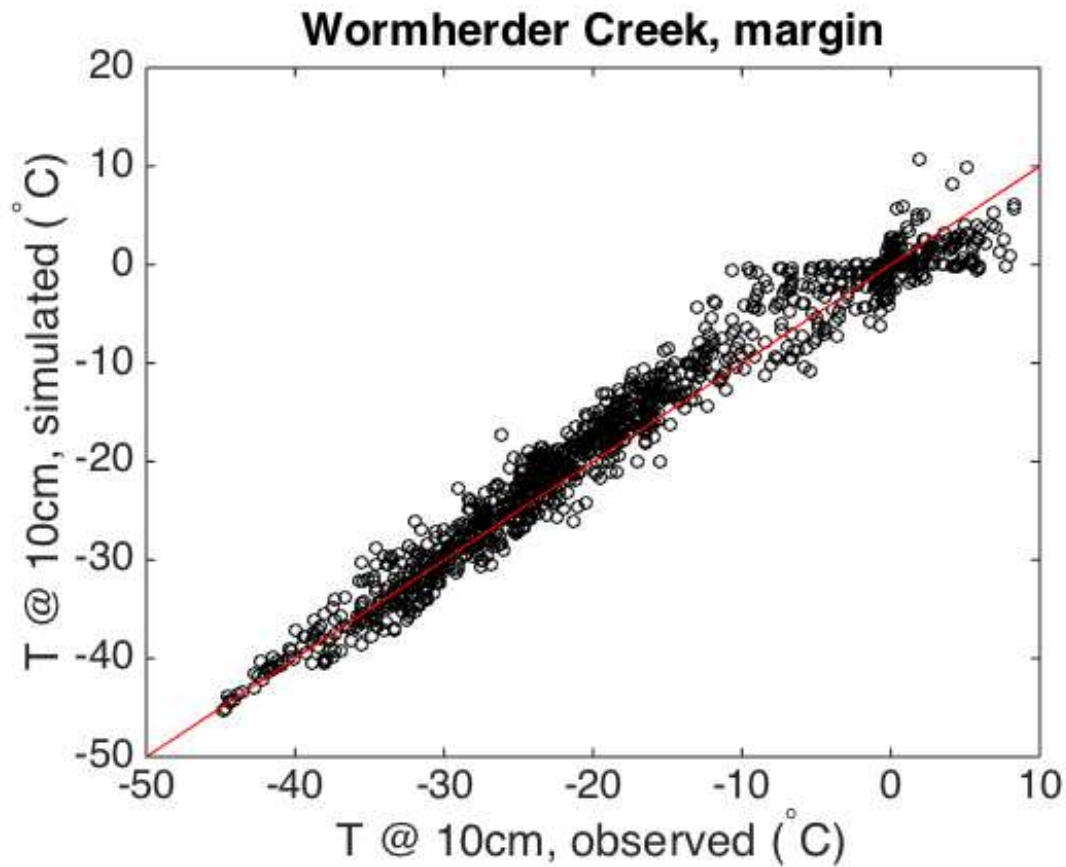


Figure 4.A8: Simulated and observed 10cm ground temperature at Wormherder Creek margin site. All available ground temperature observations are used and the 1:1 line is shown in red.

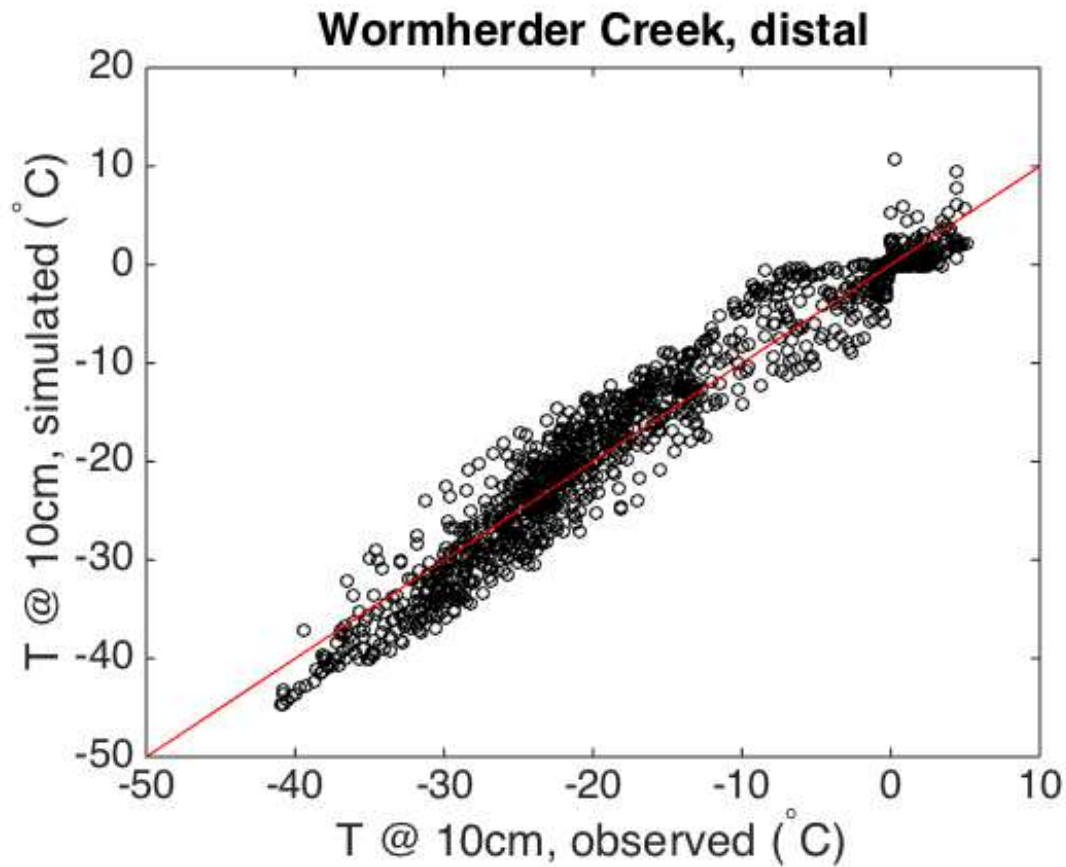


Figure 4.A9: Simulated and observed 10cm ground temperature at Wormherder Creek distal site. All available ground temperature observations are used and the 1:1 line is shown in red.

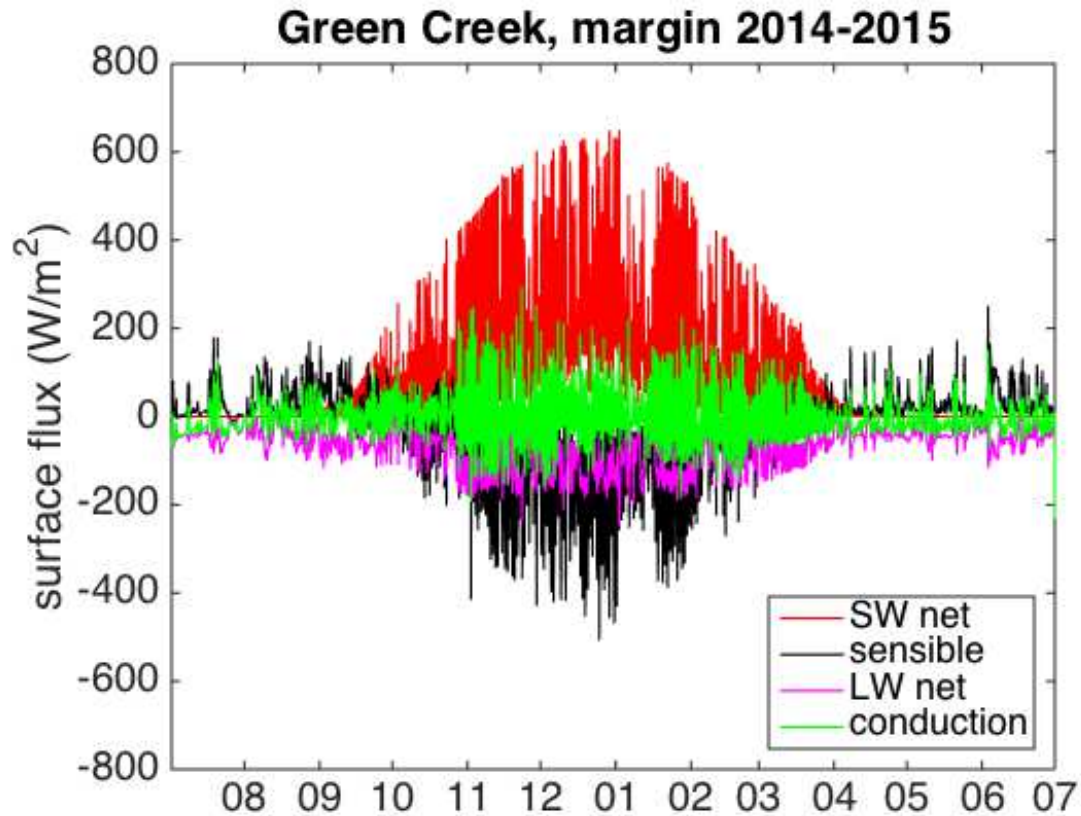


Figure 4.A10: Surface energy fluxes at GC ALMS margin location between July 2014 and July 2015. Positive values indicate energy transfer into the ground surface from the atmosphere, and negative values indicate energy transfer from the ground surface to the atmosphere. The largest positive flux is net SW radiation, which ranges from 0 – 650 W/m^2 . Sensible heat flux is positive in the winter and negative in the summer, ranging from -507 – 252 W/m^2 . Net LW radiation is predominantly negative during, but exhibits a range of -250 – 13 W/m^2 . Conduction oscillates between positive and negative on a diel basis and has a range of -190 – 295 W/m^2 .

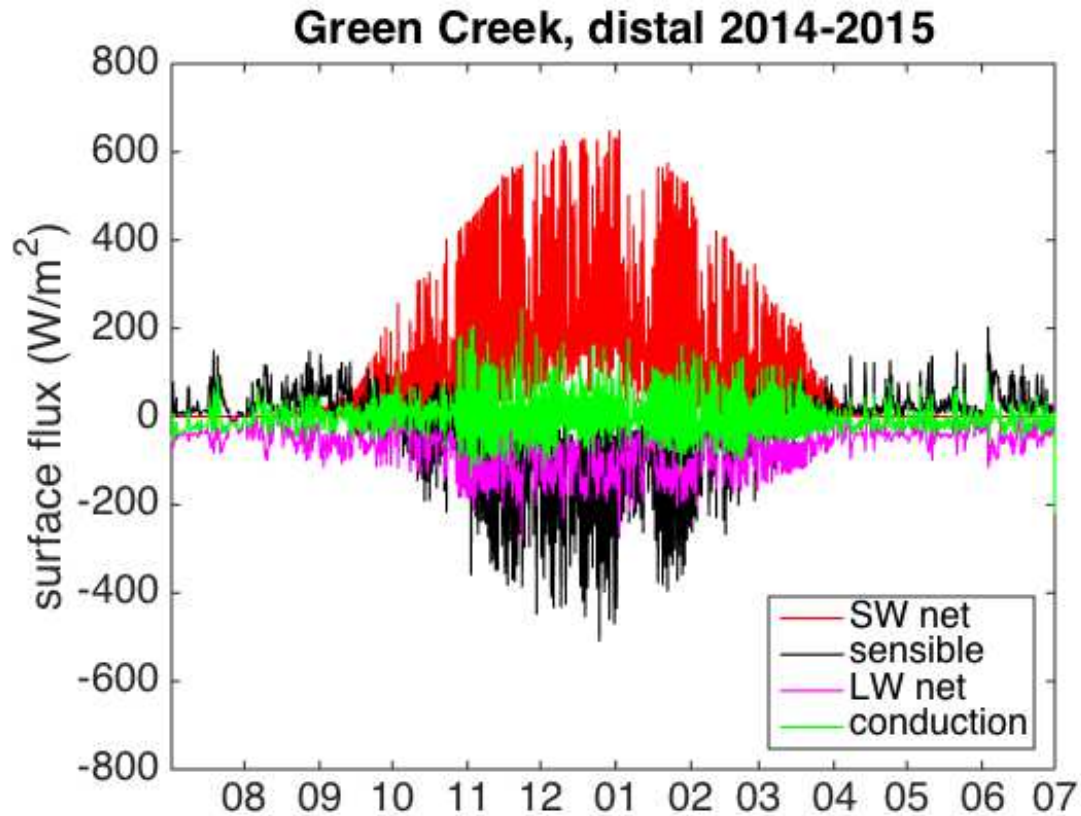


Figure 4.A11: Surface energy fluxes at GC ALMS distal location between July 2014 and July 2015. Positive values indicate energy transfer into the ground surface from the atmosphere, and negative values indicate energy transfer from the ground surface to the atmosphere. The largest positive flux is net SW radiation, which ranges from 0 – 650 W/m². Sensible heat flux is positive in the winter and negative in the summer, ranging from -510 – 203 W/m². Net LW radiation is predominantly negative during, but exhibits a range of -281 – 10 W/m². Conduction oscillates between positive and negative on a diel basis and has a range of -130 – 245 W/m².

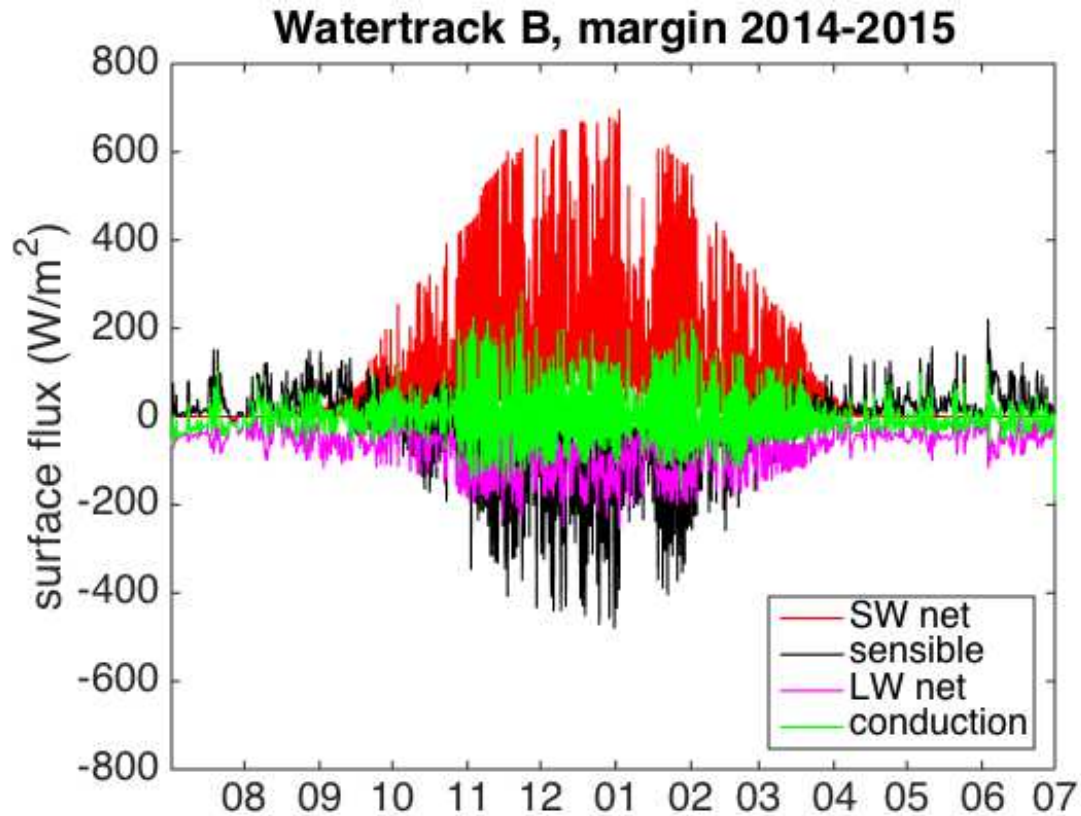


Figure 4.A12: Surface energy fluxes at WTB ALMS margin location between July 2014 and July 2015. Positive values indicate energy transfer into the ground surface from the atmosphere, and negative values indicate energy transfer from the ground surface to the atmosphere. The largest positive flux is net SW radiation, which ranges from 0 – 697 W/m². Sensible heat flux is positive in the winter and negative in the summer, ranging from -450 – 221 W/m². Net LW radiation is predominantly negative during, but exhibits a range of -252 – 12 W/m². Conduction oscillates between positive and negative on a diel basis and has a range of -162 – 285 W/m².

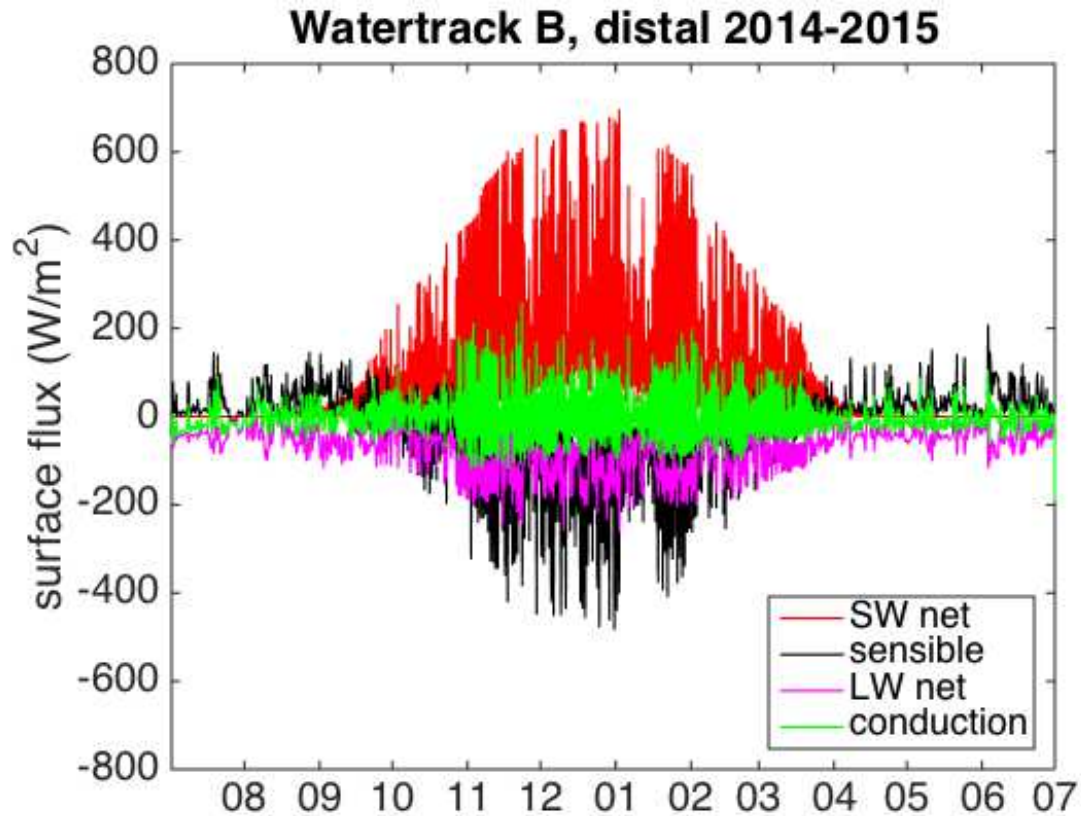


Figure 4.A13: Surface energy fluxes at WTB ALMS distal location between July 2014 and July 2015. Positive values indicate energy transfer into the ground surface from the atmosphere, and negative values indicate energy transfer from the ground surface to the atmosphere. The largest positive flux is net SW radiation, which ranges from 0 – 697 W/m². Sensible heat flux is positive in the winter and negative in the summer, ranging from -487– 194 W/m². Net LW radiation is predominantly negative during, but exhibits a range of -268 – 10 W/m². Conduction oscillates between positive and negative on a diel basis and has a range of -192 – 245 W/m².

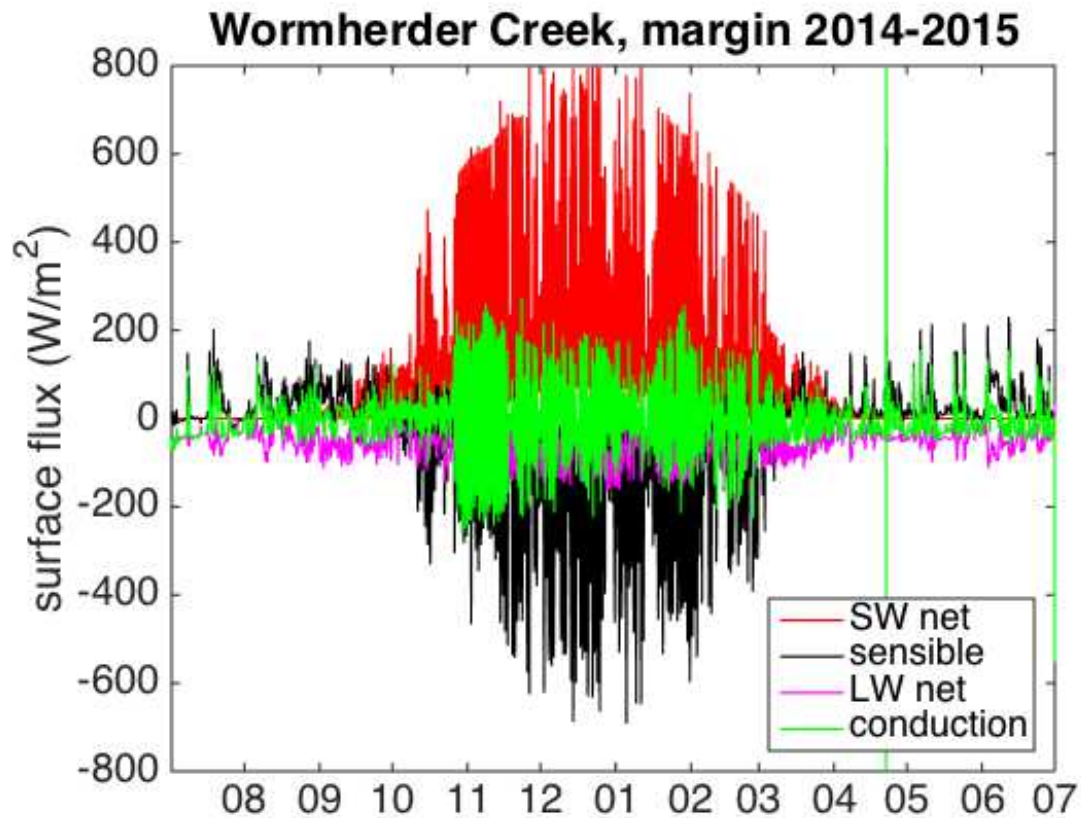


Figure 4.A14: Surface energy fluxes at WHC ALMS margin location between July 2014 and July 2015. Positive values indicate energy transfer into the ground surface from the atmosphere, and negative values indicate energy transfer from the ground surface to the atmosphere. The largest positive flux is net SW radiation, which ranges from 0 – 800 W/m². Sensible heat flux is positive in the winter and negative in the summer, ranging from -690– 231 W/m². Net LW radiation is predominantly negative during, but exhibits a range of -205 – 33 W/m². Conduction oscillates between positive and negative on a diel basis and has a range of -260 – 245 W/m².

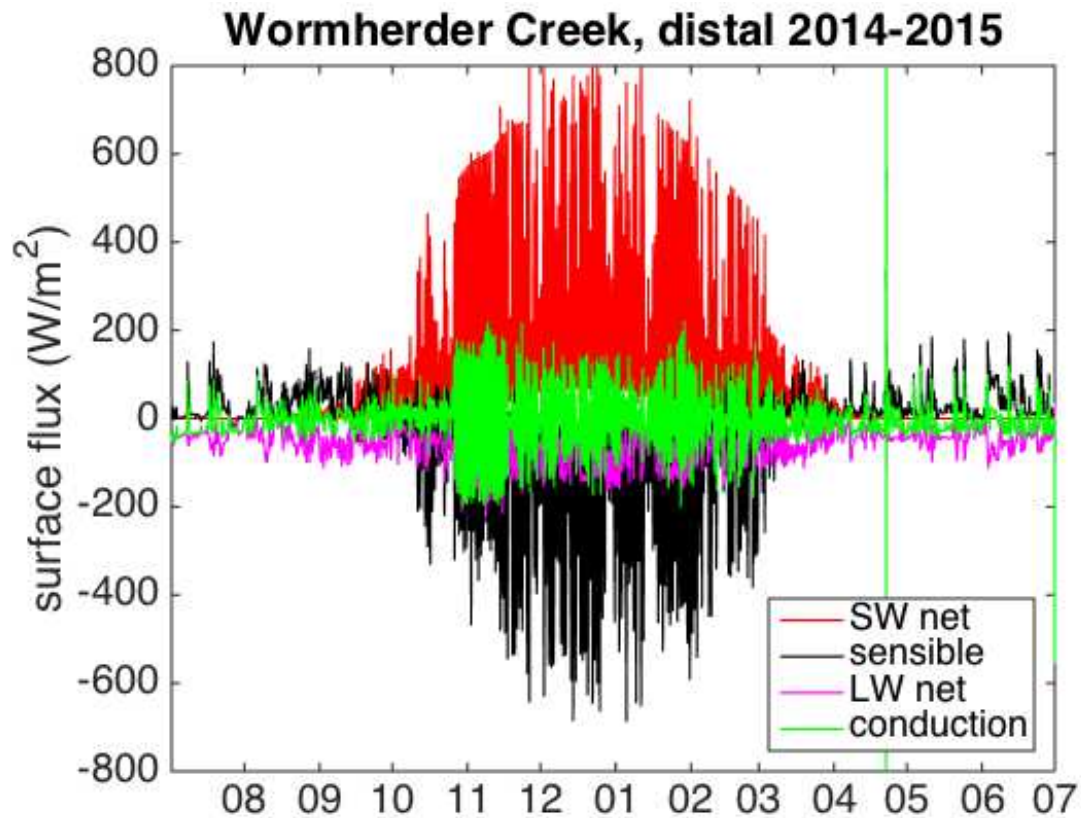


Figure 4.A15: Surface energy fluxes at WHC ALMS distal location between July 2014 and July 2015. Positive values indicate energy transfer into the ground surface from the atmosphere, and negative values indicate energy transfer from the ground surface to the atmosphere. The largest positive flux is net SW radiation, which ranges from 0 – 800 W/m². Sensible heat flux is positive in the winter and negative in the summer, ranging from -687 – 195 W/m². Net LW radiation is predominantly negative during, but exhibits a range of -245 – 37 W/m². Conduction oscillates between positive and negative on a diel basis and has a range of -200 – 212 W/m².

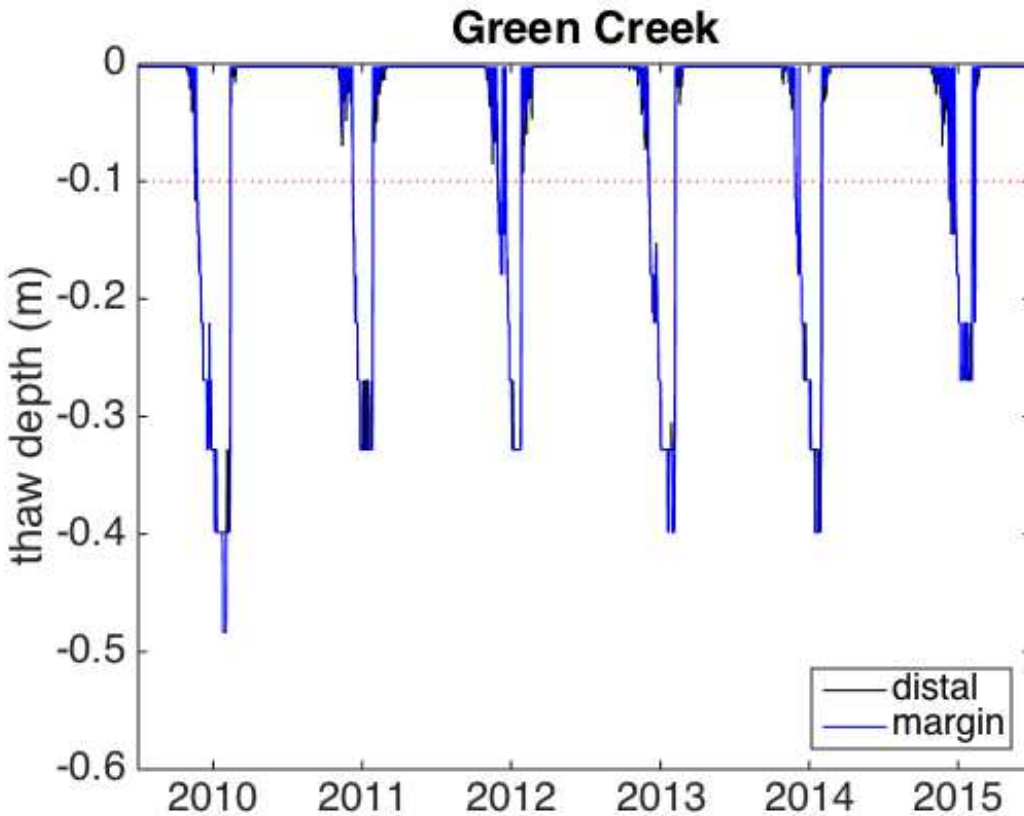


Figure 4.A16: Active layer depth at Green Creek distal ($\theta = 0.12$) and margin ($\theta = 0.25$) locations between July 2009 and July 2015. Maximum active layer depth occurred in 2010 at both distal (-0.4 m) and margin (-0.5 m) locations. The shallowest active layer thaw depth occurs in 2015 at both distal (-0.27) and margin (-0.27) locations. At Green Creek, the wetter margin location thaws deeper than or equal to the thaw depth at the distal location. . On a sub-seasonal basis, the wetter margin site begins thawing and refreezes later than the drier distal site. Also, the drier distal site exhibits more sub-seasonal variability in thaw depth than the wetter margin site.

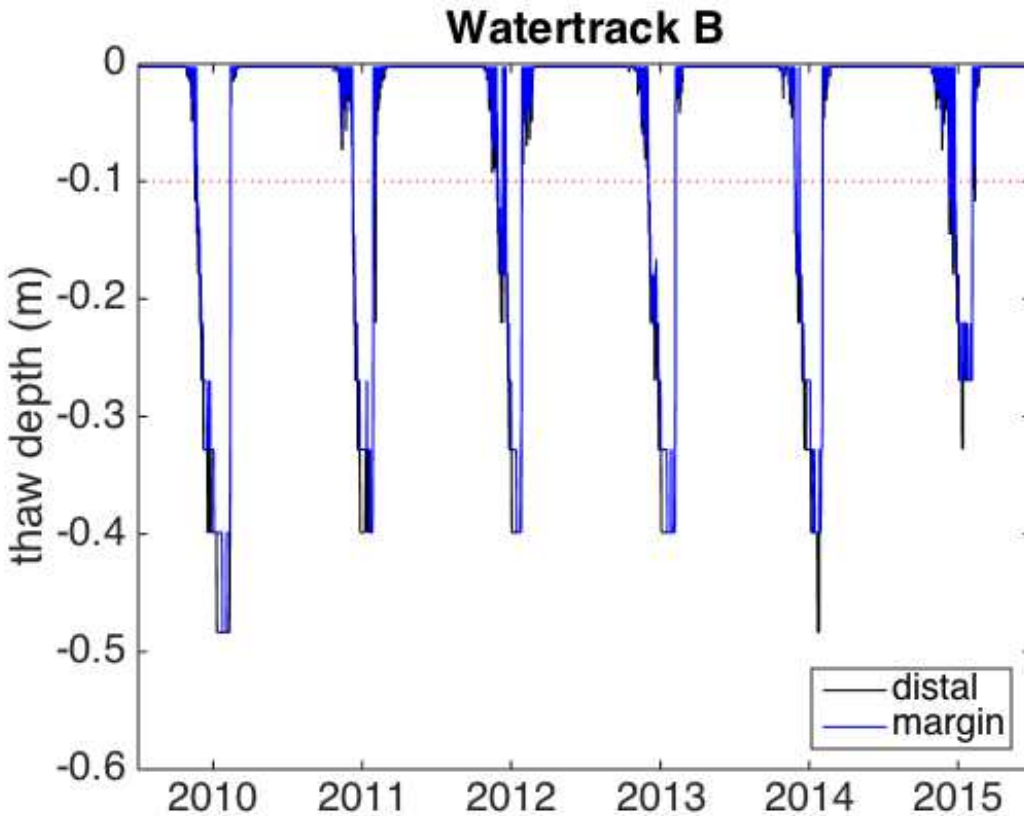


Figure 4.A17: Active layer depth at Watertrack B distal ($\theta = 0.10$) and margin ($\theta = 0.18$) locations between July 2009 and July 2015. Maximum active layer depth occurred in 2010 at both distal (-0.5 m) and margin (-0.5 m) locations. The shallowest active layer thaw depth occurs in 2015 at both distal (-0.33) and margin (-0.27) locations. At Watertrack B, the drier distal location thaws deeper than or equal to the thaw depth at the wetter margin location. On a sub-seasonal basis, the wetter margin site begins thawing and refreezes later than the drier distal site. Also, the drier distal site exhibits more sub-seasonal variability in thaw depth than the wetter margin site.

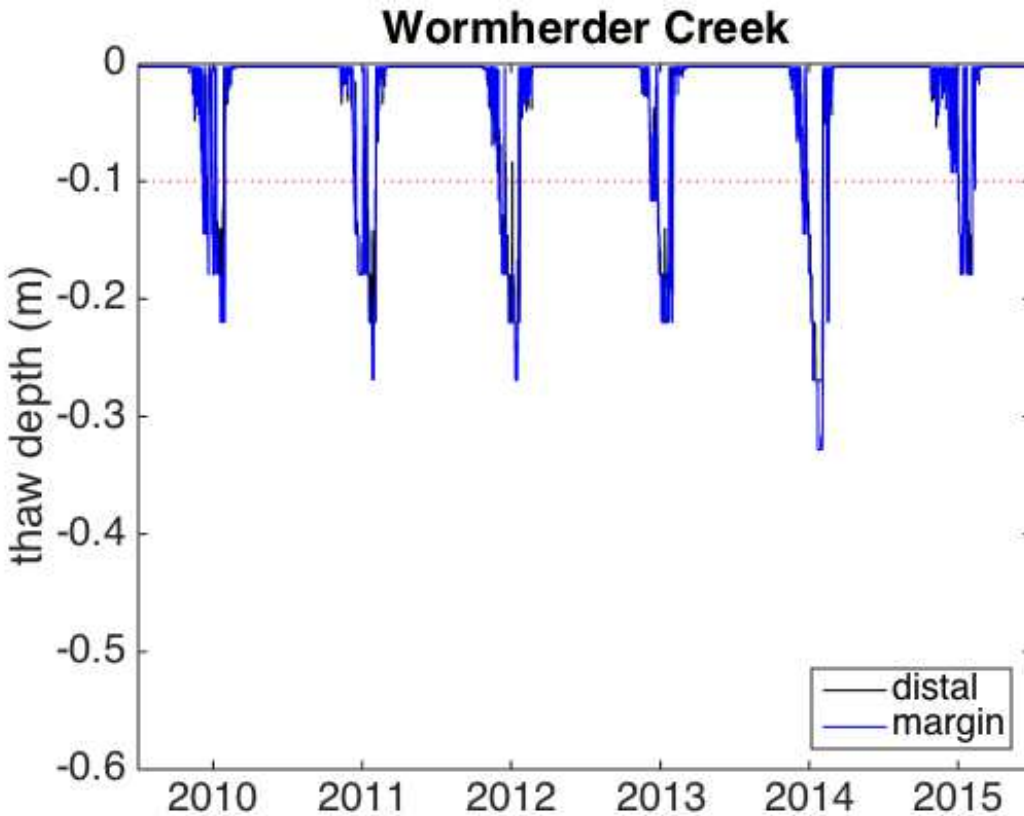


Figure 4.A18: Active layer depth at Wormherder Creek distal ($\theta = 0.16$) and margin ($\theta = 0.25$) locations between July 2009 and July 2015. Maximum active layer depth occurred in 2014 at both distal (-0.27 m) and margin (-0.33 m) locations. The shallowest active layer thaw depth occurs in 2015 at both distal (-0.18) and margin (-0.18) locations. Wormherder Creek shows the shallowest thaw depths among all other ALMS sites for all years of record considered here. Also, at Wormherder Creek the wetter margin location thaws deeper than or equal to the thaw depth at the drier distal location. On a sub-seasonal basis, the wetter margin site begins thawing and refreezes later than the drier distal site. Sub-seasonal variability between distal and margin sites is similar.

CHAPTER 5: Conclusions

Perhaps one of the most influential and controversial environmental laws in the United States is the Clean Water Act (CWA). The CWA was passed into law in 1972 during the political aftermath of widespread water quality degradation in the United States. The CWA is intended to restore and maintain the physical, chemical and biological integrity of navigable waters by establishing a regulatory framework for the discharge of pollutants and maintenance of surface water quality standards. The jurisdictional reach of the CWA is limited by interpretation. What constitutes a navigable waterway? Are tributaries to navigable waterways also regulated under the CWA?

Since the enactment of the CWA, several Supreme Court rulings have clarified the law's interpretation. Most notably, In the *Solid Waste Agency of Northern Cook Cty v. Army Corps of Engineers*, 531 U.S. 159 (2001), the court ruled the jurisdictional reach of the CWA applied to any water body possessing a “significant nexus” with “waters that are or were navigable in fact or that could reasonably be so made”. With this case, the Supreme Court effectively challenged the hydrological science community to define and quantify the nature of the “significant nexus”.

Nexus is defined in the *Miriam-Webster English Dictionary* as a “connection or series of connections linking two or more things.” In seeking to define a “significant nexus,” the hydrologic science community has coined the concept of “hydrologic connectivity”. Hydrologic connectivity is defined as the water-mediated transfer of matter and energy between landscape units [Pringle, 2003; Liebowitz et al., 2013], and provides a conceptual umbrella for

understanding how hydrologic fluxes mediate spatial and temporal patterns of biology and chemistry within and between watersheds.

The purpose of this dissertation is to quantify the magnitude, duration, and timing of hydrological connections in the McMurdo Dry Valleys of Antarctica, with a broader intention of understanding water mediated biological and chemical patterns. This dissertation provides a basic science stepping-stone for the greater hydrological science community, while simultaneously addressing specific concerns regarding a changing hydrologic regime expected under a warming climate, and subsequent ecosystem responses.

Hydrologic connectivity across the Earth's cryosphere is particularly sensitive to surface warming. In these regions, surface temperatures oscillate near water's freezing point, so small increases in temperature can result in disproportionately large increases in meltwater generation [Marshall, 2013]. The MDVs provide an ideal landscape for studying how energy-mediated hydrologic connectivity controls ecosystems [Fountain *et al.*, 1999]. The MDVs are characterized by an extremely dry and cold climate, where the glacier melt is the dominant source of liquid water to the landscape [Doran *et al.*, 2002]. Despite the harsh climate, invertebrate and microbial ecosystems are found in soils [Barrett *et al.*, 2006], streams [McKnight *et al.*, 2007], lakes [Lizotte *et al.*, 1996], and glaciers [Porazinska *et al.*, 2004]. The form and function the MDV ecosystem is heavily constrained by the paucity of liquid water [Kennedy, 1993], and henceforth vulnerable to a changing hydrologic regime.

The McMurdo Dry Valley Long Term Ecological Research project hypothesizes that climate warming in the MDV ecosystem will amplify hydrologic and biological connectivity among landscape units. This dissertation work is intended to contribute to a broader body of research addressing this hypothesis. The dissertation is divided into four chapters. Each chapter is focused on developing conceptual and/or mathematical models to understand contemporary and future patterns of water mediated fluxes of mass and energy.

Chapter 1 of this dissertation analyzes 20 years of streamflow, stream water temperature, and stream water specific conductance data to assess patterns of hydrologic connectivity between glaciers, streams, and lakes in the MDVs. Synthesis of long-term stream gauge records reveal hydrologic patterns at daily, annual, and inter-annual timescales. Together, these patterns define the hydrologic regime of MDV streams.

At the daily timescale, streams exhibited 24-hour patterns of discharge, temperature and specific conductivity. Stream hydrographs reveal the occurrence of daily flood events, caused by the downstream propagation of meltwater pulses from glacier surfaces. Stream length, glacier valley position, and the timing/intensity of solar insolation on steep glacier cliffs control the magnitude and timing of daily flood events. Stream water temperature also exhibits diel variations. The timing of daily peak water temperature is similar among streams, and coincident with the timing of solar noon. Furthermore, a unique relationship between Q and EC was observed at each stream. Some streams, such as Canada, show a daily dilution dynamic, where EC varies

inversely with Q. However, other streams, such as Aiken, show a flushing dynamic, where EC changes directly with Q.

At the annual timescale, stream length seems to affect a stream's hydrologic regime. Shorter streams are less intermittent, sustain higher flow magnitudes, and are cooler than longer streams. Also, longer streams exhibit higher solute concentrations and more chemostatic EC-Q relationships than shorter streams. Differences in annual EC and EC-Q dynamics among streams indicate that longer streams are more influenced by hyporheic exchange than shorter streams.

Annual stream flow dynamics exhibit strong inter-annual variability following the 2001/2001 "flood year". Post 2001/2002, annual streamflow has been greater and more variable, relative to pre 2001/2002 years. Future air temperature warming may further increase annual flow volumes, possibly causing a shift in stream ecosystems, specifically the abundance of diversity of benthic microbial communities.

The analyses outlined in Chapter 1 are intended to quantify the duration, magnitude, and timing of hydrologic connections at nested temporal scales. As such, Chapter 1 can provide a framework for understanding and quantifying hydrologic connectivity in polar and temperate watersheds, alike. Moreover, Chapter 1 provides the most comprehensive synthesis of stream flow, stream water temperature, and stream water specific conductance for streams in the MDVs to date. The results of this work will serve as a resource to other investigators studying long-term changes in MDV aquatic ecosystems.

A key finding of Chapter 1 is the chemostatic nature EC-Q relationships. Chemostasis implies that solute fluxes within a watershed scale proportionally with water fluxes through a watershed. The finding of chemostasis in Chapter 1 is surprising given the relatively simple structure of MDV “watersheds”. MDV watersheds are limited to the stream corridor. Hyporheic zones are the only venue of hydrologic connectivity between streams and soils, Further streams and hyporheic zones are the only geochemical filters modifying water chemistry between glaciers and lakes. As such, Chapter 2 is motivated and guided by the hypothesis that hyporheic exchange and high rates of chemical weathering control the nature of C-Q relationships for weathering-derived solutes.

Analysis of long-term geochemical data reveals that weathering-derived solutes exhibit chemostatic C-Q relationships in streams throughout the Fryxell Basin. Moreover annual Si denudation rates show a positive scaling relationship with annual specific discharge. A numerical weathering and transport model is developed to test the hypothesis that hyporheic exchange and rapid weathering rates are responsible for maintaining a chemostatic Si-Q regime. Model results show that 1) an ‘old-water’ explanation for Si-Q relationships is not plausible in MDV streams, 2) the simple combination of high (and constant) weathering rates and hyporheic exchange cannot explain Si-Q relationships, and 3) chemostatic Si-Q relationships can be simulated by a positive scaling relationship between weathering rates and discharge.

Overall, results of Chapter 2 refute the guiding hypothesis that hyporheic exchange and high weathering rates are solely responsible for shaping Si-Q relationships. Instead, model results point towards a more refined hypothesis for the mechanisms driving chemostasis: Chemostasis is maintained by hyporheic exchange and a positive scaling relationship between weathering rates and discharge. This refined hypothesis is not tested in the dissertation, but provides a benchmark for future studies.

Chapter 2 mandated the development of an unsteady solute transport model with hyporheic exchange, weathering, and a thermally dynamic hyporheic zone. This model can be used as a template for future modeling of physical, chemical and biological processes in MDV streams. Until now, solute transport modeling of MDV streams has been limited to small spatial extents (< 1km) and short temporal extents (<2 days). The model developed in Chapter 2 is intended to simulate continuous solute fate and transport along an entire stream reach for consecutive seasons. Also, this model is the only one-dimensional transport and transient storage model that considers the effect of a thermally expanding and contracting storage zone. For this reason, the model can be applied in other domains where streambeds undergo annual freezing and thawing.

Chapters 3 and 4 of this dissertation pivot from streams to soils, and investigate water-mediated energy connections between the atmosphere and soil habitat. The specific goal of these chapters is to quantify how increasing air temperature and soil moisture, expected under future climate scenarios, may alter the soil habitat. The results of Chapter 3 show that soil moisture affects the frequency and rate of freezing events in the soil habitat. Specifically, wetter soils freeze less

frequently and more gradually than drier soils. Chapter 4 shows that increases in soil moisture *and* air temperature will result in warmer average habitat temperature, an extension of the duration of time soil habitats spends above freezing, and a reduction in the rate and frequency of freezing.

Results of Chapters 3 and 4 have significant implications for soil nematode communities. Some nematode species, such as *P. antarcticus* and *E. antarcticus*, are more physiologically adapted to survive slower freezing in a wetter environment, than others, *S. lindsayae*. Under a warmer and wetter climate scenario, a reduction in freeze frequency will allow nematodes to devote fewer metabolic resources to surviving freeze stress. Furthermore, climate warming increases the duration of time the soil habitats spends above zero. As such, nematodes will have more time each year for growth and reproduction. Together, these results indicate that climate change can cause shifts in species diversity and abundance and ecosystem productivity.

Finally, it is necessary to take a step back and contemplate the relevance of this research to the broader scientific and global community. While this research is immediately relevant to the McMurdo Dry Valleys science community, the conceptual underpinnings extend much further. This research was motivated by the need to understand the nature and consequences of hydrologic connections in a non-stationary world. This dissertation provides methodological and conceptual advances, which can be utilized by other researchers and practitioners to understand the value of hydrologic connectivity in many other systems.

BIBLIOGRAPHY

- Adams, B. J. et al. (2006), Diversity and distribution of Victoria Land biota, *Soil Biol. Biochem.*, 38(10), 3003–3018, doi:10.1016/j.soilbio.2006.04.030.
- Adhikari, B. N., D. H. Wall, and B. J. Adams (2010), Effect of slow desiccation and freezing on gene transcription and stress survival of an Antarctic nematode., *J. Exp. Biol.*, 213(11), 1803–1812, doi:10.1242/jeb.032268.
- Alger, A. S. (1997), *Ecological processes in a cold desert ecosystem: The abundance and species of algal mats in glacial meltwater streams in Taylor Valley*, Boulder, CO.
- Anderson, D. M., and A. R. Tice (1973), The unfrozen interfacial phase in frozen soil water systems, in *Physical Aspects of Soil Water and Salts in Ecosystems*, pp. 107–124.
- Anderson, R. S., S. P. Anderson, and G. E. Tucker (2013), Rock damage and regolith transport by frost: an example of climate modulation of the geomorphology of the critical zone, *Earth Surf. Process. Landforms*, 38(3), 299–316, doi:10.1002/esp.3330.
- Anderson, S. P. (2005), Glaciers show direct linkage between erosion rate and chemical weathering fluxes, *Geomorphology*, 67(1–2 SPEC. ISS.), 147–157, doi:10.1016/j.geomorph.2004.07.010.
- Anderson, S. P., J. I. Drever, and N. F. Humphrey (1997a), Chemical weathering in glacial environments, *Geology*, 25(5), 399–402, doi:10.1130/0091-7613(1997)025<0399:CWIGE>2.3.CO.
- Anderson, S. P., W. E. Dietrich, R. Torres, D. R. Montgomery, and K. Loague (1997b), Concentration-discharge relationships in runoff from a steep, unchanneled catchment, *Water Resour. Res.*, 33(1), 211–225, doi:10.1029/96WR02715.
- Barnes, S. L. (1964), A Technique for Maximizing Details in Numerical Weather Map Analysis, *J. Appl. Meteorology*, 3, 396–409.
- Barrett, E. J., A. R. Virginia, and H. D. Wall (2002), Trends in Resin and KCl-extractable Soil Nitrogen Across Landscape Gradients in Taylor Valley, Antarctica, *Ecosystems*, 5(3), 289–299, doi:10.1007/s10021-001-0072-6.
- Barrett, J. E. et al. (2006), Terrestrial ecosystem processes of Victoria Land, Antarctica, *Soil Biol. Biochem.*, 38(10), 3019–3034, doi:10.1016/j.soilbio.2006.04.041.
- Barrett, J. E., R. a. Virginia, D. H. Wall, P. T. Doran, a. G. Fountain, K. a. Welch, and W. B. Lyons (2008), Persistent effects of a discrete warming event on a polar desert ecosystem, *Glob. Chang. Biol.*, 14(10), 2249–2261, doi:10.1111/j.1365-2486.2008.01641.x.
- Barrett, J. E., M. N. Gooseff, and C. Takacs-Vesbach (2009), Spatial variation in soil active-layer geochemistry across hydrologic margins in polar desert ecosystems, *Hydrol. Earth Syst. Sci. Discuss.*, 6(3), 3725–3751, doi:10.5194/hessd-6-3725-2009.
- Bockheim, J. G. (1997), Properties and Classification of Cold Desert Soils from Antarctica, *Soil Sci. Soc. Am. J.*, 231, 224–231.
- Bockheim, J. G., and M. McLeod (2008), Soil distribution in the McMurdo Dry Valleys, Antarctica, *Geoderma*, 144(1–2), 43–49, doi:10.1016/j.geoderma.2007.10.015.
- Bockheim, J. G., I. B. Campbell, and M. McLeod (2007), Permafrost Distribution and Active-Layer Depths in the McMurdo Dry Valleys, Antarctica, *Permafr. Periglac. Process.*, 227(December 2006), 217–227, doi:10.1002/ppp.
- Botter, G., S. Zanardo, A. Porporato, I. Rodriguez-Iturbe, and A. Rinaldo (2008),

- Ecohydrological model of flow duration curves and annual minima, *Water Resour. Res.*, 44(8), W08418, doi:10.1029/2008WR006814.
- Bromley, A. M. (1985), *Weather observations in Wright Valley, Antarctica*, Information Publication 11, Wellington (New Zealand).
- Campbell, I. B., G. G. C. Claridge, D. I. Campbell, and M. R. Balks (1998), The soil environment of the McMurdo Dry Valleys, Antarctica, in *Ecosystem Dynamics in a Polar Desert: The McMurdo Dry Valleys, Antarctica*, edited by J. C. Prisco, pp. 297–322, American Geophysical Union, Washington, D.C.
- Cary, S. C., I. R. McDonald, J. E. Barrett, and D. a Cowan (2010), On the rocks: the microbiology of Antarctic Dry Valley soils., *Nat. Rev. Microbiol.*, 8(2), 129–38, doi:10.1038/nrmicro2281.
- Chanat, J. G., K. C. Rice, and G. M. Hornberger (2002), Consistency of patterns in concentration-discharge plots, *Water Resour. Res.*, 38(8), 1–10, doi:10.1029/2001WR000971.
- Chapman, W. L., and J. E. Walsh (2007), A Synthesis of Antarctic Temperatures, *J. Clim.*, 20(16), 4096–4117, doi:10.1175/JCLI4236.1.
- Chinn, T. J. H. (1993), Physical hydrology of the dry valleys lakes, edited by W. J. Green and E. I. Friedmann, *Antarct. Res. Ser.*, 59, 1–51.
- Clow, D. W., and M. A. Mast (2010), Mechanisms for chemostatic behavior in catchments: Implications for CO₂ consumption by mineral weathering, *Chem. Geol.*, 269(1–2), 40–51, doi:10.1016/j.chemgeo.2009.09.014.
- Conovitz, P. A., D. M. McKnight, L. H. MacDonald, A. G. Fountain, and H. R. House (1998), Hydrologic Processes Influencing Streamflow Variation in Fryxell Basin, Antarctica, in *Ecosystem Dynamics in a Polar Desert: The McMurdo Dry Valleys, Antarctica*, edited by J. C. Prisco, American Geophysical Union, Washington, D.C.
- Conovitz, P. A., L. H. MacDonald, and D. M. McKnight (2006), Spatial and Temporal Active Layer Dynamics along Three Glacial Meltwater Streams in the McMurdo Dry Valleys , Antarctica, *Arctic, Antarct. Alp. Res.*, 38(1), 42–53.
- Cornelis, J. T., B. Delvaux, R. B. Georg, Y. Lucas, J. Ranger, and S. Opfergelt (2011), Tracing the origin of dissolved silicon transferred from various soil-plant systems towards rivers: A review, *Biogeosciences*, 8(1), 89–112, doi:10.5194/bg-8-89-2011.
- Covino, T., B. McGlynn, and J. Mallard (2011), Stream-groundwater exchange and hydrologic turnover at the network scale, *Water Resour. Res.*, 47, W12521, doi:10.1029/2011WR010942.
- Cozzetto, K., D. McKnight, T. Nylén, and A. Fountain (2006), Experimental investigations into processes controlling stream and hyporheic temperatures , Fryxell Basin , Antarctica, *Adv. Water Resour.*, 29, 130–153, doi:10.1016/j.advwatres.2005.04.012.
- Cozzetto, K. D., K. E. Bencala, M. N. Gooseff, and D. M. McKnight (2013), The influence of stream thermal regimes and preferential flow paths on hyporheic exchange in a glacial meltwater stream, *Water Resour. Res.*, 49(9), 5552–5569, doi:10.1002/wrcr.20410.
- Cullis, J. D. S., L. F. Stanish, and D. M. McKnight (2014), Diel flow pulses drive particulate organic matter transport from microbial mats in a glacial meltwater stream in the McMurdo Dry Valleys, *Water Resour. Res.*, 50(1), 86–97, doi:10.1002/2013WR014061.
- Dana, G. L., R. A. J. Wharton, and R. Dubayah (1998), Solar Radiation in the McMurdo Dry

- Valleys, Antarctica, in *Ecosystem Dynamics in a Polar Desert: The McMurdo Dry Valleys, Antarctica*, edited by J. C. Priscu, pp. 39–63, American Geophysical Union, Washington, D.C.
- Deuerling, K. M., W. B. Lyons, S. A. Welch, and K. A. Welch (2014), The characterization and role of aeolian deposition on water quality, McMurdo Dry Valleys, Antarctica, *Aeolian Res.*, *13*, 7–17, doi:10.1016/j.aeolia.2014.01.002.
- Doran, P. T., R. A. W. Wharton Jr., and W. B. Lyons (1994), Paleolimnology of the McMurdo Dry Valleys, Antarctica, *J. Paleolimnol.*, *10*, 85–114.
- Doran, P. T., C. P. McKay, G. D. Clow, G. L. Dana, A. G. Fountain, T. Nylén, and W. B. Lyons (2002), Valley floor climate observations from the McMurdo dry valleys, *J. Geophys. Res.*, *107*(D24), 1–12, doi:10.1029/2001JD002045.
- Doran, P. T., C. P. McKay, A. G. Fountain, T. Nylén, D. M. McKnight, C. Jaros, and J. E. Barrett (2008), Hydrologic response to extreme warm and cold summers in the McMurdo Dry Valleys, East Antarctica, *Antarct. Sci.*, *20*(5), 499–509, doi:10.1017/S0954102008001272.
- Ebnet, A. F., A. G. Fountain, T. H. Nylén, D. M. McKnight, and C. Jaros (2005), A temperature-index model of stream flow at below-freezing temperatures in Taylor Valley, Antarctica, *Ann. Glaciol.*, *40*, 76–82.
- EPA (2014), *Definition of “Waters of the United States” Under the Clean Water Act; Proposed Rule*.
- Esposito, R. M. M., S. L. Horn, D. M. McKnight, M. J. Cox, M. C. Grant, S. A. Spaulding, P. T. Doran, and K. D. Cozzetto (2006), Antarctic climate cooling and response of diatoms in glacial meltwater streams, *J. Geophys. Res.*, *33*, 2–5, doi:10.1029/2006GL025903.
- Esposito, R. M. M., S. A. Spaulding, D. M. McKnight, B. Van de Vijver, K. Kopalová, D. Lubinski, B. Hall, and T. Whittaker (2008), Inland diatoms from the McMurdo Dry Valleys and James Ross Island, Antarctica, *Botany*, *86*(12), 1378–1392, doi:10.1139/B08-100.
- Evans, C., and T. D. Davies (1998), Causes of concentration / discharge hysteresis and its potential as a tool for analysis of episode hydrochemistry, *Water Resour. Res.*, *34*(1), 129–137.
- Eveland, J., M. N. Gooseff, D. J. Lampkin, J. E. Barrett, and C. Takacs-vesbach (2013), Spatial and temporal patterns of snow accumulation and aerial ablation across the McMurdo Dry Valleys, Antarctica, *Hydrol. Process.*, *2875*(June 2012), 2864–2875, doi:10.1002/hyp.9407.
- Farouki, O. T. (1981), *Thermal properties of soils*, Hanover, New Hampshire.
- Foreman, C. M., C. F. Wolf, and J. C. Priscu (2004), Impact of Episodic Warming Events on the Physical, Chemical and Biological Relationships of Lakes in the McMurdo Dry Valleys, Antarctica, *Aquat. Geochemistry*, *10*, 239–268.
- Fortner, S. K., M. Tranter, A. Fountain, W. B. Lyons, and K. A. Welch (2005), The Geochemistry of Supraglacial Streams of Canada Glacier, Taylor Valley (Antarctica), and their Evolution into Proglacial Waters, *Aquat. Geochemistry*, *11*(4), 391–412, doi:10.1007/s10498-004-7373-2.
- Fountain, A. G. et al. (1999), Physical Controls on the Taylor Valley Ecosystem, Antarctica, *Bioscience*, *49*(12), 961–971.
- Fountain, A. G., T. H. Nylén, A. Monaghan, H. J. Basagic, and D. Bromwich (2010), Snow in

- the McMurdo Dry Valleys , Antarctica, *Int. J. Climatol.*, 642(30), 633–642, doi:10.1002/joc.1933.
- Fountain, A. G., J. S. Levy, M. N. Gooseff, and D. Van Horn (2014), The McMurdo Dry Valleys: A landscape on the threshold of change, *Geomorphology*, 225, 25–35, doi:10.1016/j.geomorph.2014.03.044.
- Freckman, D. W., and R. A. Virginia (1997), LOW-DIVERSITY ANTARCTIC SOIL NEMATODE COMMUNITIES : DISTRIBUTION AND RESPONSE TO DISTURBANCE, *Ecology*, 78(2), 363–369.
- Gibbs, R. J. (1970), Mechanisms controlling world water chemistry, *Science (80-.)*, 170(3962), 1088–1090, doi:10.1126/science.170.3962.1088.
- Godsey, S. E., J. W. Kirchner, and D. W. Clow (2009), Concentration – discharge relationships reflect chemostatic characteristics of US catchments, *Hydrol. Process.*, 1864(May), 1844–1864, doi:10.1002/hyp.
- Gooseff, M. N., D. M. McKnight, W. B. Lyons, and A. E. Blum (2002), Weathering reactions and hyporheic exchange controls on stream water chemistry in a glacial meltwater stream in the McMurdo Dry Valleys, *Water Resour. Res.*, 38(12), 15-1-15–17, doi:10.1029/2001WR000834.
- Gooseff, M. N., D. M. McKnight, R. L. Runkel, and B. H. Vaughn (2003a), Determining long time-scale hyporheic zone flow paths in Antarctic streams, *Hydrol. Process.*, 17(9), 1691–1710, doi:10.1002/hyp.1210.
- Gooseff, M. N., J. E. Barrett, P. T. Doran, A. G. Fountain, W. B. Lyons, A. N. Parsons, D. L. Porazinska, R. A. Virginia, and D. H. Wall (2003b), Snow-Patch Influence on Soil Biogeochemical Processes and Invertebrate Distribution in the McMurdo Dry Valleys , Antarctica, *Arctic, Antarct. Alp. Res.*, 35(1), 91–99.
- Gooseff, M. N., D. M. Mcknight, R. L. Runkel, and J. H. Duff (2004), Denitrification and hydrologic transient storage in a glacial meltwater stream , McMurdo, *Limnol. Oceanogr.*, 49(5), 1884–1895.
- Gooseff, M. N., W. B. Lyons, D. M. McKnight, B. H. Vaughn, A. G. Fountain, and C. Dowling (2006), A Stable Isotopic Investigation of a Polar Desert Hydrologic System, McMurdo Dry Valleys, Antarctica, *Arctic, Antarct. Alp. Res.*, 38(1), 60–71.
- Gooseff, M. N., J. E. Barrett, M. L. Northcott, D. B. Bate, K. R. Hill, L. H. Zeglin, M. Bobb, and C. D. Takacs-Vesbach (2007), Controls on the Spatial Dimensions of Wetted Hydrologic Margins of Two Antarctic Lakes, *Vadose Zo. J.*, 6(4), 841, doi:10.2136/vzj2006.0161.
- Gooseff, M. N., D. M. McKnight, P. Doran, A. G. Fountain, and W. B. Lyons (2011), Hydrological Connectivity of the Landscape of the McMurdo Dry Valleys, *Geogr. Compass*, 9, 666–681.
- Green, W. J., and D. E. Canfield (1984), Geochemistry of the Onyx River (Wright Valley, Antarctica) and its role in the chemical evolution of Lake Vanda, *Geochim. Cosmochim. Acta*, 48(198 1), 2457–2467.
- Green, W. J., M. P. Angle, and K. E. Chave (1988), The geochemistry of antarctic streams and their role in the evolution of four lakes of the McMurdo dry valleys, *Geochim. Cosmochim. Acta*, 52(5), 1265–1274, doi:10.1016/0016-7037(88)90280-3.
- Green, W. J., B. R. Stage, A. Preston, S. Wagers, J. Shacat, and S. Newell (2005), Geochemical processes in the Onyx River, Wright Valley, Antarctica: Major ions, nutrients, trace metals,

- Geochim. Cosmochim. Acta*, 69(4), 839–850, doi:10.1016/j.gca.2004.08.001.
- Hall, F. R. (1970), Dissolved Relationships 1 . Mixing Models, *Water Resour. Res.*, 6(3).
- Hardy, J. P., P. M. Groffman, R. D. Fitzhugh, K. S. Henry, A. T. Welman, J. D. Demers, T. J. Fahey, C. T. Driscoll, L. Geraldine, and S. Nolan (2001), Snow depth manipulation and its influence on soil frost and water dynamics in a northern hardwood forest, , 151–174.
- Herndon, E. M., A. L. Dere, P. L. Sullivan, D. Norris, B. Reynolds, and S. L. Brantley (2015), Biotic controls on solute distribution and transport in headwater catchments, *Hydrol. Earth Syst. Sci. Discuss.*, 12(1), 213–243, doi:10.5194/hessd-12-213-2015.
- Hinzman, L. D., D. J. Goering, and D. L. Kane (1998), A distributed thermal model for calculating soil temperature profiles and depth of thaw in permafrost regions, *J. Geophys. Res.*, 103(98), 28975–28991.
- Hock, R. (2003), Temperature index melt modelling in mountain areas, , 282, 104–115, doi:10.1016/S0022-1694(03)00257-9.
- Hoffman, M. J. (2011), Spatial and Temporal Variability of Glacier Melt in the McMurdo Dry Valleys, Antarctica, Portland State University.
- Hoffman, M. J., A. G. Fountain, and G. E. Liston (2008), Surface energy balance and melt thresholds over 11 years at Taylor, *J. Geophys. Res.*, 113(December), 1–12, doi:10.1029/2008JF001029.
- Hoffman, M. J., A. G. Fountain, G. E. Liston, M. J. Hoffman, A. G. Fountain, and G. E. Liston (2016), Distributed modeling of ablation (1996 – 2011) and climate sensitivity on the glaciers of Taylor Valley, Antarctica, *J. Glaciol.*, 1–15, doi:10.1017/jog.2015.2.
- Holmstrup, M., M. Bayley, and H. Ramløv (2002), Supercool or dehydrate? An experimental analysis of overwintering strategies in small permeable arctic invertebrates, *Proc. Natl. Acad. Sci. U. S. A.*, 99(8), 5716–5720, doi:10.1073/pnas.082580699.
- Van Horn, D. J., J. G. Okie, H. N. Buelow, M. N. Gooseff, J. E. Barrett, and C. D. Takacs-Vesbach (2014), Soil microbial responses to increased moisture and organic resources along a salinity gradient in a polar desert., *Appl. Environ. Microbiol.*, 80(10), 3034–43, doi:10.1128/AEM.03414-13.
- Howard-Williams, C., I. Hawes, A. M. Schwarz, and J. A. Hall (1997), Sources and sinks on nutrients in a polar desert stream, the Onyx River, Antarctica, in *Ecosystem Processes in Antarctic Ice-free Landscapes*, pp. 155–170, Balkema, Rotterdam, Netherlands.
- Huang, C. P. (1975), The removal of aqueous silica from dilute aqueous solutions, *Earth Planet. Sci. Lett.*, 27, 265–274.
- Hunt, H. W., a. G. Fountain, P. T. Doran, and H. Basagic (2010), A dynamic physical model for soil temperature and water in Taylor Valley, Antarctica, *Antarct. Sci.*, 22(4), 419–434, doi:10.1017/S0954102010000234.
- Ikard, S. J., M. N. Gooseff, J. E. Barrett, and C. Takacs-vesbach (2009), Thermal Characterisation of Active Layer Across a Soil Moisture Gradient in the McMurdo Dry Valleys , Antarctica, *Permafr. Periglac. Process.*, 20, 27–39, doi:10.1002/ppp.
- Jafarov, E. E., S. S. Marchenko, and V. E. Romanovsky (2012), Numerical modeling of permafrost dynamics in Alaska using a high spatial resolution dataset, *Cryosphere*, 6(3), 613–624, doi:10.5194/tc-6-613-2012.
- Jafarov, E. E., V. E. Romanovsky, H. Genet, A. D. McGuire, and S. S. Marchenko (2013), The effects of fire on the thermal stability of permafrost in lowland and upland black spruce

- forests of interior Alaska in a changing climate, *Environ. Res. Lett.*, 8(3), 35030, doi:10.1088/1748-9326/8/3/035030.
- Jencso, K. G., B. L. McGlynn, M. N. Gooseff, S. M. Wondzell, K. E. Bencala, and L. a. Marshall (2009), Hydrologic connectivity between landscapes and streams: Transferring reach- and plot-scale understanding to the catchment scale, *Water Resour. Res.*, 45(4), 1–16, doi:10.1029/2008WR007225.
- Jones, L. M., and G. Faure (1978), A Study of Strontium Isotopes in Lakes and Surficial Deposits of the Ice-Free Valleys, Southern Victoria Land, Antarctica, *Chem. Geol.*, 22(24), 107–120.
- Kennedy, A. D. (1993), Water as a Limiting Factor in the Antarctic Terrestrial Environment: A Biogeographical Synthesis, *Arct. Alp. Res.*, 25(4), 308–315.
- Kersten, M. S. (1949), *Thermal properties of soils*.
- Keys, H. (1980), Air Temperature, Wind, Precipitation, and Atmospheric Humidity In the McMurdo Region, Antarctica, Victoria University of Wellington, Wellington, New Zealand.
- Kirchner, J. W. (2003), A double paradox in catchment hydrology and geochemistry, *Hydrol. Process.*, 17(4), 871–874, doi:10.1002/hyp.5108.
- Kirchner, J. W., X. Feng, and C. Neal (2000), Fractal stream chemistry and its implications for contaminant transport in catchments, *Nature*, 403(February), 524–527, doi:10.1038/35000537.
- Knox, M. a., D. H. Wall, R. a. Virginia, M. L. Vandegehuchte, I. S. Gil, and B. J. Adams (2015), Impact of diurnal freeze–thaw cycles on the soil nematode *Scottinema lindsayae* in Taylor Valley, Antarctica, *Polar Biol.*, doi:10.1007/s00300-015-1809-6.
- Koch, J. C., D. M. McKnight, and R. M. Neupauer (2011), Simulating unsteady flow, anabranching, and hyporheic dynamics in a glacial meltwater stream using a coupled surface water routing and groundwater flow model, *Water Resour. Res.*, 47(5), 1–15, doi:10.1029/2010WR009508.
- Kohler, T. J., L. F. Stanish, S. W. Crisp, J. C. Koch, D. Liptzin, J. L. Baeseman, and D. M. McKnight (2015a), Life in the Main Channel: Long-Term Hydrologic Control of Microbial Mat Abundance in McMurdo Dry Valley Streams, Antarctica, *Ecosystems*, 18(2), 310–327, doi:10.1007/s10021-014-9829-6.
- Kohler, T. J., E. Chatfield, M. N. Gooseff, J. E. Barrett, and D. M. McKnight (2015b), Recovery of Antarctic stream epilithon from simulated scouring events, *Antarct. Sci.*, 27(4), 341–354, doi:10.1017/S0954102015000024.
- Lancaster, N. (2002), Flux of Eolian Sediment in the McMurdo Dry Valleys, Antarctica: A Preliminary Assessment, *Arctic, Antarct. Alp. Res.*, 34(3), 318–323.
- Langford, Z. L. (2013), Are the Dry Valleys Getting Wetter? A preliminary assessment of wetness across the McMurdo Dry Valleys landscape, The Pennsylvania State University.
- Larned, S. T., T. Datry, D. B. Arscott, and K. Tockner (2010), Emerging concepts in temporary-river ecology, *Freshw. Biol.*, 55(4), 717–738, doi:10.1111/j.1365-2427.2009.02322.x.
- Levy, J. (2013), How big are the McMurdo Dry Valleys? Estimating ice-free area using Landsat image data, *Antarct. Sci.*, 25(1), 119–120, doi:10.1017/S0954102012000727.
- Levy, J. S., A. G. Fountain, M. N. Gooseff, K. A. Welch, and W. B. Lyons (2011), Water tracks and permafrost in Taylor Valley, Antarctica: Extensive and shallow groundwater

- connectivity in a cold desert ecosystem, *Geol. Soc. Am. Bull.*, 123(11–12), 2295–2311, doi:10.1130/B30436.1.
- Levy, J. S., A. G. Fountain, K. a. Welch, and W. B. Lyons (2012), Hypersaline “wet patches” in Taylor Valley, Antarctica, *Geophys. Res. Lett.*, 39(5), L05402, doi:10.1029/2012GL050898.
- Levy, J. S., A. G. Fountain, J. L. Dickson, J. W. Head, M. Okal, D. R. Marchant, and J. Watters (2013), Accelerated thermokarst formation in the McMurdo Dry Valleys, Antarctica., *Sci. Rep.*, 3, 2269, doi:10.1038/srep02269.
- Lewin, J. C. (1961), The dissolution of silica from diatom walls, *Geochim. Cosmochim. Acta*, 21(3–4), 182–198, doi:10.1016/S0016-7037(61)80054-9.
- Lewis, K. J., A. G. Fountain, and G. L. Dana (1998), Surface energy balance and meltwater production for a Dry Valley glacier, Taylor Valley, Antarctica, *Ann. Glaciol.*, 27, 603–609.
- Liebowitz, S. G., M. McManus, A. I. Pollard, H. Raanan-Kiperwas, C. E. Ridley, K. Schotfield, and P. J. Wigington (2013), *DRAFT: Connectivity of Streams and Wetlands to Downstream Waters : A Review and Synthesis of the Scientific Evidence*, Washinton, DC.
- Ling, F., and T. Zhang (2004), A numerical model for surface energy balance and thermal regime of the active layer and permafrost containing unfrozen water, *Cold Reg. Sci. Technol.*, 38, 1–15, doi:10.1016/S0165-232X(03)00057-0.
- Liston, G. E., and K. Elder (2006), A Meteorological Distribution System for High-Resolution Terrestrial Modeling (MicroMet), *J. Hydrometeorol.*, 7, 217–234.
- Lizotte, M. P., T. R. Sharp, and J. C. Priscu (1996), Phytoplankton dynamics in the stratified water column of Lake Bonney, Antarctica, *Polar Biol.*, 16, 155–162.
- Lovell, C. W. (1957), Temperature Effects on Phase Composition and Strength of Partially-Frozen Soil, *Highw. Res. Board Bull.*, (168), 74–95.
- Lunardini, V. J. (1891), *Heat Transfer in Cold Climates*, Can Nostrand Reinhold Company, New York, NY.
- Lyons, W. B., and P. A. Mayewski (1993), The Geochemical Evolution of Terrestrial Waters in the Antarctic: The Role of Rock-Water Interactions, in *Physical and Biogeochemical Processes in Antarctic Lakes, Antarctic Research Series, Volume 59*, pp. 135–149, American Geophysical Union.
- Lyons, W. B., K. A. Welch, C. A. Nezat, K. Crick, J. K. Toxey, J. A. Mastrine, and D. M. McKnight (1997), Chemical weathering rates and reactions in the Lake Fryxell Basin, Taylor Valley: Comparison to temperate river basins, in *Ecosystem Processes in Antarctic Ice-free Landscapes*, edited by W. B. Lyons, C. Howard-Williams, and I. Hawes, pp. 147–153, A.A. Balkema, Rotterdam, Netherlands.
- Lyons, W. B., K. A. Welch, A. G. Fountain, G. L. Dana, B. H. Vaughn, and D. M. McKnight (2003), Surface glaciochemistry of Taylor Valley, southern Victoria Land, Antarctica and its relationship to stream chemistry, *Hydrol. Process.*, 17(1), 115–130, doi:10.1002/hyp.1205.
- Marra, K. R., G. S. Soreghan, M. E. Elwood Madden, L. J. Keiser, and B. L. Hall (2014), Trends in grain size and BET surface area in cold-arid versus warm-semiarid fluvial systems, *Geomorphology*, 206, 483–491, doi:10.1016/j.geomorph.2013.10.018.
- Marra, K. R., M. E. Elwood Madden, G. S. Soreghan, and B. L. Hall (2016), Chemical weathering trends in fine-grained ephemeral stream sediments of the McMurdo Dry Valleys, Antarctica, *Geomorphology*, doi:10.1016/j.geomorph.2016.12.016.

- Marshall, G. J., and J. Turner (1997), Katabatic wind propagation over the western Ross Sea observed using ERS-1 scatterometer data, *Antarct. Sci.*, 9(2), 221–226.
- Marshall, S. J. (2013), *The Cryosphere*, 1st ed., Princeton University Press, Princeton, New Jersey.
- Maurice, P., D. M. McKnight, L. Leff, J. Fulghum, and M. Gooseff (2002), Direct observations of aluminosilicate weathering in the hyporheic zone of an Antarctic Dry Valley stream, *Geochim. Cosmochim. Acta*, 66(8), 1335–1347.
- Mayewski, P. A., and W. B. Lyons (1982), Source and climatic implication of the reactive iron and reactive silicate concentration found in a core from Meserve Glacier, Antarctica, *Geophys. Res. Lett.*, 9(3), 190–192, doi:10.1029/GL009i003p00190.
- McDonnell J.J. (1990), A Rational For Old Water Discharge Through Macroporos in a Steep, Humid Catchment, *Water Resour. Res.*, 26(11), 2821–2832, doi:10.1029/WR026i011p02821.
- McGlynn, B. L., and J. J. McDonnell (2003), Quantifying the relative contributions of riparian and hillslope zones to catchment runoff, *Water Resour. Res.*, 39(11), doi:10.1029/2003WR002091.
- McKay, C. P. (2009), Snow recurrence sets the depth of dry permafrost at high elevations in the McMurdo Dry Valleys of Antarctica, *Antarct. Sci.*, 21(1), 89, doi:10.1017/S0954102008001508.
- McKay, C. P., M. T. Mellon, and E. I. Friedmann (1998), Soil temperatures and stability of ice-cemented ground in the McMurdo Dry Valleys, Antarctica, *Antarct. Sci.*, 10(1), 31–38.
- McKeague, J. A., and M. G. Cline (1962), Silica In Soil Solutions: 1 The form and concentration of dissolved silica in aqueous extractions of some soils, *Can. J. Soil Sci.*, 43, 70–83.
- McKnight, D. M., D. K. Niyogi, A. S. Alger, A. Bomblies, P. A. Peter, and C. M. Tate (1999), Dry Valley Streams in Antarctica: Ecosystems Waiting for Water, *Bioscience*, 49(12), 985–995.
- McKnight, D. M., R. L. Runkel, C. M. Tate, J. H. Duff, and D. L. Moorhead (2004), Inorganic N and P dynamics of Antarctic glacial meltwater streams as controlled by hyporheic exchange and benthic autotrophic communities Inorganic N and P dynamics of Antarctic glacial meltwater streams as controlled by hyporheic exchange and benthic aut, *J. North Am. Benthol. Soc.*, 23(2), 171–188.
- McKnight, D. M., C. M. Tate, E. D. Andrews, D. K. Niyogi, K. Cozzetto, K. Welch, W. B. Lyons, and D. G. Capone (2007), Reactivation of a cryptobiotic stream ecosystem in the McMurdo Dry Valleys, Antarctica: A long-term geomorphological experiment, *Geomorphology*, 89(1–2), 186–204, doi:10.1016/j.geomorph.2006.07.025.
- Mikucki, J. A., and J. C. Priscu (2007), Bacterial diversity associated with Blood Falls, a subglacial outflow from the Taylor Glacier, Antarctica., *Appl. Environ. Microbiol.*, 73(12), 4029–39, doi:10.1128/AEM.01396-06.
- Mikucki, J. A., C. M. Foreman, B. Sattler, W. B. Lyons, and J. C. Priscu (2004), Geomicrobiology of Blood Falls : An Iron-Rich Saline Discharge at the Terminus of the Taylor Glacier, Antarctica, *Aquat. Geochemistry*, 10, 199–220.
- Mikucki, J. A., A. Pearson, D. T. Johnston, A. V. Turchyn, J. Farquhar, D. P. Schrag, A. D. Anbar, J. C. Priscu, and P. A. Lee (2009), A Contemporary Microbially Maintained Subglacial Ferrous “Ocean,” *Science (80-.)*, 663(April), 397–400.

- Moin, P. (2010), *Fundamentals of Engineering Numerical Analysis*, 2nd ed., Cambridge University Press, New York, NY.
- Mullin, J. B., and J. P. Riley (1955), The colorimetric determination of silicate with special reference to sea and natural waters, *Anal. Chim. Acta*, 12(C), 162–176, doi:10.1016/S0003-2670(00)87825-3.
- Nezat, C. A., W. B. Lyons, and K. A. Welch (2001), Chemical weathering in streams of a polar desert (Taylor Valley, Antarctica), *GSA Bull.*, 113(11), 1401–1408.
- Nielsen, U. N., D. H. Wall, B. J. Adams, R. A. Virginia, B. A. Ball, M. N. Gooseff, and D. M. Mcknight (2012), The ecology of pulse events : insights from an extreme climatic event in a polar desert ecosystem, *Ecosphere*, 3(February), 1–15.
- Niyogi, D. K., C. M. Tate, D. M. Mcknight, J. H. Duff, and A. S. Alger (1997), Species composition and primary production of algal communities in dry valley streams in Antarctica: examination of the functional role of biodiversity, in *Ecosystem processes in Antarctic Ice-Free Landscapes*, pp. 171–179, Balkema, Brookfield.
- Northcott, M. L., M. N. Gooseff, J. E. Barrett, L. H. Zeglin, C. D. Takacs-vesbach, and J. Humphrey (2009), Hydrologic characteristics of lake- and stream-side riparian wetted margins in the McMurdo Dry Valleys , Antarctica, *Hydrol. Process.*, 1267(March), 1255–1267, doi:10.1002/hyp.
- Nylen, T. H., A. G. Fountain, and P. T. Doran (2004), Climatology of katabatic winds in the McMurdo dry valleys, southern Victoria Land, Antarctica, *J. Geophys. Res.*, 109, D03114, doi:10.1029/2003JD003937.
- Okamoto, G., T. Okura, and K. Goto (1957), Properties of silica in water, *Geochim. Cosmochim. Acta*, 12(1–2), 123–132, doi:10.1016/0016-7037(57)90023-6.
- Oleson, K. W., D. M. Lawrence, B. Gordon, M. G. Flanner, E. Kluzek, L. J. Peter, S. Levis, S. C. Swenson, and P. E. Thornton (2010), *Technical Description of version 4.0 of the Community Land Model (CLM)*.
- Outcalt, S. I., F. E. Nelson, and K. M. Hinkel (1990), The zero-curtain effect: heat and mass transfer across an isothermal region in freezing soil, *Water Resour. Res.*, 26(7), 1509–1516, doi:10.1029/90WR00139.
- Payn, R. A., M. N. Gooseff, B. L. McGlynn, K. E. Bencala, and S. M. Wondzell (2009), Channel water balance and exchange with subsurface flow along a mountain headwater stream in Montana, United States, *Water Resour. Res.*, 45, W11427, doi:10.1029/2008WR007644.
- Payn, R. A., M. N. Gooseff, B. L. McGlynn, K. E. Bencala, and S. M. Wondzell (2012), Exploring changes in the spatial distribution of stream baseflow generation during a seasonal recession, *Water Resour. Res.*, 48(February), 1–15, doi:10.1029/2011WR011552.
- Pearce, A. J., M. K. Stewart, and M. G. Sklash (1986), Storm Runoff Generation in Humid Headwater Catchments 1. Where Does the Water Come From, *Water Resour. Res.*, 22(8), 1263–1272.
- Péwé, T. L. (1960), Multiple Glaciation in the McMurdo Sound Region, Antarctica: A Progress Report, *J. Geol.*, 68(5), 498–514.
- Pokrovski, G. S., J. Schott, F. Farges, and J.-L. Hazemann (2003), Iron (III)-silica interactions in aqueous solution: Insights from X-ray absorption fine structure spectroscopy, *Geochim. Cosmochim. Acta*, 67(19), 3559, doi:10.1016/S0016-7037(03)00160-1.
- Porazinska, D. L., A. G. Fountain, T. H. Nylen, M. Tranter, R. a. Virginia, and D. H. Wall

- (2004), The Biodiversity and biogeochemistry of cryoconite holes from McMurdo Dry Valley glaciers, Antarctica, *Arctic, Antarct. Alp. Res.*, 36(1), 84–91, doi:10.1657/1523-0430(2004)036[0084:TBABOC]2.0.CO;2.
- Prentice, M. L., J. Kleman, and A. P. Stroeven (1998), The Composite Glacial Erosional Landscape of the Northern McMurdo Dry Valleys: Implications for Antarctic Tertiary Glacial History, in *Ecosystem Dynamics in a Polar Desert: The McMurdo Dry Valleys, Antarctica*, edited by J. C. Prisco, pp. 1–38, American Geophysical Union, Washington, D.C.
- Pringle, C. (2003), What is hydrologic connectivity and why is it ecologically important?, *Hydrol. Process.*, 2689(May), 2685–2689, doi:10.1002/hyp.5145.
- Romanovsky, V. E., and T. E. Osterkamp (2000), Effects of Unfrozen Water on Heat and Mass Transport Processes in the Active Layer and Permafrost, *Permafrost Periglacial Processes*, 11(June), 219–239.
- Runkel, R. L. (1998), One-Dimensional Transport with Inflow and Storage (OTIS): A Solute Transport Model for Streams and Rivers, *USGS Water-Resources Investig. Rep.*, 98–4018, 1–73.
- Runkel, R. L., and S. C. Chapra (1993), An Efficient Numerical Solution of the Transient Storage Equations for Solute Transport in Small Streams, *Water Resour. Res.*, 29(1), 211–215.
- Runkel, R. L., D. M. McKnight, and E. D. Andrews (1998), Analysis of Transient Storage Subject to Unsteady Flow : Diel Flow Variation in an Antarctic Stream, *J. North Am. Benthol. Soc.*, 17(2), 143–154.
- Sawicz, K., T. Wagener, M. Sivapalan, P. A. Troch, and G. Carrillo (2011), Catchment classification: empirical analysis of hydrologic similarity based on catchment function in the eastern USA, *Hydrol. Earth Syst. Sci. Discuss.*, 8(3), 4495–4534, doi:10.5194/hessd-8-4495-2011.
- Shiklomanov, N. I., O. a. Anisimov, T. Zhang, S. Marchenko, F. E. Nelson, and C. Oelke (2007), Comparison of model-produced active layer fields: Results for northern Alaska, *J. Geophys. Res. Earth Surf.*, 112(2), 1–12, doi:10.1029/2006JF000571.
- Simmons, B. L., D. H. Wall, B. J. Adams, E. Ayres, J. E. Barrett, and R. a. Virginia (2009), Long-term experimental warming reduces soil nematode populations in the McMurdo Dry Valleys, Antarctica, *Soil Biol. Biochem.*, 41(10), 2052–2060, doi:10.1016/j.soilbio.2009.07.009.
- Sklash, M. G., M. K. Stewart, and aA J. Pearce (1986), A Case Study of Hillslope and Low-Order Stream Response deep J ' lysimeter, *Water Resour.*, 22(8), 1273–1282, doi:10.1029/WR022i008p01273.
- Speirs, J. C., D. F. Steinhoff, H. a. McGowan, D. D. Bromwich, and A. J. Monaghan (2010), Foehn winds in the McMurdo Dry Valleys, Antarctica: The origin of extreme warming events, *J. Clim.*, 23(13), 3577–3598, doi:10.1175/2010JCLI3382.1.
- Stanish, L. F., D. R. Nemergut, and D. M. McKnight (2011), Hydrologic processes influence diatom community composition in Dry Valley streams, *J. North Am. Benthol. Soc.*, 30(4), 1057–1073, doi:10.1899/11-008.1.
- Stanish, L. F., T. J. Kohler, R. M. M. Esposito, B. L. Simmons, U. N. Nielsen, D. H. Wall, D. R. Nemergut, and D. M. McKnight (2012), Extreme streams : flow intermittency as a control

- on diatom communities in meltwater streams in, *Can. J. Aquat. Sci.*, 15(February 2010), 1–15, doi:10.1139/F2012-022.
- Stanish, L. F., S. P. O'Neill, A. Gonzalez, T. M. Legg, J. Knelman, D. M. McKnight, S. Spaulding, and D. R. Nemergut (2013), Bacteria and diatom co-occurrence patterns in microbial mats from polar desert streams, *Environ. Microbiol.*, 15(4), 1115–1131, doi:10.1111/j.1462-2920.2012.02872.x.
- Stefan, V. J. (1891), Über die Theorie der Eisbildung, insbesondere über die Eisbildung im Polarmeere, *Ann. der Phys. und Chem.*, 42, 269–286.
- Struyf, E., A. Smis, S. van Damme, P. Meire, and D. J. Conley (2010), The global biogeochemical silicon cycle, *Silicon*, 1(4), 207–213, doi:10.1007/s12633-010-9035-x.
- Stumpf, A. R., M. E. Elwood Madden, G. S. Soreghan, B. L. Hall, L. J. Keiser, and K. R. Marra (2012), Glacier meltwater stream chemistry in Wright and Taylor Valleys, Antarctica: Significant roles of drift, dust and biological processes in chemical weathering in a polar climate, *Chem. Geol.*, 322–323, 79–90, doi:10.1016/j.chemgeo.2012.06.009.
- Sudman, Z., M. N. Gooseff, A. G. Fountain, J. S. Levy, M. K. Obryk, and D. Van Horn (2017), Impacts of permafrost degradation on a stream in Taylor Valley, Antarctica, *Geomorphology*, 285, 205–213, doi:10.1016/j.geomorph.2017.02.009.
- Swoboda-Colberg, N. G., and J. I. Drever (1993), Mineral dissolution rates in plot-scale field and laboratory experiments, *Chem. Geol.*, 105(1–3), 51–69, doi:10.1016/0009-2541(93)90118-3.
- Thackston, E. L., and K. B. Schnelle (1970), Predicting Effects of Dead Zones on Stream Mixing, *Proc. Am. Soc. Civ. Eng.*, 319–331.
- Topp, G. C., J. L. Davis, and a. P. Annan (1980), Electromagnetic determination of soil water content: Measurements in coaxial transmission lines, *Water Resour. Res.*, 16(3), 574, doi:10.1029/WR016i003p00574.
- Tranter, M., A. G. Fountain, C. H. Fritsen, W. B. Lyons, J. C. Prisco, P. J. Statham, and K. A. Welch (2004), Extreme hydrochemical conditions in natural microcosms entombed within Antarctic ice, *Hydrol. Process.*, 18(2), 379–387, doi:10.1002/hyp.5217.
- Treonis, A. M., D. H. Wall, and R. A. Virginia (1999), Invertebrate biodiversity in Antarctic Dry Valley soils and sediments, *Ecosystems*, 2(6), 482–492, doi:10.1007/s100219900096.
- Treonis, A. M., D. H. Wall, and R. A. Virginia (2000), The use of anhydrobiosis by soil nematodes in the Antarctic Dry Valleys, *Funct. Ecol.*, 14(4), 460–467, doi:10.1046/j.1365-2435.2000.00442.x.
- Turner, J., J. C. Comiso, G. J. Marshall, T. A. Lachlan-Cope, T. Bracegirdle, T. Maksym, M. P. Meredith, Z. Wang, and A. Orr (2009), Non-annular atmospheric circulation change induced by stratospheric ozone depletion and its role in the recent increase of Antarctic sea ice extent, *Geophys. Res. Lett.*, 36(8), L08502, doi:10.1029/2009GL037524.
- Velbel, M. A. (1985), Geochemical mass balances and weathering rates in forested watersheds of the southern Blue Ridge, *Am. J. Sci.*, 285, 904–930.
- Walsh, J. E. (2009), A comparison of Arctic and Antarctic climate change, present and future, *Antarct. Sci.*, 21(3), 179–188, doi:10.1017/S0954102009001874.
- Welch, K. A., W. B. Lyons, C. Whisner, C. B. Gardner, M. N. Gooseff, D. M. McKnight, and J. C. Prisco (2010), Spatial variations in the geochemistry of glacial meltwater streams in the Taylor Valley, Antarctica, *Antarct. Sci.*, 22(6), 662–672, doi:10.1017/S0954102010000702.

- Wharton, D. A. (2003), The environmental physiology of Antarctic terrestrial nematodes: A review, *J. Comp. Physiol. B Biochem. Syst. Environ. Physiol.*, 173(8), 621–628, doi:10.1007/s00360-003-0378-0.
- Wharton, D. A., G. Goodall, and C. J. Marshall (2002), Freezing rate affects the survival of short-term freezing stress in *Panagrolaimus davidi*, an antarctic nematode that survives intracellular freezing, *CryoLetters*, 23, 5–10.
- White, A. F., and A. E. Blum (1995), Effects of climate on chemical weathering in watersheds, *Geochim. Cosmochim. Acta*, 59(9), 1729–1747, doi:10.1016/0016-7037(95)00078-E.
- White, A. F., A. E. Blum, T. D. Bullen, D. V. Vivit, M. Schulz, and J. Fitzpatrick (1999), The effect of temperature on experimental and natural chemical weathering rates of granitoid rocks, *Geochim. Cosmochim. Acta*, 63(19–20), 3277–3291, doi:10.1016/S0016-7037(99)00250-1.
- Wlostowski, A., M. N. Gooseff, D. M. McKnight, C. Jaros, and W. B. Lyons (2016), Patterns of hydrologic Connectivity in the McMurdo Dry Valleys, Antarctica: a synthesis of 20 years of hydrologic data, *Hydrol. Process.*, 30(17), 2958–2975, doi:10.1002/hyp.10818.
- Yadav, M., T. Wagener, and H. Gupta (2007), Regionalization of constraints on expected watershed response behavior for improved predictions in ungauged basins, *Adv. Water Resour.*, 30(8), 1756–1774, doi:10.1016/j.advwatres.2007.01.005.
- Yang, E. S., D. M. Cunnold, M. J. Newchurch, and R. J. Salawitch (2005), Change in ozone trends at southern high latitudes, *Geophys. Res. Lett.*, 32(12), 1–5, doi:10.1029/2004GL022296.
- Zeglin, L. H., R. L. Sinsabaugh, J. E. Barrett, M. N. Gooseff, and C. D. Takacs-Vesbach (2009), Landscape Distribution of Microbial Activity in the McMurdo Dry Valleys: Linked Biotic Processes, Hydrology, and Geochemistry in a Cold Desert Ecosystem, *Ecosystems*, 12(4), 562–573, doi:10.1007/s10021-009-9242-8.